Dynamics and Stochastic Properties of Passively Mode-Locked Semiconductor Lasers Subject to Optical Feedback

vorgelegt von
MSc. Lina Jaurigue
geb. in Ebersberg

von der Fakultät II – Mathematik und Naturwissenschaften –

der Technischen Universität Berlin

zur Erlangung des akademischen Grades
Doktor der Naturwissenschaften
– Dr. rer. nat. –

genehmigte Dissertation

Promotionsausschuss:

Vorsitzender:	Prof. Dr. Michael Kneissl
Berichterin:	Prof. Dr. Kathy Lüdge
Berichter:	Prof. Dr. Eckehard Schöll, PhD
Berichter:	Dr. Julien Javaloyes

Tag der wissenschaftlichen Aussprache: 26. September 2016

Berlin 2016

Abstract

Passively mode-locked semiconductor lasers produce short optical pulses at very high repetition rates. In this thesis we investigate the influence of time-delayed optical feedback on the dynamics and timing jitter of such a laser.

Using a delay differential equation model we investigate the dynamics and bifurcations of a passively mode-locked laser. When the laser is operated in the fundamental mode-locking regime it produces a pulsed output with a repetition rate which is determined by the length of the laser cavity. Adding optical feedback to the laser in this regime, the dynamics depend on resonances between the period and the feedback delay times. Feedback conditions can be selected to tune the repetition rate of the mode-locked pulse train, to induce harmonic mode-locking or to destabilise the periodic mode-locked dynamics, resulting in quasi-periodic or chaotic dynamics. Surrounding each resonantly chosen delay time there is a locking range in which fundamental mode-locking is exhibited. This locking regions becomes wider as the delay times are increased, which can lead to a large degree of multistability between solutions locked to different resonances. With feedback from two external cavities the same dynamics can be exhibited as with single cavity feedback, but the multistability of the fundamentally mode-locked solutions can be lifted if the two external cavities are of different lengths.

In the presence of noise, the regularity of the mode-locked dynamics is significantly reduced, since due to the absence of a restoring force the pulse positions can drift over time. By adding resonant optical feedback correlations between temporal pulse positions are introduced, which can lead to a significant reduction in the timing jitter. We derive an expression for the timing jitter that shows that this reduction increases with the feedback delay time. However, for long feedback cavities noise-induced modulations of the dynamics also play a role, leading to fluctuations in the pulse positions on time scales of the feedback delay time.

The noise-induced modulations that arise for long feedback delay times can be suppressed by adding a second feedback cavity. We show that a linear stability analysis of the mode-locked laser system allows predictions to made for the optimal feedback conditions for this effect. This is done by first studying the suppression of noise-induced modulations in a simple oscillatory system, the Stuart-Landau oscillator, and relating the results for this system to the mode-locked laser system. For the Stuart-Landau oscillator a simple characteristic equation, which provides the dominant Floquet exponents, can be analytically derived. By comparison with numerical results, we show that the dominant Floquet exponents of the mode-locked laser system can be described by a simple characteristic equation of the same form as that derived for the Stuart-Landau oscillator.

Using this characteristic equation, feedback delay times are found which effectively suppress the noise-induced modulations of the mode-locked pulse train. We show that this leads to a significant improvement in the regularity of the mode-locked laser output, as the suppression of noise-induced modulations reduces fluctuations in the pulse positions on time scales of the feedback delay times, as well as decreasing the variance of the temporal pulse positions on much longer time scales.

Zusammenfassung

Passiv-modengekoppelte Halbleiterlaser erzeugen kurze optische Pulse bei sehr hohen Wiederholungsraten. In dieser Arbeit wird der Einfluss von zeitverzögerter optischer Rückkopplung auf die Dynamik und und den Zeitjitter eines solchen Lasers untersucht.

Durch die Verwendung eines Differentialgleichungsmodells mit Zeitverzögerung untersuchen wir die Dynamik und Bifurkationen von passiv-modengekoppelten Halbleiterlasern. Diese Laser erzeugen im fundamentalen Modenkopplungsregime ein gepulstes Ausgangssignal mit einer Wiederholungsrate die durch die Länge des Lasers bestimmt ist. Wird nun zusätzlich ein Teil der optischen Ausgangsleistung zeitverzögert in den Laser zurückgekoppelt, lässt sich die Dynamik durch Resonanzeffekte zwischen der Periode des freilaufenden Lasers und der Zeitverzögerung der Rückkopplung beeinflussen. Durch geeignete Wahl der Rückkopplungsparameter kann die Wiederholungsrate der Pulsfolge geändert, harmonische Modenkopplung induziert oder sogar die periodische modengekoppelte Dynamik vollständig destabilisiert werden, was zu einer quasiperiodischen oder chaotischen Dynamik führt. Solange jedoch die Verzögerungszeit etwa einem Vielfachen der Wiederholungsrate des freilaufenden Lasers entspricht, ist die fundamentale Modenkopplung stabil. Diese Resonanzbereiche wachsen dabei mit steigender Rückkopplungszeit. Durch Überlapp verschiedener Resonanzbereiche mit fundamentaler Modenkopplung entstehen Bereiche mit hoher Multistabilität. Mit Hilfe einer weiteren optischen Rückkopplung über eine zweite externe Kavität lässt sich die Dynamik in gleicher Weise wie mit einer einzelnen externen Kavität beeinflussen. Dabei kann die Multistabilität der fundamentalen modengekoppelten Lösung jedoch aufgehoben werden.

Die Regelmäßigkeit der modengekoppelten Dynamik ist unter Rauscheinfluss erheblich verschlechtert, da aufgrund der Abwesenheit von einer externen Referenzfrequenz die Pulspositionen in der Zeit stochastisch variieren. Mit Hilfe von resonanter optischer Rückkopplung werden Korrelationen zwischen den Pulszeiten auf langen Zeitskalen induziert, die zu einer deutlichen Verringerung des Zeitjitters führen. In dieser Arbeit wird ein Ausdruck für den Zeitjitter hergeleitet, der zeigt, dass die Regularität der Pulse sich mit längerer Rückkopplungszeit verbessert. Für lange Rückkopplungszeiten jedoch spielen rauschinduzierte Modulationen eine zunehmend stärkere Rolle, was zu Fluktuationen der Pulspositionen auf Zeitskalen der externen Rückkopplung führt.

Diese rauschinduzierten Modulationen können durch Hinzufügen einer zweiten Rückkopplungsstrecke unterdrückt werden. In dieser Arbeit wird gezeigt, dass mit Hilfe der linearen Stabilitätsanalyse des modengekoppelten Lasersystems Vorhersagen für die optimalen Rückkopplungsparameter gemacht werden können. Zunächst wird dazu die Unterdrückung rauschinduzierter Modulationen in dem einfachen

Stuart-Landau-System untersucht und die Ergebnisse dieses Systems mit dem modengekoppelten Laser verglichen. Für das Stuart-Landau-System kann eine einfache charakteristische Gleichung für die dominanten Floquet-Exponenten analytisch hergeleitet werden und es hat sich empirisch gezeigt, dass die dabei hergeleitete Formel auch auf die Ergebnisse für das Lasersystem übertragbar ist.

Mit dieser charakteristischen Gleichung können optimale Verzögerungszeiten für die Unterdrückung der rauschinduzierten Modulationen bestimmt werden. Wir zeigen dabei auch, dass dies dann insgesamt zu einer signifikanten Verbesserung in der Regelmäßigkeit des modengekoppelten Laserlichts führt, da die Unterdrückung von rauschinduzierten Modulationen Fluktuationen der Pulspositionen auf kurzen Zeitskalen reduziert, sowie auch die Varianz der Pulspositionen auf langen Zeitskalen.

Contents

Chapter 1

Introduction

Mode-locking is a technique of producing short, high-intensity optical pulses at high repetition rates [SMI70]. Four years after the invention of the laser in 1960 [MAI60] the first clear demonstrations of mode-locking were achieved in a loss-modulated He-Ne laser [HAR64]. Since then the mode-locking of lasers has been a very active field of research [SMI70, HAU00, KEL03] and nowadays mode-locked lasers are used or envisaged as sources of short optical pulses for a wide range of applications including optical data communication, optical clocking, metrology, medical imaging and surgery [TUC88, DEL91, LOE96, HOL00, AVR00, UDE02, KEL03, SPU03, LUE11b]. Semiconductor mode-locked lasers are of particular interest, especially for telecommunications applications [BIM06, KUN07a, RAF07, SCH10g], as they are relatively easy to manufacture, have a small footprint, are integrable and can be electrically pumped. The techniques for achieving mode-locking in such devices can be classed into two groups; active mode-locking and passive mode-locking. Active mode-locking is achieved by externally modulating some parameter of the laser, for example the losses or the pump current, with a driving frequency which is resonant with the modes of laser cavity [KUI70, DER92, HAU00]. The advantage of active mode-locking is that very regular pulse trains can be produced, however the repetition rates and the pulse widths that can be achieved are limited by the speed of the external modulator. For passive mode-locking no external modulation is applied. Typically, a saturable absorber is included in the laser cavity and it is through the interplay between the dynamics in the saturable absorber section and the amplifying section of the laser that pulses are produced. In passively mode-locked lasers very short pulses can be generated at repetition rates of tenths to hundreds of Gigahertz [HAU00, AVR00]. However, passively mode-locked semiconductor lasers also have a major drawback. Due to the absence of an external reference clock the pulse trains can be relatively irregular [SOL93], which is detrimental for most applications. A third variant of achieving mode-locking,

referred to as hybrid mode-locking, combines active and passive techniques. Hybrid mode-locked lasers have a saturable absorber section, which provides the dominant mechanism for mode-locking, and a section which is electrically modulated, which improves the regularity of the pulse train [DER92, FIO10, HAB14].

The absence of an external modulation source means that passively mode-locked semiconductor lasers are substantially less expensive to manufacture than active or hybrid mode-locked lasers, which makes them very attractive for applications. Therefore a lot of research has gone into finding methods of improving the regularity of the pulse trains produced by such devices [SOL93, AHM96, AVR09, GRI09, LIN10e, BRE10, REB10, DRZ13a]. One approach is to optically inject the passively mode-locked laser with emission from a second laser [AHM96, REB10, REB11]. However, like hybrid mode-locking, this method requires additional active elements. Another method, which requires no additional active elements, is to subject the passively mode-locked laser to optical self-feedback. Already in the 90's it was shown experimentally that under certain conditions optical feedback can lead to a reduction in the timing jitter [SOL93]. The timing jitter being a measure of the temporal regularity of the pulse train, which can be calculated from the power spectrum of the laser output [LIN86].

Passively mode-locked semiconductor lasers subject to optical feedback are also interesting from a non-linear dynamics point of view. The dynamics of single mode semiconductor lasers subject to feedback have been extensively studied both theoretically and experimentally [LAN80b, MOR88, MOR92, ALS96, KRA00a, ERN10b, OTT12, KIM14]. Through the addition of time-delayed feedback these devices are found to exhibit rich dynamics ranging from continuous wave emission to low frequency fluctuations to chaos. Passively mode-locked lasers without feedback already exhibit complex periodic dynamics. As such, they are an ideal test bed for the influence of time-delayed feedback on periodic dynamical systems.

In the following sections we will give brief introductions to semiconductor lasers, mode-locking and time-delayed feedback. Then, in Section 1.4 an outline of this thesis is given.

1.1. Semiconductor lasers

A laser[1] is a source of coherent light which is generated via stimulated emission. The stimulated emission of photons is a quantum mechanical process in which an incident photon, of the appropriate energy, interacts with an electron in an excited state and causes it to relax to a lower energy state (ground state) by emitting a photon [EIN17]. The emitted photon has the same frequency, polarisation, phase and direction of travel as the incident photon. For this to occur the difference in

[1]The word "laser" is an acronym for "light amplification by stimulated emission of radiation".

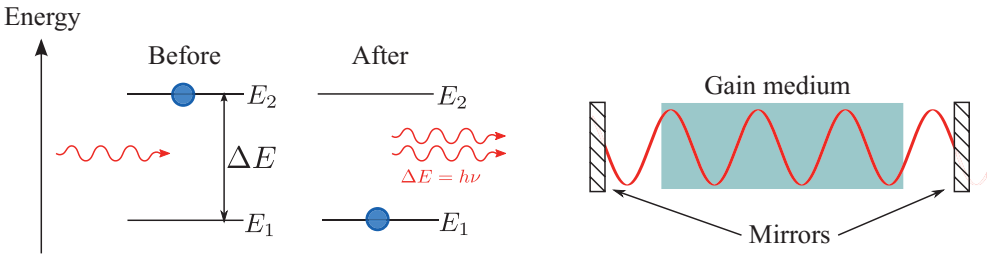

Figure 1.1.: Left: Sketch of the stimulated emission of a photon. Right: Sketch of a standing wave in a laser cavity.

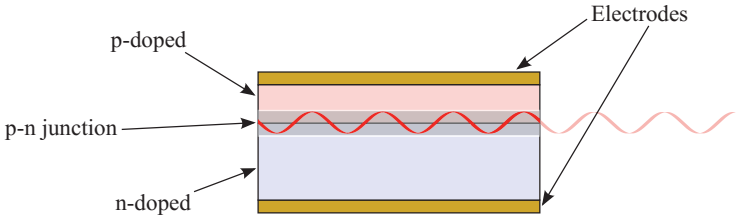

Figure 1.2.: Sketch of a semiconductor laser.

the electronic energy levels must be equal to the energy of the incident photon, $E_2 - E_1 = h\nu$. This is illustrated in Fig. 1.1. If the medium (gain medium) in which the stimulated emission is occurring is confined to a cavity, for example by the placement of two mirrors, then large numbers of photons can build as they pass back and forth through the gain medium. Each time a stimulated emission event occurs, an electron drops from the excited state to the ground state, thereby reducing the gain of the amplifying medium. For lasing to be sustained the gain medium must remain inverted, i.e. there must be more electrons in the excited state than in the ground state. One of the advantages of semiconductor lasers is that this can be achieved by electrical pumping. The alternative method is to optically excite electrons using an external light source.

In the simplest form of a semiconductor laser the optical transitions occur at a p-n junction and the charge carrier inversion is achieved by electrical pumping. Figure 1.2 shows a simplified sketch of such a semiconductor laser. The active region is indicated by the grey shading near the p-n junction. The first semiconductor lasers were of this type [HAL62, HOL62, NAT62]. However, they required very high pump currents and they had to be operated at very low temperatures. To overcome these issues the spatial confinement of the charge carriers is crucial. Over the years many confinement structures have been developed. One of the earliest examples that enabled room temperature operation used a thin layer of GaAs between two bulk layers of AlGaAs, which has a larger band-gap, thereby forming a

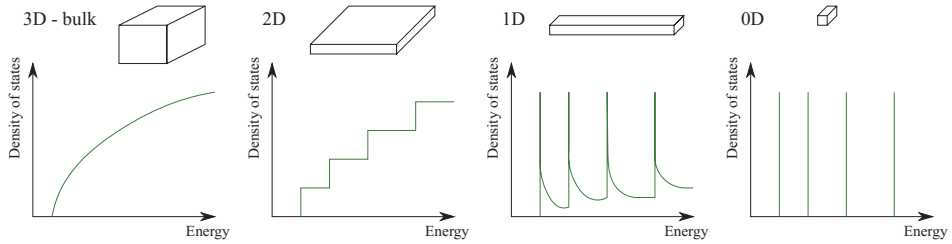

Figure 1.3.: Sketch of the density of states for 3D, 2D, 1D and 0D structures.

quantum well [ALF68]. A quantum well is a quasi-two dimensional structure which confines charge carriers, in one spatial direction, to a region narrower than their de-Broglie wavelength, but allows them to move freely transverse to this direction. This confinement causes a discretisation of the energy levels the charge carriers can occupy and leads to a lower threshold current density and lasing at higher temperatures. Confinement in two and three spatial dimensions is also possible, leading to quantum wires and quantum dots, respectively. Figure 1.3 shows a sketch of the density of states for different degrees of confinement. In recent years devices based on semiconductor quantum dots have received a lot of attention owing to their discrete states, which can lead to lower threshold currents and increased temperature stability compared with quantum-well structures [SUG05, RAF07, LUE11b, OTT14, LIN15].

The modelling of a semiconductor laser can be done to varying degrees of complexity and depending on the structure of the gain medium different processes need to be included to accurately describe the charge-carrier dynamics. In a minimalistic approach, a single mode semiconductor laser can be modelled using two coupled rate equations,

$$\frac{dS}{dt} = G_N \left(N - N_{tr}\right) S - \frac{S}{T_{\mathrm{ph}}} \tag{1.1}$$

and

$$\frac{dN}{dt} = J - \frac{N}{T_1} - G_N \left(N - N_{tr}\right) S, \tag{1.2}$$

where dynamical variables are the number of photons S and the number of charge carriers N in the active medium. The interaction between the charge carriers and photons is taken into account with the gain function $G_N \left(N - N_{tr}\right)$, where N_{tr} is the charge-carrier number at transparency. The photon lifetime T_{ph} accounts for the optical losses. When the number of charge carriers is large enough that the gain can compensate for these losses, then the light can be amplified. The number charge carriers depends on the pumping rate J and on the non-resonant carrier losses, which are taken into account by the charge-carrier lifetime T_1.

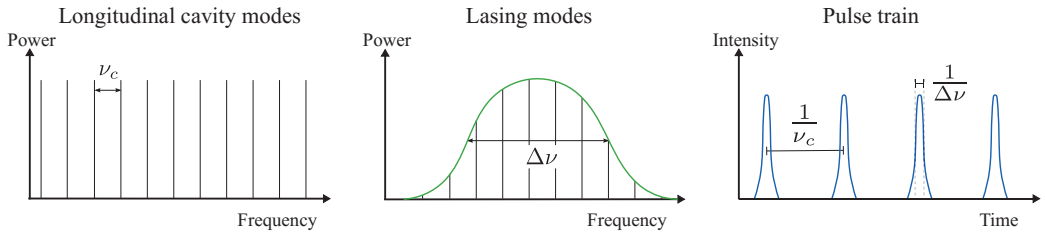

Figure 1.4.: Frequency and time domain sketches of a mode-locked electric field.

In depth introductions to general laser theory, and specifically to semiconductor lasers, can be found in [HAK86, HAK86a] and [CHO99], respectively.

1.2. Mode-locking

The frequencies of lasing modes are determined by the gain spectrum of the amplifying medium and by the boundary conditions imposed by the laser cavity. The frequencies which are resonant with the laser cavity form standing waves which are referred to as longitudinal modes. These modes have a fixed frequency spacing which is dependent on the length of the cavity. Of these modes, only those which fall within the bandwidth of the gain medium can be amplified. This is sketched in Fig. 1.4. If, in addition to the mode spacing ν_c, the relative phases of the lasing modes are equal, then pulses will be formed as the lasing modes periodically undergo constructive interference. The time between pulses, i.e. the period of the mode-locked dynamics, will be determined by the reciprocal of the mode spacing $1/\nu_c$, and the width of the pulses will be given approximately by the reciprocal of the width of the optical spectrum $1/\Delta\nu$. Mode-locking can also occurs between modes which are separated by multiples of the fundamental frequency of the laser cavity ν_c. This is referred to as harmonic mode-locking and results periodic dynamics in which multiple pulses circulate in the laser cavity.

To demonstrate more clearly why pulses are formed under equal phase conditions we consider the superposition of a set of N longitudinal modes at some fixed point in the laser cavity. The total field is given by

$$E_{\mathrm{T}}(t,z) = \sum_{n=1}^{N} E_n e^{i(2\pi\nu_n t+\phi_n)}, \tag{1.3}$$

where E_n is the amplitude of the n^{th} mode, ν_n is the frequency and ϕ_n is the relative phase [SMI70]. The frequencies are all offset from one another by integer multiples of the mode spacing ν_c, i.e. $\nu_n = \nu_0 + n\nu_c$ where ν_0 is a fast optical

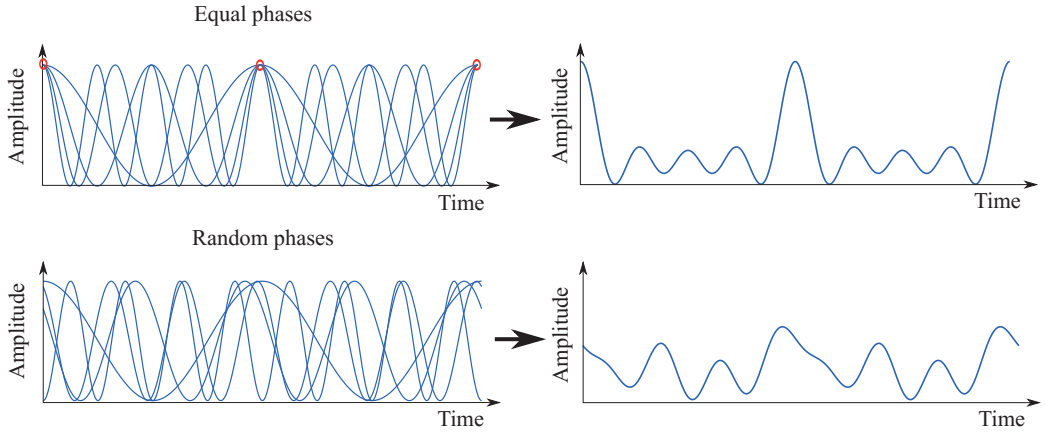

Figure 1.5.: Sinusoidal waveforms with frequencies of $n\nu_c$ for $n = 1, 2, 3, 4$. In the top diagram the phases ϕ_n are equal and the waveforms interfere constructively every $1/\nu_c$, resulting in pulses. In the bottom diagram the phase are randomly chosen, consequently the waveforms are never all in phase at the peaks.

frequency. Factoring out the fast optical component, $E_{\mathrm{T}} = \mathcal{E}_{\mathrm{T}} e^{i2\pi\nu_0 t}$, the slowly varying electric field envelope is given by

$$\mathcal{E}_{\mathrm{T}}(t, z) = \sum_{n=1}^{N} E_n e^{i(2\pi n\nu_c t + \phi_n)}, \tag{1.4}$$

which is periodic in $1/\nu_c$. If the relative phases are all equal, for simplicity let $\phi_n = 0$, then all modes will interfere constructively for all $t = m/\nu_c$, where m is an integer. If the relative phases are not all equal, then at no point in time will all modes interfere completely constructively. This is illustrated in Fig. 1.5 which shows four sinusoidal waveforms with equal relative phases on the top and with different relative phases on the bottom. In the top diagram all four waveforms are completely in phase at each time marked by the red circles, whereas on the bottom they are never simultaneous in phase. When there is a large number of modes which all have the same relative phases, then the total electric field amplitude will be large when they are all in phase and between these points in time the modes will interfere destructively resulting in close to zero intensity between the pulses.

1.2.1. Passive mode-locking

Passively mode-locked lasers typically consist of a saturable absorber section and a gain section.[2] For semiconductor passively mode-locked lasers these two sections

[2] Passive mode-locking techniques that do not involve a saturable absorber also exist. For example in Kerr lens mode-locking Kerr lensing in the gain medium leads to mode-locking [BRA92], or

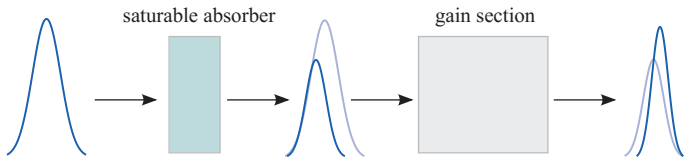

Figure 1.6.: Sketch of the pulse shaping that occurs in the saturable absorber and gain sections of a passively mode-locked laser.

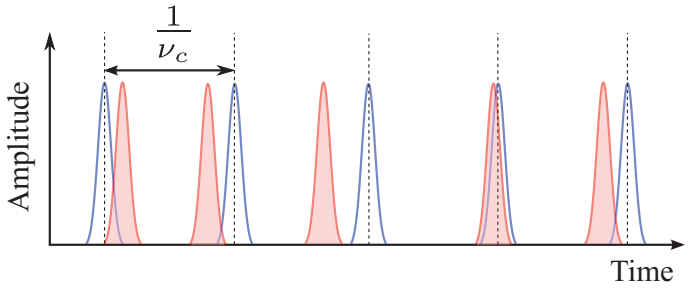

Figure 1.7.: Sketch of a perfectly regularity pulse train (blue) and an irregular pulse train in which noise causes the time interval between the pules to vary (red).

can be made of the same material and the behaviour is characterised by the pump conditions. The gain section is electrically pumped, thereby generating an inversion of charge carriers, and the absorber section has a reverse bias applied to it [DER92]. To understand how mode-locking is achieved via the addition of the saturable absorber it is helpful to consider the electric field in the time domain. Consider a pulse travelling in the laser cavity. As the pulse enters the saturable absorber the front of the pulse is absorbed, which excites charge carries, until the absorber saturates, at which point it is transparent to the rest of the pulse. In the gain section the front of the pulse will be amplified, leaving the charge carriers depleted for the trailing edge for the pulse, meaning that non-resonant losses are not compensated for the trailing edge. A sketch of the pulse shaping in the absorber and gain sections is shown in Fig. 1.6. If the absorber saturates at a lower energy than the gain section, then this results in a narrow positive net gain window for the center of the pulse and stable mode-locking can be achieved.

1.2.2. Timing jitter

In the ideal case a passively mode-locked laser would produce a perfectly regular pulse train. However, due to inevitable noise sources the temporal positions of

in [JAV06] a mode-locking technique that utilises the polarisation degrees of freedom of light is discussed.

pulses can fluctuate. This is illustrated in Fig. 1.7. For actively mode-locked lasers the pulse is pulled back towards its ideal position each round trip due to the external modulation. However, for passively mode-locked lasers there is no restoring force, which means the pulse position can drift randomly over time. In semiconductor passively mode-locked lasers the dominant noise source is spontaneous emission, which leads to comparatively large timing fluctuations [HAU93a, SOL93]. The temporal fluctuations of the pulse positions are referred to as the timing jitter.

1.3. Time-delayed feedback

The control of dynamical systems via time-delayed feedback is an extensively studied topic that is of relevance to a wide range of fields. Examples of feedback control are found in electronics [JUS00], quantum mechanics [BRA10a], neuroscience [ROS04] and optics [SOL93, LAN80b, ERZ07, SLO15], among many others. Relevant to passively mode-locked lasers, time-delayed feedback can be used to improve the regularity of noisy oscillatory dynamics [SOL93, OTT12a, OTT14]. Time-delayed feedback can also be used to induce and control chaos [PYR92, SCH07], stabilise unstable steady states or periodic orbits [HOE05, MIC14a], or generate complex temporal patterns [YAN14].

The introduction of time-delayed variables into a dynamical system causes the system to be infinitely dimensional as the initial conditions must be defined on the entire interval $[-\tau, 0]$, where τ is the delay time [HAL93]. This can generally lead to a system exhibiting more complex dynamics than the same system without the time-delayed feedback term, and can also lead to multistability, especially for long delay times. For periodic systems subject to feedback a general result is that solutions reappear at all delay times that are increased by integer multiples of the period of the solution [YAN09]. The influence of varying the feedback delay time between these discrete values is that the stability of the solutions is affected; the general trend being that solutions become less stable for longer delay times.

For systems in the presence of noise, feedback can be used to suppress or enhance noise induced effects [GOL03, BAL04, FLU07]. This is of relevance for the passively mode-locked laser subject to feedback as experimental studies have shown that noise can excite modes which are resonant to the feedback cavity [DRZ13, ARS13]. Analogous to the suppression of noise-induced oscillations in single mode lasers [FLU07], an additional feedback cavity can be used to suppress these modes in the mode-locked laser system subject to feedback [HAJ12, JAU16].

1.4. Outline

In this thesis we study the dynamics and timing jitter of a passively mode-locked laser subject to optical feedback and the suppression of noise-induced modulations in periodic systems with feedback. The thesis is structured as follows.

In Chapter 2 the model for a passively mode-locked semiconductor laser is presented. The model is a delay differential equation system for a ring cavity laser [VLA04, VLA05]. In Section 2.2 the model is derived. Then in Section 2.3 this model is discussed, particularly the comparison with travelling-wave models used for linear laser cavity geometries.

In Chapter 3 we investigate the feedback induced dynamics of passively mode-locked semiconductor lasers. First, a recap of the parameter dependence of the solitary mode-locked laser is given in Section 3.2.3. Then we investigate the influence on the dynamics of optical feedback from one external cavity in Section 3.3. In this section the dynamics are investigated in the regimes of short, intermediate and long feedback delay times. The dynamics are investigated by both direct numerical simulations and by using path continuation techniques. In Section 3.4 the influence of a second external feedback cavity is studied. A summary of this chapter is presented in Section 3.5.

Chapter 4 is concerned with the timing jitter of the mode-locked solutions. First, the various methods of calculating the timing jitter are defined in Section 4.2. One of these methods is a semi-analytic approach which allows us to analytically derive the feedback dependence of the timing jitter under certain conditions. In Section 4.3 we investigate the timing jitter of the solitary laser, then in Sections 4.4 and 4.5 the influence of one and two external feedback cavities is examined. For the dual feedback cavity case we present a comparison with experimental results.

The results of Chapter 4 will show that for long feedback delay times noise excites weakly stable eigenmodes, which causes a modulation of the oscillatory dynamics. In Chapter 5 the suppression of these noise-induced modulations, using the second feedback cavity, is studied. First, we investigate the suppression of noise-induced modulations in a simple oscillatory system in Subsection 5.2.1. Then, these results are used to study the suppression of noise-induced modulations in the mode-locked laser system in Subsection 5.2.2. Following this, the influence of the modulation suppression on the timing jitter is examined in Section 5.3. Finally, in Section 5.4 the results of this chapter are summarised.

A summary of this thesis is presented in Chapter 6, along with a discussion of open questions and possible directions for future work.

Chapter 2

Mode-locked laser model

2.1. Introduction

Various models exist for passively mode-locked lasers, each with their own advantages and restrictions. One of the earliest models was a master equation approach developed by Haus which allows the mode-locked pulses to be described analytically under the assumption of only small changes in the gain and losses per cavity round trip [HAU75a]. This approach works well for solid state lasers, however the assumption of small changes in the gain and losses per round trip is not applicable to semiconductor lasers. For accurate modelling of semiconductor passively mode-locked lasers, finite-difference travelling-wave models are typically used [MUL06, AVR09, JAV10, JAV11, ROS11c, ROS11d, RAD11a, SIM12a, MOS14]. However the numerical integration of such models is computationally very expensive and this makes it infeasible to use such an approach to study the influence of feedback over a wide range of feedback delay times. In [MUL06], [AVR09] and [SIM12a] the impact of feedback is studied, but in each case only in the regime of short feedback cavities. An alternative modelling approach is to use a delay differential equation (DDE) model. This was first proposed in [VLA04, VLA05] and extended to include optical feedback in [OTT12a]. This approach assumes a ring cavity with unidirectional propagation and uses a lumped element method to include non-resonant losses and spectral filtering. Using this model the computationally cost is greatly reduced and feedback can easily be incorporated. However, the simplifying assumptions mean that this model is strictly only applicable to ring cavities, whereas linear cavity geometries are commonly used for monolithic passively mode-locked semiconductor lasers. Despite this limitation most of the qualitative trends, especially in dependence of feedback parameters, are very similar to experimental results for linear cavities [SAN90, BAN06, ARS13, MAR14c, OTT14b].

Due to its suitability to studying optical feedback, we will use the DDE model in this thesis.

The modelling of the charge carriers is dependent on the choice of semiconductor material and can be done to varying degrees of complexity [CHO99, VLA05, ROS11c, LIN13, LIN14, LIN15a]. We will use a simple model for a quantum-well gain medium. Despite this, in subsequent chapters we will compare our results with experiments using quantum-dot lasers and show that the qualitative dependence on the feedback parameters is captured by the DDE model.

This chapter is structured as follows. In Section 2.2 we present the derivation of the DDE model. Then in Section 2.3 we discuss the assumptions that underlie this model. We also discuss key differences that arise compared with travelling wave models, as well as extensions that have been made to this model.

2.2. Derivation of the DDE model

In this section we present the derivation of the DDE model for a passively mode-locked semiconductor laser which is introduced in [VLA04a, VLA05]. In [OTT12a] the model is extended to include optical feedback from one external cavity. Here we present extension to multiple feedback cavities. The derivation follows those of [VLA11] and [OTT12a].

The light-matter interaction needed for lasing to occur can be described using a semi-classical theory [HAK83a, CHO99]. In this approach the light field is described classically, but the motion of the charge carriers is described quantum-mechanically. Although the quantum-mechanical treatment of the carriers is necessary for lasing to be described, the classical treatment of the light field is sufficient when considering devices that involve macroscopic numbers of charge carriers and photons. The results of the semi-classical theory are the Maxwell-Bloch equations, which describe the evolution of the electric field, the charge carrier inversion and the microscopic polarisation. The derivation for a simple two-level system is given in [HAK83a]. For a semiconductor gain medium the derivation is somewhat more complicated due to inhomogeneous broadening (distribution of charge carrier kinetic energies), many-body Coulomb interactions and carrier-phonon interactions. A comprehensive derivation of the semiconductor Bloch equations is given in [CHO99].

We will start the derivation of the DDE model directly from the standard travelling wave model for semiconductor quantum-well lasers [TRO94, TAR98a, SCH88j]:

$$\pm \frac{\partial \mathcal{E}_r^{\pm}(t,z)}{\partial z} + \frac{1}{v}\frac{\partial \mathcal{E}_r^{\pm}(t,z)}{\partial t} = \frac{g_r \Gamma_r}{2}(1 - i\alpha_r)\left[n_r(t,z) - n_r^{\mathrm{tr}}\right]\mathcal{E}_r^{\pm}(t,z) \tag{2.1}$$

$$\frac{\partial n_r(t,z)}{\partial t} = \eta \frac{j_r(t,z)}{ed} - \gamma_r n_r(t,z) - v g_r \Gamma_r \left[n_r(t,z) - n_r^{\mathrm{tr}}\right] \sum_{\pm} |\mathcal{E}_r^{\pm}(t,z)|^2. \tag{2.2}$$

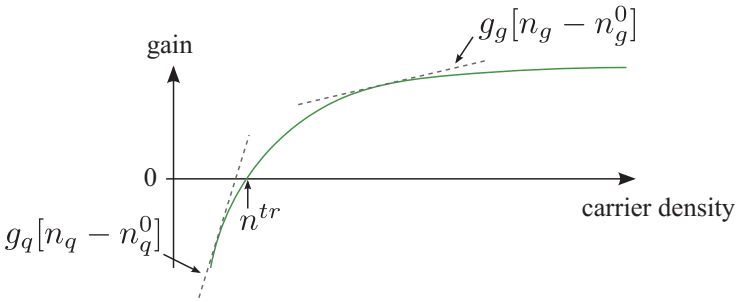

Figure 2.1.: Sketch of the carrier dependence of the gain for a semiconductor quantum-well material.

The dynamical variables are the left (+) and right (-) propagating slowly varying complex electric field amplitudes $\mathcal{E}_r^{\pm}$ and the carrier density n_r. In this model the slowly varying envelope approximation has been made, hence the total electric field is given by

$$E(t,z) \equiv \left(\mathcal{E}_r^{+}(t,z)\, e^{-ikz} + \mathcal{E}_r^{-}(t,z)\, e^{+ikz}\right) e^{-i\Omega_0 t}, \tag{2.3}$$

where k is the reference wavenumber which is related to the optical frequency Ω_0 via the linear dispersion relation $k \equiv \Omega_0/v$, with group velocity v. To arrive at Eqs. (2.1)-(2.2) the polarisation has been adiabatically eliminated. This simplification is possible because semiconductor quantum-well lasers are generally of class B [ARE84], meaning that the polarisation dephasing time is much faster than other time scales of the system.

The carrier-field interaction is described by the complex gain function

$$g_r \Gamma_r (1 - i\alpha_r) \left[n_r(t,z) - n_r^0\right], \tag{2.4}$$

which is the gain linearised about the carrier density at some operation point and written in terms of the effective transparency carrier density of this linearised function, n_r^0. The differential gain is given by g_r and transverse modal confinement is accounted for by the factor Γ_r. Carrier-induced refractive index changes are modelled by the amplitude-phase coupling factors α_r (linewidth enhancement factors). The factor of 1/2 in Eq. (2.1) is included because expression (2.4) describes the intensity gain. In Fig. 2.1 a sketch of the carrier dependence of the gain is shown for a semiconductor quantum-well material [ASA84, LAU87a, CHO99]. If the same material is used for the gain ($r = g$) and absorber ($r = q$) sections then the difference in the gain comes from the difference in the carrier densities of the two sections. Due to the reverse bias the absorber section will always be below transparency. The operation range of the gain section will be at some higher carrier density due to the pump current. Therefore, for the gain and absorber section

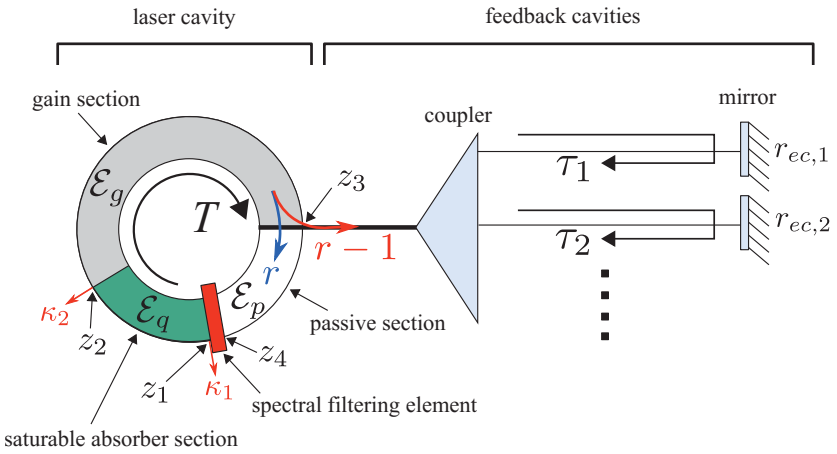

Figure 2.2.: Schematic diagram of a ring-cavity laser subject to optical feedback from multiple external cavities.

the gain function is linearised about different point, leading to different values for the differential gain g_r.

In Eq. (2.2) the injection of charge carriers is described by the pump current density j_r. Included in the pump term are the injection efficiency factor η, the electron charge e and the thickness of the active region d. The lifetime of charge carriers in the quantum-well states is limited by non-radiative scattering processes, which are included via the carrier decay rate γ_r. Inspection of the carrier-field interaction term in Eq. (2.2) shows that the electric field is scaled to the dimensions $(\text{length})^{-3/2}$ such that $|\mathcal{E}_r^{\pm}|^2$ gives the photon density.

A two section passively mode-locked laser consists of two active sections, a gain section which is electrically pumped and an absorber section which is negatively biased. Depending on the geometry of the laser, passive sections could also be included. For the derivation of the DDE model a ring cavity geometry must be assumed. A schematic of such a cavity is shown in Fig. 2.2. Equations (2.1) and (2.2) are applied in each section of the laser cavity. The index $r \in \{g, q, p\}$ is used to denote the gain, absorber and passive sections, respectively. In the passive section there are no carriers, hence the evolution of the electric field envelope is described solely by Eq. (2.1) with the right-hand side equal to zero. In the absorber section $j_q = 0$ holds, and the influence of the applied reverse bias is manifested in the carrier decay rate γ_q and the gain of this section (Eq. (2.4)). A lumped-element approach is used to include non-resonant losses at the facets between each of the sections (κ_1 and κ_2 in Fig. 2.2). Mirror losses as well as coupling to and from the feedback cavities is included between the gain and passive sections. Also using a lumped-element approach, a filtering element $\hat{f}(\omega)$ is included between the passive

and absorber sections (red bar in Fig. 2.2). The purpose of this filter is to account for the finite width of the gain spectrum. The z-direction is chosen along the axis of the cavity and is the propagation direction of longitudinal modes of the laser. Along with the ring cavity geometry, the second main assumption of the DDE model is unidirectional propagation of the light field. Here clockwise propagation is chosen, i.e. $\mathcal{E}_r^- = 0$ and $\mathcal{E}_r^+ = \mathcal{E}$. The validity and implications of these two assumptions will be discussed in Section 2.3.

Including the losses and feedback contributions as described above, the boundary conditions between each of the sections are

$$\mathcal{E}_g\left(t, z_2\right) = \sqrt{\kappa_2}\mathcal{E}_q\left(t, z_2\right), \tag{2.5}$$

$$\begin{aligned}\mathcal{E}_p\left(t, z_3\right) = \sqrt{r}\mathcal{E}_g\left(t, z_3\right) + (1-r)\sum_{n=1}^{N}\left(\sum_{l=1}^{\infty} r^{(l-1)/2}k_n^l r_{ec,n}^{l/2}\mathcal{E}_g\left(t - l\tau_n, z_3\right)e^{ilC_n}\right)\\ +(1-r)\sum_{n=1}^{N}\sum_{n'\neq n}\left(\sum_{l=1}^{\infty} r^{l/2}k_n^l r_{ec,n}^{l/2}k_{n'}r_{ec,n'}^{1/2}\mathcal{E}_g\left(t - \tau_{n'} - l\tau_n, z_3\right)e^{i(C_{n'}+lC_n)}\right)\\ +(1-r)\sum_{n=1}^{N}\sum_{n'\neq n}\left(\sum_{l=1}^{\infty} r^{(l+1)/2}k_n^l r_{ec,n}^{l/2}k_{n'}^2 r_{ec,n'}\mathcal{E}_g\left(t - 2\tau_{n'} - l\tau_n, z_3\right)e^{i(2C_{n'}+lC_n)}\right)\\ +\cdots\end{aligned} \tag{2.6}$$

and

$$\hat{\mathcal{E}}_q\left(\omega, z_1 + L\right) = \sqrt{\kappa_1}\hat{f}\left(\omega\right)\hat{\mathcal{E}}_p\left(\omega, z_1 + L\right) = \sqrt{\kappa_1}\hat{f}\left(\omega\right)\hat{\mathcal{E}}_p\left(\omega, z_4\right). \tag{2.7}$$

In Eqs. (2.5) and (2.7) κ_1 and κ_2 account for the internal non-resonant loss. These depend on the length of the active sections according to $\kappa_x = e^{-aL_x}$, where a is a loss rate per unit length and L_x is the length of the active section for which the losses are being accounted for.

In Eq. (2.6) feedback contributions from an arbitrary number N of external feedback cavities has been included. To experimentally implement such a feedback scheme there are several options. These include using beam-splitters or optical couplers to distribute the light among the feedback cavities [HAJ12, ARS13, NIK16]. Here we do not choose a particular scheme, but rather account for this with the factor k_n which gives the percentage of the light coupled into feedback cavity $n \in \{1, 2, .., N\}$, with $\sum_{n=1}^{N} k_n = 1$. The sum over l accounts for feedback contributions after multiple roundtrips in the feedback cavities. Also included are contributions from light that has made roundtrips in different feedback cavities. The reflectivity of the end facets of each of the feedback cavities is given by $r_{ec,n}$. This factor primarily determines the feedback strength. The fast oscillating reference frequency Ω_0 also plays a role in the feedback terms, as due to these fast oscillations a phase shift can accumulate with respect to the light in

the laser cavity. This can be understood by considering the delayed electric field $E(t-\tau, z_3) = \mathcal{E}_r^+(t-\tau, z_3)\, e^{-ikz_3} e^{-i\Omega_0(t-\tau)}$ at the out-coupling facet (position z_3). Over the delay time τ a phase shift of $\Omega_0\tau$ accumulates. For each of the feedback cavities the phase shift per roundtrip is then given by $C_n \equiv \Omega_0\tau_n$. Since the optical frequency $\Omega_0\tau$ is very large (THz) very small changes in the delay times τ_n results in variations in the phase that are greater then 2π. Due to this we can essentially treat the feedback phase independently from the delay time. In Eqs. (2.5)-(2.7) the non-resonant losses and reflectivities are all given with respect to the intensity, hence the respective electric field losses are given by the square root of these terms.

In the limit of weak feedback, i.e. small external cavity reflectivities $r_{ec,n}$, the feedback terms in Eq. (2.6) can be simplified by making the approximation that contributions after multiple roundtrips in the feedback cavities are negligible. Including only the terms that correspond to one roundtrip in a feedback cavity Eq. (2.6) becomes

$$\mathcal{E}_p(t, z_3) = \sqrt{r}\mathcal{E}_g(t, z_3) + \sqrt{r}\sum_{n=1}^{N} K_n \mathcal{E}_g(t-\tau_n, z_3)\, e^{iC_n}, \tag{2.8}$$

where

$$K_n \equiv (1-r)k_n \left(r_{ec,n}/r\right)^{1/2}. \tag{2.9}$$

In the boundary condition Eq. (2.7), $\hat{\mathcal{E}}_r$ is the Fourier transformed electric field and ω is the angular frequency. In this boundary condition several assumptions are made. Firstly, the filtering element is assumed to be infinitely thin, meaning that $z_1 = z_4$. Secondly, since $z_1 + L = z_4$ in the ring cavity geometry, the boundary conditions are periodic, i.e.

$$\mathcal{E}_r(t, z) = \mathcal{E}_r(t, z+L), \tag{2.10}$$

where L is the length of the laser cavity. The laser cavity modes are therefore restricted to

$$\Omega_L = n\frac{2\pi v}{L} \tag{2.11}$$

for $n = 1, 2, 3, ...$ All modes fulfilling this condition can exist in the laser cavity. This is shown schematically in Fig. 2.3. The grey lines in this diagram indicate modes with a spacing of $\Delta\nu = T'^{-1} = \frac{v}{L}$, where T' is the cold cavity roundtrip time. Without a spectral filter, according to Eqs. (2.1) and (2.2), all of these modes are equally amplified and would have the same output power. However in real devices only a finite number of modes will have positive net gain [HOH93, UKH04]. The spectral filter (blue curve) is added to account for this by increasing the losses for modes away from the maximum gain mode. In the derivation of the DDE model a Lorentzian shaped filter is chosen;

$$\hat{f}(\omega) \equiv \frac{\gamma}{\gamma + i(\omega - \Delta\Omega)}. \tag{2.12}$$

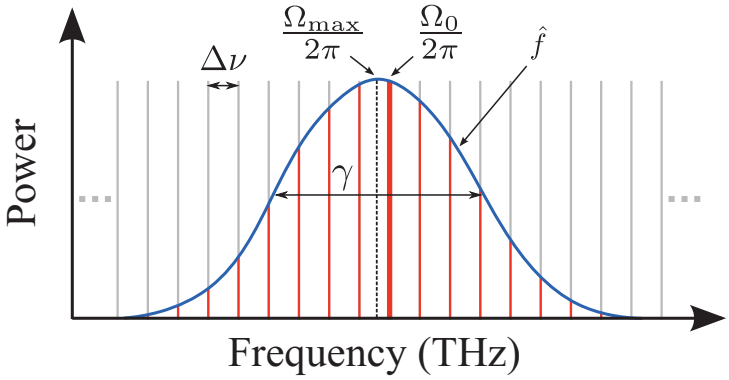

Figure 2.3.: Schematic diagram of the optical spectrum of a semiconductor mode-locked laser. The grey lines indicate the cavity modes and the red lines indicate the modes that can lase. The blue curve represents the spectral filter that is applied to account for the frequency dependence of the gain.

This expression is written in the frame of the slowly varying amplitude, i.e. the optical frequencies are given by $\omega' = \Omega_0 + \omega$. $\Delta\Omega \equiv \Omega_0 - \Omega_{\max}$ is the detuning between the frequency of the maximum of the filter $\Omega_{\max}$ and the reference optical frequency. The full-width at half maximum of the filter is given by γ. This parameter determines the number of modes that participate in the mode-locking, which is roughly given by $\gamma T'$ [VLA05]. The Lorentzian filter shape is chosen as it allows the derivation of a system of delay differential equations.

Before applying the boundary conditions it is useful to make a change of coordinates to a frame co-moving with the electric field: $(t, z) \mapsto (t', z')$ with $t' = t - z/v$ and $z' = z/v$. In this coordinate system Eqs. (2.1)-(2.2), applied to each section of the laser, are given by

$$\frac{\partial A_r}{\partial z'} = \frac{1}{2}\left(1 - i\alpha_r\right) N_r\left(t', z'\right) A_r\left(t', z'\right), \tag{2.13}$$

$$\frac{\partial N_g}{\partial t'} = \mathcal{J}_g\left(t', z'\right) - \gamma_g N_g\left(t', z'\right) - N_g\left(t', z'\right) \left|A_g\left(t', z'\right)\right|^2 \tag{2.14}$$

and

$$\frac{\partial N_q}{\partial t'} = -\mathcal{J}_q\left(t', z'\right) - \gamma_q N_q\left(t', z'\right) - \tilde{r}_s N_q\left(t', z'\right) \left|A_q\left(t', z'\right)\right|^2, \tag{2.15}$$

with $N_p\left(t', z'\right) \equiv 0$. Here the dynamical variables have been rescaled such that $A_r \equiv \sqrt{v g_g \Gamma_g}\mathcal{E}_r$ and $N_r \equiv v g_r \Gamma_r [n_r - n_r^0]$. Accordingly, the rescaled pump parameters are $\mathcal{J}_g \equiv v g_g \Gamma_g \left(j_g - \gamma_g n_g^0\right)$ and $\mathcal{J}_q \equiv v g_q \Gamma_q \gamma_q n_q^0$, and the saturation energy ratio $\tilde{r}_s \equiv g_q \Gamma_q / g_g \Gamma_g$ has been introduced [HAU00, OTT14]. The saturation energies describe how much energy must be absorbed or emitted for the absorber and gain sections to become transparency. The ratio of these energies is a crucial parameter;

for mode-locking to occur the absorber must have a smaller saturation energy than the gain section, i.e. $\tilde{r}_s > 1$ as the saturation energies are proportional to $(g_r \Gamma_r)^{-1}$.

In this co-moving frame the evolution of the electric field amplitude along the sections of the laser is now described by ordinary differential equations (Eq. (2.13)). Integrating these equations over each section yields

$$A_q\left(t', z_2'\right) = e^{-\frac{1}{2}(1-i\alpha_q)Q(t')} A_q\left(t', z_1'\right), \tag{2.16}$$

$$A_g\left(t', z_3'\right) = e^{\frac{1}{2}(1-i\alpha_g)G(t')} A_g\left(t', z_2'\right) \tag{2.17}$$

and

$$A_p\left(t', z_3'\right) = A_p\left(t', z_4'\right), \tag{2.18}$$

where

$$Q\left(t'\right) \equiv -\int_{z_1'}^{z_2'} N_q\left(t', z'\right) dz' \quad \text{and} \quad G\left(t'\right) \equiv \int_{z_2'}^{z_3'} N_g\left(t', z'\right) dz'$$

are the dimensionless carrier densities integrated over the absorber and gain sections, which we shall refer to as the gain and losses, respectively. Next, the boundary conditions can be applied to obtain the evolution of the electric field amplitude over one roundtrip in the laser cavity. Using Eqs. (2.5) and (2.8), transformed to the co-moving frame, the evolution from $A_q\left(t', z_1'\right)$ to $A_p\left(t', z_4'\right)$ is given by

$$\begin{aligned} A_p\left(t', z_4'\right) &= \sqrt{r\kappa_2} e^{\frac{1}{2}(1-i\alpha_g)G(t') - \frac{1}{2}(1-i\alpha_q)Q(t')} A_q\left(t', z_1'\right) \\ &+ \sqrt{r\kappa_2} \sum_{n=1}^{N} K_n e^{iC_n} e^{\frac{1}{2}(1-i\alpha_g)G(t'-\tau_n) - \frac{1}{2}(1-i\alpha_q)Q(t'-\tau_n)} A_q\left(t' - \tau_n, z_1'\right). \end{aligned} \tag{2.19}$$

In order to apply Eq. (2.7), it must first be transformed to the time domain and the co-moving frame. The transformation to the time domain is done using the convolution theorem which states

$$\mathcal{F}[g * h\left(t\right)] = \mathcal{F}[g\left(t\right)]\mathcal{F}[h\left(t\right)], \tag{2.20}$$

where g and h are functions of t, $\mathcal{F}$ is the Fourier transform and $(*)$ denotes a convolution product. In the co-moving frame, and in terms of the rescaled field, Eq. (2.7) can now be rewritten as

$$\begin{aligned} A_q\left(t' - T', z_1' + T'\right) &= \sqrt{\kappa_1}\Big(f\left(t' - T'\right) * A_p\left(t' - T', z_4'\right)\Big) \\ &= \sqrt{\kappa_1} \int_{-\infty}^{t'-T'} f\left(t' - T' - \theta\right) A_p\left(\theta, z_4'\right) d\theta, \end{aligned} \tag{2.21}$$

once again T' is the cold cavity roundtrip time given by L/v. The upper limit of the integral has been set to $t' - T'$, instead of infinity, in order to preserve causality.

This is done under the assumption that $A_q(\theta, z_4') = 0$ for $\theta > t' - T'$. Substituting Eq. (2.19) into Eq. (2.21) yields

$$A_q(t', z_1') = \int_{-\infty}^{t'-T'} f(t' - T' - \theta) R(\theta) A_q(\theta, z_1') d\theta + \sum_{n=1}^{N} K_n e^{iC_n} \int_{-\infty}^{t'-T'} f(t' - T' - \theta) R(\theta - \tau_n) A_q(\theta - \tau_n, z_1') d\theta, \tag{2.22}$$

where we have defined

$$R(\theta) \equiv \sqrt{\kappa} e^{\frac{1}{2}(1-i\alpha_g)G(\theta) - \frac{1}{2}(1-i\alpha_q)Q(\theta)} \tag{2.23}$$

which describes the gain and losses accumulated over one roundtrip in the laser cavity. Here we also define $\kappa \equiv \kappa_1 \kappa_2 r$. This parameter accounts for all the non-resonant and mirror losses per roundtrip. To obtain the left hand side of Eq. (2.22) the periodic boundary condition has been applied, which in the co-moving coordinates is expressed as

$$A_q(t', z_1') = A_q(t' - T', z_1' + T'). \tag{2.24}$$

The form of which can be derived by substituting $z + L$ for z in the transformation, i.e. $(t, z + L) \mapsto \left(t - \frac{(z+L)}{v}, \frac{(z+L)}{v}\right) = (t' - T', z' + T')$.

The evolution of the field over one roundtrip is now expressed entirely in terms of the electric field amplitude in the saturable absorber section at position z_1', which we relabel $A(t') \equiv A_q(t', z_1')$. In order to obtain a differential equation for the time evolution of $A(t')$ Eq. (2.22) is differentiated with respect to t'. To do this we first substitute in the filtering function, which in the time domain is written as

$$f(t') \equiv \gamma e^{(-\gamma + i\Delta\Omega)t'}. \tag{2.25}$$

With some slight rearrangement this yields

$$A(t') e^{(\gamma - i\Delta\Omega)t'} = \int_{-\infty}^{t'-T'} \gamma e^{(\gamma - i\Delta\Omega)(T+\theta)} R(\theta) A(\theta) d\theta + \sum_{n=1}^{N} K_n e^{iC_n} \int_{-\infty}^{t'-T'} \gamma e^{(\gamma - i\Delta\Omega)(T+\theta)} R(\theta - \tau_n) A(\theta - \tau_n) d\theta, \tag{2.26}$$

Differentiating Eq. (2.26) then results in a DDE for the time evolution of $A(t')$;

$$\frac{dA}{dt'} + (\gamma - i\Delta\Omega) A(t') = \gamma R(t' - T') A(t' - T') + \gamma \sum_{n=1}^{N} K_n e^{iC_n} R(t' - T' - \tau_n) A(t' - T' - \tau_n). \tag{2.27}$$

To obtain differential equations for the time evolution of the integrated carrier densities $G(t')$ and $Q(t')$, we integrate Eqs. (2.14) and (2.15) over the gain and absorber sections, respectively:

$$\frac{\partial G}{\partial t'} = J_g(t') - \gamma_g G(t') - \int_{z_2}^{z_3} N_g(t', z') \, |A_g(t', z')|^2 dz', \tag{2.28}$$

$$\frac{\partial Q}{\partial t'} = J_q(t') - \gamma_q Q(t') + \tilde{r}_s \int_{z_1}^{z_2} N_q(t', z') \, |A_q(t', z')|^2 dz'. \tag{2.29}$$

Here we have introduced the unsaturated gain and absorption parameters

$$J_g(t') \equiv \int_{z_2}^{z_3} \mathcal{J}_g(t', z') \, dz' \tag{2.30}$$

and

$$J_q(t') \equiv \int_{z_1}^{z_2} \mathcal{J}_q(t', z') \, dz', \tag{2.31}$$

respectively. To express the integrals in Eqs. (2.28) and (2.29) in terms of $G(t')$, $Q(t')$ and $A(t')$ we must make use of the equations describing the evolution of the field along the gain and absorber sections (Eqs. (2.13), (2.16) and (2.17), and boundary condition Eq. (2.5)). From Eq. (2.13) we obtain

$$A_r^* \frac{\partial A_r}{\partial z'} + A_r \frac{\partial A_r^*}{\partial z'} = \frac{1}{2}(1 - i\alpha_r) N_r A_r^* A_r + \frac{1}{2}(1 + i\alpha_r) N_r A_r A_r^* \tag{2.32}$$

by multiplying by the complex conjugate of the field amplitude A_r^* and adding the complex conjugate of Eq. (2.13) multiplied by A_r. This expression gives

$$\frac{\partial |A_r|^2}{\partial z'} = N_r(t', z') \, |A_r(t', z')|^2. \tag{2.33}$$

Integrating over the gain and absorber sections then gives

$$|A_{g,q}\left(t', z'_{3,2}\right)|^2 - |A_{g,q}\left(t', z'_{2,1}\right)|^2 = \int_{z'_{2,1}}^{z'_{3,2}} N_{g,q}(t', z') \, |A_{g,q}(t', z')|^2 dz'. \tag{2.34}$$

Using Eqs.(2.16), (2.17) and (2.5) the left hand side can be expressed in terms of $G(t')$, $Q(t')$ and $A(t')$, which we then substitute into Eqs. (2.28) and (2.29) to obtain

$$\frac{\partial G}{\partial t'} = J_g(t') - \gamma_g G(t') - \kappa_2 e^{-Q(t')}\left(e^{G(t')} - 1\right)|A(t')|^2 \tag{2.35}$$

and

$$\frac{\partial Q}{\partial t'} = J_q(t') - \gamma_q Q(t') - \tilde{r}_s e^{-Q(t')}\left(e^{Q(t')} - 1\right)|A(t')|^2. \tag{2.36}$$

Equations (2.27), (2.35) and (2.36) now describe the evolution of the electric field amplitude at position z_1 and the gain and absorption per roundtrip in the

laser cavity. As of yet the influence of spontaneous emission is not included. We treat this effect in a phenomenological manner by adding a complex Gaussian white noise term to the electric field equation (Eq. (2.27)). Adding this noise term and making the transformation $A(t') \equiv \frac{1}{\sqrt{\kappa_2}}\mathcal{A}(t')\, e^{i\Delta\Omega t'}$ we obtain the final system of coupled DDEs;

$$\begin{aligned}\frac{d\mathcal{A}}{dt'} &= -\gamma\mathcal{A}(t') + \gamma R(t'-T')\, e^{-i\Delta\Omega T'}\mathcal{A}(t'-T') + \sqrt{R_{sp}}\xi(t') \\ &+\gamma\sum_{n=1}^{N} K_n e^{iC_n} R(t'-T'-\tau_n)\, e^{-i\Delta\Omega(T'+\tau_n)}\mathcal{A}(t'-T'-\tau_n), \end{aligned} \tag{2.37}$$

$$\frac{\partial G}{\partial t'} = J_g(t') - \gamma_g G(t') - e^{-Q(t')}\Big(e^{G(t')}-1\Big)|\mathcal{A}(t')|^2 \tag{2.38}$$

and

$$\frac{\partial Q}{\partial t'} = J_q(t') - \gamma_q Q(t') - r_s e^{-Q(t')}\Big(e^{Q(t')}-1\Big)|\mathcal{A}(t')|^2. \tag{2.39}$$

Here the ratio of excitation energies has been rescaled, $r_s \equiv \tilde{r}_s/\kappa_2$. The noise strength is given by R_{sp} and $\xi(t') = \xi_R + i\xi_I$ has the properties

$$\langle \xi_i(t')\rangle = 0 \tag{2.40}$$

and

$$\langle \xi_i(t')\,\xi_j(t'')\rangle = \delta_{i,j}\delta(t'-t''), \tag{2.41}$$

for $i, j \in \{R, I\}$.

2.2.1. Dimensionless formulation of the DDE system

For numerical simulations it is convenient to rescale the DDE system such that the parameters are all dimensionless. In [VLA05] the authors do this by rescaling by the absorber recovery rate γ_q. We shall take the same approach as in [OTT12a] and use the cold cavity roundtrip time T'. This is a convenient time scale of the system to use when studying the system with feedback as features in the feedback delay time dependence vary on this time scale, as will be shown in the next chapter.

We write the dimensionless form of Eqs. (2.37)-(2.39) as

$$\begin{aligned}\frac{d\mathcal{E}}{dt} &= -\gamma\mathcal{E}(t) + \gamma R(t-T)\, e^{-i\Delta\Omega T}\mathcal{E}(t-T) + \sqrt{R_{sp}}\xi(t) \\ &+\gamma\sum_{n=1}^{N} K_n e^{iC_n} R(t-T-\tau_n)\, e^{-i\Delta\Omega(T+\tau_n)}\mathcal{E}(t-T-\tau_n), \end{aligned} \tag{2.42}$$

$$\frac{\partial G}{\partial t} = J_g(t) - \gamma_g G(t) - e^{-Q(t)}\Big(e^{G(t)}-1\Big)|\mathcal{E}(t)|^2 \tag{2.43}$$

and

$$\frac{\partial Q}{\partial t} = J_q\left(t\right) - \gamma_q Q\left(t\right) - r_s e^{-Q(t)}\left(e^{Q(t)} - 1\right)|\mathcal{E}\left(t\right)|^2, \tag{2.44}$$

where time has been rescaled as $t = t'/T'$, the cold cavity roundtrip time is now $T = T'/T' = 1$ and $\mathcal{E} = \sqrt{T'}\mathcal{A}$. For the other parameters we use the same symbols as in Eqs. (2.37)-(2.37), but they now represent the rescaled quantities. All times are rescaled by dividing by T' and all rates are rescaled by multiplying by T'. $R\left(t\right)$ is as defined in Eq. (2.23).

For all the numerical simulations we use the dimensionless form of the DDE system and all for results that will be presented in the subsequent chapters, we will refer to the dimensionless parameter values.

2.2.2. Parameter values

In this subsection we will briefly discuss some of the final parameters of the DDE model (Eqs. (2.42)-(2.44)) and the values that will be used.

In an experiment the tunable parameters that determine the light output of a passively mode-locked laser are the pump current that is injected into the gain section and the reverse bias which is applied to the absorber section. In our final system of equations these control parameters are related to J_g in Eq. (2.43) and J_q and γ_q in Eq. (2.44). J_g is related to the pump current, but not directly as it referenced to the current needed to achieve transparency in the gain section, i.e. it is proportional to the excess pump current. In the absorber section the applied bias modifies the energy barrier which needs to be overcome for carriers to escape the quantum-well [MAL06d]. This influences the carrier recovery rate γ_q and hence the carrier density about which the gain should be linearised. The carrier recovery rate γ_q, the differential gain g_q and the effective transparency carrier density n_q^0 all enter into the unsaturated absorption parameter J_q, meaning that the bias dependence is manifested in J_q and γ_q.

In the subsequent chapters will we see that the amplitude-phase coupling factors, α_g and α_q, can strongly influence the dynamics. These parameters are included to account for carrier-induced refractive index changes and are proportional to $\frac{\partial(\delta n)/\partial N}{\partial g/\partial N}$, where δn is the carrier-induced refractive index change and $\partial g/\partial N$ is the differential gain [CHO99]. For quantum-well based gain media δn and g depend non-linearly on the carrier densities leading to carrier dependent α-factors. In the model presented here these factors are assumed to be constant. We will partially account for the carrier dependence of the α-factors by investigating scenarios where the values are different in the gain and absorber sections. However, our default values for α_g and α_q will be zero.

For the charge-carrier recovery rates we will use values that are typical for semiconductor quantum-well materials. In the gain section the carrier lifetimes can

typically range from 0.1-1 ns [GOE83, HAD04, JON95b]. In the absorber section the carrier lifetimes are lower due to the reverse bias which sweeps out the carriers. Typical values which can be found in the literature are in the range 5-50 ps [KAR94]. However, in both cases the recovery times strongly depend on the structure of the gain material.

The parameter values that we will use throughout this thesis, unless stated otherwise, are those given in Table 2.1. We choose a cold-cavity roundtrip time of 25 ps, which results in a repetition rate of about 40 GHz in the fundamental mode-locking regime. For a linear cavity, this roundtrip time corresponds to a length of about 1 mm, which is a typical length for a passively mode-locked semiconductor laser [FIO11, FIO11a, ARS13].

parameter	value	dimensionless	parameter	value	dimensionless
T	25 ps	1	γ	2.66 ps^{-1}	66.5
γ_g	1 ns^{-1}	0.025	γ_q	75 ns^{-1}	1.875
J_g	0.12 ps^{-1}	3.0	J_q	0.3 ps^{-1}	7.5
r_s	25.0	25.0	C_m	0	0
κ	0.1	0.1	$\Delta\Omega$	0	0
α_g	0	0	α_q	0	0

Table 2.1.: Parameter values used in numerical simulations, unless stated otherwise.

2.3. Discussion of the DDE model

The main assumptions made to be able to derive the DDE system (Eqs. (2.37)-(2.39)) are that the laser has a ring cavity geometry and that the propagation of light is unidirectional. This approach has been widely, and successfully, employed to study the dynamics of various laser systems. These include hybrid mode-locked lasers [FIO10, ARK13], passively mode-locked lasers with optical injection [REB11, PIM14, HAB14] or optical feedback [OTT12a, OTT14b, SIM14, JAU16] and Fourier domain mode-locking [SLE13]. In many of these cases experimental comparison is made with devices that have a linear cavity geometry and bidirectional propagation. Despite this difference the DDE models have been shown to reproduce the qualitative behaviour of the dynamics very well [PIM14, ARS13, FIO10, NIK16]. There are however still some qualitative differences that will be discussed in this section.

In [VLA09] the authors numerically study a travelling-wave model for a monolithic-semiconductor passively mode-locked laser with a linear cavity geometry. The carrier and field equations are the same as those used in the DDE model and spectral filtering is also included in a lumped element approach, i.e. the essential difference

between the DDE system of [VLA05] and the travelling-wave system of [VLA09] is the laser-cavity geometry and hence that in the latter case there are two counter-propagating fields. The bifurcation diagrams for these two systems are qualitatively very similar. The main difference that arises is in the 2nd harmonic mode-locking regime. In this regime there are two pulses travelling in the laser cavity. In the linear-cavity model these two pulses collide, which leads to faster saturation of the medium at the point of the collision. For the cavity model used in [VLA09], this collision takes place in the gain section. This is unfavourable for mode-locking and consequently leads to a break-up of the symmetry of the pulses (period doubling bifurcation). The heights and separation of the pulses change such that the collision only occurs in the gain section every second roundtrip, thereby reducing the saturation of the gain section. This is not observed in the DDE model as the two pulses cannot interact.

In a linear cavity pulse interaction can also occur in the fundamental mode-locking regime. As the pulse is reflected at the end facets there is an interaction between the forward and backward moving parts of the pulse, this again leads to faster saturation of the medium at the point of interaction. This effect is utilised in the so-called self-colliding-pulse mode-locking, where the saturable absorber is placed near the high reflectivity facet to increase its modulation [JON95b]. Such interaction effects in the fundamental mode-locking regime are also not present in the DDE model. There are however other factors related to the geometry of the cavity, which have been shown to have a greater influence on the modulation of the absorber section, that can be observed in the DDE model. In [JAV11] the effect of the positioning of the saturable absorber in a two section laser, i.e. whether or not the absorber is located at the end of the cavity with the anti-reflection coated facet, is studied using a travelling-wave model. Here the authors predict that the output power of the pulses is increased, the pulse widths are decreased and the amplitude and timing jitter is reduced, when the absorber is placed in front of the anti-reflection coated facet. The reasoning for this is that despite a reduction in the interaction of the counter-propagating fields due to the reduced reflectivity, the power of the pulse impinging on the absorber from the gain section is now much greater since there are less mirror losses at the end of the gain section. This leads to faster saturation of the absorber [SIM13], which is known to improve the mode-locking properties [HAU75a]. This dependence on the absorber position has subsequently been demonstrated experimentally [MOS15, ZHU15a]. In the DDE model similar effects can be observed by placing the out-coupling losses before or after the absorber section [ROS11d].

Depending on the heterostructure of the laser under investigation, refinements can be made to the DDE model by choosing more sophisticated models for the carriers. In [VLA10], [ROS11d] and [SIM14] the respective authors have used the DDE approach with charge-carrier equations tailored to quantum-dot lasers.

However, comparisons between the results that will be presented in the subsequent sections, and those present in [SIM14], show that the qualitative trends of the feedback dependence are the same for the simple DDE we use (Eqs. (2.42)-(2.44)) and the more complicated quantum-dot based DDE models.

Aside from the ring-cavity geometry and the unidirectional propagation, there are other simplifying assumptions that mean that the DDE model can only be used to make qualitative not quantitative predicts for experiments. One of these is the lumped-element approach to including the internal non-resonant losses. By including the internal losses only at the ends of the gain and absorber sections the electric field is larger than it should be as it propagates through these sections, which affects the dynamics of the charge carriers. This can be improved upon by dividing the gain and absorber in to multiple sections and including internal losses between each section. The authors of [ROS11d] have done this for a quantum-dot mode-locked laser and have shown that by adding more sections to the ring cavity they obtained better agreement with a travelling-wave model for an equivalent linear cavity. This is however at the expense of a greater computational cost, as each added section requires an additional carrier equation.

Chapter 3

Mode-locked laser dynamics

3.1. Introduction

In this chapter the dynamics of a passively mode-locked semiconductor laser will be studied using the model presented in Chapter 2. The dynamics are studied via direct numerical simulations and by performing numerical path continuation to analyse the bifurcations and stability of the solutions of the DDE model (Eqs. (2.42)-(2.44)). The path continuation is carried out using the software package DDE-BIFTOOL [ENG01]. Throughout this chapter we will be considering the underlying deterministic dynamics of the DDE system, i.e. $R_{sp} = 0$.

This chapter is structured as follows. First a brief introduction to the types of bifurcations that will be encountered will be given in Subsection 3.1.1. Then the dynamics of the solitary laser will be reviewed in Section 3.2. In Sections 3.3 and 3.4 the dynamics arising due to optical feedback from one and two external cavities, respectively, will be investigated.

3.1.1. Bifurcations

A bifurcation occurs when there is a sudden qualitative change in the behaviour of a dynamical system, which is brought on by the smooth change of some parameter of that system. There are two classes of bifurcations, local bifurcations and global bifurcations. In the following analysis of the mode-locked laser system (Eqs. (2.42)-(2.44) we will only encounter local bifurcations. These can be characterised by investigating the stability of solutions near the bifurcation point. The stability of a solution is in turn characterised by the eigenvalues of the linearised system[1], or

[1] A DDE system is linearised as demonstrated for the following two dimensional example with one delay time. Let us consider a system of the form

$$\dot{\mathbf{x}}(t) = \mathbf{F}(\mathbf{x}(t), \mathbf{x}(t-\tau)),$$

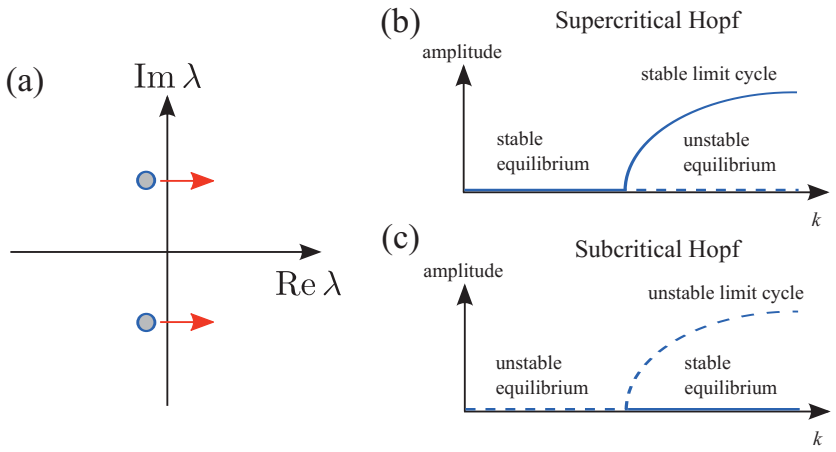

Figure 3.1.: **Hopf bifurcation:** (a) Complex conjugate eigenvalues λ passing through the real axis in a Hopf bifurcation of a steady state solution. Bifurcation diagram of a supercritical (b) and subcritical (c) Hopf bifurcation in dependence of some bifurcation parameter k.

in case of periodic systems by the Floquet multiplers or Floquet exponents (see Appendix A).

Here we give a brief overview of the bifurcations that will be encountered in the DDE model (Eqs. (2.42)-(2.44)). For a rigorous introduction to bifurcation theory see, for example, [KUZ95, GUC86].

Hopf and torus bifurcations

In a Hopf (Andronov-Hopf) bifurcation a limit cycle (periodic solution) is generated out of a steady state (equilibrium) solution of a dynamical system. At the bifurcation point the equilibrium changes stability via a pair of purely imaginary complex conjugate eigenvalues (Fig. 3.1a). The limit cycle that is created can be either stable or unstable depending on the criticality of the bifurcation. In a supercritical Hopf bifurcation a stable equilibrium becomes unstable and a stable limit cycle is generated (Fig. 3.1b). In a subcritical Hopf bifurcation an unstable equilibrium stabilises and an unstable limit cycle is generated (Fig. 3.1c). The frequency of the limit cycle generated in the Hopf bifurcation is given by the imaginary eigenvalues at the bifurcation point.

---

where $\mathbf{x} = (x_1, x_2)^{\mathrm{T}}$ are the dynamical variables and $\mathbf{F} = (F_1, F_2)^{\mathrm{T}}$ are functions of the dynamical variables $\mathbf{x}$ at time t and at the delayed time $t - \tau$. Then the linearised system, about a fixed point $\mathbf{x_0}$, is given by

$$\dot{\delta\mathbf{x}}(t) = \mathbf{A}\delta\mathbf{x}(t) + \mathbf{B}\delta\mathbf{x}(t-\tau),$$

where $\delta\mathbf{x} = \mathbf{x} - \mathbf{x_0}$ and the Jacobi matrices are defined as $A_{ij} = \frac{\partial F_i}{\partial x_j(t)}$ and $B_{ij} = \frac{\partial F_i}{\partial x_j(t-\tau)}$ evaluated at $\mathbf{x_0}$, for $i, j = \{1, 2\}$.

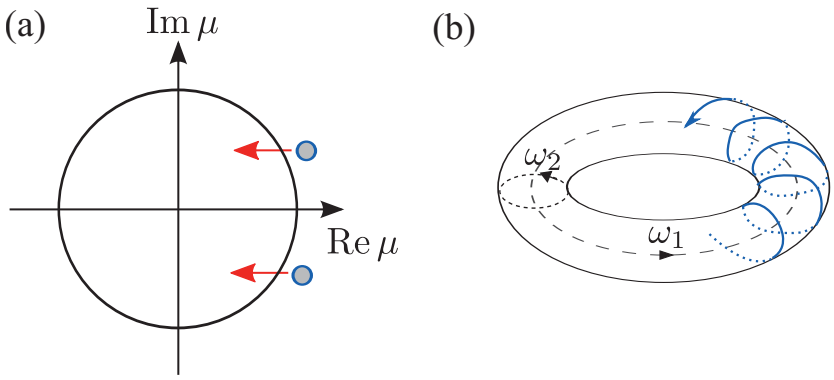

Figure 3.2.: **Torus bifurcation:** (a) Complex conjugate characteristic multipliers μ passing through the unit circle ($|\mu| = 1$) in a torus bifurcation of a limit cycle. (b) Motion on a two-dimensional invariant torus.

A torus bifurcation, also referred to as a secondary Hopf bifurcation, is the bifurcation of a limit cycle in which a two-dimensional invariant torus is created. At the bifurcation point the limit cycle changes stability via two complex conjugate characteristic (Floquet) multipliers passing through the unit circle (Fig. 3.2a). Like the Hopf bifurcation, the torus bifurcation can be supercritical or subcritical. The periodicity of the motion on the torus depends on the frequency of the original limit cycle (ω_1) and the frequency that is introduced in the torus bifurcation (ω_2) (Fig. 3.2b). If the ratio of these two frequency is rational then the motion on the torus will be periodic. However, if the frequencies are incommensurable the motion can be quasi-periodic, which means that the trajectory completely fills in the surface of the torus.

Saddle-node bifurcation

In a saddle-node bifurcation two equilibria (or limit cycles) of a dynamical system collide and disappear. The bifurcation is characterised by one real eigenvalue passing through zero, or in the case of a saddle-node bifurcation of limit cycles, one real characteristic multiplier passing through unity (Fig. 3.3). A typical scenario involving a saddle-node bifurcation is depicted in Fig. 3.4. Here an unstable limit cycle is first created in a subcritical Hopf bifurcation. Following the limit cycle solution from the Hopf bifurcation point, the bifurcation parameter k decreases until the solution becomes stable in a saddle-node bifurcation and folds back in k to continue to exist for larger k values. Due to this folding of the solution as a function of the bifurcation parameter, saddle-node bifurcations are also referred to as fold bifurcations.

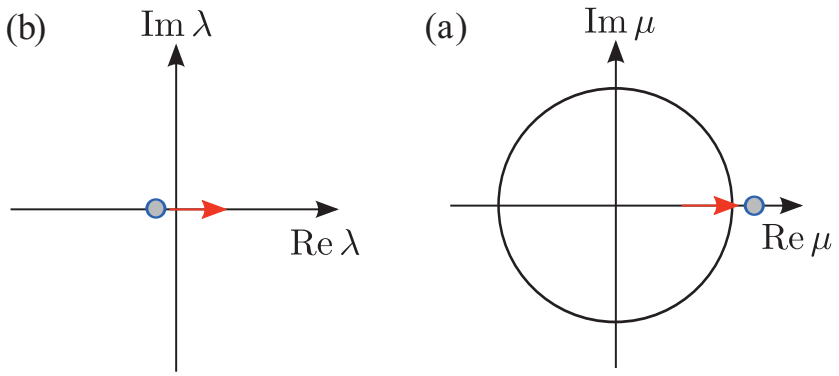

Figure 3.3.: **Saddle-node bifurcation:** (a) One real eigenvalue λ passing through zero in a saddle-node bifurcation of equilibria. (b) One real characteristic multiplier μ passing through unity ($\mathrm{Re}\,\mu = 1$) in a saddle-node bifurcation of limit cycles.

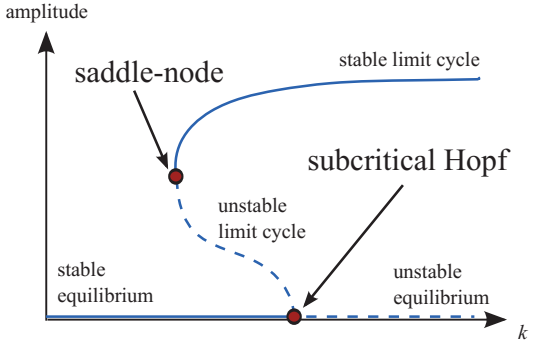

Figure 3.4.: Bifurcation diagram showing a subcritical Hopf bifurcation followed by a saddle-node bifurcation of limit cycles.

Period-doubling bifurcation

A period-doubling bifurcation of a limit cycle involves the creation of a second limit cycle which has approximately twice the period of the original limit cycle. This occurs by a change in the height of the maxima of the limit cycle, as illustrated in Fig. 3.5. This bifurcation can be characterised by one real characteristic multiplier passing though the negative side of the unit circle, i.e. $\mu = -1$ (see Fig. 3.6a). Period-doubling bifurcations also come in subcritical and supercritical variants. In a supercritical period-doubling bifurcation a stable limit becomes unstable and a second stable limit cycle is born. This scenario is depicted in Fig. 3.6b. In the subcritical period-doubling bifurcation an unstable limit cycle becomes stable and a second unstable limit cycle is created, as depicted in Fig. 3.6c. When the bifurcation point is approached from the side of limit cycle with twice the period,

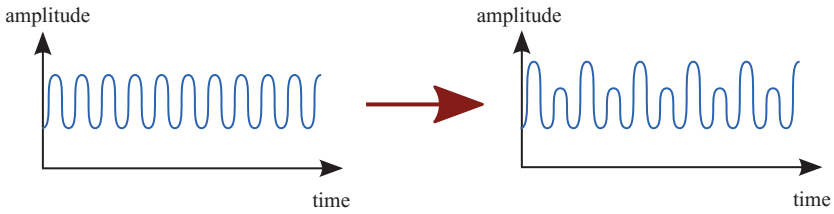

Figure 3.5.: Illustration of a limit cycle before and after a period-doubling bifurcation.

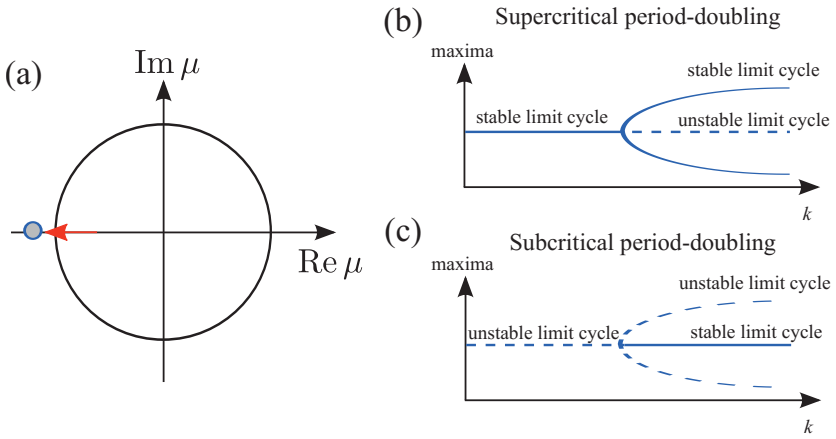

Figure 3.6.: **Period-doubling bifurcation:** (a) One real characteristic multipliers passing through $\mathrm{Re}\,\mu = -1$ in a period-doubling bifurcation. Bifurcation diagram of a supercritical (b) and subcritical (c) period-doubling bifurcation in dependence of some bifurcation parameter k.

which then disappears at the bifurcation point, then this bifurcation is also referred to as a period-halving bifurcation.

Pitchfork bifurcation

In a pitchfork bifurcation one steady state solutions changes stability and two additional solutions are created. A pitchfork bifurcation can be subcritical or supercritical and the bifurcation diagram has the same form as those depicted in Fig. 3.6b-c. The difference being that in this case the two bifurcating branches belong to different steady state solutions instead of one limit cycle solution.

3.2. Solitary mode-locked laser dynamics

In this section we will explore the dynamics of the passively mode-locked laser in the absence of feedback. We will largely be recapping the results of [VLA05, VLA11] which are necessary for understanding the dynamics of the system with feedback in the subsequent sections. We will be addressing the bifurcations of the continuous wave solutions of Eqs. (2.42)-(2.44) (with $K_n = 0$ and $R_{sp} = 0$), as well as the bifurcations of the mode-locked solutions. Further, we will investigate the dependence of the mode-locked solutions on several key parameters by numerical integration of the DDE system.[2]

3.2.1. Lasing threshold

For a semiconductor mode-locked laser to start lasing, a sufficiently large pump current must be applied such that all losses can be overcome. Below this threshold pump current, the laser is in the off state. The off state is a steady state solution of Eqs. (2.42)-(2.44) and is given by

$$\mathcal{E} = 0, \quad G = J_g/\gamma_g \quad \text{and} \quad Q = J_q/\gamma_q, \tag{3.1}$$

where the solutions for G and Q are obtained by setting the derivatives in Eqs. (2.43)-(2.44) to zero. At the threshold pump current the off state becomes unstable and lasing begins. The simplest lasing states are continuous wave solutions of the form $\mathcal{E}(t) = \mathcal{E}_0 e^{i\omega t}$, where ω is referenced to the optical frequency Ω_0. Substituting this continuous wave solution into Eq. (2.42) yields

$$\omega^2 + \gamma^2 = \gamma^2 \kappa e^{G-Q} \tag{3.2}$$

and

$$\frac{\omega}{\gamma} = -\tan\left(\frac{1}{2}\left(\alpha_g G - \alpha_q Q\right) + (\Delta\Omega + \omega)\, T\right) \tag{3.3}$$

[VLA05]. Here G and Q are steady state solutions of Eqs. (2.43) and (2.44), and are given by the equations

$$0 = J_g - \gamma_g G - e^{-Q}\left(e^{G} - 1\right)|\mathcal{E}_0|^2 \tag{3.4}$$

and

$$0 = J_q - \gamma_q Q - r_s e^{-Q}\left(e^{Q} - 1\right)|\mathcal{E}_0|^2. \tag{3.5}$$

This set of transcendental equations has multiple solutions for the frequency ω and the intensity $|\mathcal{E}_0|^2$, which correspond to different lasing modes. Modes with

[2] In certain limits the DDE model can also be analysed analytically, this was done in [VLA05, VLA11]. Also present in these works are comparisons with the models of Haus [HAU75a] and New [NEW74].

increasing detuning from the center of the spectral filter, i.e. the gain maximum of the lasing medium, have a smaller effective gain and hence the threshold current is mode dependent. At the lasing threshold of each mode, Eqs. (3.2)-(3.5) must be fulfilled with $\mathcal{E}_0 = 0$. From Eqs. (3.2), (3.5) and (3.4) the mode dependent threshold current is

$$J_g^{\mathrm{th}}(\omega) = \gamma_g \left(\frac{J_q}{\gamma_q} - \ln(\kappa) + \ln\left(1 + \frac{\omega^2}{\gamma^2}\right) \right) \tag{3.6}$$

where ω must still fulfil Eq. (3.3).

The mode with the smallest absolute detuning from the center of the spectral filter, ω_{min}, has the lowest threshold current, and it is at this threshold current that the off state becomes unstable. All other modes bifurcate from the off state when it is already unstable, and are themselves also unstable. For the bifurcation analysis that follows we choose $\Delta\Omega$, α_g and α_q equal to zero. In this case the maximum gain continuous wave solution has $\omega = \omega_{\mathrm{min}} = 0$. The mode-locked solutions that are of interest bifurcate from this continuous wave solution.

3.2.2. Continuous wave solutions

Using the path continuation software package DDE-BIFTOOL [ENG01] we investigate the pump current dependence of the continuous wave solution that is generated at the lasing threshold (Eq. (3.6) with $\omega = \omega_{\mathrm{min}}$). Figure 3.7 shows the results for this solution. In Fig. 3.7a the electric field amplitude $\mathcal{E}_0$ (red line), the gain G (green line) and the losses Q (blue line) are plotted. The electric field intensity $I = |\mathcal{E}_0|^2$ depends linearly on the pump current, hence $\mathcal{E}_0$ has a square-root dependence. The stability of the solutions is indicated by the thickness of the lines in Fig. 3.7a; stable solutions are plotted with thick lines. A close-up of the current region near threshold, which is $J_g^{\mathrm{th}} = 0.153$ for the parameters used here, is shown Fig. 3.7b. The grey region indicates the current range for which the off state is stable. Here we see that the continuous wave solution is initially stable (as it is born in a supercritical Hopf bifurcation), but loses stability slightly above the threshold current. At relatively large currents ($J_g > 60 J_g^{\mathrm{th}}$) the continuous wave solution restabilises. Within the current range where the solution is unstable, the number of unstable eigenmodes varies. In Fig. 3.7c-d the real parts of eigenvalues are plotted. Since this is a DDE system there are infinitely many eigenmodes, however only a finite number of these can have eigenvalues above any given finite threshold value. Here we only depicted those with $\mathrm{Re}[\lambda]$ close to zero. Those above zero are plotted in red to indicate that these correspond to unstable eigenmodes. In this case each line that crosses $\mathrm{Re}[\lambda] = 0$ corresponds to a Hopf bifurcation, meaning that a pair of complex conjugate eigenvalues crosses the real axis. In Fig. 3.8 this is shown for the Hopf bifurcation (H_1) between the vertical dashed blue lines in

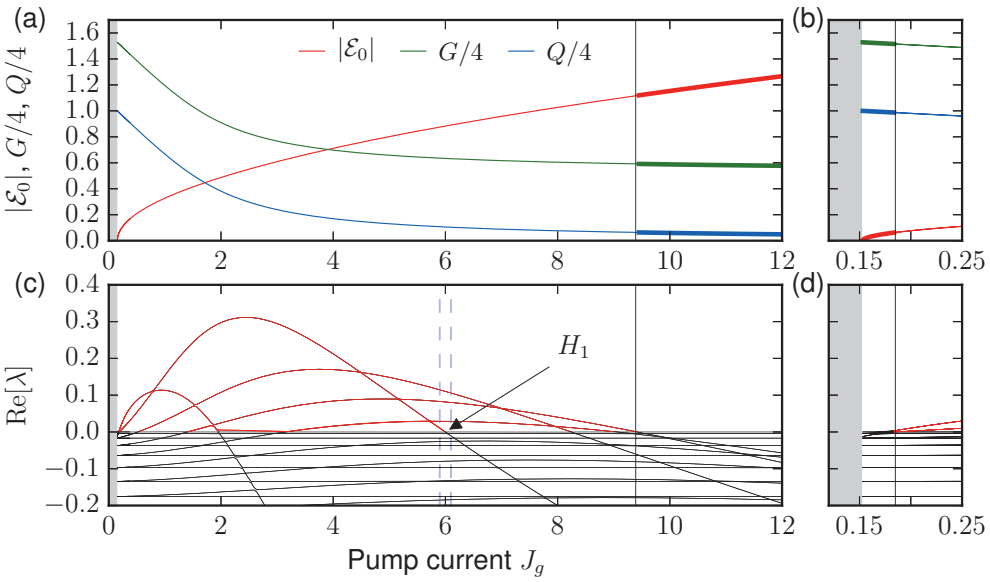

Figure 3.7.: (a) Electric amplitude $\mathcal{E}_0$ (red line), gain G (green line) and losses Q (blue line) of the maximum gain continuous wave solution in dependence of the pump current J_g. A close-up of the current region near threshold is shown in (b). Thick lines indicate where the continuous wave solution is stable and the vertical black lines indicate the pump current values where the solution changes stability. In the grey region the off state (Eq. (3.1)) is stable. (c) Real parts of the eigenvalues λ corresponding to the solutions plotted in (a). Eigenvalues with Re[λ] > 0 are plotted in red. In (d) a close-up of the eigenvalues near threshold is shown. Parameters: $\kappa = 0.121$, $\omega = \omega_{\min} = 0$, all other parameters as in Table 2.1.

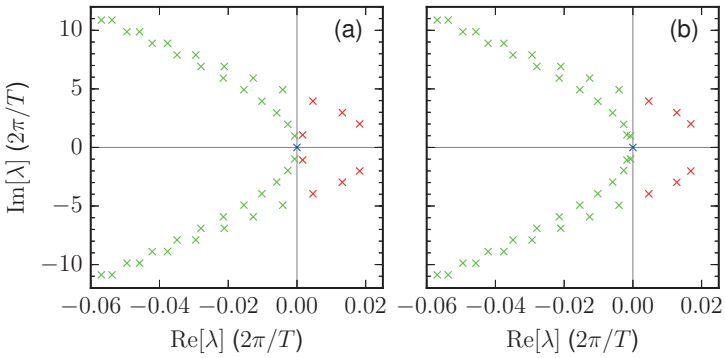

Figure 3.8.: Eigenvalues of the maximum gain continuous wave solution for the pump current values indicated by the left (a) and right (b) vertical dashed blue lines in Fig.3.7c. Parameters: $\omega = \omega_{\min} = 0$, (a) $J_g = 5.9$, (b) $J_g = 6.1$, $\kappa = 0.121$, all other parameters as in Table 2.1.

Fig. 3.7c. Plotted in Fig. 3.8a-b are the real and imaginary parts of the eigenvalues

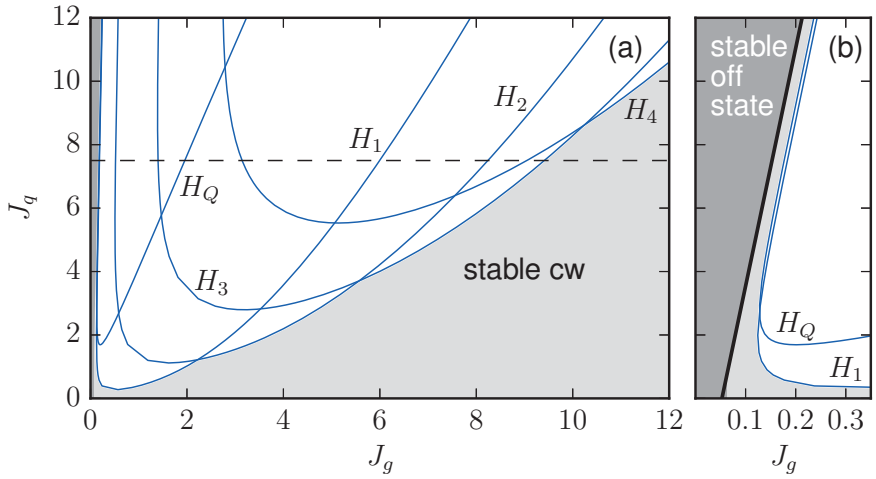

Figure 3.9.: (a) Hopf bifurcation curves in the J_g-J_q plane. A close-up of the region near the threshold pump current is shown in (b). In the light grey regions the continuous wave (cw) solution is stable and in the dark grey region the off state (Eq. (3.1)) is stable. Parameters: $\omega = \omega_{\min} = 0$, $\kappa = 0.121$, all other parameters as in Table 2.1.

before and after the Hopf bifurcation. Comparing subplots (a) and (b) of Fig. 3.8 it can be seen that one pair of eigenvalues changes stability (stable eigenvalues are plotted in green and unstable ones in red).

Post fabrication, the tunable parameters of a passively mode-locked semiconductor laser are the pump current and the bias voltage. As discussed in Subsection 2.2.2, the influence of the bias voltage is largely manifested in the unsaturated absorption J_q. Hence J_q crucially influences the operation of the laser. In Fig. 3.9 the stability and bifurcations of the maximum gain continuous wave solution are shown in the J_g-J_q plane. In the light grey areas the continuous wave solution is stable and in the dark grey area the off state is stable. The blue curves indicate the Hopf bifurcations. The solutions presented in Fig. 3.7 correspond to the position of the horizontal dashed line in Fig. 3.9a. The period of the limit cycle that is generated in each of the Hopf bifurcations is determined by the purely imaginary eigenvalues at the bifurcation point. The Hopf curve labelled H_1 generates a limit cycle with a frequency approximately equal to the fundamental frequency of the laser cavity $\Omega_f = 2\pi/T$ (frequency separation of the cavity modes, i.e. $\Omega_f = 2\pi\Delta\nu$ in Fig. 2.3). This can be seen in Fig. 3.8, which shows eigenvalues for solutions before and after the H_1 Hopf bifurcation. Comparing subplots (a) and (b) of Fig. 3.8, it can be seen that $\mathrm{Im}[\lambda] \approx 2\pi/T$ for the eigenvalues that cross the real axis. It is out of H_1 Hopf bifurcation that the fundamental mode-locked solution develops. The Hopf curves labeled H_n, for $n = 2, 3, 4$, generate limit cycles with frequencies given approximately by $n\Omega_f$. These limit cycles evolve into harmonically mode-

locked solutions. Lastly, the Hopf curve labeled H_Q has a much lower frequency, approximately an order of magnitude lower than Ω_f for the chosen parameters. This bifurcation is related to the Q-switching found in single-mode lasers with a saturable absorber [YAM93, DUB99a, LUE11b].

The general trends shown in Fig. 3.9 are: For increasing unsaturated absorption J_q the stability range of the continuous wave solution decreases and the number of Hopf bifurcations the system goes through increases. The additional Hopf bifurcations that are introduced at higher J_q values produce higher frequency limit cycles. The stability of the limit cycles that are produced in the Hopf bifurcations depend on the criticality of the bifurcation and on the stability of the solution it is bifurcating from. The Hopf curves in Fig. 3.9 do not contain information about the criticality, however this can be obtained by investigating the stability and bifurcations of the emerging limit cycles. For the fundamental Hopf curve H_1 this is done in the next section.

3.2.3. Mode-locked solutions

As indicated by the multitude of Hopf bifurcations depicted in Fig. 3.9, the DDE system for the mode-locked laser has several periodic solutions. In this section we will focus on the fundamental mode-locked solution. The stability and bifurcations of this solution in the J_g-J_q plane are depicted in Fig. 3.10. Torus and saddle-node bifurcations of the fundamental periodic solution are indicated by blue and green lines, respectively. The H_1 Hopf curve out of which the fundamental mode-locked solution emerges is plotted in black. This is the same curve that is shown in Fig. 3.9, however now the criticality is also shown. In the dashed regions the H_1 bifurcation is subcritical and in the solid range it is supercritical. The change in criticality of the H_1 curve occurs at the point where the H_1 and saddle-node branches meet (green circle). The supercritical part of H_1 and the saddle-node branch enclose the parameter region where the fundamental periodic solution exists, and the green shaded part of this region is where this solution is stable. The Hopf curves H_Q and H_2-H_4 are depicted by the thin grey lines. The points where these branches intersect the H_1 curve are Hopf-Hopf points and are indicated by the red circles. A Hopf-Hopf point is where two branches of Hopf bifurcations intersect. Generally two branches of torus bifurcations emanate from a Hopf-Hopf point. Here we only show the torus bifurcations of the periodic solution generated in the H_1 bifurcation. Hence there are four branches of torus bifurcations depicted in Fig. 3.10, which emanate from the Hopf-Hopf points marked by the red circles.

To better understand this bifurcation diagram it is helpful to consider cuts along J_g. Starting at the low current part of the H_1 curve, the fundamental periodic solution is generated in a supercritical Hopf bifurcation. If J_q is below the Hopf-Hopf point where the H_Q curve intersects H_1, then the solution that is generated is

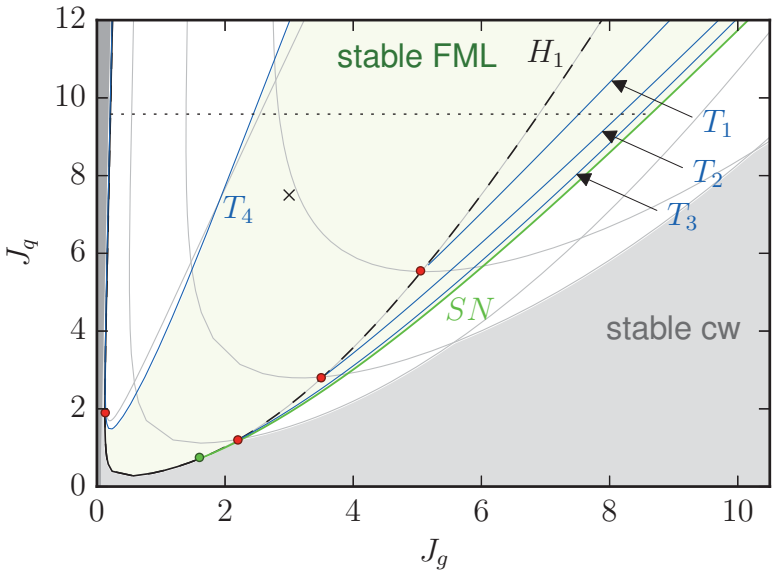

Figure 3.10.: Bifurcations of the fundamental mode-locked solution in the J_g-J_q plane. Blue lines is indicate Torus bifurcations (T_1-T_4) and the green line is a saddle-node bifurcation (SN). The black line is the fundamental Hopf bifurcation curve of the continuous wave solution (H_1), with the solid segment being supercritical and the dashed segment subcritical. The green circle marks the point where the H_1 curve changes criticality. The thin grey lines show the remaining Hopf bifurcations of the continuous wave solution (compare with Fig. 3.9). Hopf-Hopf points involving the H_1 curve are indicated by red circles. Shaded in green is the stability region of the fundamental mode-locked (FML) solution. In the light grey regions the continuous wave solution is stable and in the dark grey region the off state (Eq. (3.1)) is stable. The black cross indicates the position of the parameters corresponding to Table 2.1. Parameters: $\kappa = 0.121$, $\omega = \omega_{\min} = 0$, all other parameters as in Table 2.1.

stable. However if J_q is above this point then the solution is unstable, even though the bifurcation is supercritical, because the continuous wave solution is already unstable when the H_1 bifurcation occurs (see Fig. 3.9 (b)). In the latter case, if J_g is increased, the solution first becomes stable after the torus bifurcation T_4. Increasing the pump current further, the solution remains stable until the saddle-node bifurcation. At this point the solution coalesces with the unstable periodic solution that is generated in the subcritical part of the H_1 curve. This is depicted in Fig. 3.11 for the unsaturated absorption J_q value indicated by the horizontal dotted black line in Fig. 3.10. In Fig. 3.11a the electric field maxima are plotted and in Fig. 3.11b the period of the solutions is shown. Stable solutions are indicated by the green symbols in Fig. 3.11a and by the solid line in Fig. 3.11b. Also indicated in Fig. 3.11b are the positions of the bifurcations, which have the same labelling as in Fig. 3.10. The solution generated in the subcritical H_1 bifurcation can have

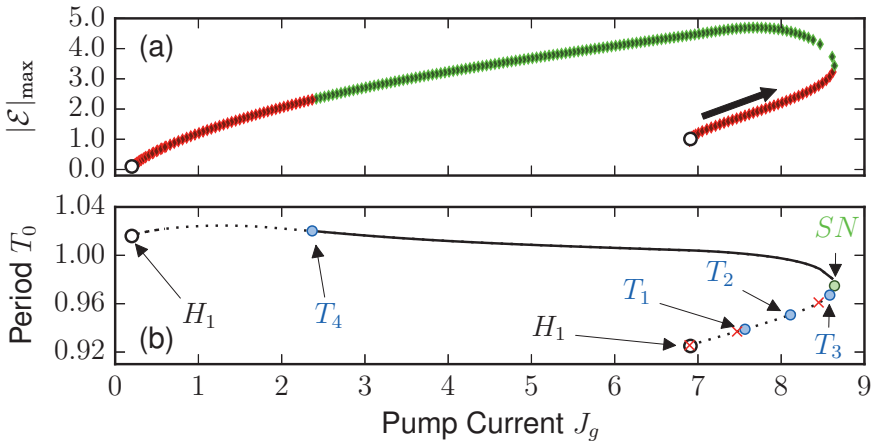

Figure 3.11.: Branch of periodic solutions continued from the H_1 curve, corresponding to the dotted black line in Fig.3.10. Electric field maxima $|\mathcal{E}_{\max}|$ are plotted in (a) and the period T_0 is plotted in (b). Stable section of the branch are plotted in green (solid lines) and unstable in red (dotted lines). In (b) the positions of the Hopf, torus and saddle-node bifurcations are indicated by the black, blue and green circles, respectively. The red crosses correspond to Fig. 3.12a-c. Parameters: $J_q = 9.58$, $\kappa = 0.121$, all other parameters as in Table 2.1.

multiple unstable directions, the number of which depend on J_q. These added unstable directions are related to the stability of the continuous wave solution at the point of the H_1 bifurcation (e.g. see Fig. 3.8). Starting from the subcritical H_1 bifurcation at about $J_g = 6.9$ in Fig. 3.11, the solution is unstable and has relatively small maxima. First there are three pairs of complex conjugate multipliers with $|\mu| > 0$, because the continuous wave solution has an additional three pairs of unstable eigenvalues at the bifurcation point. This is shown in Fig. 3.12a. As the periodic solution is continued one real multiplier, which was equal to one at the bifurcation, becomes larger than one (Fig. 3.12b). Then, as J_g is increased further the height of the maxima increases and the solution goes through a series of torus bifurcations (T_1-T_3) in which unstable pairs of multipliers enter the unit circle. Figure 3.12c shows the multipliers for a solution between T_2 and T_3 at $J_g = 8.45$ and compared with Fig. 3.12b two pairs of multipliers have entered the unit circle. After the T_3 bifurcation there is only one real characteristic multiplier with $|\mu| > 1$. Following the three torus bifurcations, as the solution is continued further this branch folds over in J_g and the solutions becomes stable after the saddle-node bifurcation. As the branch is continued further, J_g decreases and eventually the solutions lose stability after the torus bifurcation T_4. Finally, the solution disappears in the H_1 bifurcation near $J_g = 0.2$.

Near the H_1 bifurcations, in which the fundamental periodic solution is generated, the oscillations are initially sinusoidal with a very small amplitude. As the

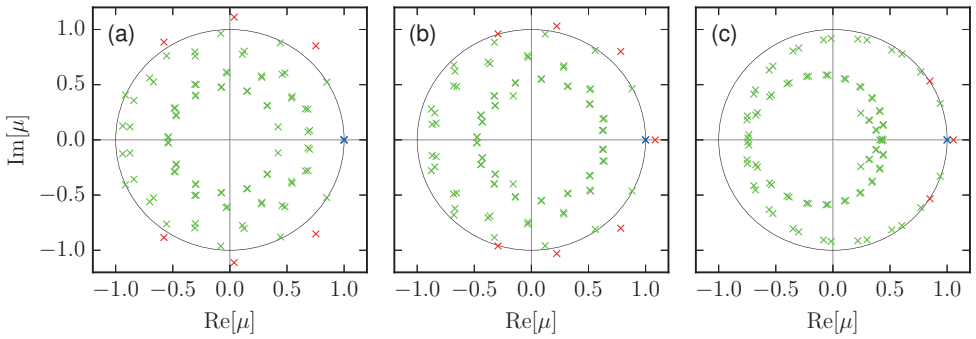

Figure 3.12.: Characteristic multipliers of the fundamental periodic solution bifurcating from the subcritical part of H_1 at $J_q = 9.58$. The solutions correspond to the red crosses in Fig. 3.11b. Parameters: (a) $J_g = 6.9$, (b) $J_g = 7.47$, (c) $J_g = 8.45$, $\kappa = 0.121$, all other parameters as in Table 2.1.

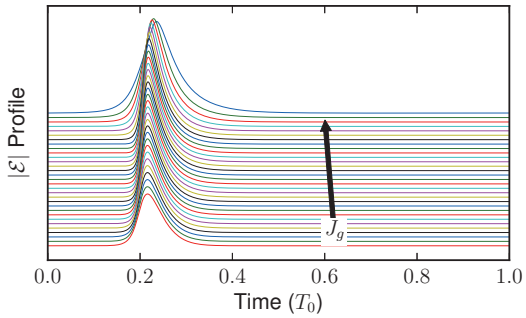

Figure 3.13.: Electric field profiles for the stable mode-locked solutions of the branch depicted in Fig. 3.11. The time axis spans one period T_0 of the solutions. Parameters: $J_q = 9.58$, $\kappa = 0.121$, all other parameters as in Table 2.1.

solution is continued it then evolves into the mode-locked solution. The pulse profiles, for the stable section of the branch depicted in Fig. 3.11, are shown in Fig. 3.13. As the current is increased the pulse amplitude increases (also see Fig. 3.11a), the pulses become wider and the period T_0 decreases (Fig. 3.11b). Between pulses the electric field amplitude drops to zero. Physically these pulsed solutions, and their dependence on the pump current, can be understood by considering the gain and absorber dynamics. Figure 3.14 shows an example of the dynamics of the gain, losses and electric field amplitude in the mode-locked regime. Shown here are time traces of the electric field amplitude (blue), the gain (green) and the total losses $Q_{\mathrm{tot}} = Q - \ln(\kappa)$ (red), which are the sum of the absorber losses and the non-resonant internal and mirror losses. Also shown is the net gain $\mathcal{G} = G - Q_{\mathrm{tot}}$ (black). From this time trace it is evident that the dynamics evolve in two stages;

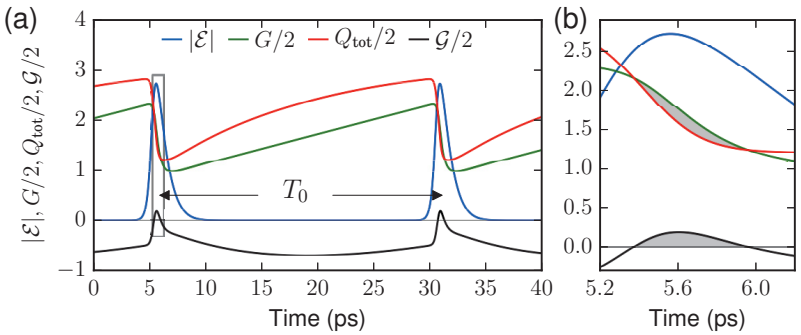

Figure 3.14.: (a) Time trace of the electric field amplitude $|\mathcal{E}|$ (blue), gain G (green), total losses $Q_{\text{tot}} = Q - \ln(\kappa)$ (red) and the net gain $\mathcal{G} = G - Q_{\text{tot}}$ (black). (b) Close-up of the region enclosed in the grey box in (a). This solution corresponds to the black cross in Fig. 3.10. Parameters: $\kappa = 0.121$, all other parameters as in Table 2.1.

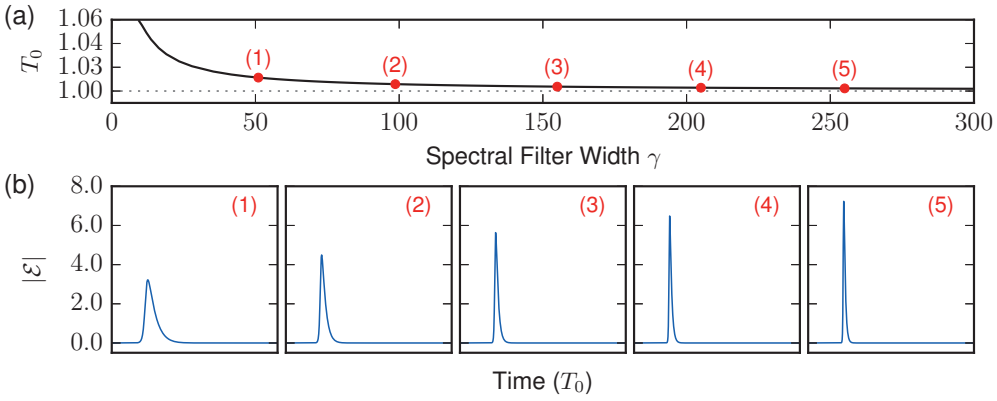

Figure 3.15.: (a) Period T_0 and (b) pulse profiles of the fundamental mode-locked solution as a function of the Lorentzian spectral filter width. The pulse profiles are plotted over one period. Parameters: $J_g = 5.01$, $J_q = 9.58$, $\kappa = 0.121$, all other parameters as in Table 2.1.

a slow stage and a fast stage. The fast stage occurs when the pulse enters the gain and absorber media. As the leading edge of the pulse enters the gain section the inverted charge carriers are depleted, this causes G to decrease. In the absorber section the leading edge of the pulse is absorbed which causes the creation of electron-hole pairs and drives the absorber towards transparency, meaning that the losses Q_{tot} decrease. The rates at which the gain and absorber sections saturate is determined by the linear gain coefficients g_g and g_q, respectively. Since $g_q > g_g$, the absorber saturates faster than the gain section, which leads to a window of positive net gain (shaded region in Fig. 3.14b). This net gain window allows the center of the pulse to be amplified. After the pulse has passed, G and Q recover

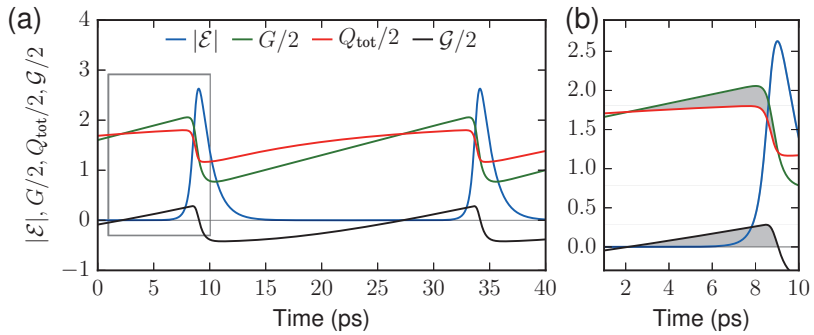

Figure 3.16.: (a) Time trace of the electric field amplitude $|\mathcal{E}|$ (blue), gain G (green), total losses $Q_{\mathrm{tot}} = Q - \ln(\kappa)$ (red) and the net gain $\mathcal{G} = G - Q_{\mathrm{tot}}$ (black). (b) Close-up of the region enclosed in the grey box in (a). Parameters: $J_q = 3$, $\kappa = 0.121$, all other parameters as in Table 2.1.

in the slow stage, at time scales given by γ_g and γ_q. The absorber recovery rate is faster than that of the gain section, which leads to the losses dominating during the slow stage and hence to the electric field amplitude being close to zero between pulses. The slow and fast stages can, under certain approximations, be described analytically due to the separation of the dominating time scales [VLA05].

The pulse repetition period is slightly longer than the cold cavity roundtrip time; in the example depicted in Fig. 3.14 the period is $T_0 = 1.014T$. This is a consequence of the response time of the spectral filter, and the time it takes for the absorber to saturate, i.e. the leading edge of the pulse is absorbed causing the effective pulse group velocity to be smaller than v. If the leading edge of the pulse has a higher intensity then the absorber takes less time to saturate, causing a decrease in T_0. The intensity of the leading edge of the pulse is determined by the pulse energy and the pulse width. As the pump current is increased the pulse energy increases and hence the period decreases (stable section of Fig. 3.11b). The pulse width is dependent on the number of modes participating in the mode-locking, which is determined by the width of the spectral filter. The laser cavity mode spacing is T^{-1}, therefore the number of lasing modes can be estimated as γT^{-1}. If γT^{-1} is large the pulse width is given approximately by γ^{-1} [VLA05, VLA11]. Therefore, for increasing γ, the period decreases due to the decreased filter response time and due to the increased peak intensity. The dependence of the pulse profile and the period T_0 on the spectral filter width is illustrated in Fig. 3.15.

In the example depicted in Fig. 3.14 the net gain is negative during the entire slow stage. According to New's stability criterion, this is a necessary condition for

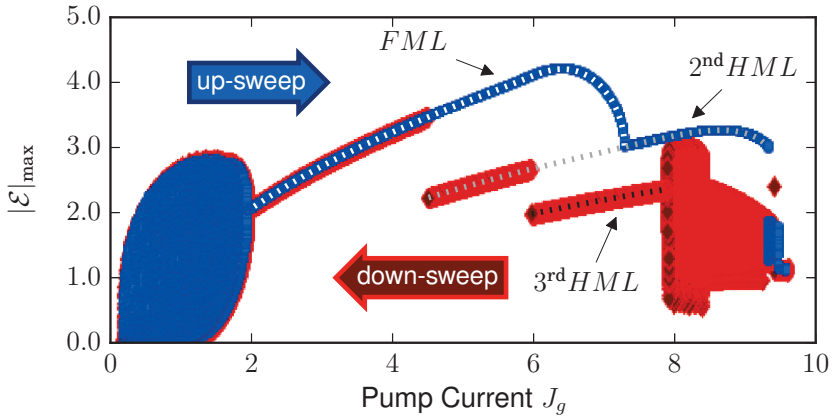

Figure 3.17.: Numerical bifurcation diagram showing the pump current dependence of the mode-locked laser output. Plotted in blue (red) are electric field maxima $|\mathcal{E}|_{\max}$ for an up-sweep (down-sweep) in the initial conditions. The dotted white line indicates the stable fundamental mode-locked (FML) solution. The dotted grey and black lines indicated 2^{nd} and 3^{rd} order harmonic mode-locking (HML), respectively. Parameters: $\kappa = 0.121$, all other parameters as in Table 2.1.

the background to be stable against perturbations [NEW74].[3] There are however other mode-locked solutions for which New's criterion is not fulfilled. Figure 3.16 shows such an example for $J_q = 3$. Here the positive net gain window is open before the arrival of the pulse. In this case, this behaviour is caused by the relatively low unsaturated absorption J_q. Because J_q is small the absorber is fully recovered before the pulse returns, whereas the gain is still recovering. Within this region of positive net gain the system can be very sensitive to perturbations as these can be amplified. However, the authors of [VLA11] have shown that mode-locked solutions are not necessarily unstable against noise perturbations if New's criterion is violated. The relative group velocities of the pulse and the perturbations also play a role in determining the stability of the background. Background stability will be important for the investigation of the DDE system subject to noise, which is presented in Chapter 4.

Outside the current range where the fundamental mode-locked solution is stable, a mode-locked laser can display various dynamics. We investigate these via direct numerical integration of Eqs. (2.43)-(2.44).[4] Figure 3.17 shows a numerical bifurcation diagram of the pump current dependence. Plotted are maxima

[3] What we mean by "stable against perturbations" is whether the solutions still exist in the presence of noise, or if the dynamics are significantly changed when a small noise term is added.

[4] For the numerical simulation of the DDE system (Eqs. (2.42)-(2.44)) we use the Euler integration method with a time step of $h = 10^{-4}$. For the initial conditions we generally use $(\mathcal{E}_R, \mathcal{E}_I, G, Q) = (0.4, 0, 4, 1)$ over the entire time interval $[-\tau', 0]$, where $\mathcal{E}_R$ and $\mathcal{E}_I$ are the real

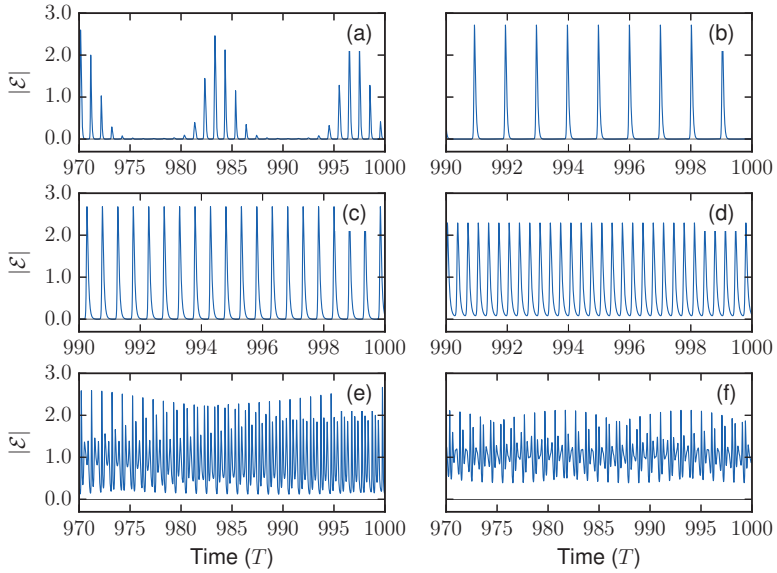

Figure 3.18.: Time traces of the mode-locked laser output for various pump currents. Parameters: (a) $J_g = 1$, (b) $J_g = 3$, (c) $J_g = 6$, (d) $J_g = 7.5$, (e) $J_g = 8$, (f) $J_g = 9$, $\kappa = 0.121$, all other parameters as in Table 2.1.

of the electric field amplitude which are collected over a time span of one hundred cold-cavity roundtrip times. The results plotted in blue were obtained by performing an up-sweep in the initial conditions. This means that the history of the previous current step was used as the initial conditions for the next, as the current was incrementally increased. In the down-sweep (red symbols) the current was incrementally decreased. The idea behind such an approach is to stay on one solution branch as long as possible in regions of multistability. In regions of Fig. 3.17 where the red and blue symbols do not overlap the system has landed on different solutions for the up- and down-sweeps, i.e. these are regions of bistability or multistability. For the current values where only one maxima is plotted the system is exhibiting mode-locked dynamics. The regions of fundamental, 2^{nd} and 3^{rd} order harmonic mode-locking are indicated by the white, grey and black dotted lines, respectively. At low currents, and at high currents, there are solutions with varying pulse heights. Examples of the electric field amplitude dynamics in each of the qualitatively different regions of Fig. 3.17 are shown in Fig. 3.18. Starting at low pump currents the system is in a regime of Q-switched mode-locking. These dynamics arise out of the T_4 torus bifurcation of the fundamentally mode-locked solution (see Fi.g 3.10). In this regime the amplitude of the mode-locked pulses is

and imaginary components of the complex electric field amplitude $\mathcal{E}$ and τ' is the longest total delay time.

strongly modulated on time scales of the Q-switching frequency (frequency of the H_Q Hopf bifurcation) and the pulses appear in bunches, with a near zero electric field amplitude for several laser cavity roundtrips between the pulse bunches (see Fig. 3.18a). Such Q-switched solutions arise at low currents because they are energetically favourable. As the current is increase past the torus bifurcation (near $J_g = 2$), fundamental mode-locking becomes stable (Fig. 3.18b). In agreement with these results, Q-switched mode-locking and the transition to fundamental mode-locking has been observed experimentally in both quantum well and quantum dot semiconductor passively mode-locked lasers [PAL91, BAN06, KUN07a, VLA10]. As the current is increased further, 2^{nd} and 3^{rd} harmonic mode-locking also become stable. These are mode-locked regimes with repetition frequencies that are integer multiples of the fundamental repetition rate, i.e. in the 2^{nd} and 3^{rd} harmonic cases there are two (see Fig. 3.18c) and three (see Fig. 3.18d) peaks per laser cavity roundtrip, respectively. Multistability between different orders of harmonic mode-locking has also been observed experimentally, particularly in devices with relatively long passive sections [SAN90, MAR14c]. An example of harmonic mode-locking in a semiconductor ring-cavity laser was demonstrated in [HOH93]. At relatively high currents the harmonic mode-locked solutions break-up and the system exhibits chaotic oscillations of the peak intensity. The break-up of harmonic mode-locking occurs at high currents because the gain and absorber do not have time to recover between pulses, causing an interaction between subsequent pulses [NIZ06, VLA11].

Experimentally it is typically the power spectrum of the laser output that is measured. For easier comparison with experimental results, the power spectra corresponding to the time traces of Fig. 3.18 are shown in Fig. 3.19. The fundamental repetition frequency of the simulated laser is approximately $\nu_f = 40\text{GHz}$ $((T_0 \cdot 25\text{ps})^{-1})$, accordingly for fundamental mode-locking there is a peak in the power spectra near 40 GHz and at higher harmonics (Fig. 3.19b). For Q-switched mode-locking additional peaks are present with a frequency separation corresponding to the modulation frequency (Fig. 3.19a). The power spectra of the harmonically mode-locked solutions show only peaks at multiples of $n\nu_f$, where $n = 2, 3$ is the harmonic order (see Fig. 3.19c-d).

Influence of amplitude-phase coupling

So far we have investigated the dynamics in the absence of amplitude-phase coupling. However in semiconductor quantum-well materials α-factor values are typically in the range 2-6 [HAR83, OSI87, FOR07]. Furthermore, it is know from other laser systems in which the phase of the light plays a role, that the amplitude-phase coupling can strongly influence the behaviour, generally leading to more complex dynamics. For example in optically injected lasers the α-factor affects the extent

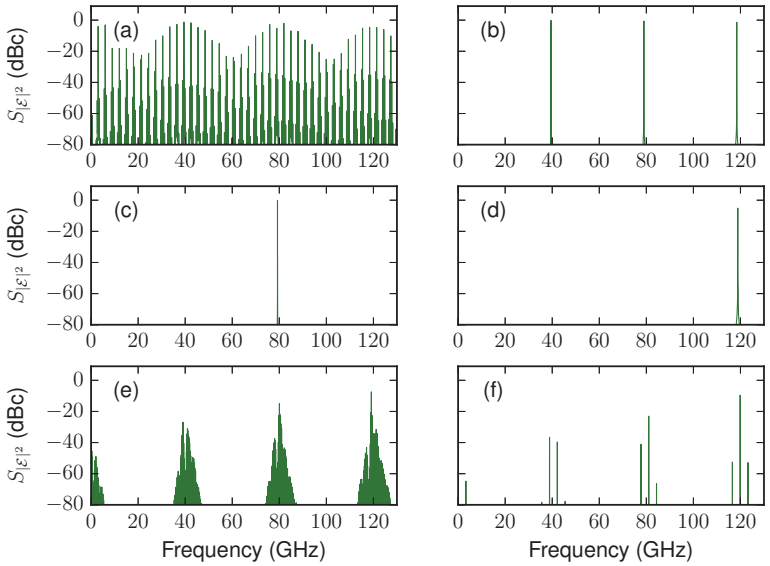

Figure 3.19.: Power spectra of the electric field amplitude, $S_{|\mathcal{E}|^2}$, of the mode-locked laser output corresponding to the dynamics depicted in Fig. 3.18. Parameters: (a) $J_g = 1$, (b) $J_g = 3$, (c) $J_g = 6$, (d) $J_g = 7.5$, (e) $J_g = 8$, (f) $J_g = 9$, $\kappa = 0.121$, all other parameters as in Table 2.1.

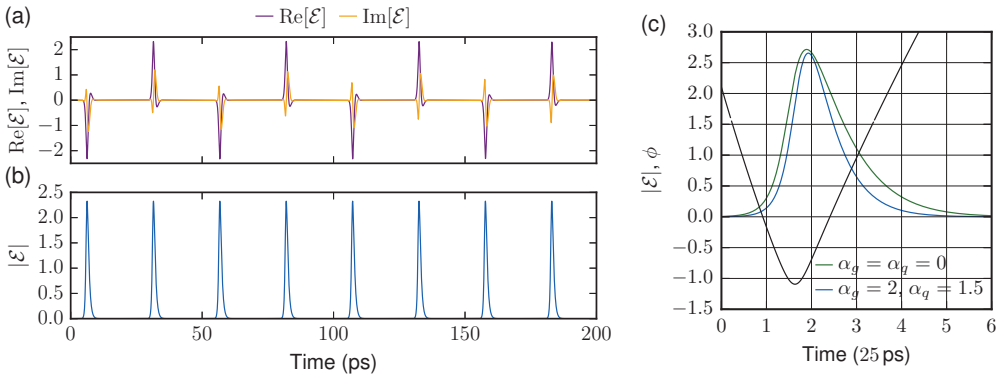

Figure 3.20.: (a) Time trace of the real (Re[$\mathcal{E}$]) and imaginary (Im[$\mathcal{E}$]) parts of the complex electric field amplitude for $\alpha_g = 2$ and $\alpha_q = 1.5$. (b) Corresponding time trace of electric field amplitude $|\mathcal{E}|$. (c) Pulse profile (blue) and electric field phase ϕ (black) for $\alpha_g = 2$ and $\alpha_q = 1.5$, pulse profile for $\alpha_g = \alpha_q = 0$ (green). Parameters: $\kappa = 0.121$, all other parameters as in Table 2.1.

of the locking cone and in semiconductor lasers with feedback the α-factor is related the stability range of continuous wave solutions [MOR92, ROT07, ERN10b, OTT12, LIN15]. Therefore, in this section the influence of amplitude-phase coupling on the mode-locked laser dynamics will be addressed.

From Eqs. (3.3) and (3.6) it is known that the lasing threshold is dependent on the amplitude-phase coupling. For non-zero α-factors the lasing modes are detuned from the center of the spectral filter. Hence the gain of the central mode is reduced and therefore the lasing threshold is increased. The shift of the lasing modes with respect to the spectral filter also means that the modes are detuned from the reference rotating frame (Ω_0). In the simulations this leads to an added rotation of the complex electric field amplitude, as shown in Fig. 3.20a which depicts a time trace of the real (Re[$\mathcal{E}$]) and imaginary (Im[$\mathcal{E}$]) parts of the complex electric field amplitude for $\alpha_g = 2$ and $\alpha_q = 1.5$. In this example the rotation frequency of the complex electric field is incommensurable with the pulse repetition frequency, meaning the Re[$\mathcal{E}$] and Im[$\mathcal{E}$] are quasi-periodic, but $|\mathcal{E}|$ is periodic. The quasi-periodic dynamics of the electric field components can be compensated for by shifting the rotating frame of the system. However, in addition to the shift of the modes, non-zero amplitude-phase coupling also causes the pulses to become chirped. Meaning that the instantaneous frequency $\frac{d\phi}{dt}$ varies within the pulse, where ϕ is the phase of the electric field. Figure 3.20c shows an example of the non-linear variation of the phase for $\alpha_g = 2$ and $\alpha_q = 1.5$ (black line), the corresponding electric field amplitude is depicted in blue. For comparison the pulse profile for zero amplitude-phase coupling is also plotted (green line). In this case the addition of amplitude-phase coupling leads to narrower pulses. Experimental studies have shown that the self-phase modulation caused by the amplitude-phase coupling leads to a wider optical spectrum [DER92], however this does not necessarily mean that the pulses become narrower in the time domain. If the lasing modes are not all phase-locked then, despite the wider optical spectrum, the pulse can also become wider [KUI70, JON95b].

In the fundamental mode-locked regime the pulse repetition frequency, i.e $1/T_0$, varies only slightly with the amplitude-phase coupling, however the shift of the optical frequencies is relatively pronounced. This can be seen in Fig. 3.21 in which optical spectra are shown for various values of $\alpha_g = \alpha_q$. The frequency is given in reference to the center of the spectral filter Ω_0. Due to the shift of the lasing modes a phase-shift accumulates as a pulse travels around the ring cavity, i.e. there is a phase difference between the electric field at time t and delayed field from time $t - T$. This will be important for understanding the dependence of the dynamics under the influence of optical feedback, which will be presented in the next section.

In Fig. 3.22 the impact of non-zero amplitude-phase coupling on the pump current dependence of the mode-locked laser output is shown. In real devices the α-factor in the gain and absorber sections should be different due to the difference in the charge-carrier densities, however, here we start our analysis with case that $\alpha_g = \alpha_q$. Plotted in Fig. 3.22 are the maxima in the electric field amplitude for up- and down-sweeps in the initial conditions for α-factor values of 1-5. The results were obtained in the same manner as Fig. 3.17. For low values of the

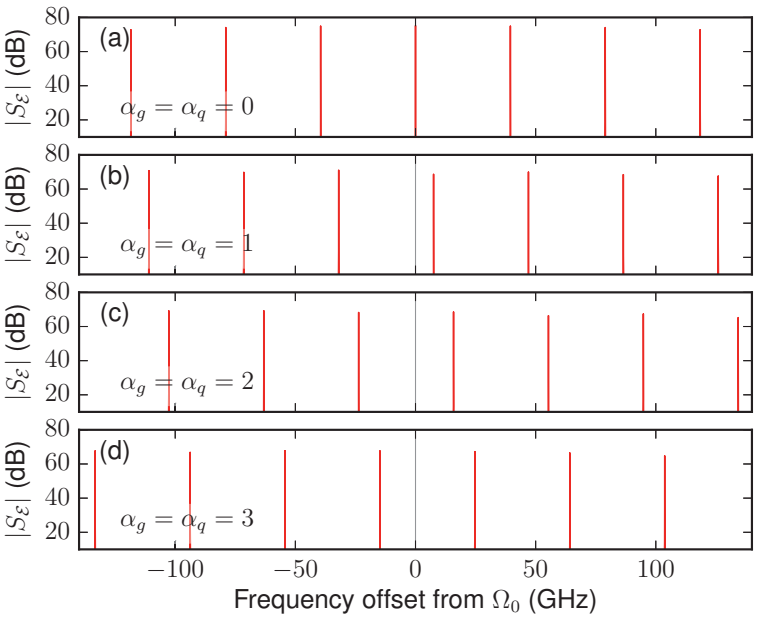

Figure 3.21.: Optical spectra $|S_\mathcal{E}|$ of the mode-locked laser output for various α-factor values. Parameters: $\kappa = 0.121$, all other parameters as in Table 2.1.

amplitude-phase coupling the current dependence is very similar to that present in Fig. 3.17 for $\alpha_g = \alpha_q = 0$. At low currents there is a regime of Q-switched mode-locking, which can be identified in Fig. 3.22 by the low current ranges with many maxima of varying heights. Past the regime of Q-switched mode-locking, fundamental mode-locking becomes stable. As the pump current is increased further there are ranges of 2^{nd} and 3^{rd} order harmonic mode-locked. For increasing values of the amplitude-phase coupling the ranges of fundamental and harmonic mode-locking decrease and the onset of fundamental mode-locking is pushed to higher pump currents. These results are qualitatively similar to those presented in [VLA05, VLA11], where $\alpha_g = \alpha_q$ was used as the bifurcation parameter for a fixed pump current and it was found that for increasing amplitude-phase coupling there is a sudden transition from fundamental mode-locking to chaotic dynamics.

The type of dynamics exhibited for large amplitude-phase coupling can vary slightly from those presented previously for the case where amplitude-phase coupling is absent (Fig. 3.18). Examples of the electric field dynamics are shown for $\alpha_g = \alpha_q = 4$ in Fig. 3.23. The Q-switched mode-locking regime develops into a mode-locked regime with modulated pulse heights, as shown for $J_g = 3$ in Fig. 3.23a. The harmonic mode-locked solutions can also exhibit pulse height modulation, as depicted in Fig. 3.23b for $J_g = 4.5$. In this case there are two pulse height envelopes corresponding to the two pulses in the laser cavity. In Fig. 3.23c

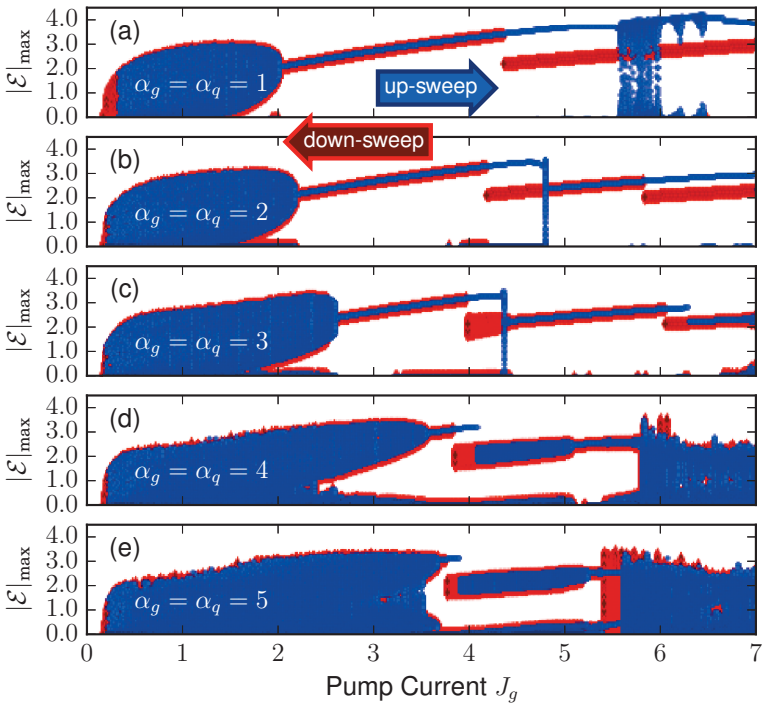

Figure 3.22.: Numerical bifurcation diagram showing the pump current dependence of the mode-locked laser output for various α-factor values. Plotted in blue (red) are electric field maxima $|\mathcal{E}|_{\max}$ for an up-sweep (down-sweep) in the initial conditions. Parameters: $\kappa = 0.121$, all other parameters as in Table 2.1.

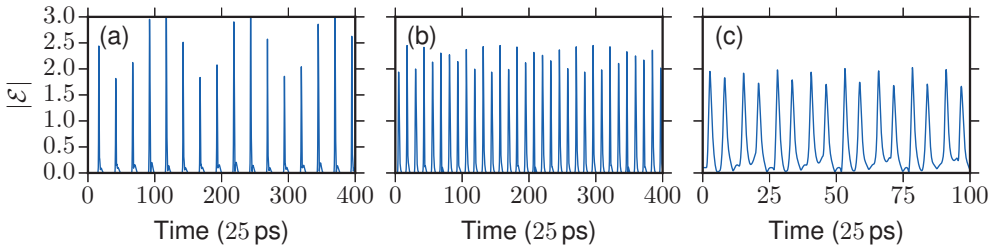

Figure 3.23.: Time trace of the electric field amplitude $|\mathcal{E}|$ for $\alpha_g = \alpha_q = 4$ and (a) $J_g = 3$, (b) $J_g = 4.5$, (c) $J_g = 6.5$. Parameters: $\kappa = 0.121$, all other parameters as in Table 2.1.

($J_g = 6.5$) the dynamics are similar to 4^{th} order harmonic mode-locked, however the pulse heights vary non-periodically, as does the electric field amplitude between pulses.

As was discussed in Section 2.2.2 the carrier dependence of the α-factor means that the values should be different in the gain and absorber sections. To investigate

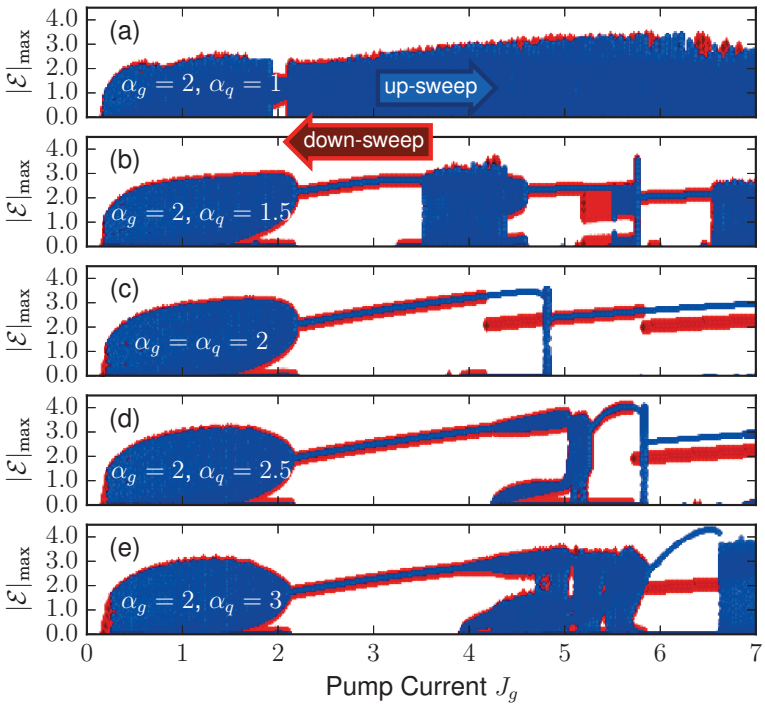

Figure 3.24.: Numerical bifurcation diagram showing the pump current dependence of the mode-locked laser output for various α-factor values. Plotted in blue (red) are electric field maxima $|\mathcal{E}|_{\max}$ for an up-sweep (down-sweep) in the initial conditions. Parameters: $\kappa = 0.121$, all other parameters as in Table 2.1.

the impact of detuning α_g and α_q, the pump current dependence is shown in Fig. 3.24 for various α_q values with $\alpha_g = 2$ fixed. The general trend displayed in these numerical bifurcation diagrams is that the dynamics are most regular if α_q is equal to, or slightly larger than α_g. This can be understood by considering how the α-factors enter Eq. (2.42). The α-factors enter the exponent in Eq. (2.23) in the form $\alpha_g G - \alpha_q Q$. Therefore the contributions compensate each other if $\alpha_g G \approx \alpha_q Q$, which occurs best when $\alpha_q \gtrapprox \alpha_g$ [VLA05].

Overall, similar dynamics can be exhibited when amplitude-phase coupling is included and, at least for low α-factor values, the pump current dependence displays the same qualitative trends as in the absence of amplitude-phase coupling. However, amplitude-phase coupling causes the pulses to become chirped, and can lead to a non-periodic modulation of the pulsed dynamics.

3.3. Dynamics induced by feedback from a single external cavity

Adding optical feedback to the mode-locked laser greatly influences the dynamics that can be exhibited. This has previously been demonstrated by the theoretical studies presented in [AVR09, OTT12a, OTT14, SIM14]. In [AVR09] the authors used a finite-difference travelling-wave model for a linear cavity to study the influence of feedback from a short external cavity (feedback delay times up to $\approx 3T_0$), whereas in [SIM14] the DDE-model approach is used to study the influence of long feedback delay times on a laser with a quantum-dot gain medium. In [OTT12a, OTT14] the same model is used as in this thesis and the dynamics are investigated in the regimes of short and intermediate feedback delay times. Also using the DDE-modelling approach, the dynamics arising from coupling to an external passive cavity, with a roundtrip time lower than that of the laser cavity, were studied in [ARK15a]. In this study the focus was on inducing harmonic mode-locking via the coupling to the external cavity. We add to the knowledge provided by these previous studies by presenting an analysis of the dynamics over a wide range of feedback delay times, and establishing how the dynamics in different feedback delay regimes are related. Furthermore, we analyse the bifurcations of the mode-locked solutions in dependence of the feedback parameters in order to gain a deeper understanding of the mechanisms leading to various feedback induced dynamics.

With feedback from one external cavity there are three additional parameters; the feedback delay time $\tau = \tau_1$, the feedback strength $K = K_1$ and the feedback phase $C = C_1$ (Eqs.(2.42)-(2.44) with $N = 1$). In this section the dynamics arising in dependence of these feedback parameters will be investigated. We shall consider the dynamics in three regimes, short ($\tau \approx 1$), intermediate ($\tau \approx 10$) and long ($\tau \approx 100$) delay times.

3.3.1. Short delay

We are primarily interested in the influence of feedback on the fundamentally mode-locked solution. Since the mode-locked solution is periodic, the dynamics that can arise with feedback are strongly dependent on the ratio of the period of the mode-locked solution and the delay time that is introduced by the feedback. The equation for the electric field amplitude, in the single feedback cavity case, is

$$\begin{aligned} \frac{d\mathcal{E}}{dt} &= -\gamma\mathcal{E}(t) + \gamma R(t-T)\, e^{-i\Delta\Omega T}\mathcal{E}(t-T) \\ &+\gamma K e^{iC} R(t-T-\tau)\, e^{-i\Delta\Omega(T+\tau)}\mathcal{E}(t-T-\tau)\,. \end{aligned} \tag{3.7}$$

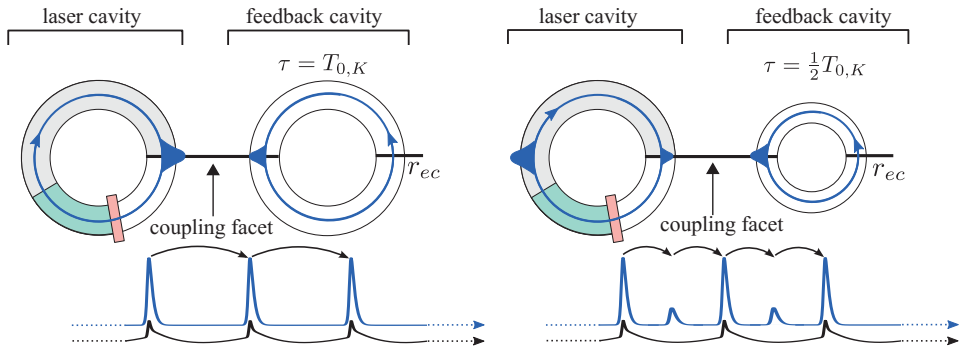

Figure 3.25.: Schematic diagrams of the laser cavity coupled to one external feedback cavity, for external cavity delay times of $\tau = T_{0,K}$ (left) and $\tau = \frac{1}{2}T_{0,K}$ (right), and sketches of the resulting pulse trains. The blue line represents the electric field and the black line represents the net gain.

If one considers the system with instantaneous feedback, i.e. $\tau = 0$ and $C = 0$, then the system is equivalent to that without feedback, but with modified internal losses $\kappa' = \kappa (1 + K)^2$, i.e.

$$\frac{d\mathcal{E}}{dt} = -\gamma\mathcal{E}(t) + (1 + K)\gamma R(t - T) e^{-i\Delta\Omega T}\mathcal{E}(t - T). \tag{3.8}$$

If $\mathcal{E}_0(t)$ is a mode-locked solution of Eq. (3.8), with period $T_{0,K}$,[5] then $\mathcal{E}_0(t)$ is also a solution of Eq. (3.7) for all $\tau = nT_{0,K}$, where n is an integer. This means that for all feedback delay times that are integer multiples of $T_{0,K}$, which will be referred to as resonant feedback delay times, the dynamics are unchanged. For delay times between these resonant values various dynamics are exhibited. More generally it is also true that if one considers a solution to Eq. (3.7) with τ between 0 and $T_{0,K}$, and if that solution is periodic, with period T_0, then this is also a solution to the system with the feedback delay time $\tau + nT_0$, for integer n [YAN09]. This means that all periodic solutions that arise for $\tau \in [0, T_{0,K}]$, repeat for larger delay times.[6] Therefore, to characterise the type of dynamics that can emerge with feedback, we first study the feedback delay range from zero to $T_{0,K}$.

$\tau - K$ dependence

In this section the influence on the dynamics of the feedback strength and feedback delay time are investigated. Here we consider the influence of these parameters separately from phase effects, i.e. for $C = 0$ and $\alpha_g = \alpha_q = 0$ (the influence of these parameters is discussed later in this section).

[5] The subscript K is included to indicate that the resonant period is K dependent. From now on we will refer to the period of the solitary laser ($K = 0$) as $T_{0,S}$.

[6] The stability of the solutions can vary with n. This will be discussed in Section 3.3.4.

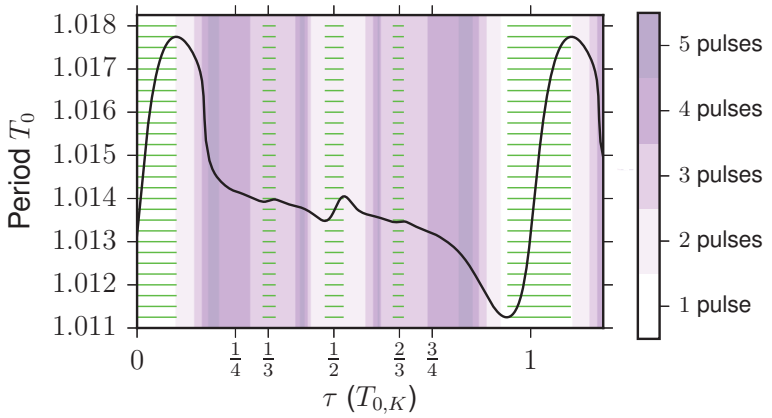

Figure 3.26.: **Path continuation:** Period of the mode-locked solution (black line) as a function of the feedback delay time τ, which is given in units of $T_{0,K} = 1.013$. The background colour indicates the number of pulses in the laser cavity. The green striped regions indicate various main and higher order resonance locking regions. Parameters: $K = 0.1$, all other parameters as in Table 2.1.

When $\tau = nT_{0,K}$ for integer n, the feedback delay time is resonant with the dynamics, meaning that pulses from the feedback and laser cavities are coincident at the coupling facet. This is shown schematically on the left of Fig. 3.25 for $\tau = T_{0,K}$. Synchronisation effects can also occur for non-integer multiples of $T_{0,K}$. For example when $\tau = \frac{1}{2}T_{0,K}$ the pulse from the feedback cavity is coupled into the laser cavity when the main pulse is on the opposite side of the cavity. This induces a second pulse which is shifted from the main pulse by a time of $\frac{1}{2}T_{0,K}$. Feedback from this second pulse is then synchronised with the main pulse. This scenario is also depicted in Fig. 3.25. Synchronisation can also occur for other fractional multiples of $T_{0,K}$, i.e. when

$$\tau = \frac{q}{p}T_{0,K} \quad \text{for} \quad p, q \in \mathbb{N} \tag{3.9}$$

[OTT12a]. The integer p gives the number of pulses within one $T_{0,K}$ interval, or in other words the number of pulses in the laser cavity.[7] This includes the main pulse and $p-1$ feedback induced pulses. We shall refer to τ values which are fractional multiples of $T_{0,K}$ as higher order resonances, where the order is given by p.

Synchronisation cannot occur for an arbitrarily large number of pulses in the laser cavity. The number of feedback induced pulses is restricted by the width of the pulses and length of the laser cavity. The finite width of the pulses also means

[7] The exact value of $T_{0,K}$ is dependent on the feedback strength, however we remind the reader that $T_0 \approx T = 1$.

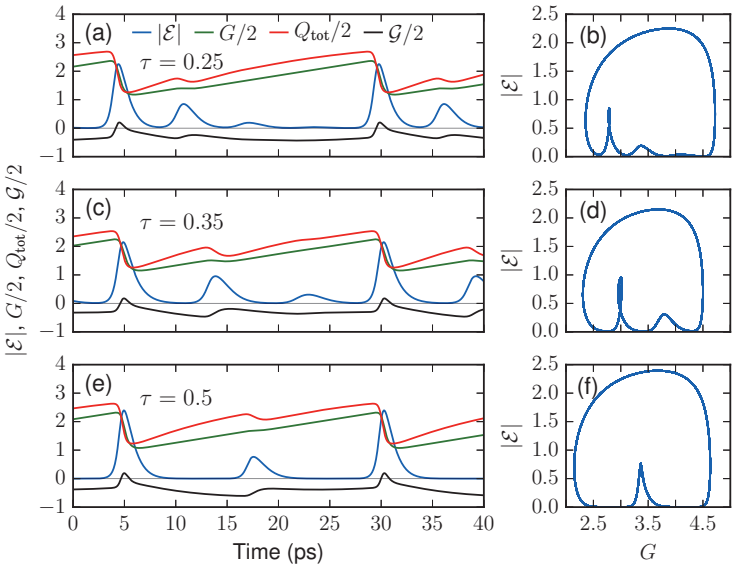

Figure 3.27.: **Inside resonances:** Time traces and phase space portraits of the feedback induced dynamics for (a)-(b) $\tau = 0.25$, (c)-(d) $\tau = 0.35$ and (e)-(f) $\tau = 0.5$. The time traces (a),(c) and (d) show the electric field amplitude $|\mathcal{E}|$ (blue), gain G (green), total losses $Q_{\rm tot} = Q - \ln(\kappa)$ (red) and the net gain $\mathcal{G} = G - Q_{\rm tot}$ (black). The phase space portraits (b), (d) and (f) show the dynamics in the $G - |\mathcal{E}|$ plane. Parameters: (a)-(b) $K = 0.12$, (c)-(f) $K = 0.15$, all other parameters as in Table 2.1.

that synchronisation does not only occur exactly at the resonances, but rather extends over a range of τ values. We will define the locking ranges of the main and higher order resonances as the τ ranges in which the period of the solutions changes monotonically with τ, the number of pulses in the laser cavity remains constant and the solutions remain stable. This is illustrated in Fig. 3.26, where the period of the mode-locked solutions are plotted as a function of the feedback delay time for $K = 0.1$. The number of pulses in the laser cavity is indicated by the background colour and the striped green lines indicate the locking regions for various resonances. In this case the solutions are stable for the entire τ range that is depicted. As the feedback delay time is changed, the system adapts such that the pulses in the laser cavity are synchronised with the pulses in the feedback cavity. However if the delay time is tuned too far from one of the resonances the system cannot adapt sufficiently and the pulses become deformed. The locking range for each resonance, main and higher order, depends on the order of n and p, and on the feedback strength. The parameter dependence of the main resonance locking regions, and the change in the period in these regions, will be discussed in more detail in Section 3.3.4.

Examples of the dynamics within the $\frac{q}{p} = \frac{1}{4}$, $\frac{q}{p} = \frac{1}{3}$ and $\frac{q}{p} = \frac{1}{2}$ locking ranges are shown in Fig. 3.27. Depicted are time traces of the electric field amplitude, the gain, the total losses and the net gain, where the total losses and net gain are as defined previously; $\mathcal{Q}_{tot} = Q - \ln(\kappa)$ and $\mathcal{G} = G - \mathcal{Q}_{tot}$.[8] Also shown are phase portraits of the dynamics projected on the $G - |\mathcal{E}|$ plane. Figure 3.27a-b shows the dynamics arising for τ in the $\frac{q}{p} = \frac{1}{4}$ locking region. In this example there are four pulses within one $T_{0,K}$ interval ($\approx$ 25ps since $T_{0,K} \approx T$). The largest pulse is the main pulse that is generated due to the gain and absorber dynamics. The three satellite pulses are induced by the feedback and since they do not coincide with positive net gain windows they are sustained by continual rejection of pulses from the feedback cavity rather than by amplification within the laser cavity. The amplitude of the satellite pulses decreases within one $T_{0,K}$ interval as each pulse is the seed for the next. Similar results are seen for $\tau = 0.35$ and $\tau = 0.5$ in Fig. 3.27c-f, which exhibit dynamics with three and two pulses within one period, respectively, corresponding to the $\frac{q}{p} = \frac{1}{3}$ and $\frac{q}{p} = \frac{1}{2}$ locking regions. Examples of the dynamics outside the resonance locking regions are shown in Fig. 3.28. In these regions pulses are deformed or not well separated. Figure 3.28a is near the edge of the zeroth-order main resonance (see Fig. 3.26). For this delay time the pulses from the feedback cavity are coupled into the laser just after the main pulse has passed the coupling facet, causing a long trailing edge. This influences the recovery of the absorber, meaning that the positive net gain window decays more slowly. Although New's stability criterion is still fulfilled [NEW74], as shall be discussed further in Chapter 4, this makes the dynamics less robust against noise perturbations. In Fig. 3.28b τ is chosen to the left of the first main resonance locking region. In this case pulses are coupled into the laser cavity just before the main pulse passes the coupling facet, leading to a higher net gain before the pulse.

The feedback delay time determines the number of pulses within the feedback cavity, but the type of dynamics that are exhibited by the system also depends on the feedback strength. The periodic dynamics with additional feedback induced pulses (Fig. 3.27) occur for low feedback strenghs. For slightly higher feedback strengths the system can exhibit dynamics with periodically modulated pulse heights. Examples of such dynamics are shown in Fig. 3.29. Figure 3.29a shows a time trace of the electric field amplitude for $\tau = 0.25$ and $K = 0.2$. A close up of the dynamics is shown in Fig. 3.29b, where the net gain has also been plotted (black line). Here it can be seen that there are four pulses in the laser cavity (i.e. within a time interval of $\approx$ 25ps) and that between these pulses there is a competition for the gain. Within the time interval that is depicted here the net gain window is transferred from one pulse to the next, and accordingly the pulse amplitudes change. Physically the situation in this parameter regime is that the pulses that

[8] The net gain does not include the feedback contributions.

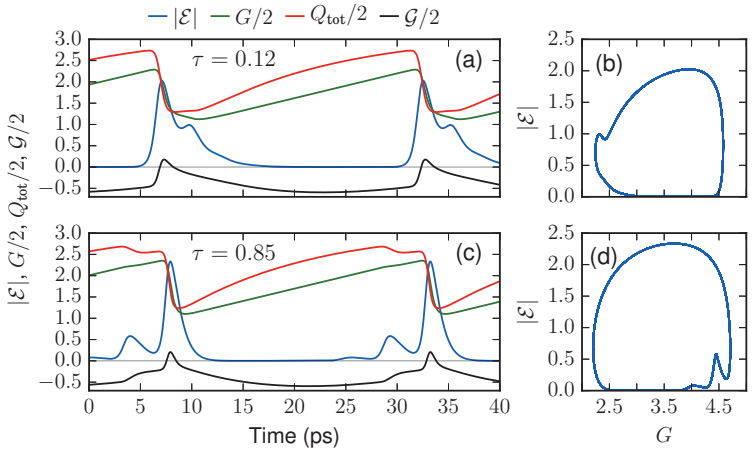

Figure 3.28.: **Outside resonances:** Time traces and phase space portraits of the feedback induced dynamics for (a)-(b) $\tau = 0.12$ and (c)-(d) $\tau = 0.85$. The time traces (a) and (c) show the electric field amplitude $|\mathcal{E}|$ (blue), gain G (green), total losses $Q_{\rm tot} = Q - \ln(\kappa)$ (red) and the net gain $\mathcal{G} = G - Q_{\rm tot}$ (black). The phase space portraits (b) and (d) show the dynamics in the $G - |\mathcal{E}|$ plane. Parameters: $K = 0.1$, all other parameters as in Table 2.1.

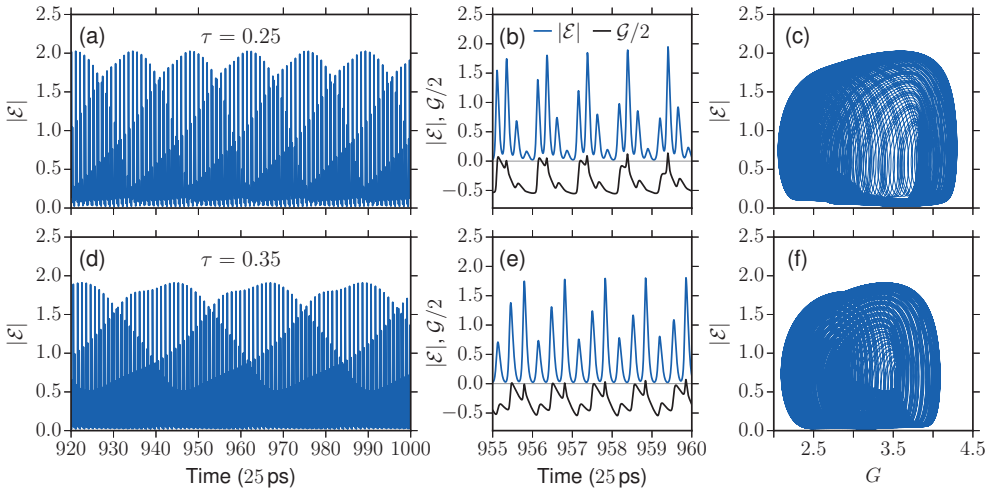

Figure 3.29.: **Quasi-periodic dynamics:** Time traces and phase space portraits of the feedback induced dynamics for (a)-(c) $\tau = 0.25$ and (d)-(f) $\tau = 0.35$. The time traces (a) and (d) show the electric field amplitude $|\mathcal{E}|$ (blue). In (b) and (e) at shorter time interval is depicted and the net gain $\mathcal{G} = G - Q_{\rm tot}$ (black) is also plotted. The phase space portraits (c) and (f) show the dynamics in the $G - |\mathcal{E}|$ plane. Parameters: $K = 0.2$, all other parameters as in Table 2.1.

get coupled back into the laser cavity are large enough to significantly influence the net gain window, but there is not enough energy in the system to sustain all four

pulses. This leads to competition for the gain between the four pulses in the laser. The dynamics exhibited for $\tau = 0.35$, with $K = 0.2$, are shown in Fig. 3.29d-f. In this case there are three competing pulses in the laser cavity. In both cases, $\tau = 0.25$ and $\tau = 0.35$, the slow modulation period of the pulse amplitudes is approximately 45 laser cavity roundtrips. This coincides approximately with the recovery time of the gain section, $1/\gamma_g = 40$, indicating that the transfer of energy between the pulses in the laser cavity is mediated by the relatively slow recovery of the gain section. This slow modulation period is incommensurable with the much faster pulse repetition period. Consequently the dynamics are quasi-periodic. This can be seen by looking at the trajectories of the system in its phase space. Projections on to the $G - |\mathcal{E}|$ plane, for $\tau = 0.25$ and $\tau = 0.35$, are shown in Fig. 3.29c and Fig. 3.29f, respectively. The projections shown here depict the trajectories for the time interval shown in subplots (a) and (d) of Fig. 3.29. As the dynamics are not quite periodic the trajectories fill in more and more of the phase space over longer time intervals. If the feedback strength is increased further, eventually there is a transition to harmonic mode-locking for τ values near the higher-order resonances. This occurs because for higher feedback strengths the losses are reduced and therefore multiple pulses can be sustained.

The type of dynamics arising for delay times that do not correspond to main resonances, i.e. periodic dynamics with satellite pulses and quasi-periodic dynamics at higher feedback strengths, are in agreement with the findings presented in [AVR09]. In this work the dynamics of a Fabry-Perot passively mode-locking laser subject to optical feedback was numerically investigated using a travelling-wave model. The destabilisation of periodic mode-locked dynamics via optical feedback has also been observed experimentally [GRI09, NIK16]. In [NIK16] feedback induced harmonic mode-locking was also observed.

A more complete picture of the dependence of the dynamics on τ and K is shown in Fig. 3.30. Depicted are maps of the dynamics in the $\tau - K$ parameter plane which are obtained by numerically integrating the DDE system and colour coding the regions according to the dynamics that are exhibited. White indicates fundamental mode-locking with only one pulse in the laser cavity, blues indicate various orders of harmonic mode-locking and grey indicates continuous wave lasing. In the purple regions the dynamics have the fundamental periodicity but there are additional feedback induced pulses (see Fig. 3.27) and in the green regions the dynamics are quasi-periodic (see Fig. 3.29).[9] To obtain the number of pulses we only look for maxima in the electric field amplitude. This means that no distinction is made between pulses which are well separated and pulses which have multiple maxima. Therefore the boundaries of the various dynamical regimes are not the

[9] The green regions are labelled CD, for complex dynamics, as in later figures the colour code does not distinguish between quasi-periodic and chaotic dynamics. However, for the parameters used here all green regions correspond to quasi-periodic dynamics.

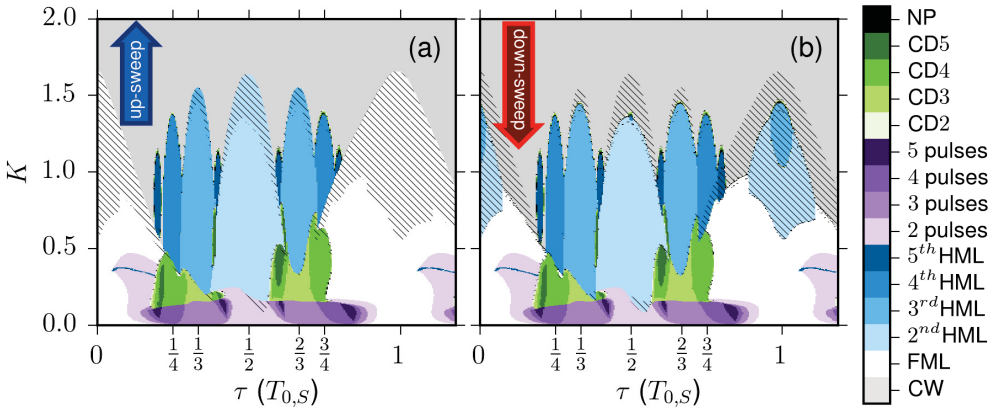

Figure 3.30.: Maps of the dynamics in dependence of τ and K obtained for (a) up- and (b) down-sweeps in K. The feedback delay time is plotted in units of the period for $K = 0$, $T_{0,S} = 1.014$. The colour code indicates the number of pulses in the laser cavity and the type of dynamics that are exhibited. White indicates fundamental mode-locking (FML), purples indicate fundamental mode-locking with feedback induced pulses, greens indicate complex dynamics (in this case quasi-periodic) with 2-5 pulses in the laser cavity (CD2-CD5) and blues indicate harmonic mode-locking (HML). The grey regions indicate continuous-wave solutions. Hatching indicates regions in which different results are obtained in the up- and down-sweeps. Parameters: all other parameters as in Table 2.1.

same as the resonance locking regions. As shown in Fig. 3.26, the locking ranges are narrower than the regions exhibiting dynamics with the same number of electric field maxima. Figure 3.30a is obtained by preforming an up-sweep in K, meaning that for each K value the history of the solution for the previous K value is used for the initial conditions. Results obtained for the down-sweep in K are shown in Fig. 3.30b. The hatching indicates the regions where different results are obtained for the up- and down-sweeps. The K range depicted here is relatively large and past a certain value more light is being coupled back into the laser cavity than what is coupled out. Physically this would require the light in the feedback cavity to be amplified before it is coupled back into the laser.[10] Furthermore, for large feedback

[10] For single cavity feedback, from Eq. (2.9), the feedback strength is given by

$$K = (1 - r)\,(r_{ec}/r)^{1/2}\,. \tag{3.10}$$

In this definition of the feedback strength a factor of $\sqrt{1-r}$ is included to account for how much light is coupled from the laser cavity into the feedback cavity and the term is scaled by $1/\sqrt{r}$. The fraction of the out-coupled light that is coupled back into the laser is given by $K\sqrt{r/(1-r)}$. This value is limited by the transmittance of the coupling facet $\sqrt{1-r}$. If the light is not amplified in the feedback cavity the maximal feedback strength is given for $r_{ec} = 1$, which, if we assume an end facet reflectivity (or transmittance in the ring cavity case) of 30%, gives $K \approx 1.3$. In experimental studies the feedback strength is typically given in terms of the percentage of the out-coupled light that is coupled back, therefore to compare

strengths it is no longer valid to neglect contributions from light that has made multiple roundtrips in the feedback cavity.[11] However, we look at such a large range to gain an understanding of the mathematical boundaries of the dynamics that can be exhibited by the system under investigation (Eq. (3.7) and Eqs.(2.43)-(2.44)). The feedback delay time is plotted in units of the period for $K = 0$, $T_{0,S} = 1.014$. Although the resonant periods $T_{0,K}$ are dependent on K, the variation is small and the positions of the resonances do not deviate much from the $K = 0$ case.

For $\tau \approx 0$ and $\tau \approx T_{0,S}$ there are large regions of fundamental mode-locking. Within these regions locking to the zeroth and first-order main resonances occurs ($\tau = nT_{0,K}$ for $n = 0, 1$). At large K values these regions are bounded by continuous wave lasing. The transition to continuous wave lasing at large K values is similar to what is observed for large pump currents in the solitary laser case. The electric field becomes so large that the gain and absorber sections are continually saturated leading to continuous wave emission. Between the main resonances, at low feedback strengths, there is locking to the higher-order resonances, i.e. $\tau = \frac{1}{5}T_{0,K}, \frac{1}{4}T_{0,K}, ...$ (purple regions in Fig. 3.30). Around each of these higher-order resonances dynamics with p pulses are exhibited, where p is the order of the resonance. The width of the regions with p pulses decreases for increasing p. As can be seen from Fig. 3.26 the locking regions show the same trend. Furthermore, these regions can be ordered into a Farey sequence, as was shown in [OTT12a]. At large feedback strengths, harmonic mode-locking is observed near the higher-order resonances. The order of the harmonic mode-locking is given by p and the number of harmonic mode-locked regions of each order is given by $p - 1$. For example, between $\tau = 0$ and $\tau = T_{0,S}$ there are two $p = 3$ locking regions corresponding to $\tau = \frac{1}{3}T_{0,K}$ and $\tau = \frac{2}{3}T_{0,K}$, and hence two regions of 3^{rd} order harmonic mode-locking. Stable regions of harmonic mode-locking are also found at the main resonances. For the $\tau = \frac{1}{2}T_{0,K}$ locking region there is a direct transition to 2^{nd} order harmonic mode-locking from the satellite pulse dynamics (2 pulses). For the locking regions corresponding to larger p's the transition is mediated by regions of quasi-periodic dynamics with the same number of pulses in the laser cavity as the harmonic order. Also, the onset of harmonic mode-locking occurs at larger K values for larger p's. This is because the available net gain has to be distributed over more pulses.

The sequence of dynamics displayed in dependence of the feedback strength in Fig. 3.30, for the feedback delay time $\tau = \frac{1}{2}T_{0,S}$, is the same as what is reported

with experiments K should be scaled by $\sqrt{r}/(1-r)$. It is also important to note that we are simulating the dynamics in the laser cavity, whereas in experiments the electric field that is coupled out is observed. Therefore the simulation results will show increased intensities for larger feedback strengths, whereas experimentally decreased intensities will be observed as less light is coupled out of the system.

[11] For example, if $K = 0.5$ then, assuming an end facet reflectivity of 30%, the feedback strength after two roundtrips in the feedback cavity would be $K^2 = 0.1$.

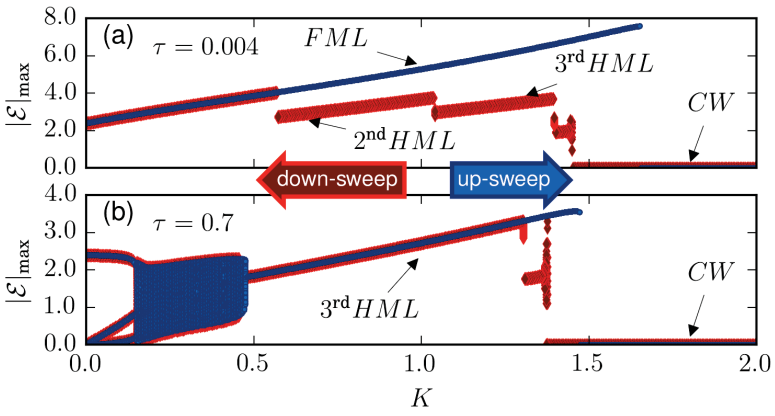

Figure 3.31.: Numerical bifurcation diagrams showing the K dependence of the mode-locked laser output for (a) $\tau = 0.004$ and (b) $\tau = 0.7$. Plotted in blue (red) are electric field maxima $|\mathcal{E}|_{\max}$ for an up-sweep (down-sweep) in the initial conditions. Labelled are regions of fundamental mode-locking (FML), harmonic mode-locking (HML) and continuous wave (CW) lasing. Parameters: all other parameters as in Table 2.1.

in [ARK15a]. In this work the authors use the DDE model to study the influence of coupling the laser cavity to a short external cavity. However, in contrast to our modelling approach for the feedback contribution, in [ARK15a] feedback from the external cavity is incorporated by including a differential equation for the electric field in the feedback cavity, which is coupled to the equation for the electric field in the laser cavity. In doing so, feedback contributions from light that has made multiple roundtrips in the feedback cavity are included. The qualitative agreement between our results and those of [ARK15a] indicates that, even if contributions to the feedback from light that has made multiple roundtrips in the external cavity are neglected, the qualitative trends observed for high feedback strengths are still the same.

In the main resonant regions ($\tau \approx 0$ and $\tau \approx T_{0,S}$), at large feedback strengths, there is multistability between the fundamentally mode-locked solution and harmonically mode-locked solutions (hatched regions in Fig. 3.30). Similar results were obtained for the pump current dependence of the solitary laser (see Fig. 3.17). This can be understood by considering that the feedback reduces the non-resonant losses and hence reduces the lasing threshold and the threshold for the onset of mode-locked dynamics. There are also regions of multistability between mode-locking and the continuous wave lasing state.

Within the various dynamical regions depicted in Fig. 3.30 the pulse heights change with τ and K. This is illustrated in the one-parameter numerical bifurcation diagrams in Figs. 3.31 and 3.32. Plotted are maxima in the electric field amplitude, counted over a time span of one hundred cold-cavity roundtrip times, for up- (blue)

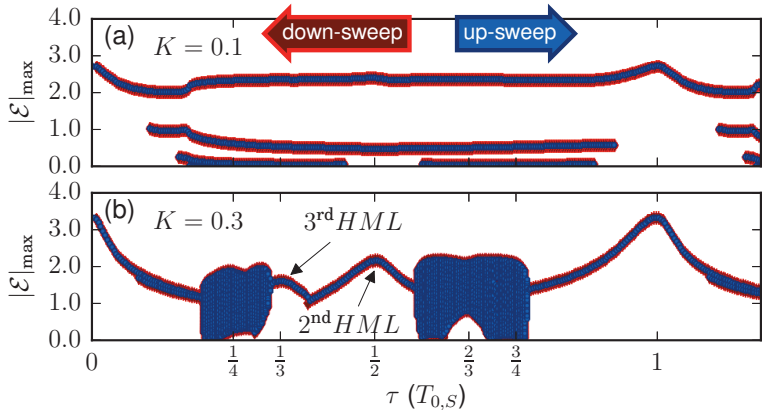

Figure 3.32.: Numerical bifurcation diagrams showing the τ dependence of the mode-locked laser output for (a) $K = 0.1$ and (b) $K = 0.3$. Plotted in blue (red) are electric field maxima $|\mathcal{E}|_{\max}$ for an up-sweep (down-sweep) in the initial conditions. The feedback delay time is plotted in units of the period for $K = 0$, $T_{0,S} = 1.014$. Parameters: all other parameters as in Table 2.1.

and down-sweeps (red) in the initial conditions. In Fig. 3.31 the results are show in dependence of the feedback strength for (a) $\tau = 0.004$ and (b) $\tau = 0.7$. For $\tau = 0.004$ the system is within the locking region of the zeroth-order main resonance. The pulse heights of the fundamentally and harmonically mode-locked solutions increase with K, and as already shown in Fig. 3.30 there are regions of multistability between these solutions. For $\tau = 0.7$ the system is in the locking region of the $\tau = \frac{2}{3}T_{0,K}$ higher-order resonance. Accordingly, for low feedback strengths there are three maxima with different heights. The quasi-periodic region has maxima of many different heights. Near $K = 0.5$ there is a small range of multistability between the quasi-periodic and 3^{rd} order harmonically mode-locked solutions. Figure 3.32 shows the τ dependence for (a) $K = 0.1$ and (b) $K = 0.7$. The main-resonance locking regions can be identified in these plots as the regions near $\tau = 0$ and $\tau = T_{0,K}$ where there is only one maximum. Within these regions the pulse heights are largest at the exact main resonances, $\tau = 0$ and $\tau = T_{0,K}$. Comparing Figs. 3.32a-b it can be seen that the maximum in the pulse height is shifted slightly closer to $\tau = 1$ for $K = 0.7$. This is because the period $T_{0,K}$ decreases with K. The reasoning for this is the same as for the pump current dependence of the period (see Section 3.2.3). The pulse heights decrease as τ is tuned away from the main resonances because pulses from the feedback cavity are coupled in at the flanks of the pulse in the laser cavity, rather than at the center. This also causes the pulse to become wider. Changes in the pulses shape within the main-resonance locking regions will be discussed further in Section 3.3.4 (see Figs. 3.63 and 3.66).

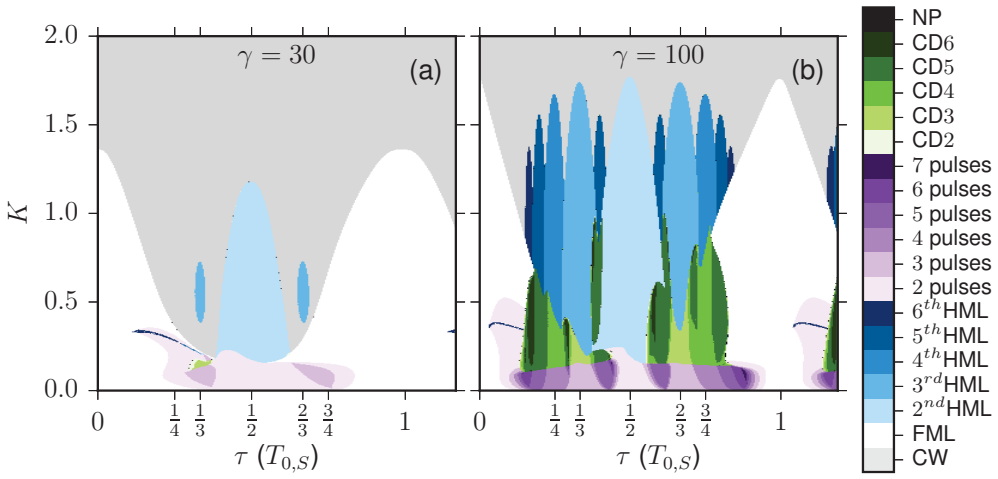

Figure 3.33.: **Influence of the spectral filter width:** Maps of the dynamics in dependence of τ and K obtained for up-sweeps in K for $\gamma = 30$ and $\gamma = 100$. The feedback delay time is plotted in units of the period for $K = 0$, (a) $T_{0,S} = 1.031$ and (b) $T_{0,S} = 1.009$. The colour code indicates the number of pulses in the laser cavity and the type of dynamics that are exhibited. White indicates fundamental mode-locking (FML), purples indicate fundamental mode-locking with feedback induced pulses, greens indicate complex dynamics (in this case quasiperiodic) with 2-7 pulses in the laser cavity (CD2-CD6) and blues indicate harmonic mode-locking (HML). The grey regions indicate continuous-wave solutions. Parameters: all other parameters as in Table 2.1.

Influence of the pulse width

As mentioned briefly near the beginning of this section, the number of pulses that can exist in the laser cavity, and hence number of feedback induced pulses which can be created, is limited by the pulse widths. This is illustrated in Fig. 3.33, where τ-K maps of the dynamics are shown for filter widths (a) $\gamma = 30$ and (b) $\gamma = 100$ (see Fig. 3.15 for the influence of spectral filter width on the pulse width). With decreased pulse widths (Fig. 3.33b) the maximum order of harmonic mode-locking is increased (blue regions), as well as the maximum number of feedback induced satellite pulses (purple regions), and the widths of the multi-pulse regions are decreased. Otherwise, all features of the map are qualitatively similar to the $\gamma = 66.5$ case shown in Fig. 3.30. For very wide pulses (Fig. 3.33a) parameter regions exhibiting quasi-periodic dynamics are greatly reduced.

The asymmetry of the mode-locked pulses also has an influence on the feedback parameter dependence. In the solitary laser case the pulses have a longer trailing edge compared with the leading edge and the net gain decreases more slowly than it rises during the fast stage (see Fig. 3.14). As a consequence of this, the system behaves differently if pulses are coupled into the laser cavity before or after the

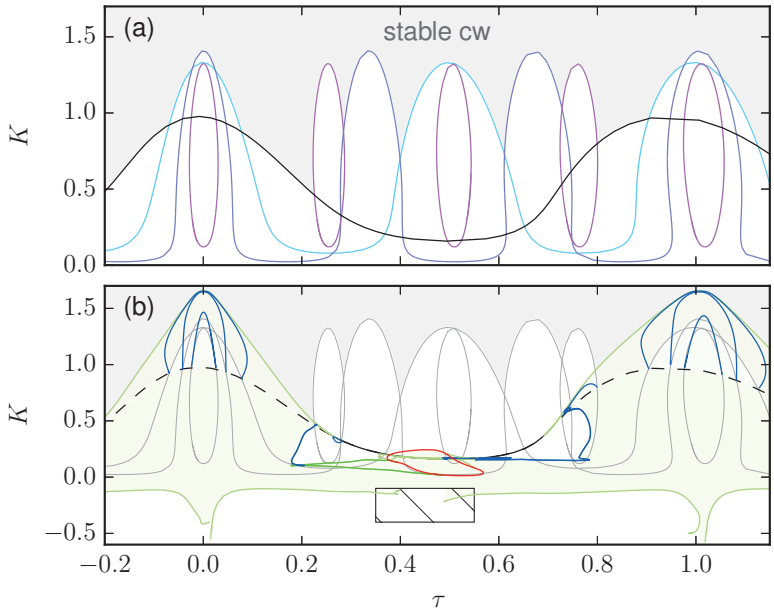

Figure 3.34.: **Path continuation:** (a) Hopf bifurcations of the maximum-gain continuous-wave solution in the $\tau - K$ parameter space. In black is the H_1 Hopf curve. The H_2, H_3 and H_4 Hopf curves are depicted in light blue, purple and pink, respectively. (b) Bifurcations of the fundamental mode-locked solution. Blue lines indicate torus bifurcations and green lines are saddle-node bifurcations and the red line is a period-halving bifurcation. The black line is the fundamental Hopf bifurcation curve of the continuous wave solution (H_1), with the solid segment being supercritical and the dashed segments subcritical. The thin grey lines show the remaining Hopf bifurcations of the continuous-wave solution (compare with (a)). Shaded in green is the stability region of the fundamental mode-locked solution. In the grey regions the continuous-wave solution is stable. Parameters: all other parameters as in Table 2.1.

main pulse has passed the coupling facet, leading to asymmetries in the dynamics for delay times that are tuned from the resonances. This can be clearly seen in Figs. 3.30 and 3.33, which all show a large region of two pulse dynamics on the right border of the first main resonance region, but not on the left. When the delay time is larger than the resonant value, then the pulses from the feedback cavity are coupled in after the main pulse. As the net gain is high on this side of the pulse, the fed-back pulses experience lower losses, leading to two pulse dynamics at smaller positives detuning from the main resonance compared with negative detuning.

Path continuation

By numerically integrating the DDE system only the stable solutions can be found. However, a deeper understanding of the dynamics can be gained through knowledge of the underlying bifurcation structure. As with the solitary laser, the mode-

locked solutions that arise with feedback bifurcate from the continuous-wave solution which has the maximum gain (see Section 3.2.1). In Fig. 3.34a Hopf bifurcations of the continuous-wave solution are depicted in the $\tau - K$ parameter space (here we again use our standard value for the spectral filter width, $\gamma = 66.5$). These bifurcation curves were obtained using DDE-BIFTOOL [ENG01]. The H_1 Hopf bifurcation which gives rise to the periodic solution with the fundamental frequency of the laser cavity $\Omega_f = 2\pi/T$, i.e. the solution out of which the fundamentally mode-locked solution evolves, is plotted in black. The H_2, H_3 and H_4 Hopf curves are plotted in light blue, purple and pink, respectively. In the grey region the continuous-wave solution is stable. The τ range that is depicted includes negative delay times. The negative τ values are unphysical, however mathematically nothing significantly changes here since the total delay time in the feedback term, $T + \tau$, is still positive (Eq. (3.7)). The τ dependence of the Hopf curves is related to their frequency. At τ values that are integer multiples of $2\pi/\Omega_n$ there are peaks in the K dependence of the H_n Hopf bifurcations, where $\Omega_n = n\Omega_f$ for $n = 1, 2, 3, 4$. In the H_4 case, the curves form closed ellipses at integer multiples of $2\pi/\Omega_4$.

In Fig. 3.34b the bifurcations of the fundamentally mode-locked solution, which is generated in the H_1 Hopf bifurcation, are shown (these are shown again in Fig. 3.35 with labels). Torus bifurcations are depicted in blue, saddle-node bifurcations in green and period-halving in red. The regions of stable fundamental mode-locking are indicated by the green shading. The positions of the Hopf bifurcations are indicated by the grey lines and the criticality of the H_1 curve is indicated by the dashed (subcritical) and solid (supercritical) segments. The bifurcations of the fundamental mode-locked solution extend into negative K regions. Physically negative feedback strengths mean that the fed-back light has a phase shift of π, i.e. $-K$ is equivalent to $Ke^{i\pi}$. The box near $\tau = 0.5$, $K = -0.2$ marks a region where the bifurcations of the fundamental solution could not be continued using DDE-BIFTOOL.

In order to understand how the periodic solutions evolve out of the H_1 bifurcation we consider line scans along K at various positions in the bifurcation diagram. The positions of the line scans are indicated by the dotted black lines (1)-(4) in Fig. 3.35 and the results are shown in Fig. 3.36. Plotted in Fig. 3.36 is the period of the solutions. The stability is indicated by the solid (stable) and dotted (unstable) segments. In line scan (1) the periodic solution is born in a subcritical section of the H_1 curve; the start of the line scan is indicated by the point labelled H_1 in Fig. 3.36 (1). As the solution is continued in K the period increases and the system goes through a series of three torus bifurcations (T_1, T_2 and T_1). These torus bifurcations emanate from the Hopf-Hopf points where the H_1 Hopf branch crosses the H_2, H_3 and H_4 branches (see Figs. 3.34 and 3.35). In each of these torus bifurcations one pair of characteristic exponents enter the unit circle, i.e.

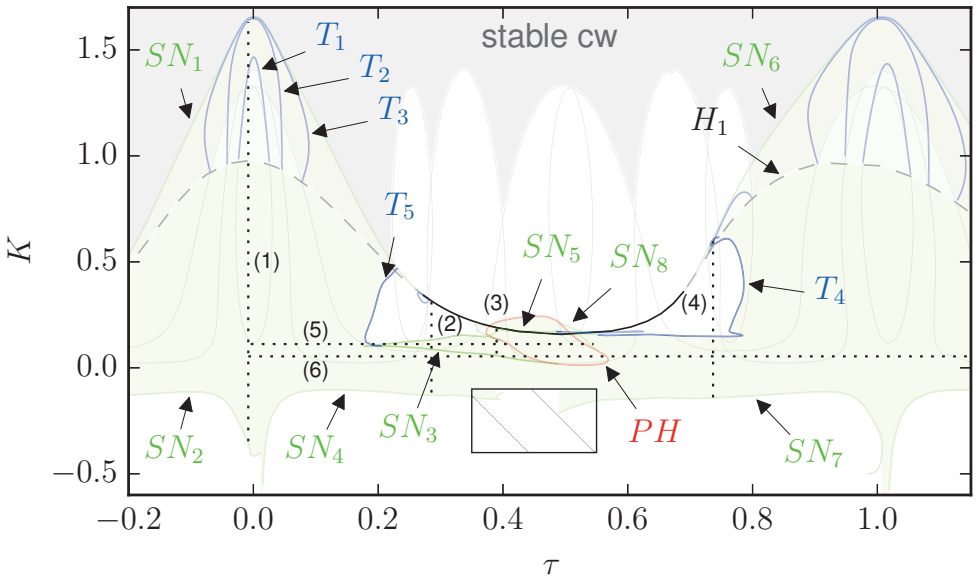

Figure 3.35.: **Path continuation:** Bifurcations of the fundamental mode-locked solution. Blue lines indicate torus bifurcations (T) and green lines are saddle-node bifurcations (SN) and the red line is a period-halving bifurcation (PH). The black line is the fundamental Hopf bifurcation curve of the continuous wave solution (H_1), with the solid segment being supercritical and the dashed segments subcritical. The thin grey lines show the remaining Hopf bifurcations of the continuous-wave solution (compare with Fig. 3.34 (a)). Shaded in green is the stability region of the fundamental mode-locked solution. In the grey regions the continuous-wave solution is stable. The dotted black lines numbered (1)-(6) indicate the positions of the line scans that are shown in Figs. 3.36 and 3.37. Parameters: all other parameters as in Table 2.1.

the number of unstable directions decreases. The solution then becomes stable after a saddle-node bifurcation (SN_1). After this fold in the line scan, the solution continues to be stable until the second saddle-node bifurcation (SN_2) near $K = -0.4$. How the solution continues after the SN_2 bifurcation is not depicted in Fig. 3.36 (1), as the remaining section of this solution branch remains unstable after this point. In the section of the line scan between the two saddle-node bifurcations the solution for the electric amplitude has the typical mode-locked pulse profile (see Fig. 3.14) and within this range the period decreases with increasing K. Line scan (2) (Fig. 3.36 (2)) starts in a supercritical part of H_1, however the solution is initially unstable. The additional unstable directions are related to H_3. Line scan (2) becomes stable after two saddle-node bifurcations (SN_3) and then loses stability again in the third saddle-node bifurcation (SN_4). At the τ position of line scan (3) the H_1 bifurcation is also supercritical, but there are four additional unstable multipliers which are related to H_2 and H_3. This branch also goes through a series of three saddle-node bifurcations, however the solutions remain unstable

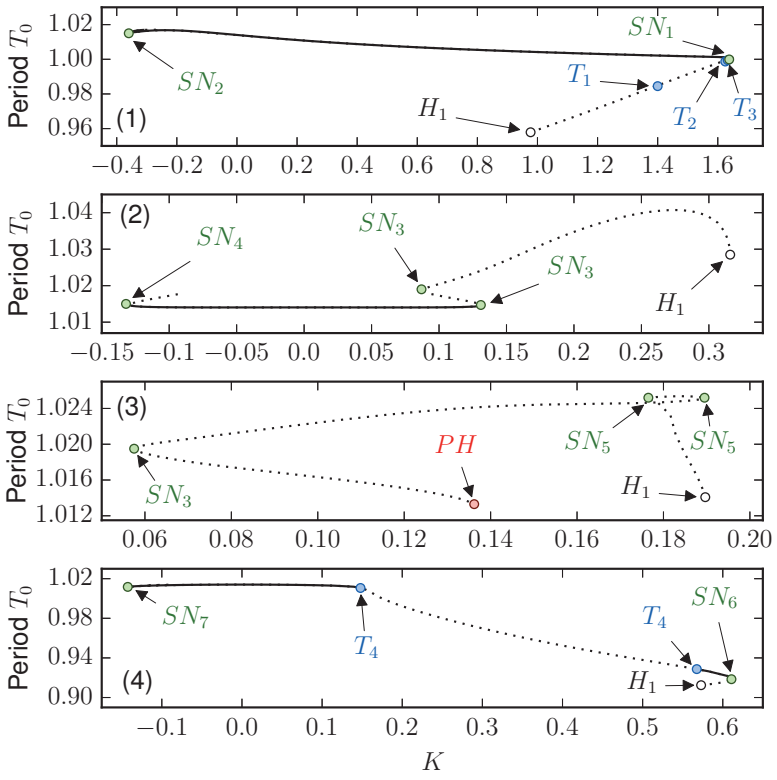

Figure 3.36.: **Path continuation:** Line scans along K corresponding to the vertical dotted lines (1)-(4) plotted in Fig. 3.35. Plotted is the period of the solutions. Solid lines indicate stable solutions and dotted lines indicate unstable solutions. The bifurcations that occur along the line scans are labelled in accordance with the labelling in Fig. 3.35. Parameters: (1) $\tau = -0.008$, (2) $\tau = 0.285$, (3) $\tau = 0.390$, (4) $\tau = 0.737$, all other parameters as in Table 2.1.

(Fig. 3.36 (3)). The line scan terminates in the lower part of the period halving bifurcation shown in Fig. 3.35 (and Figs. 3.34b). Finally, line scan (4) starts in the second subcritical region of H_1. The solution branch first becomes stable after the saddle-node bifurcation SN_6 (Fig. 3.36 (4)). Then there is an unstable section of the line which is bordered by the torus bifurcation branch T_4. After the second T_4 bifurcation the solution is stable until the saddle-node bifurcation SN_7.

In Fig. 3.37 line scans in τ are shown. These are started from points on line (1) and their positions in the bifurcation diagram are indicated by the horizontal dotted lines (5)-(6) in Fig. 3.35. Line scan (5) starts from a stable part of line (1). Near $\tau = 0.2$ the solutions becomes unstable after the torus bifurcation T_5. The unstable solution continues past the period-halving bifurcations depicted in Fig. 3.35, as these are not bifurcations of this section of the solution branch. Near $\tau = 0.55$ the branch then turns around in a saddle-node bifurcation (SN_8) and

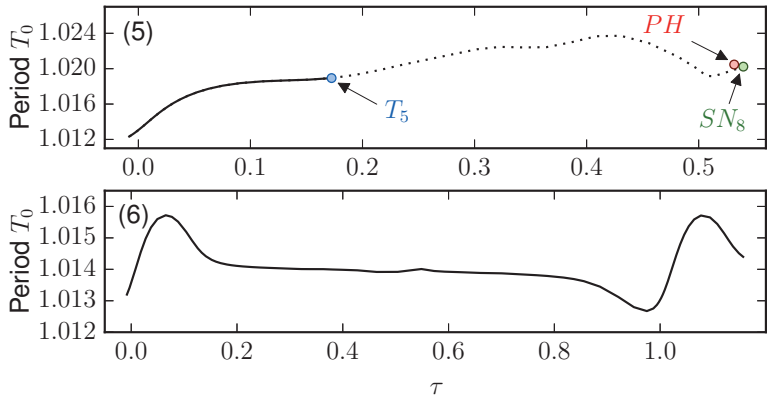

Figure 3.37.: **Path continuation:** Line scans along τ corresponding to the horizontal dotted lines (5)-(6) plotted in Fig. 3.35. Plotted is the period of the solutions. Solid lines indicate stable solutions and dotted lines indicate unstable solutions. The bifurcations that occur along the line scans are labelled in accordance with the labelling in Fig. 3.35. Parameters: (5) $K = 0.112$, (6) $K = 0.054$, all other parameters as in Table 2.1.

then terminates on the right side of the period-halving curve. Line scan (6) is at a slightly low K level. This branch of solutions does not undergo any bifurcations in the depicted τ range (see Fig. 3.37 (6)), i.e. the SN_3 and PH curves that line (6) cuts across in Fig. 3.35 are not bifurcations of these solutions. We have shown line scans that terminate on the lower (line scan (3)) and right (line scan (5)) parts of the period-halving curve. If a solution were continued upward in K from line (6), near $\tau = 0.5$, then this solution would remain stable until it terminates in the upper part of the PH curve. Likewise, solutions continued from line (4), for $K \approx 0.1 - 0.15$, would remain stable until they terminate in the left part of the PH curve.

We now compare the path continuation results with the maps of the dynamics obtained by direct numerical integration. To aid with this comparison the bifurcation curves have been plotted with the numerically obtained maps in Figs. 3.38 and 3.39. Looking first at Fig. 3.38a, within the main resonance regions (white), the upper boundaries of fundamental mode-locking are given by the saddle-node bifurcations (labelled SN_1 and SN_6 in Fig. 3.35). The down-sweep results (Fig. 3.38b) show that the continuous wave stability boundaries are given by the Hopf curves.[12] There are no features in the numerical maps related to the three torus bifurcation

[12] At the boundaries with harmonic mode-locking there is a slight discrepancy between the Hopf curves and the numerically obtained boundaries for stable continuous wave lasing. This could be due the inaccuracies in the path continuation, since the accuracy of the stability calculations depends on the delay times and for the higher-order Hopf curves the time scale separation between the delay times and the frequencies of the Hopf bifurcations is greater.

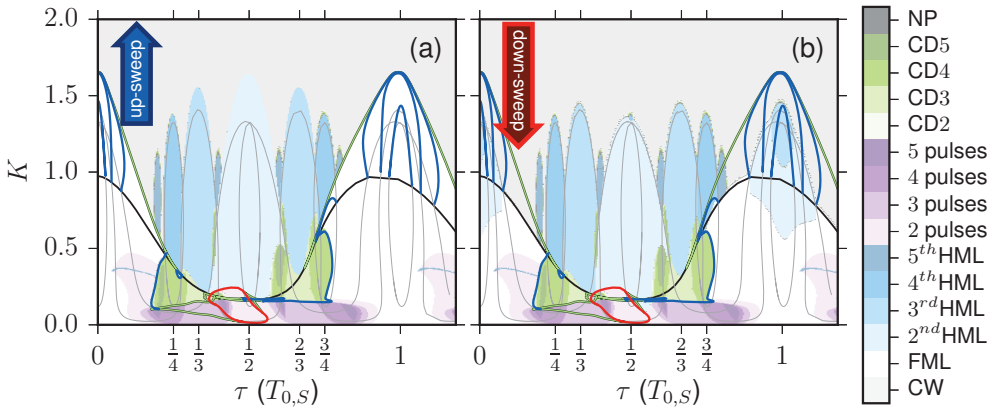

Figure 3.38.: **Comparison of numerics and path continuation:** Maps of the dynamics in dependence of τ and K obtained for (a) up- and (b) down-sweeps in K and the bifurcations of the continuous wave and fundamental mode-locked solutions. The feedback delay time is plotted in units of the period for $K = 0$, $T_{0,S} = 1.014$. Blue lines indicate torus bifurcations and green lines are saddle-node bifurcations and the red line is a period-halving bifurcation. The black line is the fundamental Hopf bifurcation curve of the continuous wave solution. The thin grey lines show the remaining Hopf bifurcations of the continuous-wave solution (compare with Fig. 3.34 (a)). The colour code indicates the number of pulses in the laser cavity and the type of dynamics that are exhibited. White indicates fundamental mode-locking (FML), purples indicate fundamental mode-locking with feedback induced pulses, greens indicate complex dynamics (in this case quasi-periodic) with 2-5 pulses in the laser cavity (CD2-CD5) and blues indicate harmonic mode-locking (HML). The grey regions indicate continuous-wave solutions. Parameters: all other parameters as in Table 2.1.

branches in the main resonance regions. This is because these are bifurcations of unstable solutions (see Fig. 3.36 (1)). For comparisons in the low K regions a smaller τ-K range is plotted in Fig. 3.39. Here it can be seen that the boundaries between the fundamental mode-locked regions (both with (purple) and without (white) additional feedback induced pulses) are given by torus and saddle-node bifurcations. The torus bifurcations add an extra incommensurable frequency, leading to the quasi-periodic dynamics. In the $\tau = \frac{1}{2}T_{0,K}$ resonance region, the boundary between the two pulse dynamics (purple) and 2^{nd} order harmonic mode-locking (blue) is given by the period-halving bifurcation. In this region, starting from low feedback strengths, the amplitude of the second feedback induced pulse increases with K, until it has the same amplitude as the main pulse. At this point the solution is identical to the 2^{nd} order harmonic mode-locked solution and the fundamental mode-locked solution ceases to exist. In the low K regions ($K < 0.1$), the results of the path continuation show that the stable solutions do not undergo any bifurcations (Fig. 3.37 (6)). This means that the profile of the solutions changes continuously between the higher-order resonance regions. Based on these results

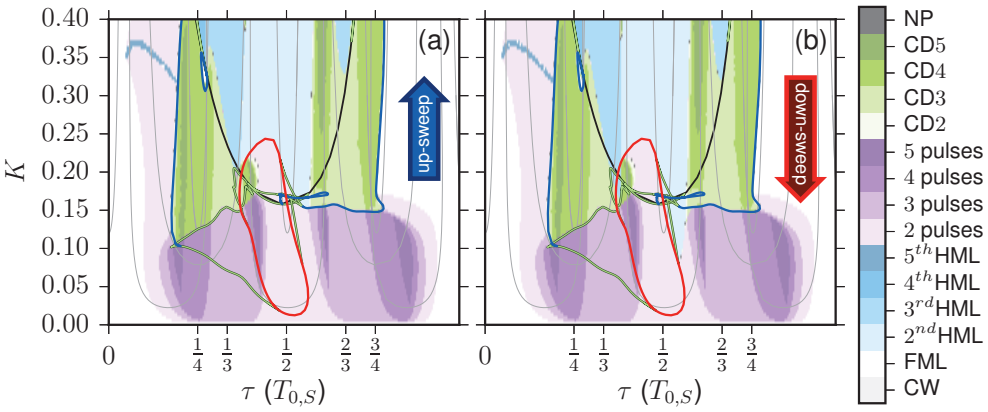

Figure 3.39.: **Comparison of numerics and path continuation:** Maps of the dynamics in dependence of τ and K obtained for (a) up- and (b) down-sweeps in K and the bifurcations of the continuous wave and fundamental mode-locked solutions. The feedback delay time is plotted in units of the period for $K = 0$, $T_{0,S} = 1.014$. Blue lines indicate torus bifurcations and green lines are saddle-node bifurcations and the red line is a period-halving bifurcation. The black line is the fundamental Hopf bifurcation curve of the continuous wave solution. The thin grey lines show the remaining Hopf bifurcations of the continuous-wave solution (compare with Fig. 3.34 (a)). The colour code indicates the number of pulses in the laser cavity and the type of dynamics that are exhibited. White indicates fundamental mode-locking (FML), purples indicate fundamental mode-locking with feedback induced pulses, greens indicate complex dynamics (in this case quasi-periodic) with 2-5 pulses in the laser cavity (CD2-CD5) and blues indicate harmonic mode-locking (HML) Parameters: all other parameters as in Table 2.1.

we will classify the feedback strength into three regimes; low, intermediate and high. Low feedback strengths are values for which the fed-back pulses are not large enough to cause gain competition, i.e. values up to the onset of quasi-periodic dynamics caused by the torus bifurcations. For the laser parameters used here this regime corresponds to $K < 0.15$. The intermediate feedback strength regime we shall classify up to the onset of harmonic mode-locking in the main resonances, which in this case is up to approximately $K = 0.6$ and also coincides approximately with the upper boundary of the torus bifurcations which lead to the quasi-periodic dynamics (T_4 and T_5). High feedback strengths are $K > 0.6$.

Path continuation has only been carried out for the continuous wave and fundamentally mode-locked solutions. This is because increased calculation times are required for the stability analysis of the harmonically mode-locked solutions due to the larger time-scale separation between the period of these solutions and the feedback delay time. However, the bifurcations of the harmonically mode-locked solutions would need to be continued in order to determine how the quasi-periodic regions (green regions) are related to the harmonically mode-locked solutions, i.e. whether or not the upper boundaries of the quasi-periodic regions (green regions)

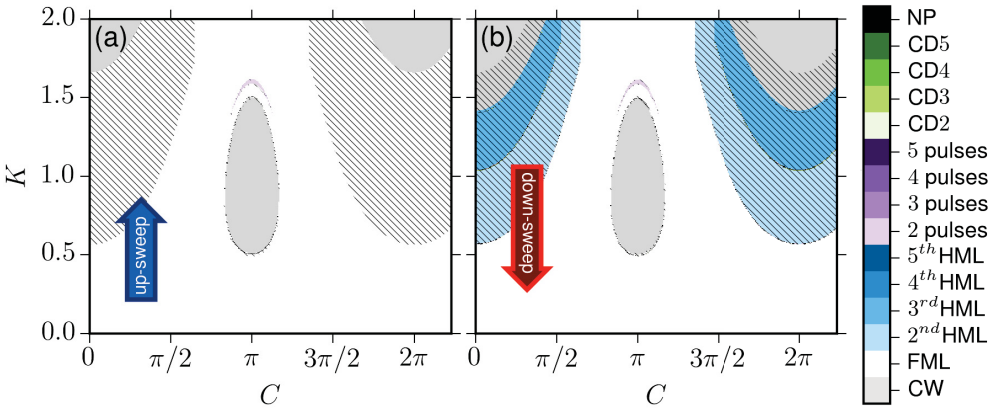

Figure 3.40.: Maps of the dynamics in dependence of C and K obtained for (a) up- and (b) down-sweeps in K. The colour code indicates the number of pulses in the laser cavity and the type of dynamics that are exhibited. White indicates fundamental mode-locking (FML), purples indicate fundamental mode-locking with feedback induced pulses, greens indicate complex dynamics (in this case quasiperiodic) with 2-5 pulses in the laser cavity (CD2-CD5) and blues indicate harmonic mode-locking (HML). The grey regions indicate continuous-wave solutions. Hatching indicates regions in which different results are obtained in the up- and down-sweeps. Parameters: $\tau = 0$, all other parameters as in Table 2.1.

are given by torus bifurcations of the harmonically mode-locked solutions emanating form the Hopf-Hopf points from which the torus bifurcations of the fundamentally mode-locked solution start.

Feedback phase dependence

In this section the dependence of the solutions on the feedback phase C is investigated in the short feedback delay regime.

In Fig. 3.40 maps of the dynamics in the C-K parameter plane are shown for zeroth-order resonant feedback, $\tau = 0$. These maps are obtained in a similar fashion to Fig. 3.30, i.e. by performing (a) up- and (b) down-sweeps in K. Due to the 2π phase-shift symmetry of Eq. (3.7), solutions repeat when C is varied by multiples of 2π. At low feedback strengths there is no qualitative dependence on C. For $K > 0.5$ there are regions of multistability between fundamental and harmonic mode-locking near $C = 0$ and $C = 2\pi$. Note that not all regions of multistability have been captured in these sweeps. For instance the parabolic lower bound for the onset of harmonic mode-locking actually continues past $K = 0.2$. In accordance with the results shown in the τ-K plane (eg. Fig. 3.38), at high feedback strengths continuous wave lasing restabilises. Near the center of the C-K maps there is also a region of continuous wave lasing. Previously the authors of [AVR09] and [OTT12a, OTT14] have discussed that there are parallels between

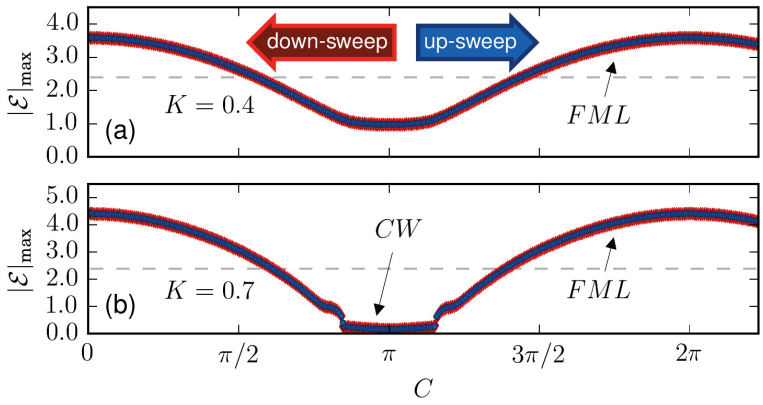

Figure 3.41.: Numerical bifurcation diagrams showing the C dependence of the mode-locked laser output for (a) $K = 0.4$ and (b) $K = 0.7$. Plotted in blue (red) are electric field maxima $|\mathcal{E}|_{\max}$ for an up-sweep (down-sweep) in the initial conditions. The horizontal dashed line indicates the mode-locked pulse amplitude in the solitary laser case. Parameters: $\tau = 0$, all other parameters as in Table 2.1.

a mode-locked laser with resonant feedback and a single-mode laser subject to feedback. The re-stabilisation of continuous wave lasing for intermediate to high feedback strengths near $C = \pi$ is another example of such a parallel. In the single-mode laser case, for short feedback delay times, a similar region is found, however in this case it is the off state that restabilises [ROT07]. For single-mode lasers, including devices with quantum dot gain materials, it is also found that for low feedback strengths there is no qualitative dependence on the feedback phase [LEV95, TAR95a, TAR98a, ROT07, OTT10].

To understand why there is a region of stable continuous wave lasing for a range of intermediate to high K values it is helpful to consider the influence of the feedback phase on the effective non-resonant losses. For instantaneous feedback ($\tau = 0$) pulses are coupled back directly and interfere with themselves. If $C = n2\pi$, for integer n, they interfere constructively and the influence of the feedback term is essentially a reduction in the non-resonant losses, i.e. Eq. (3.7) is reduced to Eq. (3.8) with internal losses given by $\kappa\,(1+K)^2$. This reduction in the losses leads to an increase in the pulse amplitude compared with the solitary laser. This is illustrated in Fig. 3.41, where the electric field maxima are plotted for up- and down-sweeps in C. For $C = 0$ and $C = 2\pi$ there are maxima in the pulse amplitude and the pulse amplitude is increased compared with the solitary laser case (dashed grey line). As C is increased from zero, pulses are coupled into the laser cavity with a phase shift, leading to partial destructive interference and a decrease in the pulse amplitude. For $C = \pi$ all the light is coupled back destructively. In this case Eq. (3.7) can also be reduced to Eq. (3.8), however with the internal losses now given

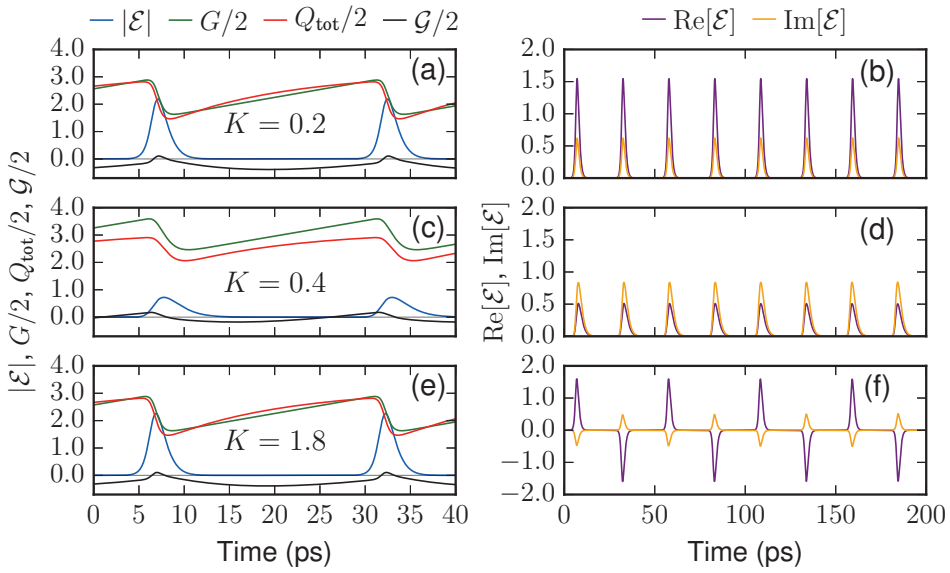

Figure 3.42.: Time traces of the feedback induced dynamics for $C = \pi$ with feedback strengths (a)-(b) $K = 0.2$. (c)-(d) $K = 0.4$ and (e)-(f) $K = 1.8$. The time traces (a), (c) and (e) show the electric field amplitude $|\mathcal{E}|$ (blue), gain G (green), total losses $Q_{\rm tot} = Q - \ln\left(\kappa\,(1-K)^2\right)$ (red) and the net gain $\mathcal{G} = G - Q_{\rm tot}$ (black). The time traces (b), (d) and (f) show the real (purple) and imaginary (orange) parts of the complex electric field amplitude $\mathcal{E}$. Parameters: $\tau = 0$, all other parameters as in Table 2.1.

by $\kappa\,(1-K)^2$, since $Ke^{i\pi} = -K$. If K is small the increased internal losses just lead to a reduction in the pulse height, as is the case in Fig. 3.41a. However, above a critical value, $K_{\rm crit}$, the losses are too high for mode-locking to occur. Effectively the threshold current for the onset of mode-locking is increased and if this threshold is pushed passed our operation current, $J_g = 3$, mode-locking ceases and continuous wave lasing becomes stable. From the effective losses, $\kappa\,(1-K)^2$, it can be seen that if the feedback strength is increased past $K = 1$ the internal losses are again reduced, and at $K = 2 - K_{\rm crit}$ mode-locking restarts. Examples of time traces for $C = \pi$ are shown for various feedback strengths in Fig. 3.42. In (a), (c) and (d) of Fig. 3.42 the electric field amplitude (blue), the gain (green), the total losses (red) and the net gain (black) are depicted. Here the term for the total losses is modified to include the influence of the feedback strength, $Q_{\rm tot} = Q - \ln\left(\kappa\,(1-K)^2\right)$. In (b), (d) and (f) of Fig. 3.42 the real (purple) and imaginary (orange) parts of the complex electric amplitude $\mathcal{E}$ are shown. Comparing Fig. 3.42a and Fig. 3.42c it can be seen that as K is increased towards $K_{\rm crit}$ ($K_{\rm crit} \approx 0.5$) the solutions develop a leading edge instability [NEW74], i.e. the net gain is positive before the pulse arrives. This is because small pulses cannot saturate the gain and absorber sections

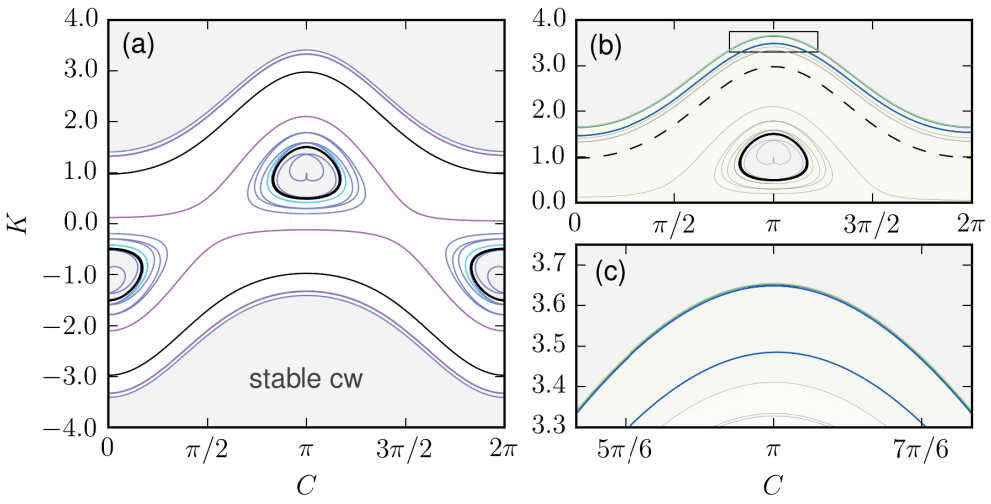

Figure 3.43.: **Path continuation:** (a) Hopf bifurcations of the continuous-wave solution in the C-K parameter space. In black is the H_1 Hopf curve. The H_2, H_3 and H_4 Hopf curves are depicted in light blue, purple and pink, respectively. (b) Bifurcations of the fundamental mode-locked solution. Blue lines indicate torus bifurcations and green lines are saddle-node bifurcations and the red line is a period-halving bifurcation. The black line is the fundamental Hopf bifurcation curve of the continuous wave solution (H_1), with the solid segment being supercritical and the dashed segments subcritical. The thin grey lines show the remaining Hopf bifurcations of the continuous-wave solution (compare with (a)). Shaded in green is the stability region of the fundamental mode-locked solution. Shown in (c) is a close-up of the region enclosed in the black rectangle in (b). In the grey regions the continuous-wave solution is stable. Parameters: $\tau = 0$, all other parameters as in Table 2.1.

as fast. For the feedback strengths used in Fig. 3.42a and Fig. 3.42e the effective internal losses are the same ($\kappa\,(1-K)^2 = \kappa \cdot 0.8^2$ for $K = 0.2$ and $K = 1.8$), and hence the pulse, gain, and loss profiles are identical. However for $K = 1.8$ the cavity modes are shifted by a frequency of $\nu_{\mathrm{rep}}/2$, where $\nu_{\mathrm{rep}} = 1/T_0$ is the repetition rate of the mode-locked solution. This can be seen in Fig. 3.42f as $\mathrm{Re}[\mathcal{E}]$ and $\mathrm{Im}[\mathcal{E}]$ have twice the period of the amplitude (i.e. $2T_0$) due to the added rotation with respect to the optical reference frequency Ω_0.

Path continuation

In Fig. 3.43 the results of path continuation in the C-K plane are presented. Figure 3.43a shows Hopf bifurcations of the maximum-gain continuous-wave solution, where the H_1 bifurcation is again plotted in black. The bifurcations show the expected symmetry, i.e. that the bifurcations in the negative K half-plane are the same as those in the positive half-plane with a phase shift of π. In Fig. 3.43b the bifurcations of the fundamental mode-locked solution are shown, as well as

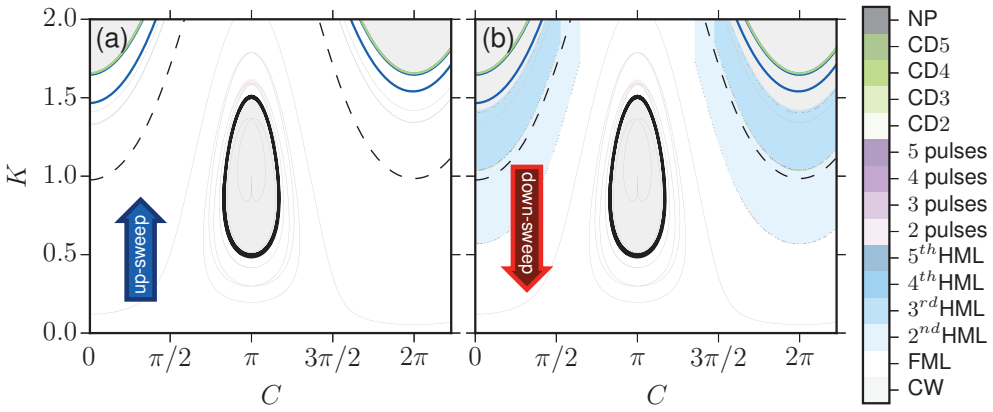

Figure 3.44.: **Comparison of numerics and path continuation:** Maps of the dynamics in dependence of C and K obtained for (a) up- and (b) down-sweeps in K and the bifurcations of the continuous wave and fundamental mode-locked solutions. Blue lines indicate torus bifurcations and green lines are saddle-node bifurcations. The black line is the fundamental Hopf bifurcation curve of the continuous wave solution. The thin grey lines show the remaining Hopf bifurcations of the continuous-wave solution (compare with Fig. 3.34 (a)). The colour code indicates the number of pulses in the laser cavity and the type of dynamics that are exhibited. White indicates fundamental mode-locking (FML), purples indicate fundamental mode-locking with feedback induced pulses, greens indicate complex dynamics (in this case quasiperiodic) with 2-5 pulses in the laser cavity (CD2-CD5) and blues indicate harmonic mode-locking (HML). The grey regions indicate continuous-wave solutions. Parameters: $\tau = 0$, all other parameters as in Table 2.1.

the criticality of the H_1 curves (here we focus only on the positive K half-plane due the symmetry of the system). The green shading indicates the regions where the fundamentally mode-locked solution is stable. Solutions that are generated on the subcritical H_1 branch (dashed black line) are initially unstable. Similar to the case depicted in Fig. 3.36 (1), as the solution branch is continued in K it goes through three torus bifurcations and then becomes stable after a saddle-node bifurcation (the second two torus bifurcations and the saddle-node bifurcation are very close together, see Fig. 3.43c). Depending on the value of C the stable solution branch either continues to exist as it is continued into the negative K half-plane, where it then goes through the same sequence of bifurcations and terminates on the subcritical H_1 curve that must exist in the negative K half-plane, or if C is sufficiently close to π the solution branch terminates in the supercritical H_1 curve (solid black line). Within the area enclosed by the supercritical H_1 curve no fundamental mode-locked solution exists. Comparing the path continuation results with the numerically obtained maps (see Fig. 3.44) shows that this is the area where continuous wave lasing was found numerically. The bounds for fundamental mode-locking that were obtained by direct numerical simulation are given by the

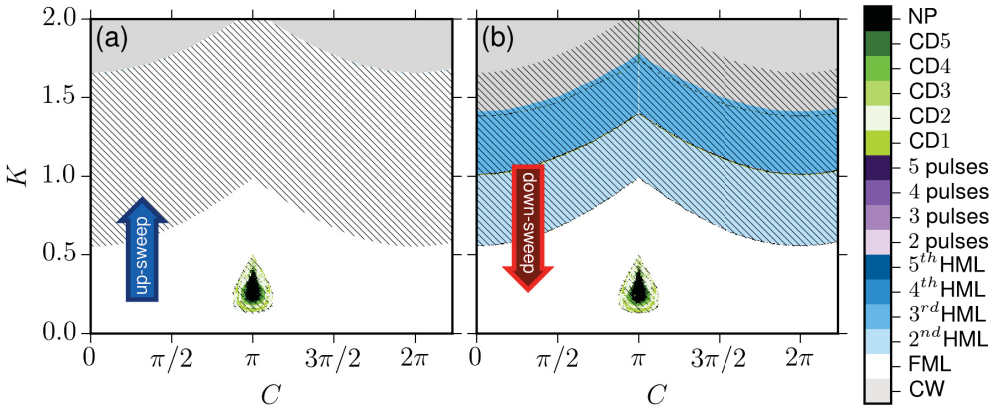

Figure 3.45.: Maps of the dynamics in dependence of C and K obtained for (a) up- and (b) down-sweeps in K for third order main resonant feedback. The colour code indicates the number of pulses in the laser cavity and the type of dynamics that are exhibited. White indicates fundamental mode-locking (FML), purples indicate fundamental mode-locking with feedback induced pulses, greens indicate complex dynamics (quasi-periodic and chaotic) with 2-5 pulses in the laser cavity (CD2-CD5), blues indicate harmonic mode-locking (HML) and black indicates non-periodic (NP) dynamics that do not fall into the previous categories. The grey regions indicate continuous-wave solutions. Hatching indicates regions in which different results are obtained in the up- and down-sweeps. Parameters: $\tau = 3T_{0,S}$, all other parameters as in Table 2.1.

supercritical H_1 bifurcation and the saddle-node bifurcation of the fundamentally mode-locked solution (see Fig. 3.44a).

Feedback phase dependence for $\tau = 3T_{0,S}$

The authors of [AVR09] have numerically studied the feedback phase dependence of a Fabry-Perot passively mode-locked laser with a main-resonant feedback delay time of $\tau = 3T_{0,S}$. For $C = \pi$[13] they found a feedback strength dependence that they likened to coherence collapse in single-mode lasers subject to feedback [LEN85]. For low feedback strengths they found mode-locked dynamics with periodically modulated pulse heights, then as the feedback strength was increased the pulse shapes became increasingly irregular, until after a critical feedback strength, fundamental mode-locking was recovered. Similar results are exhibited by the DDE model. Here we elaborate on the findings presented in [OTT12a, OTT14] for the DDE model with $\tau = 3T_{0,S}$. Maps of the dynamics in the C-K plane, for up- and down-sweeps in K, are shown in Fig. 3.45. The region of continuous wave

[13] In the model used in [AVR09] a transmittance phase of $\pi/2$ is included for the facet of the laser that couples to the external cavity. Therefore an external mirror phase shift of zero is equivalent to $C = \pi$ for the DDE system.

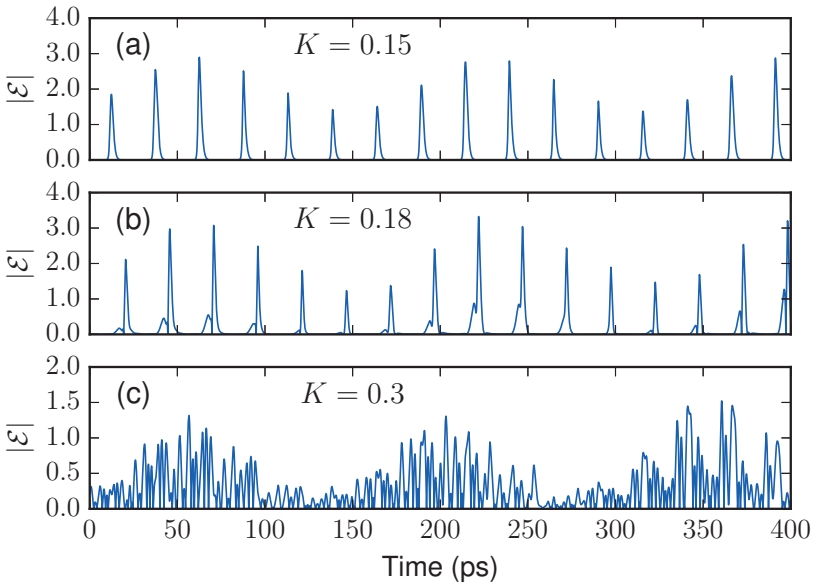

Figure 3.46.: Time traces of the electric field amplitude for $C = \pi$ and $\tau = 3T_{0,S}$ with (a) $K = 0.15$, (b) $K = 0.18$, (c) $K = 0.3$. Parameters: all other parameters as in Table 2.1.

lasing near $C = \pi$ is no longer present for this feedback delay time. Instead, at lower K values, there is a region of quasi-periodic and chaotic dynamics (green and black regions). The regions plotted in black exhibit non-periodic (NP in the colour code) dynamics that do not fall into any of the other categories. Examples of the dynamics in this parameter regime are shown in Fig. 3.46. First, at the edge of the low feedback strength regime, there are mode-locked dynamics with a modulated pulse height (shown in Fig. 3.46a). The modulation frequency is similar to the Q-switching frequency in the solitary laser case (compare with Fig. 3.18a), we therefore speculate that these dynamics arise out of the T_4 torus bifurcation that is also seen for low currents in the solitary laser case (see Fig. 3.10). Then, as the feedback strength is increased the pulses become deformed (Fig. 3.46b) and eventually the dynamics are chaotic (Fig. 3.46c). Below and above this tear-drop shaped region in Fig. 3.45, fundamental mode-locking is exhibited. At high feedback strengths there are again regions of multistability between fundamental mode-locking, harmonic mode-locking and continuous wave lasing. Compared with the $\tau = 0$ case (Fig. 3.40) regions of harmonic mode-locking are wider.

The disappearance of the continuous wave region near $C = \pi$ in Fig. 3.45, and the increased width of the regions of harmonic mode-locking, can be attributed to the fact that τ is non-zero. In the $\tau = 0$ case the period of the mode-locked solutions, and hence the frequency of the lasing modes, vary with the feedback phase. An example of the phase dependence of T_0 is shown in Fig. 3.47 for $K = 0.4$.

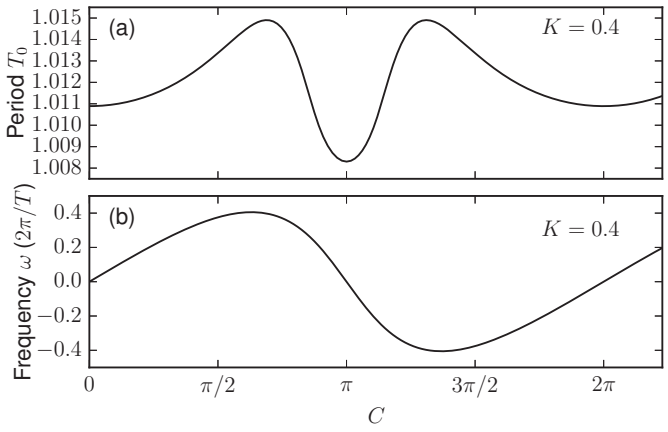

Figure 3.47.: (a) Period of the fundamentally mode-locked solution as a function of C for zeroth-order main resonant feedback and $K = 0.4$. (b) Frequency of the of the central lasing mode with respect to the reference frequency Ω_0. Parameters: $\tau = 0$, all other parameters as in Table 2.1.

In Fig. 3.47b the frequency of the lasing mode which is closest to the center of the spectral filter is shown (given with respect to the reference frequency Ω_0). Despite this change in the period of the solutions the pulses that are coupled back still overlap perfectly with the main pulses and interfere destructively because the feedback delay time is zero. If the delay time is non-zero, then the phase induced changes in the frequency of the lasing modes reduces the destructive interference, since due to the shift of the modes a phase difference of $\omega\tau$ accumulates between the light in the laser and feedback cavities, and this phase shift can compensate for the phase feedback. Due to this reduction in the destructive interference, the mode-locked solutions can remain stable over larger C ranges.

Feedback phase dependence for $\tau = \frac{1}{2}T_{0,S}$

When the feedback delay time is shifted from the main resonances the phase dependence is qualitatively very similar. An example of the dynamics in the C-K plane is displayed in Fig. 3.48 for $\tau = \frac{1}{2}T_{0,S}$. For low feedback strengths the system exhibits fundamental mode-locking with one satellite pulse, since $p = 2$. As the feedback phase is increased from zero the electric field intensity varies only slightly, but a phase difference develops between the main pulse and the satellite pulse. For $C = \pi$ the phase difference is π. In this case the intensity profile is identical to that for $C = 0$ because it is the satellite pulse that gets coupled with the main pulse after one round trip in the feedback cavity, and the additional feedback phase shift of π results in constructive interference. Due to this the features in Fig. 3.48 have a π periodicity in C. As the feedback strength is increased there is a transition

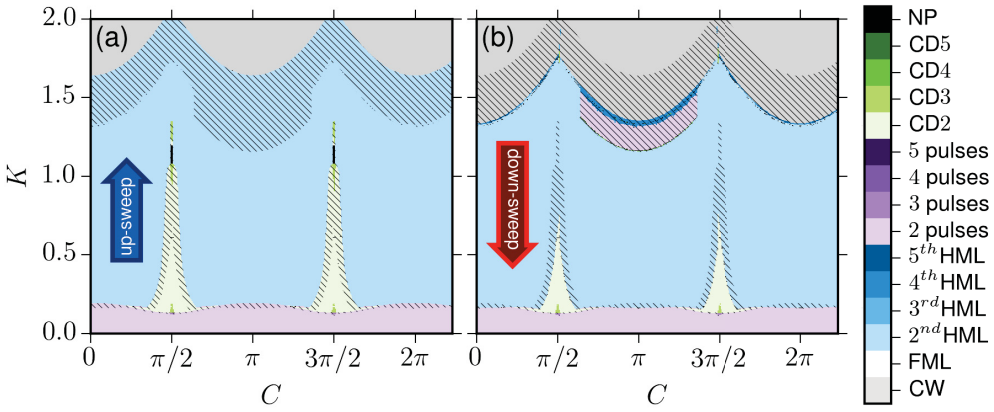

Figure 3.48.: Maps of the dynamics in dependence of C and K obtained for (a) up- and (b) down-sweeps in K for $p = 2$ higher order resonant feedback. The colour code indicates the number of pulses in the laser cavity and the type of dynamics that are exhibited. White indicates fundamental mode-locking (FML), purples indicate fundamental mode-locking with feedback induced pulses, greens indicate complex dynamics (quasi-periodic and chaotic) with 2-5 pulses in the laser cavity (CD2-CD5), blues indicate harmonic mode-locking (HML) and black indicates non-periodic (NP) dynamics that do not fall into the previous categories. The grey regions indicate continuous-wave solutions. Hatching indicates regions in which different results are obtained in the up- and down-sweeps. Parameters: $\tau = \frac{1}{2}T_{0,S}$, all other parameters as in Table 2.1.

to 2$^{\text{nd}}$ harmonic mode-locking, except for C ranges near $C = \pi/2$ and $C = 3\pi/2$ where the dynamics become quasi-periodic. For $C = \pi/2$ and $C = 3\pi/2$ the pulses interfere destructively, thereby increasing the effective non-resonant losses, which leads to the gain being insufficient to sustain harmonic mode-locking. For other feedback delay times the dynamics show the similar trends.

Influence of amplitude-phase coupling

In this section the feedback induced dynamics in the presence of amplitude-phase coupling will be studied. The results for the solitary laser showed that amplitude-phase coupling leads to more complex dynamics and smaller parameter ranges in which clean mode-locking is exhibited (see Section 3.2.3). This becomes more pronounced when α_g and α_q, or the difference between these values, are large. For this section we choose one set of representative values, $\alpha_g = 2$ and $\alpha_q = 1.5$, for which the solitary laser still exhibits fundamental mode-locking at our standard pump current ($J_g = 3$).

Maps of the dynamics in the τ-K plane are shown in Fig. 3.49 for (a) up- and (b) down-sweeps in K. The overall structure of these maps is the same as in the zero α-factor case shown in Fig. 3.30. The most obvious differences are that

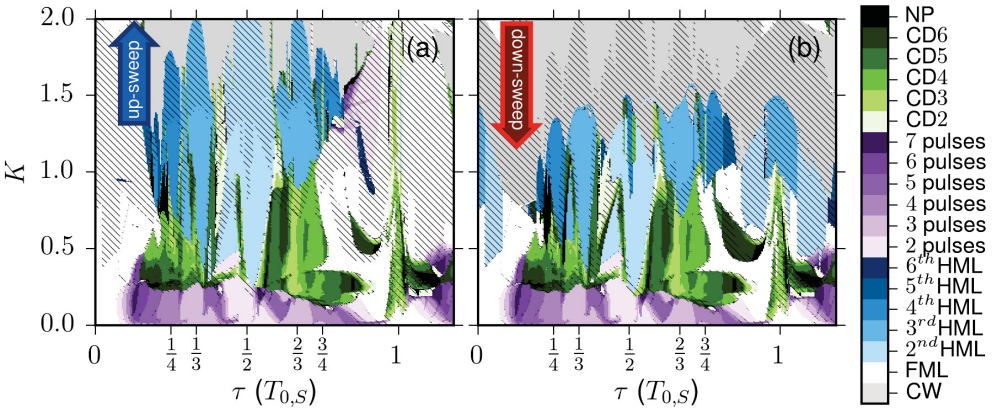

Figure 3.49.: **Influence of amplitude-phase coupling:** Maps of the dynamics in dependence of τ and K obtained for (a) up- and (b) down-sweeps in K with $\alpha_g = 2$ and $\alpha_q = 1.5$. The feedback delay time is plotted in units of the period for $K = 0$, $T_{0,S} = 1.0102$. The colour code indicates the number of pulses in the laser cavity and the type of dynamics that are exhibited. White indicates fundamental mode-locking (FML), purples indicate fundamental mode-locking with feedback induced pulses, greens indicate complex dynamics (quasi-periodic and chaotic) with 2-5 pulses in the laser cavity (CD2-CD5), blues indicate harmonic mode-locking (HML) and black indicates non-periodic (NP) dynamics that do not fall into the previous categories. The grey regions indicate continuous-wave solutions. Hatching indicates regions in which different results are obtained in the up- and down-sweeps. Parameters: all other parameters as in Table 2.1.

the boundaries between the various dynamical regimes are very distorted, quasi-periodic and chaotic dynamics are found in the first main resonance region and there are larger regions of bistability between solutions obtained in the up- and down-sweeps in K. This increased complexity of the dynamics is due to the carrier induced shift of the lasing modes (see Fig. 3.50) and the increased phase sensitivity in the presence of amplitude-phase coupling. The influence of the carrier induced shift of the lasing modes can be understood as follows. The detuning between the lasing modes and the reference rotating frame causes a phase difference to accumulate between the pulses in the laser and feedback cavities. This occurs because the light in the laser cavity continues to rotate, while the light in the feedback cavity is coupled back unchanged after time τ. The accumulated phase difference is given by $\Delta\phi = \omega\tau$, where ω is the frequency offset of the central mode from the reference frequency Ω_0. This means that although the feedback phase was set to zero for the calculation of the results presented in Fig. 3.49, the phase difference is non-zero and, more importantly, it is τ and K dependent.[14] Therefore, in Fig. 3.49 the structure is influenced by phase effects as well as K and τ, whereas in Fig. 3.30 purely the K and τ dependence of the dynamics are shown. In order

[14]The K dependence arises implicitly via the K dependence of ω.

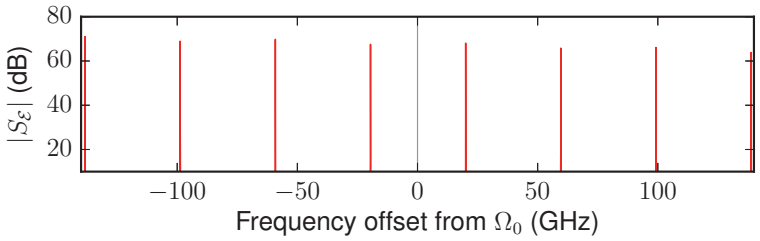

Figure 3.50.: Optical spectrum $|S_\mathcal{E}|$ of the mode-locked laser output for $\alpha_g = 2$ and $\alpha_q = 1.5$. Parameters: all other parameters as in Table 2.1.

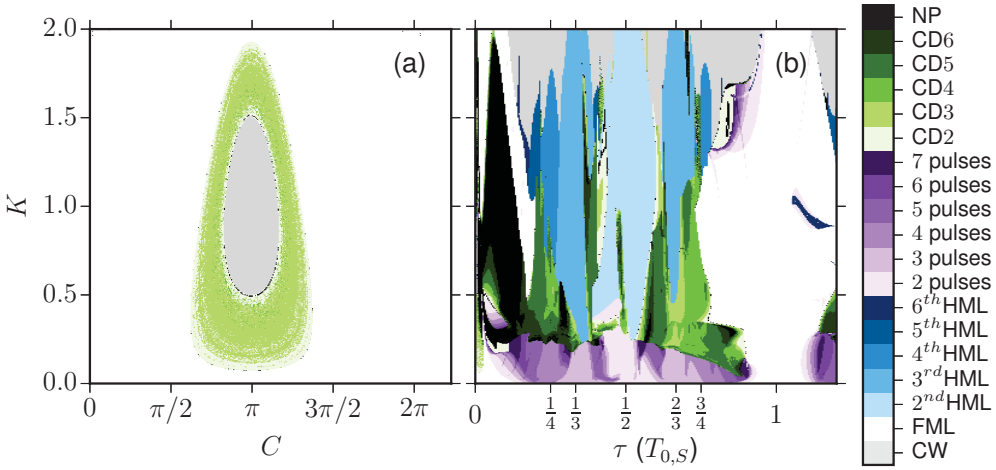

Figure 3.51.: **Influence of amplitude-phase coupling:** Maps of the dynamics in dependence of (a) C and K, and (b) τ and K, with $\alpha_g = 2$ and $\alpha_q = 1.5$. The results are obtained by performing up-sweeps in K. The feedback delay time is plotted in units of the period for $K = 0$, $T_{0,S} = 1.0102$. The colour code indicates the number of pulses in the laser cavity and the type of dynamics that are exhibited. White indicates fundamental mode-locking (FML), purples indicate fundamental mode-locking with feedback induced pulses, greens indicate complex dynamics (quasi-periodic and chaotic) with 2-5 pulses in the laser cavity (CD2-CD5), blues indicate harmonic mode-locking (HML) and black indicates non-periodic (NP) dynamics that do not fall into the previous categories. The grey regions indicate continuous-wave solutions. Parameters: (a) $\tau = 0$, (b) $C = \pi$, all other parameters as in Table 2.1.

to separate the influence of the phase difference from affects that may purely arise due to the chirp of the pulses, C would need to be selected in such a way that it compensates for $\Delta\phi$. However, since ω is dependent on the dynamical variables it is not known in advance, which makes it very difficult to obtain a map over which $\Delta\phi - C$ is constant.

To investigate the increased phase sensitivity with non-zero amplitude-phase coupling, the dynamics in the C-K plane are shown for $\tau = 0$ in Fig. 3.51a. Comparing

this map with the equivalent map for zero amplitude-phase coupling, Fig. 3.40a, it can be seen that there is now a large region of quasi-periodic or chaotic dynamics (green regions) surrounding the oval shaped region of stable continuous wave lasing near $C = \pi$. This plot shows that, even for low feedback strengths, a π phase shift between the light in the feedback and laser cavities can lead to complex, non-periodic dynamics, which was not the case for zero amplitude-phase coupling (for $\tau = 0$). It is this sensitivity to the phase difference that causes the regions of quasi-periodic and chaotic dynamics at first-order main resonance ($\tau = T_{0,S}$) in Fig. 3.49. This can be understood as follows. For $\alpha_g = 2$ and $\alpha_q = 1.5$ the shift of the central lasing modes from the reference frequency Ω_0 is approximately 20 GHz, i.e. half of the fundamental repetition rate $((T_0 \cdot 25\text{ps})^{-1}/2)$, as can be seen in Fig. 3.50. Therefore, in a time interval of $T_{0,S}$ a phase shift of approximately π accumulates between the laser and feedback cavities, leading to destructive interference for $\tau = T_{0,S}$. If we compensate for this phase difference by setting $C = \pi$, then regular mode-locked dynamics are recovered at $\tau = T_{0,S}$. This is shown in Fig. 3.51b. Here, the non-periodic dynamics now occur at the zeroth-main resonance. Non-periodic dynamics occurring for main resonant feedback was also investigated in [OTT14] (also using the DDE model). The author showed that the dynamics transition from periodic to quasi-periodic to chaotic, similar to the quasi-periodic route to chaos shown in Fig. 3.46 for $C = \pi$ with zero amplitude-phase coupling.

3.3.2. Intermediate delay

In the previous section the feedback induced dynamics in the regime of very short delay times was discussed. As mentioned at the beginning of Section 3.3.1, all of the periodic solutions that were found for the system in this short delay regime, are also solutions of the system for larger delay times fulfilling $\tau = \tau_S + nT_0$, for integer n, where τ_S is a small delay offset (i.e. within the range $[0, T_{0,K}]$) and T_0 is the period of the solution for $\tau = \tau_S$. Since T_0 is dependent on K and τ_S (see Figs. 3.36 and 3.37) the shape of the various dynamical regions changes for increasing delay times. And, although the same solutions exist for larger delay times, their stability can change [YAN09]. Furthermore, different non-periodic solutions can arise when the delay time is changed. Therefore, in this section the stable dynamics arising in the intermediate τ regime ($\tau \sim 10$) are investigated.

$\tau - K$ dependence

Figure 3.52 depicts maps of the dynamics in the τ-K plane between the 10^{th} and 11^{th} main resonances. As in the short delay case (compare with Fig. 3.30), there are regions of fundamental mode-locking around the main resonances, however the τ range of these dynamics is wider, especially for large feedback strengths (note that the K range in Fig. 3.52 is smaller than in Fig. 3.30, but as in the short

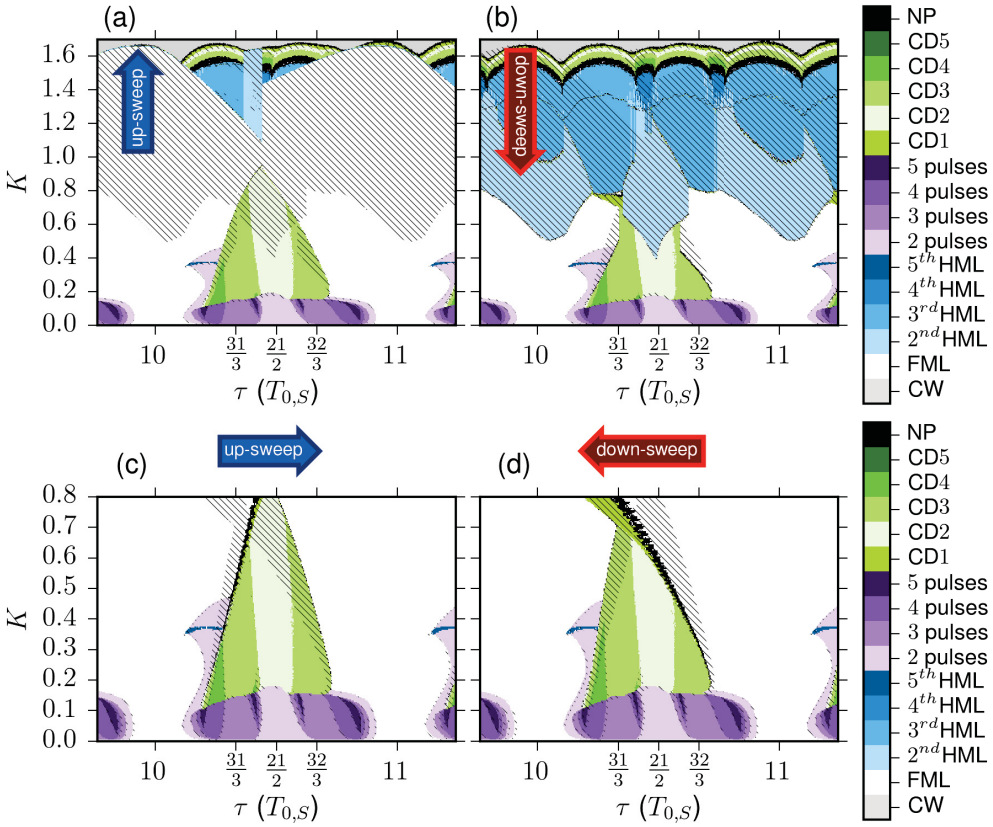

Figure 3.52.: Maps of the dynamics in dependence of τ and K obtained for (a) up- and (b) down-sweeps in K and (c) up- and (d) down-sweeps in τ. The feedback delay time is plotted in units of the period for $K = 0$, $T_{0,S} = 1.014$. The colour code indicates the number of pulses in the laser cavity and the type of dynamics that are exhibited. White indicates fundamental mode-locking (FML), purples indicate fundamental mode-locking with feedback induced pulses, greens indicate complex dynamics (in this case quasi-periodic) with 2-5 pulses in the laser cavity (CD2-CD5) and blues indicate harmonic mode-locking (HML). The grey regions indicate continuous-wave solutions. Hatching indicates regions in which different results are obtained in the up- and down-sweeps. Parameters: all other parameters as in Table 2.1.

delay case, above $K \approx 1.7$ the system only exhibits continuous wave lasing). Due to the increased width of the fundamental mode-locking regions, there are now large regions of multistability between fundamental and harmonic mode-locking. The feedback delay time does not affect the critical K values at which harmonic mode-locking starts for resonant feedback. Therefore the onset of 2$^{\text{nd}}$ and 3$^{\text{rd}}$ order harmonic mode-locking at the main resonances, $\tau = 10T_{0,K}$ and $\tau = 11T_{0,K}$, happens at the same feedback strengths as at the zeroth ($\tau = 0$) and first ($\tau = T_{0,K}$) main resonances. At low feedback strengths the multi-pulse regions (purples) have the same structure as in the short delay case. However, the region of quasi-periodic

dynamics (greens) has changed and extends to larger feedback strengths. A notable difference is also that in the intermediate delay case there is no direct transition from two pulse dynamics to 2$^{\text{nd}}$ order harmonic mode-locking. Instead, this transition is now mediated by quasi-periodic dynamics with two pulses in the laser cavity. Such dynamics were not observed in the short delay case. There are now also regions of multistability between fundamental mode-locking and quasi-periodic dynamics. This is seen most clearly in Fig. 3.52c-d which shows maps obtained for (c) up- and (d) down-sweeps in τ for low to intermediate feedback strengths. These multistability regions suggest that the torus bifurcations bordering the fundamental mode-locking regions (white) are subcritical,[15] whereas in the short delay case they appeared to be supercritical (see Figs. 3.38 and 3.39).

The increased width of the fundamental mode-locking regions is due to the change in the period within the main resonance locking range (see Fig. 3.26). This will be discussed further in Section 3.3.4. In the multi-pulse regions the solutions all have very similar periods (see Figs. 3.26 and 3.37 (6)), which is why these regions have not changed much compared with the short delay case.

Feedback phase dependence

In the short delay regime it was shown that the regions of harmonic mode-locking become wider when τ is increased from the zeroth to the third main resonance (see Figs. 3.40 and 3.45). At the tenth resonance these regions are again wider, causing multistability between solutions with the same order of harmonic mode-locking. This can be seen by the hatched regions centered on $C = \pi$ in Fig. 3.53, which shows maps of the dynamics in the C-K plane for (a) up- and (b) down-sweeps in C. There are also regions of bistability between fundamentally mode-locked solutions. These regions develop for increasing feedback delay times because smaller shifts in the frequency of the lasing modes are needed to reduce the feedback phase induced destructive interference when the feedback delay time is longer. This is because the phase difference that accumulates between the laser and feedback cavities is proportional to τ ($\Delta\phi = \omega\tau$). The reduced destructive interference leads to a reduction in the influence of C on the period of the solutions. The difference in the influence of C on the period, and frequency shift of the lasing modes, for $\tau = 0$ and $\tau = 10T_{0,S}$, can be seen by comparing Figs. 3.47 and 3.54. The results presented in Fig. 3.54 are obtain by path continuation. Due to the substantially increased computation time needed for $\tau \approx 10$ we have not calculated a complete bifurcation diagram. However, the stability of the solutions continued in C, for $K = 0.4$,

[15] From the numerical integration results we cannot know whether the boundaries are still given by torus bifurcations. However, path continuation results for selected feedback strengths show that this is indeed the case (see Fig. 3.64).

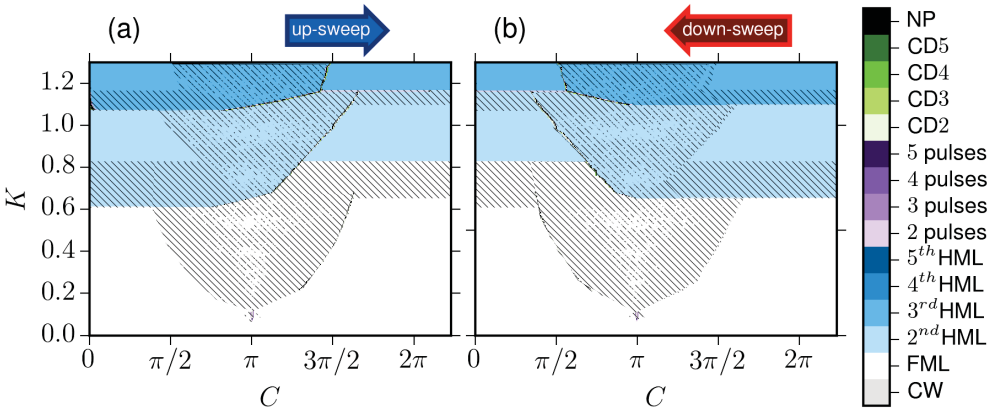

Figure 3.53.: Maps of the dynamics in dependence of C and K obtained for (a) up- and (b) down-sweeps in C for 10^{th} order main resonant feedback. The colour code indicates the number of pulses in the laser cavity and the type of dynamics that are exhibited. White indicates fundamental mode-locking (FML), purples indicate fundamental mode-locking with feedback induced pulses, greens indicate complex dynamics (in this case quasiperiodic or chaotic) with 2-5 pulses in the laser cavity (CD2-CD5) and blues indicate harmonic mode-locking (HML). The grey regions indicate continuous-wave solutions. Hatching indicates regions in which different results are obtained in the up- and down-sweeps. Parameters: $\tau = 10T_{0,S}$, all other parameters as in Table 2.1.

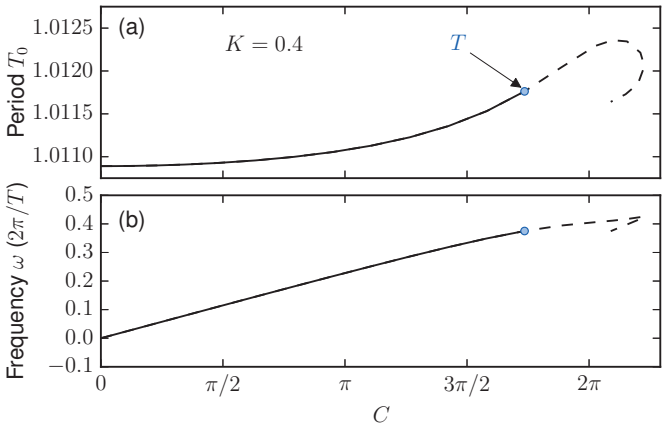

Figure 3.54.: **Path continuation:** (a) Period of the fundamental mode-locked solution as a function of C for 10^{th} order main resonant feedback and $K = 0.4$. (b) Frequency of the central lasing mode with respect to the reference frequency Ω_0. The stability of the solutions is indicated by the solid (stable) and dashed (unstable) lines. The blue circle indicates a torus (T) bifurcation. Parameters: $\tau = 10T_{0,S}$, all other parameters as in Table 2.1.

show that the bistable regions of fundamental mode-locking are bounded by torus bifurcations.

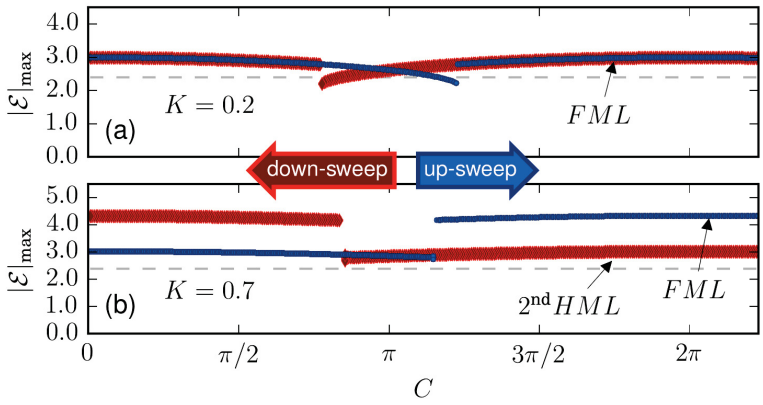

Figure 3.55.: Numerical bifurcation diagrams showing the C dependence of the mode-locked laser output for (a) $K = 0.2$ and (b) $K = 0.7$ for 10^{th} order main resonant feedback. Plotted in blue (red) are electric field maxima $|\mathcal{E}|_{\max}$ for an up-sweep (down-sweep) in the initial conditions. The horizontal dashed line indicates the mode-locked pulse amplitude in the solitary laser case. Parameters: $\tau = 10T_{0,S}$, all other parameters as in Table 2.1.

In Fig. 3.55 cuts through the maps of the dynamics (Fig. 3.53) are shown for $K = 0.2$ and $K = 0.7$. Here the pulse amplitudes show the most variation near the boundaries of the stable regions, i.e. near the torus bifurcations (the boundaries of the stable regions are indicated by abrupt jumps in the electric field maxima). In these plots the regions of bistability between solutions of the same mode-locking order can clearly be seen. For $K = 0.2$ there are overlapping fundamentally mode-locked solutions near $C = \pi$ and for $K = 0.7$ overlapping 2^{nd} harmonic mode-locked solutions can be seen, although the difference in the amplitude of these solutions is small. Figure 3.55b also clearly shows the bistability between fundamental and 2^{nd} harmonic mode-locking.

3.3.3. Long delay

In this section the dynamics in the regime of long feedback delay times ($\tau \sim 100$) is investigated. For such long delay times the transients of the system are substantially increased, which leads to significantly longer integration times. Due to this increased computational cost, in this section we shall focus only the feedback strength range which is relevant for experiments, i.e. low to intermediate feedback strengths.

$\tau - K$ dependence

In the long feedback delay regime the trends observed for intermediate delays are continued. The width of the fundamentally mode-locked regions is increased. At

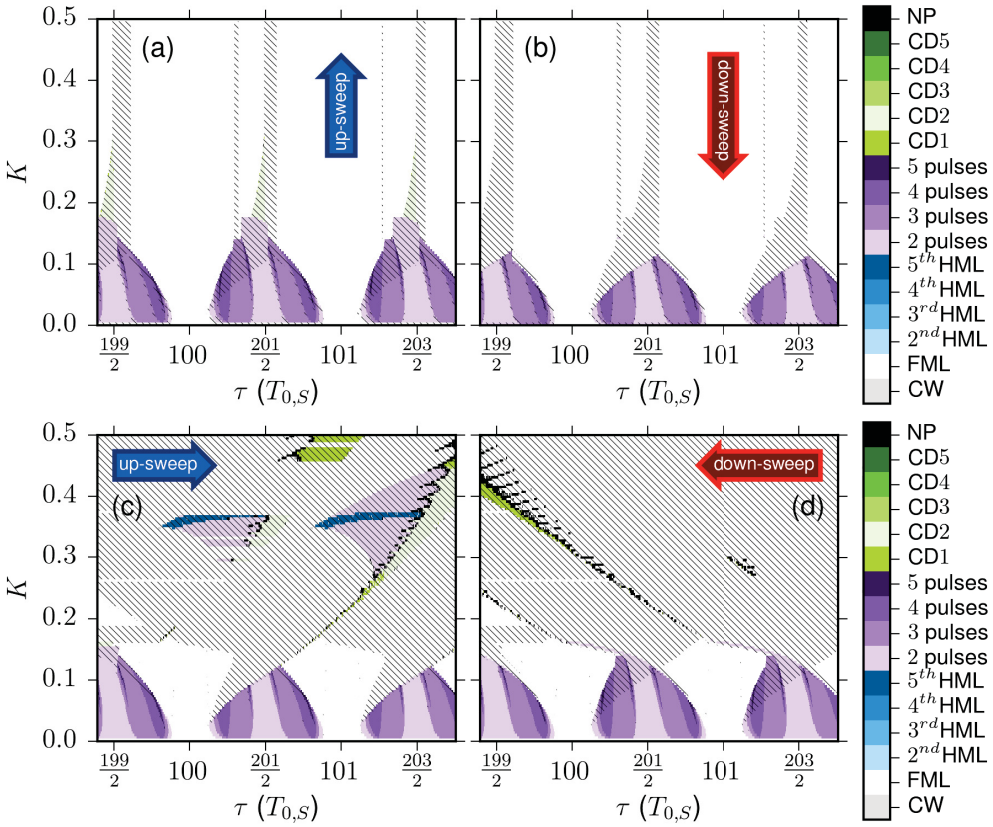

Figure 3.56.: Maps of the dynamics in dependence of τ and K obtained for (a) up- and (b) down-sweeps in K and (c) up- and (d) down-sweeps in τ. The feedback delay time is plotted in units of the period for $K = 0$, $T_{0,S} = 1.014$. The colour code indicates the number of pulses in the laser cavity and the type of dynamics that are exhibited. White indicates fundamental mode-locking (FML), purples indicate fundamental mode-locking with feedback induced pulses, greens indicate complex dynamics (in this case quasi-periodic) with 2-5 pulses in the laser cavity (CD2-CD5) and blues indicate harmonic mode-locking (HML). The grey regions indicate continuous-wave solutions. Hatching indicates regions in which different results are obtained in the up- and down-sweeps. Parameters: all other parameters as in Table 2.1.

intermediate feedback strengths ($K \approx 0.15 - 0.5$) this leads to regions of multi-stability between solutions that are locked to neighbouring resonances. At low feedback strengths there are now regions of bistability between the fundamentally mode-locked dynamics and multi-pulse dynamics. This information is summarised in Fig. 3.56 which shows maps of the dynamics in the τ-K plane for (a) up- and (b) down-sweeps in K and (c) up- and (d) down-sweeps in τ. Due to the overlap of neighbouring main resonance, only small regions of quasi-periodic dynamics are found near the borders of the main resonance locking regions for intermediate feedback strengths (Fig. 3.56c-d). Larger regions of stable quasi-periodic dynam-

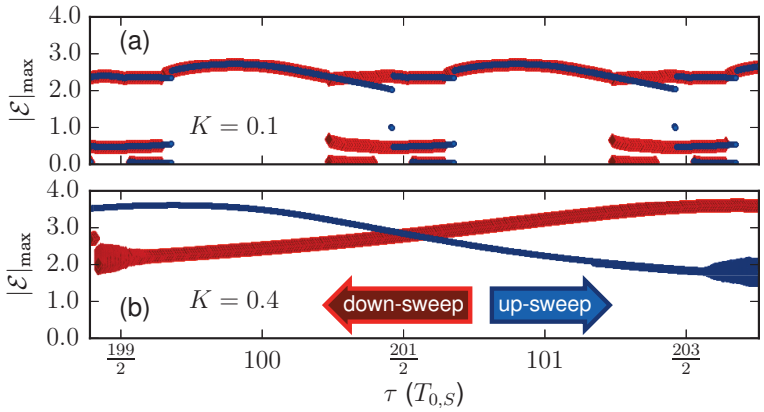

Figure 3.57.: Numerical bifurcation diagrams showing the τ dependence of the mode-locked laser output for (a) $K = 0.1$ and (b) $K = 0.4$. Plotted in blue (red) are electric field maxima $|\mathcal{E}|_{\max}$ for an up-sweep (down-sweep) in the initial conditions. The feedback delay time is plotted in units of the period for $K = 0$, $T_{0,S} = 1.014$. Parameters: all other parameters as in Table 2.1.

ics could still exist, however none were found for the initial condition sweeps that were performed. In the low feedback strength regime, the regions of bistability are larger on the right of the main resonances than on the left. This is due to the pulse asymmetry and will be discussed further in Section 3.3.4 (pulse profiles are shown in Fig. 3.63).

Figure 3.57 shows examples of the pulse height variation for up- and down-sweeps in τ. These plots correspond to cuts through Fig. 3.56c-d at $K = 0.1$ and $K = 0.4$. In the $K = 0.4$ case (Fig. 3.57b) the multistability between fundamentally mode-locked solutions can clearly been seen. Here the up-sweep solution is locked to the 100^{th} main resonance and the down-sweep solution is locked to the 102^{nd} main resonance (not the 101^{st} main resonance). Solutions corresponding to the 101^{st} main resonance also exist in this τ range, and are stable , they were merely not found in this sweep because the up- and down-sweeps both start outside the locking region of 101^{st} main resonance. At each main resonance the solution locked to that particular resonance has the largest, and narrowest, pulses. As shall be seen in Chapter 4, these solutions are generally those that are most stable against noise perturbations.

Feedback phase dependence

For long feedback delay times the feedback phase dependence of the system is greatly reduced. Within the low to intermediate feedback strength regimes there is no qualitative dependence of the dynamics on C. The only influence of varying the feedback phase is small changes in the pulse heights and period. In Fig. 3.58

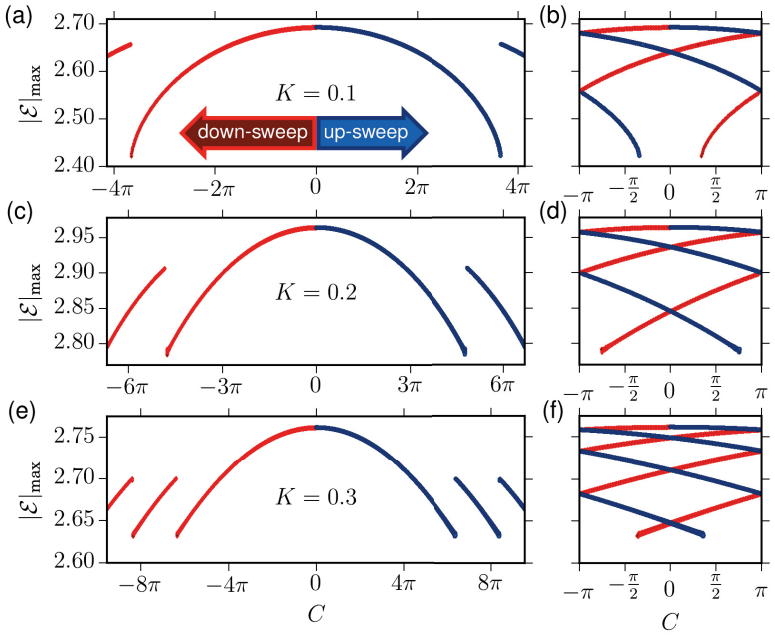

Figure 3.58.: Numerical bifurcation diagrams showing the C dependence of the mode-locked laser output for (a)-(b) $K = 0.1$, (c)-(d) $K = 0.2$ and (e)-(f) $K = 0.2$. Plotted in blue (red) are electric field maxima $|\mathcal{E}|_{\max}$ for an up-sweep (down-sweep) in the initial conditions. In (b), (d) and (f) the phases are shifted into the range $-\pi$ to π. Parameters: $\tau = 100T_{0,S}$, all other parameters as in Table 2.1.

the results of C sweeps are shown for main resonant feedback with $\tau = 100T_{0,S}$. In order to find all fundamentally mode-locked solutions, C was swept up and down from zero. As the solution is swept away from $C = 0$ the pulse amplitude gradually decreases until there is an abrupt jump to higher pulse amplitudes. After such a jump no new solutions are found, previous solutions are merely repeated at phases shifted by integer multiples of 2π. The solutions are swept over C ranges that are greater than 2π, which means that there is multistability. To illustrate the degree of multistability, in subplots (b), (d) and (f) of Fig. 3.58 the solutions are plotted from $-\pi$ to π. These plots are obtained by shifting solutions for $|C| > \pi$ by multiples of 2π. Here, for example, it can be seen that for $K = 0.1$ there are three stable solutions for $C = 0$. One solution (the maximum pulse amplitude solution) for which the central cavity mode has zero detuning from the center of the spectral filter, and two solutions that correspond to positive (blue) and negative (red) detuning from the center of the spectral filter. As the feedback strength is increased the number of stable solutions also increases. This is similar to the behaviour found in single mode lasing with optical feedback [ERN10b].

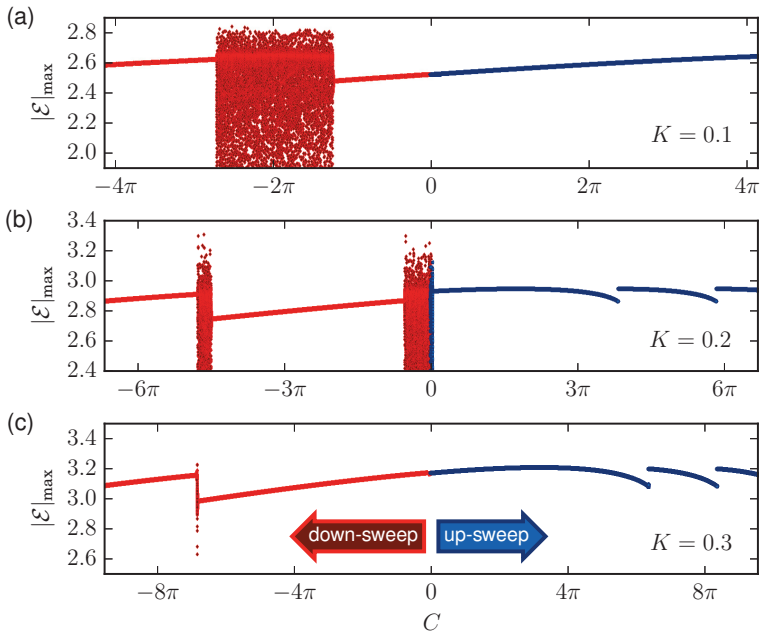

Figure 3.59.: **Influence of amplitude-phase coupling:** Numerical bifurcation diagrams showing the C dependence of the mode-locked laser output for (a) $K = 0.1$, (b) $K = 0.2$ and (c) $K = 0.3$, with $\alpha_g = 2$ and $\alpha_q = 1.5$. Plotted in blue (red) are electric field maxima $|\mathcal{E}|_{\max}$ for an up-sweep (down-sweep) in the initial conditions. Parameters: $\tau = 100T_{0,K}$, all other parameters as in Table 2.1.

Influence of amplitude-phase coupling

In Subsection 3.3.1 we showed that in the presence of amplitude-phase coupling the mode-locked laser system is more sensitive to the phase difference between the light in the laser and feedback cavities. Here we will address whether the phase sensitivity is also reduced for longer feedback delay times when the amplitude-phase coupling is non-zero.

In Fig. 3.59 maxima of $|\mathcal{E}|$ are plotted for sweeps of the feedback phase, with $\tau = 100T_{0,K}$. In contrast to the zero amplitude-phase coupling case (Fig. 3.58) there are solutions which exhibit quasi-periodic or chaotic dynamics (these can be identified in Fig. 3.59 by C values with many maxima of different heights). However, Fig. 3.59 also shows that there are large spans of C with fundamentally mode-locked solutions (C values with one $|\mathcal{E}|_{\max}$ value). The influence of the feedback phase is therefore reduced, as in the zero α-factor case, however the multistability between solutions exhibiting qualitatively different dynamics means that choice of initial conditions is more important.

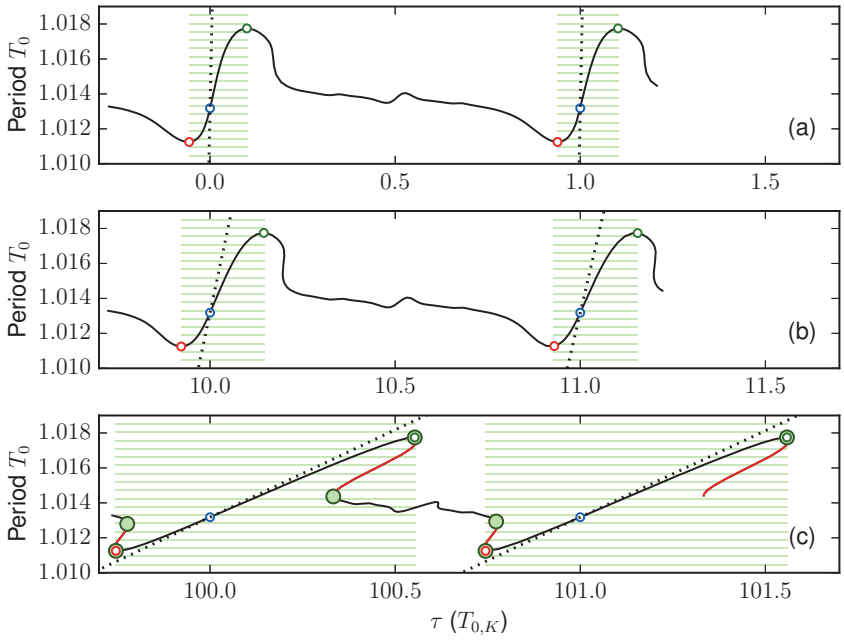

Figure 3.60.: **Low feedback strength regime:** Period of the mode-locked solutions as a function of the feedback delay time in the regime of low feedback strengths. Blue circles indicate the main resonances, and the red and green circles indicate the extent of the main resonance locking regions. The dotted lines indicate the period change necessary for perfect synchronisation in each of the main resonance locking regions. In (c) the filled green circles indicate saddle-node bifurcations and the unstable sections of solutions are plotted in red. Parameters: $K = 0.1$, all other parameters as in Table 2.1.

3.3.4. Frequency pulling and delay-induced multistability

In the previous sections we have investigated in depth the range of dynamics that are exhibited in dependence of the feedback parameters. However, for most practical applications it is only the periodic mode-locked solutions that are of interest. In this section we will investigate more closely the solutions in the main resonance locking regions. Particularly, we will investigate how the feedback delay time influences the pulse repetition rate and the pulse shape, as well as the degree of multistability between different fundamentally mode-locked solutions.

In the previous sections it was already shown that the period (or equivalently, the pulse repetition rate) of the fundamentally mode-locked solutions is dependent on the feedback delay time (see Figs. 3.26 and 3.37). This has also been observed experimentally and is refered to as frequency pulling [SOL93, MER09, GRI09, BRE10, LIN10e, FIO11, LIN11d, ARS13]. This effect occurs because for feedback delay times which are detuned from the main resonances, the system needs to adapt its periodicity for synchronisation to occur between the pulses in the laser

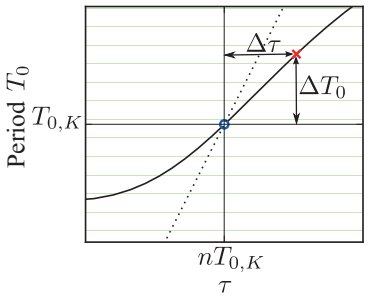

Figure 3.61.: Illustration of the period of solutions near the n^{th} main resonance.

and feedback cavities. Examples of the delay induced period change are shown in Fig. 3.60 for various main resonances. The main resonances are indicated by the blue circles at integer multiples of $T_{0,K}$. In Subsection 3.3.1 we had defined the locking regions of the resonances as the τ ranges in which

- the period of the solutions changes monotonically with τ,
- the number of pulses in the laser cavity remains constant
- and the solutions are stable.

As per this definition, the extent of the locking regions of the main resonances is from the red to the open green circle on either side of each main resonances depicted in Fig. 3.60 (the locking ranges are also indicated by the green striped regions).

Comparing the 100^{th} resonance (c) with the zeroth (a) in Fig. 3.60, it is evident that for a small delay offset $\Delta\tau$ from the main resonances the resulting change in the period is smaller when the feedback delay time is longer. This can be understood by considering the condition that is necessary for the arrival times of pulses to be synchronised at the coupling facet between the laser and feedback cavities. Pulses are perfectly synchronised if

$$\tau = nT_0 \tag{3.11}$$

for integer n, where T_0 is the τ dependent period of the adapted system [OTT12a, OTT14]. Expressed in terms of the resonant delay time and period, the relation is given by

$$nT_{0,K} + \Delta\tau = n\left(T_{0,K} + \Delta T_0\right), \tag{3.12}$$

where $\Delta\tau$ is a small delay offset from the n^{th} main resonance and ΔT_0 is the delay induced change in the period, as illustrated in Fig. 3.61. Rearranging this expression, the change in the period which is needed for synchronisation to occur is

$$\Delta T_0 = \frac{\Delta\tau}{n} \tag{3.13}$$

for $n > 0$. For $n = 0$ the necessary change in the period is given by $\Delta T_0 = \Delta\tau$. Equation (3.13) is the condition for perfect synchronisation, meaning that the fed-back pulses align perfectly with the pulse in the laser cavity. For each main resonance shown in Fig. 3.60 the period given by Eq. (3.13) is indicated by the dotted line. The actual change in the period within the locking regions is smaller than what is predicted by Eq. (3.13). This is because perfect synchronisation is not achieved within the locking ranges as the delay offset is also partially compensated for by changes in the pulse shape (see Figs. 3.63 and 3.66). However, for large n Eq. (3.13) gives a good approximation of the period change for small $|\Delta\tau|$, and shows that the change in the period is reduced for larger n. This is essentially because the change in the pulses arrival time, caused by the delay offset, is distributed over more laser-cavity roundtrips.

To understand why the discrepancy, between the period change predicted by Eq. (3.13) and the actual period change in the locking ranges, is reduced for increasing n, it is useful to consider the relationship between solutions in each of a resonance regions. As previously stated, all periodic solutions are also solutions of the system for feedback delay times that are increased by integer multiples of the period [YAN09]. This means that the solutions in all the main resonance locking regions can be expressed in terms of the solutions at the zeroth main resonance. Let τ_0 be a delay time within the locking range of the zeroth main resonance,[16] i.e. between the red and green circles near the zeroth main resonance in Fig. 3.60a. Then, for all τ_0 the same solutions reappear at feedback delay times given by

$$\tau = \tau_0 + nT_0 \tag{3.14}$$

for integer n, where T_0 is the τ_0 dependent period. Inserting $\tau = nT_{0,K} + \Delta\tau$ and $T_0 = T_{0,K} + \Delta T_0$ to this expression we obtain

$$n\Delta T_0 = \Delta\tau - \tau_0. \tag{3.15}$$

For large n the contribution from τ_0 is negligible, since the values are limited to the narrow locking region of the zeroth main resonance. Hence, for large n the period change in dependence of the delay offset from the main resonance is given by

$$\Delta T_0 \approx \frac{\Delta\tau}{n}. \tag{3.16}$$

This means that for large n and small $|\Delta\tau|$, changes in the pulse shape are negligible.

[16] We remind the reader that physically the feedback delay time cannot be negative, however mathematically this is fine and the total delay time, $T + \tau$, is still positive. We use this delay range as it is useful to characterise the solutions in terms of the zeroth main resonance.

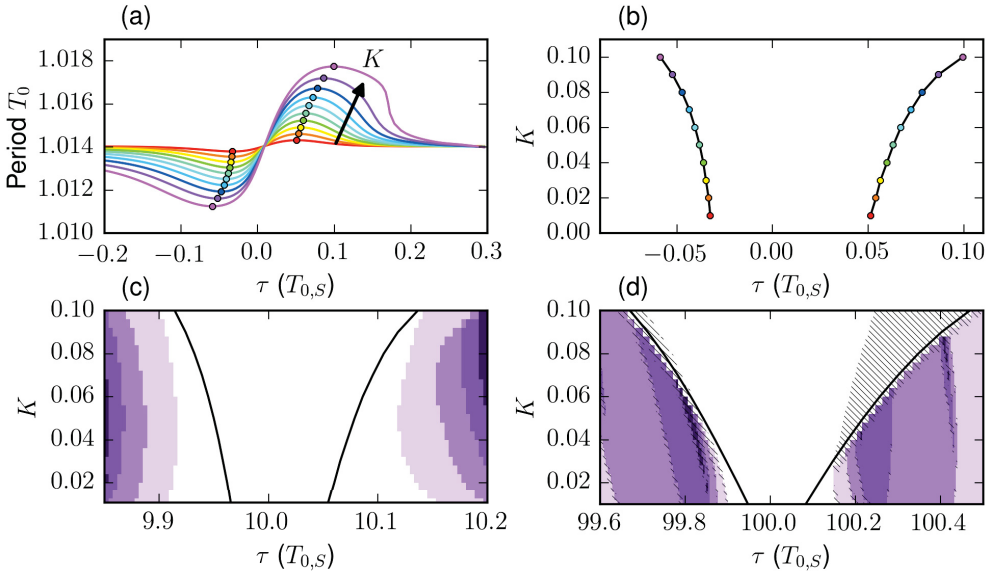

Figure 3.62.: **Low feedback strength regime:** (a) Period of the mode-locked solutions as a function of the feedback delay time for feedback strengths from $K = 0.01$ to $K = 0.1$. (b) Points defining the main resonance locking region, obtained from minima and maxima in the period plotted in (a). (c)-(d) Maps of the dynamics in the τ-K plane near the 10^{th} and 100^{th} main resonances. The colour code of the map is the same as in Fig. 3.56. The black lines indicate the main resonance locking regions obtained from Eqs. (3.17)-(3.18). The hatching in (c) indicates regions of bistability between single-pulse and multi-pulse solutions. Parameters: all other parameters as in Table 2.1.

Low feedback strength regime

Figure 3.60 shows results for $K = 0.1$, which is in the low feedback strength regime. In this regime all solutions in the range from $\tau = 0$ to $\tau = T_{0,K}$ are periodic. This means that not only the solutions in the main resonance locking regions repeat at larger feedback delay times, but all solutions that are found in this delay range. Hence, all solution shown in Fig. 3.60a can be mapped on to Fig. 3.60b-c by added $10T_0$ and $100T_0$, respectively, to the delay times given in (a). Comparing (a), (b) and (c), the shape of the line that is plotted becomes distorted due to the difference in the period of the solutions. This is illustrated clearly by the open coloured circles. Each circle of the same colour corresponds to the same solution repeated for different n. Because the period of the solution marked by the red circles is smaller than the period marked by the green circles, these solutions move further apart in τ space as n is increased. Hence, the locking regions become wider.

All of the solutions for the delay range shown in Fig. 3.60a are stable. However as n is increased saddle-node bifurcations develop at solutions which correspond to

local minima and maxima in the period, for example at the edges of the main resonance locking regions (open red and green circles). In Fig. 3.60c the saddle-node bifurcations bordering the main resonance regions are indicated by the large filled green circles. Within the locking regions, main and higher-order, the solutions remain stable. But between locking regions there are unstable solutions where the branch has folded over. These folds in the branch of solutions lead to regions of bistability between fundamentally mode-locked solutions and solutions with multiple feedback induced pulses, as was previously shown in Fig. 3.56. These stable solutions are connected by sections of unstable solutions, which are indicated in Fig. 3.60c by the red parts of the curve.

For the low feedback strength regime, because the solutions in the locking regions remain stable, the main resonance locking range is characterised by the solutions with the minimum (open red circles) and maximum (open green circles) periods. In Fig. 3.62a the period of solutions near the zeroth main resonance is plotted for low feedback strengths ranging from $K = 0.01$ to $K = 0.1$. The coloured circles are plotted at the minima and maxima in the period and define the locking ranges for the various feedback strengths. The resulting locking cone is plotted in the τ-K plane in Fig. 3.62b. These results show that the width of the locking region increases with K, as does the feedback delay induced change in the period. The width of the locking cone does not converge to zero as K tends to zero. This is due to the finite width of the pulses. For higher main resonances the locking regions can be obtained from the information in Fig. 3.62a-b. Let $T_0^{\min}$ and $T_0^{\max}$ be the K dependent minimum and maximum periods in Fig. 3.62a, and $\tau_0^{\min}$ and $\tau_0^{\max}$ the K dependent feedback delay times of these solutions. Then, the edges of the locking regions for all other main resonance are given by

$$\tau^{\min} = \tau_0^{\min} + nT_0^{\min} \tag{3.17}$$

and

$$\tau^{\max} = \tau_0^{\max} + nT_0^{\max}. \tag{3.18}$$

The black lines in Fig. 3.62c-d show the resulting locking cones for the 10^{th} and 100^{th} main resonance, respectively. In Fig. 3.62d the hatched region indicates the region of bistability with the multi-pulse dynamics.

The locking ranges extend to further positive offsets from the main resonances than they do to negative offsets, i.e. $|\tau^{\max} - T_{0,K}| > |\tau^{\min} - T_{0,K}|$, as can be seen in Fig. 3.62. This is due to the asymmetry of the pulses and the net gain window. The pulse shape change within the locking regions, for $K = 0.1$, is illustrated in Fig. 3.63. Near the edges of the locking region the pulses become highly asymmetric and develop plateaus in the amplitude to one side of the pulse. For positive offsets from the main resonance the side plateau has a higher amplitude, this is due to the higher net gain at the trailing edge of the pulse compared with the leading

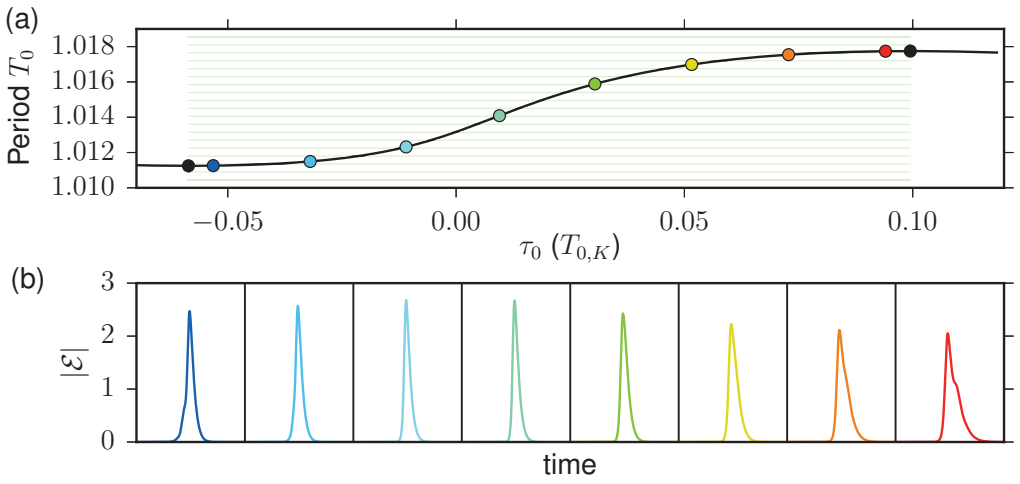

Figure 3.63.: **Low feedback strength regime:** Pulse amplitude profiles for feedback delay times spanning the main resonance locking regions for $K = 0.1$. In (a) the period is shown in dependence of the delay offset τ_0 from the zeroth main resonance. In (b) pulse profiles, corresponding to the τ_0 values of the coloured circles in (a), are shown. The profiles each span over one period. The black circles in (a) mark the edges of the locking region. Parameters: all other parameters as in Table 2.1.

edge (see Fig. 3.14). The higher net gain at the trailing edge is also why the pulses can adapt better to positive delay offset and hence why the locking regions extend further in this direction. Near the edges of the locking regions the pulses become more deformed, this is because the system cannot sufficiently adapt the period of the solutions to compensate for the delay offset. As will be discussed further in Chapter 4 the shape of the pulses is related to the timing jitter; the narrower pulses near the exact main resonances have a lower timing jitter than the wider pulses towards to edge of the locking regions.

Intermediate feedback strength regime

Examples of the feedback delay induced period change, in the intermediate feedback strength regime, are shown in Figs. 3.64-3.65. This regime is qualitatively different to the low feedback strength regime because for sufficiently large offsets from the main resonances the mode-locked solutions can lose their stability in torus bifurcations. For $K = 0.2$ the period of the mode-locked solutions is shown as a function of the feedback delay time in Fig. 3.64. In the short (a) and intermediate (b) delay regimes the stability of the solutions has been calculated using DDE-BIFTOOL [ENG01]. Stable solution segments are plotted with a solid line and unstable segments with a dashed line. The stable section of the solutions is bounded by torus

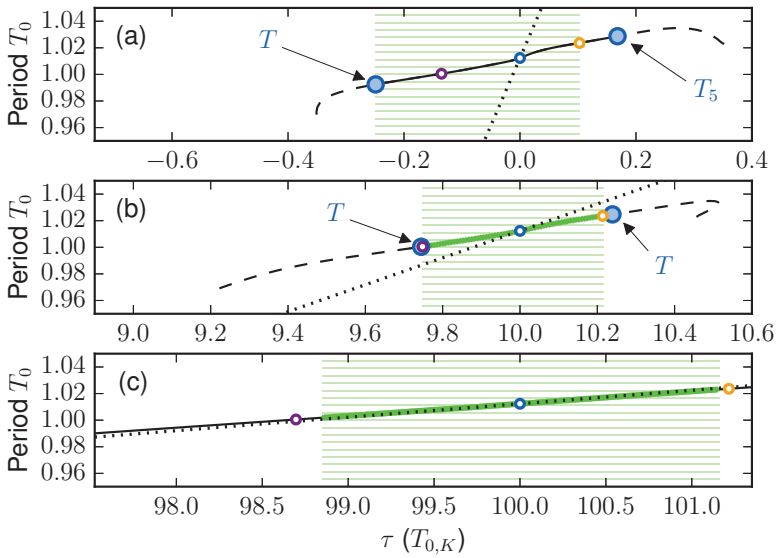

Figure 3.64.: **Intermediate feedback strength regime:** Period of the mode-locked solutions as a function of the feedback delay time in the regime of intermediate feedback strengths. In (a) and (b) the solid (stable) and dashed (unstable) segment indicate the stability of the solutions and the large filled blue circles indicate torus bifurcations (T). The open blue circles indicate the main resonances in (a), (b) and (c). The purple (orange) circles are the same solutions repeated for $q = 0, 10, 100$. The thick green lines in (b) and (c) indicate the period obtained for stable sections of the solution branch via direct numerical simulation. Parameters: $K = 0.2$, all other parameters as in Table 2.1.

bifurcations, which are indicated by the filled blue circles. For the 100$^{\text{th}}$ resonance (c) the stability has not been calculated due to the high computational cost. In all three subplots the open blue circles indicate the main resonance and the purple (orange) circles indicate repeats of the same solution. The locking ranges are indicated by the green horizontal lines. For 100$^{\text{th}}$ resonance (c) the locking range was determined by direct numerical integration by sweeping the initial conditions up and down from the main resonance, the results of which are plotted in the solid green line. Comparing the positions of the purple and orange circles relative to the locking ranges in the short (a), intermediate (b) and long (c) feedback delay regimes, it is evident that for increasing delay lengths the torus bifurcations shift to solutions with a smaller change in the period. This means that the range over which the period can be tuned (i.e. the frequency pulling range) is reduced. Similar results are seen for higher feedback strengths. In Fig. 3.65 results are shown for $K = 0.4$. In this example the upper limit of the locking regions remains at the same solution, but the shift of the the lower bound is more pronounced. The fact that the upper bound does shift in these examples is related to the K depen-

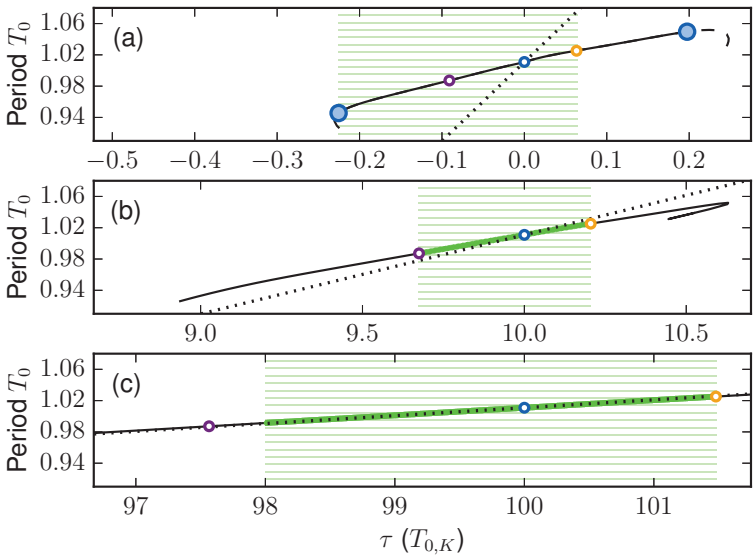

Figure 3.65.: **Intermediate feedback strength regime:** Period of the mode-locked solutions as a function of the feedback delay time in the regime of intermediate feedback strengths. In (a) the solid (stable) and dashed (unstable) segment indicate the stability of the solutions and the large filled blue circles indicate torus bifurcations. The open blue circles indicate the main resonances in (a), (b) and (c). The purple (orange) circles are the same solutions repeated for $q = 0, 10, 100$. The thick green lines in (b) and (c) indicate the period obtained for stable sections of the solution branch via direct numerical simulation. Parameters: $K = 0.4$, all other parameters as in Table 2.1.

dence of this torus bifurcation. For the zeroth main resonance, this is the torus bifurcation labelled T_5 in Fig. 3.35. For larger K values this bifurcation occurs at greater offsets from the main resonance and is separated from the locking region by a parameter range where two-pulse dynamics are exhibited (also see Fig. 3.39). Because the stability of solutions changes in dependence of n, in the intermediate feedback strength regime the locking region cannot be defined as it was for the low feedback strength regime.

For intermediate feedback strengths the pulses become more deformed near the edges of the locking regions compared with low feedback strengths. An example of the pulse shape variation is shown for $K = 0.4$ in Fig. 3.66. These pulse profiles correspond to points on the solution branch in Fig. 3.65a. The yellow to red pulses are not within the locking regions as these pulses have two peaks. In the maps of the dynamics shown earlier, this pulses correspond to the two-pulse region to the right of the main resonances (for example, see Figs. 3.30, 3.52 and 3.56).

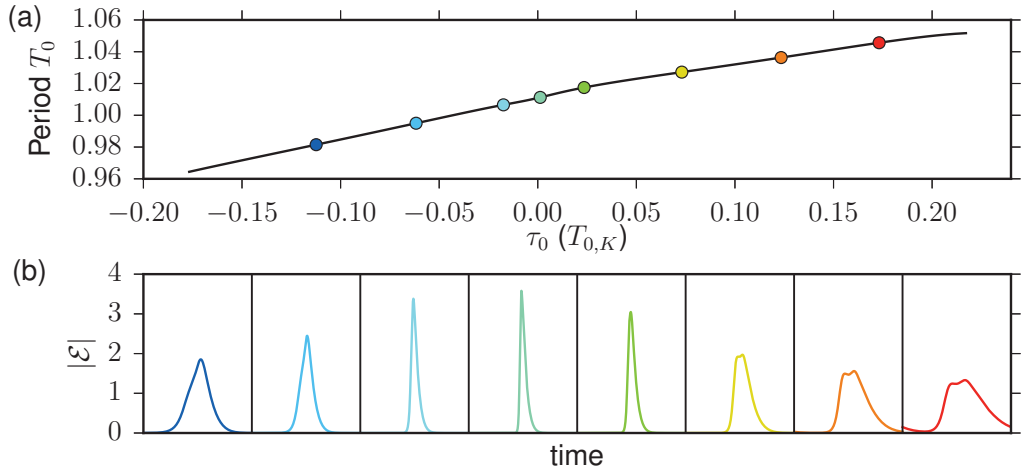

Figure 3.66.: **Intermediate feedback strength regime:** Pulse amplitude profiles for feedback delay times spanning the main resonance locking regions for $K = 0.4$. In (a) the period is shown in dependence of the delay offset τ_0 from the zeroth main resonance. In (b) pulse profiles, corresponding to the τ_0 values of the coloured circles in (a), are shown. The profiles each span over one period. Parameters: all other parameters as in Table 2.1.

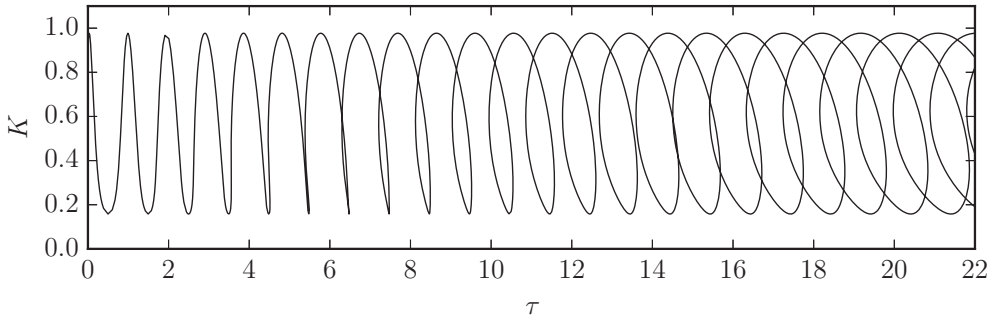

Figure 3.67.: H_1 Hopf bifurcation in the τ-K parameter plane. Parameters: all other parameters as in Table 2.1.

Feedback delay induced multistability

The locking ranges in subplot (c) of Figs. 3.64-3.65 span over more than one main resonance, and the results in the low feedback strength regime (Fig. 3.62) indicate that for longer delay times the locking regions will also span over multiple main resonances. This means that there are feedback regimes where there is multistability between solutions that are locked to neighbouring resonances. Figure 3.67 shows the H_1 Hopf-bifurcations curve in the τ-K plane. As τ is increased the curve

forms loops, which leads to a coexistence between solutions generated at different points on the curve. Form this curve the degree of multistability cannot be estimated without further information about the stability of the periodic solutions that are generated. However, in the low feedback strength regime the degree of multistability can be worked out directly from the locking cone that is defined by Eqs. (3.17)-(3.18). It can be estimated by

$$M \approx \left(\tau^{\max} - \tau^{\min}\right) \bmod T_{0,K} \approx \left(n\left(T_0^{\max} - T_0^{\min}\right)\right) \bmod T_{0,K}, \tag{3.19}$$

where M is the degree of multistability and mod stands for the modulus. Since the locking regions become wider for increasing feedback strength, this also gives a lower bound for the degree of multistability in the intermediate feedback strength regime. In addition to this source of multistability, for long feedback delay times there is also multistability with solutions for which the lasing modes are detuned from the center of the spectral filter. This was shown in Subsection 3.3.3.

For experimental studies the large degree of multistability for long delay times can be problematic, since it can be difficult to ensure that the system exhibits the desired dynamics. Furthermore, in case where solutions are close together in the state space of the system, noise can induce switching between solutions. In [SOL93] the feedback delay time dependence of a passively mode-locked laser as studied experimentally. In this study abrupt jumps in the repetition rate of the mode-locked solutions were observed when the delay time (i.e. the length of the external cavity) was varied over one period of the mode-locked dynamics, corresponding to jumps between solutions which are locked to different main resonances.

3.4. Dynamics induced by feedback from two external cavities

As mentioned in the introduction, one motivation for adding a second feedback cavity is that it can be used to suppress undesired noise effects. This will be investigated in Chapter 5. A second motivation has to do with the frequency pulling effects that were discussed in the previous section. The repetition rate of a monolithic passively mode-locked semiconductor laser is primarily determined by the length of the laser, however small variations between devices limits the reproducibility of precise repetition rates. For example, cleaving tolerances can lead to repetition rate variations of the order of 100 MHz [HAB14]. The results of the previous section, as well as experimental results for semiconductor quantum-well and quantum-dot based devices [SOL93, MER09, GRI09, BRE10, LIN10e, FIO11, LIN11d, ARS13], show that with feedback from one external cavity the period (or repetition frequency) of the mode-locked solutions can be tuned by varying the feedback delay time within the locking regions. However, when the delay times are long the variation in the period is small and there is a large degree of multistability between different fundamentally mode-locked solutions. By adding a second feedback cavity, one has an additional control parameter. This can have positive or negative effects, as will be shown in this section. We will first investigate the dynamics that can arise for the system coupled to two external feedback cavities. Then we will study the frequency pulling in the main resonance regions.

Parts of this section are published in [JAU15a], [JAU16] and [NIK16].

3.4.1. Feedback induced dynamics

Feedback delay and feedback strength dependence

With feedback from two external cavities the equation for the slowly varying electric field amplitude (Eq.(2.42)) becomes

$$\begin{aligned}\frac{d\mathcal{E}}{dt} &= -\gamma\mathcal{E}(t) + \gamma R(t-T)\, e^{-i\Delta\Omega T}\mathcal{E}(t-T) \\ &+\gamma K_1 e^{iC_1} R(t-T-\tau_1)\, e^{-i\Delta\Omega(T+\tau_1)}\mathcal{E}(t-T-\tau_1) \\ &+\gamma K_2 e^{iC_2} R(t-T-\tau_2)\, e^{-i\Delta\Omega(T+\tau_2)}\mathcal{E}(t-T-\tau_2)\,. \end{aligned} \tag{3.20}$$

The second external cavity adds an extra delay time, τ_2, to the system, which is subject to the same resonance conditions as the first (Eq.(3.9)). For resonant feedback both feedback delay times must fulfil the resonance condition, meaning that

$$\tau_1 = \frac{q_1}{p_1}T_0 \quad \text{and} \quad \tau_2 = \frac{q_2}{p_2}T_0 \quad \text{for} \quad p_1, p_2, q_1, q_2 \in \mathbb{N}. \tag{3.21}$$

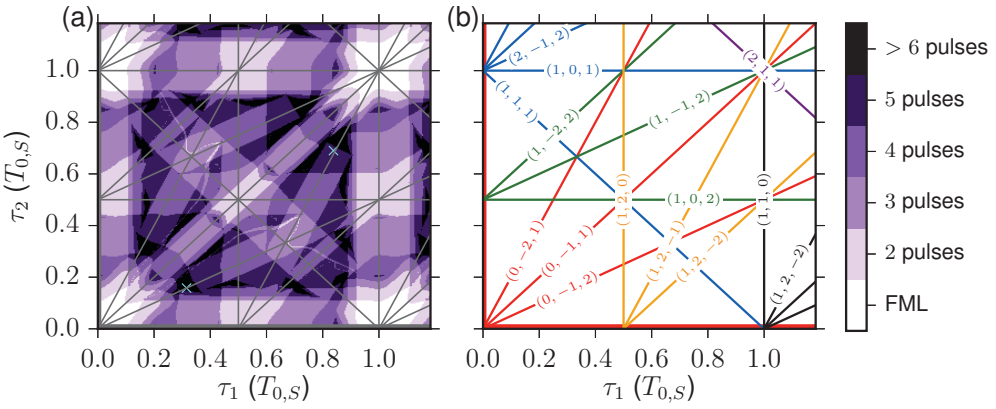

Figure 3.68.: (a) Map of the dynamics in dependence of τ_1 and τ_2 for $K_1 = 0.05$ and $K_2 = 0.05$. The feedback delay times are plotted in units of the period for $K = 0$, $T_{0,S} = 1.014$. The colour code indicates the number of pulses in the laser cavity and the type of dynamics that are exhibited. White indicates fundamental mode-locking (FML), purples indicate fundamental mode-locking with feedback induced pulses. The grey lines correspond to the resonance lines defined by Eq. (3.25). (b) Resonances lines, defined by Eq. (3.25), along which features can be identified in (a). Parameters: all other parameters as in Table 2.1.

In this case the number of pulses in the laser cavity is determined by a combination of p_1 and p_2. If $p_1 = p_2 = 1$ then main resonant feedback conditions are met and there is one pulse in the laser cavity that is perfectly synchronised at the out-coupling facet with pulses from both feedback cavities. For higher order resonant feedback, i.e. $p_1 > 1$ or $p_2 > 1$, the number of pulses in the laser cavity is determined by the lowest common multiple of p_1 and p_2. However, the maximum number of pulses is again restricted by the ratio of the pulse width to the cold cavity roundtrip time.

In Fig. 3.68a a map of the dynamics in the τ_1-τ_2 plane is shown. These results are obtained via direct numerical integration of the DDE system (Eq. (3.20) and Eqs. (2.43)-(2.44)) and regions are colour-coded according to the number of pulses (or electric field maxima) in the laser cavity. The feedback parameters are chosen in the short delay and low feedback strength regimes ($K_1 = 0.05$ and $K_2 = 0.05$). Regions of fundamental mode-locking, with one pulse in the laser cavity, are found near main resonances which are located at (0,0), (0,1), (1,0) and (1,1), in the coordinates of this map.[17] As in the single feedback cavity case, between the main resonance regions dynamics with multiple feedback induced pulses are exhibited (compare with Fig. 3.30). However, compared with single cavity feedback, different

[17] The exact positions of the main resonances is actually slightly shifted from the integer values in the map shown in Fig. 3.68a. This because in this map the delay times are given in units of $T_{0,S} = 1.01405$, not $T_{0,K} = 1.01318$.

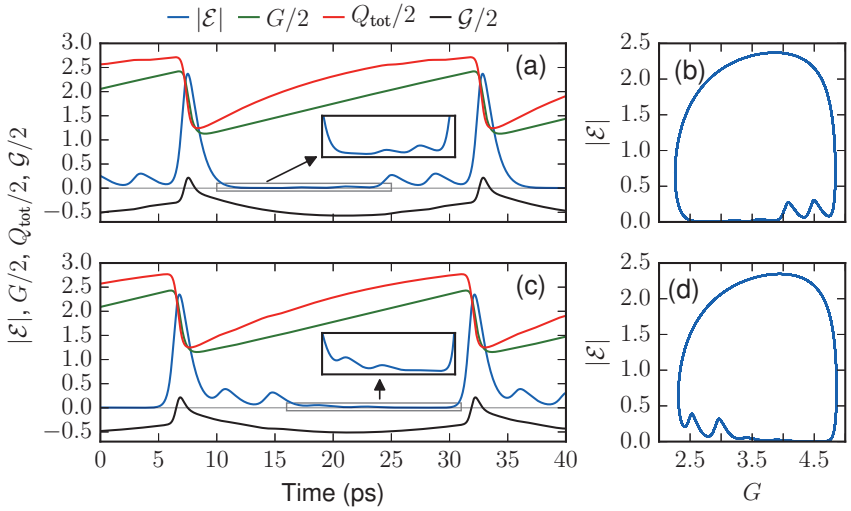

Figure 3.69.: Time traces and phase space portraits of the feedback induced dynamics for (a)-(b) $\tau_1 = 0.85$, $\tau_2 = 0.7$ and (c)-(d) $\tau_1 = 0.32$, $\tau_2 = 0.16$. The time traces (a) and (c) show the electric field amplitude $|\mathcal{E}|$ (blue), gain G (green), total losses $Q_{\text{tot}} = Q - \ln(\kappa)$ (red) and the net gain $\mathcal{G} = G - Q_{\text{tot}}$ (black). The phase space portraits (b) and (d) show the dynamics in the $G - |\mathcal{E}|$ plane. The feedback delay times correspond to the positions of the green crosses in Fig. 3.68a. Parameters: $K_1 = 0.05$, $K_2 = 0.05$, all other parameters as in Table 2.1.

multi-pulse dynamics can be exhibited. Examples of time traces for two delay configurations, corresponding to the positions of the green crosses in Fig. 3.68a, are shown in Fig. 3.69. In both examples there are multiple feedback induced pulses. Because the two delay times are not synchronised with each other, feedback from the two cavities induces pairs of satellite pulses which approximately have the same amplitude. In the dual feedback cavity case two satellite pulses can have similar heights, because they can both be seeded by the main pulse, which cannot happen for single cavity feedback. For single cavity feedback with the same total feedback strength, and for the same laser parameters, the maximum number of feedback induced pulses was $p - 1 = 4$. In the dual feedback case more pulses can be induced because the system cannot adapt as easily to achieve locking to low-order resonances when there are two external delay times which are not equal.

The main and higher order resonances in Fig. 3.68a form a resonance structure which is emphasised by the grey lines. These lines connect various main and higher order resonances and are determined by the three characteristic times of this system; T_0, τ_1 and τ_2. A similar resonance pattern has been found in systems of two coupled oscillators with self-feedback [ZIG09, PAN12]. In these systems the coupling delay time and the two feedback delay times define the resonance structure. Following the analysis presented in [PAN12], the relation between T_0, τ_1 and τ_2,

which defines the resonance lines can be derived. If a pulse is coupled into feedback cavity one at time t, and the period is T_0, then at time $t + \tilde{n}\tau_1$ this pulse will coincide with the laser-cavity pulse if

$$l_1 T_0 = \tilde{n}\tau_1, \tag{3.22}$$

for integer $\tilde{n}$ and l_1. The same is true for the second feedback cavity, i.e.

$$l_2 T_0 = \tilde{m}\tau_2, \tag{3.23}$$

for integer $\tilde{m}$ and l_2. For resonant feedback, main or higher order, both of these conditions must be fulfilled simultaneously. Therefore

$$(l_1 + l_2)\, T_0 = \tilde{n}\tau_1 + \tilde{m}\tau_2, \tag{3.24}$$

must hold. This equation is obtained by adding Eqs. (3.22) and (3.23), however the resonance conditions could also have been combined by subtracting these expressions. Taking both of these combinations of the individual resonance conditions into account, the relation

$$l T_0 = n\tau_1 + m\tau_2, \tag{3.25}$$

is obtained, where l, n and m are now positive or negative integers. This is the same relation that is obtained in the case of coupled oscillators, however with T_0 replacing the coupling delay time. In both cases it is the presence of three delay times that leads to this resonance behaviour.

In Fig. 3.68b the resonance lines defined by Eq. 3.25 are labelled according to (l, n, m). The lines for which resonance features can be identified correspond to $|n|, |m| = 0, 1, 2$, i.e. values for which the out-coupled pulses meet the main pulse in the laser cavity after at most two roundtrips. The line $(0, -1, 1)$ is the delay configuration in which $\tau_1 = \tau_2$. Along this line the dual feedback cavity system reduces to the single feedback cavity case. This resonance line is prominent as the pulses in the two feedback cavities are synchronised. The $(1, 1, 1)$ line is also very prominent. This is because along this line the sum of the two delay times is always equal to T_0, which means that out-coupled pulses only have to travel once around each feedback cavity before meeting the main pulse again at the coupling facet. The resonance lines for $(l, 1, 0)$ and $(l, 0, 1)$ are the most pronounced, as along these lines either τ_1 or τ_2 is exactly resonant with T_0. We will see in the next chapter that it is along the prominent resonance lines that the best timing jitter reduction is achieved (see Fig. 4.21).

In [PAN12] resonance features where observed in the period of the coupled oscillators. In the mode-locked laser system features along the resonance lines can also be observed in the period. This is shown in Fig. 3.70. Along the $(0, -1, 1)$ line ($\tau_1 = \tau_2$) the period varies as shown in Fig. 3.60. Whereas along the $(1, 1, 1)$ line the period is nearly constant. When one of the two feedback delay times is resonant, then the second has only a small affect on the period.

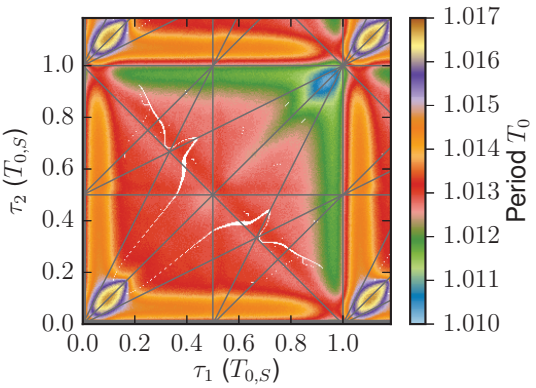

Figure 3.70.: The period of mode-locked solutions in dependence of τ_1 and τ_2 for $K_1 = 0.05$ and $K_2 = 0.05$. The feedback delay time is plotted in units of the period for $K = 0$, $T_{0,S} = 1.014$. Parameters: all other parameters as in Table 2.1.

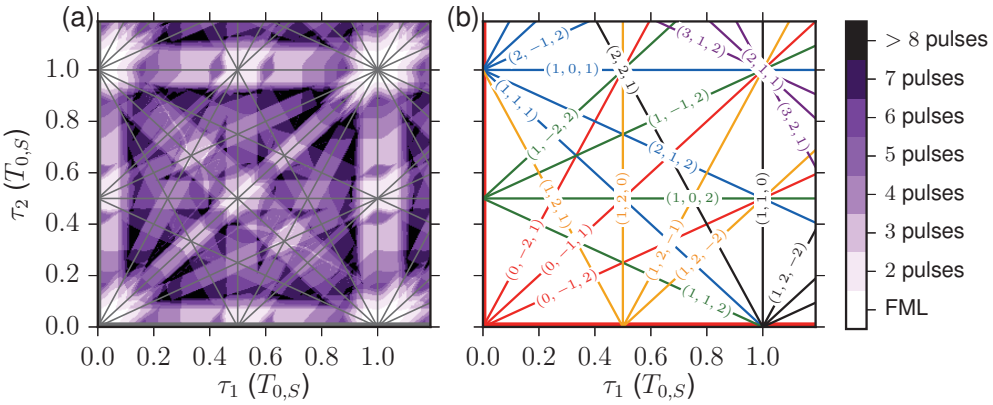

Figure 3.71.: **Influence of the spectral filter width:** (a) Map of the dynamics in dependence of τ_1 and τ_2 for $K_1 = 0.05$ and $K_2 = 0.05$ with $\gamma = 100$. The feedback delay times are plotted in units of the period for $K = 0$, $T_{0,S} = 1.014$. The colour code indicates the number of pulses in the laser cavity and the type of dynamics that are exhibited. White indicates fundamental mode-locking (FML), purples indicate fundamental mode-locking with feedback induced pulses. The grey lines correspond to the resonance lines defined by Eq. (3.25). (b) Resonances lines, defined by Eq. (3.25), along which features can be identified in (a). Parameters: all other parameters as in Table 2.1.

Influence of the pulse width

As in the single feedback cavity case, the width of the resonances and the maximum number of feedback induced pulses is related to the width of the main pulse. This can be seen by comparing Figs. 3.68 and 3.71. In Fig. 3.71 the spectral filter width has been increased to $\gamma = 100$, hence the pulses are narrower (see Fig. 3.15 for the

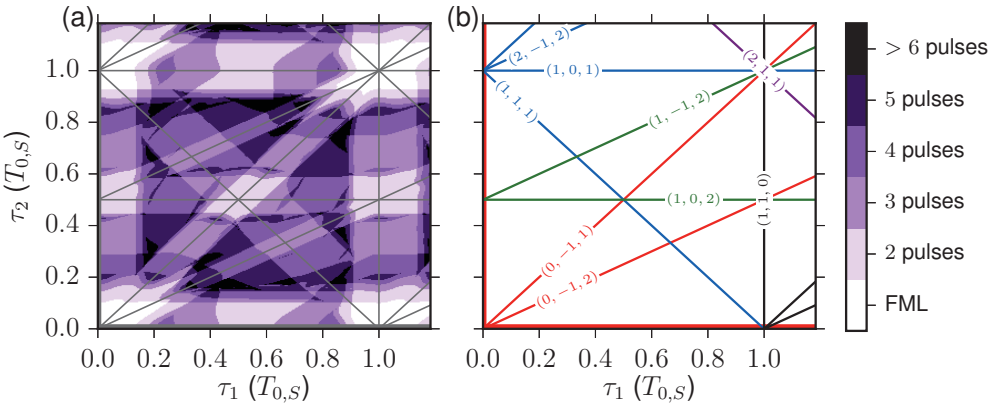

Figure 3.72.: **Influence of the feedback strength ratio:** (a) Map of the dynamics in dependence of τ_1 and τ_2 for $K_1 = 0.02$ and $K_2 = 0.08$. The feedback delay times are plotted in units of the period for $K = 0$, $T_{0,S} = 1.014$. The colour code indicates the number of pulses in the laser cavity and the type of dynamics that are exhibited. White indicates fundamental mode-locking (FML), purples indicate fundamental mode-locking with feedback induced pulses. The grey lines correspond to the resonance lines defined by Eq. (3.25). (b) Resonances lines, defined by Eq. (3.25), along which features can be identified in (a). Parameters: all other parameters as in Table 2.1.

influence of the filter width on the pulses). In this case features along resonance lines that were not present in Fig. 3.68 can be identified. For example along the line $(1, 2, 1)$, for which $2\tau_1 + \tau_2 = T_0$. The line with the opposite slope, $(1, 2, -1)$ is more pronounced and was also present in Fig. 3.68.

Influence of the feedback strength ratio

The relative feedback strengths also influence the resonance patterns. In Fig. 3.68 the feedback contributions from the two external cavities is equal, therefore the resonance patterns are symmetric about $(0, -1, 1)$. If the relative feedback strengths are varied, but the total $K_{\mathrm{TOT}} = K_1 + K_2$ is kept the same, then the solutions along $(0, -1, 1)$ remain unchanged, but are changed for other delay configurations. The invariance of the solutions along $(0, -1, 1)$, with respect to the ratio of K_1 and K_2, is due to the pulses from the two feedback cavities being perfectly synchronised, which means that the contributions are indistinguishable from the single feedback cavity case with $K = K_{\mathrm{TOT}}$. Figure 3.72 shows an example of the dynamics for $K_1 = 0.02$ and $K_2 = 0.08$. Because the feedback strength from cavity two is much greater than from cavity one, resonance features for $n = 2$ are no longer present, but $m = 2$ resonance lines are more pronounced than in Fig. 3.68.

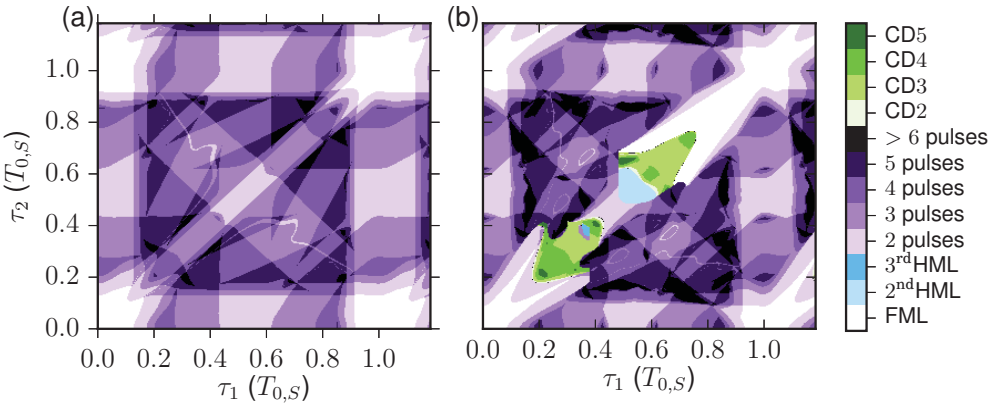

Figure 3.73.: **Influence of the total feedback strength:** Maps of the dynamics in dependence of τ_1 and τ_2 for (a) $K_1 = K_2 = 0.025$ and (b) $K_1 = K_2 = 0.1$. The feedback delay times are plotted in units of the period for $K = 0$, $T_{0,S} = 1.014$. The colour code indicates the number of pulses in the laser cavity and the type of dynamics that are exhibited. White indicates fundamental mode-locking (FML), purples indicate fundamental mode-locking with feedback induced pulses, greens indicate complex dynamics (in this case quasi-periodic) with 2-5 pulses in the laser cavity (CD2-CD5) and blues indicate harmonic mode-locking (HML). Parameters: all other parameters as in Table 2.1.

Influence of the total feedback strength

The dependence of the solutions on the total feedback strength is similar to the single feedback cavity case. For low feedback strengths the system exhibits only periodic dynamics with the fundamental periodicity of the laser cavity and, depending on the delay times, feedback induced satellite pulses can be present. If the feedback strengths are increased the system can exhibit quasi-periodic dynamics or harmonic mode-locking. Figure 3.73a-b shows maps of the dynamics for $K_1 = K_2 = 0.025$ and $K_1 = K_2 = 0.1$, respectively. In Fig. 3.73b quasi-periodic dynamics and harmonic mode-locking occur along $\tau_1 = \tau_2$, but no where else in the map. This can be understood by considering that the onset of such dynamics occurs when the fed-back pulses are large enough to cause gain competition with the main pulse in the laser cavity. When the pulses from the two feedback cavities are synchronised then the pulses which are fed-back into the laser cavity are larger than if they enter individually. Therefore, with dual cavity feedback the onset of quasi-periodic dynamics and harmonic mode-locking depends strongly on the combination of the delay times. If the total feedback strength is increased further then quasi-periodic dynamics appear first at resonant delay values where p_1 and p_2 have a low common multiple.

The presence of a second feedback cavity can also have a stabilising effect on the dynamics. In Fig. 3.74a-b a time trace and a phase-space portrait projected

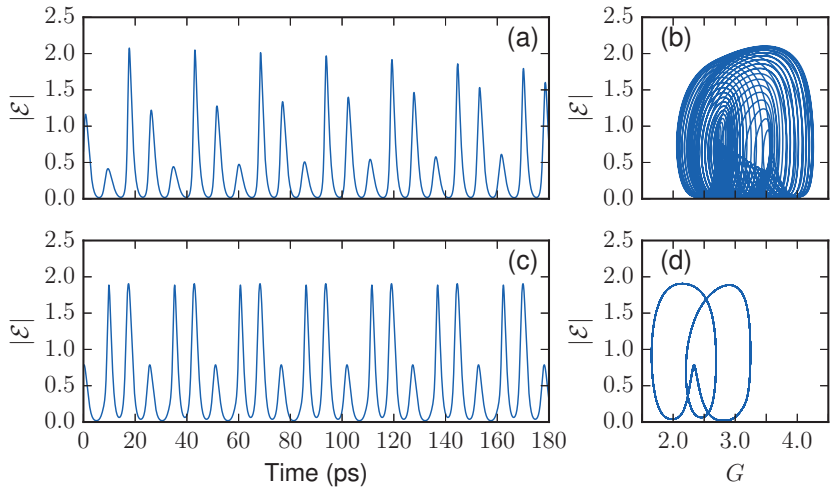

Figure 3.74.: (a)-(b) Time traces and phase space portraits of the electric field amplitude $|\mathcal{E}|$ for single cavity feedback, with $\tau = 0.325T_{0,S}$ and $K = 0.2$. (c)-(d) Time traces and phase space portraits of the electric field amplitude $|\mathcal{E}|$ for dual cavity feedback, with $\tau_1 = T_{0,S}$, $\tau_2 = 0.325T_{0,S}$ and $K_1 = K_2 = 0.2$. The phase space portraits, (b) and (d), show the dynamics projected on to the $G - |\mathcal{E}|$ plane. Parameters: all other parameters as in Table 2.1.

onto the $|\mathcal{E}|$-G plane are shown for feedback from a single external cavity with $K = 0.2$ and $\tau = 0.325T_{0,S}$. Under these feedback conditions the system exhibits quasi-periodic dynamics with three competing pulse trains. If a second feedback cavity is added, with the same feedback strength, but with the delay time chosen resonant with $T_{0,S}$, then periodic dynamics can be stabilised. Figure 3.74c-d shows the corresponding results for this feedback scenario. Due to the added resonant feedback, the main pulse effectively has reduced losses, meaning that the pulse which is coupled in non-resonantly is no longer large enough to cause gain competition. Instead, because the losses are reduced, the gain is now sufficient to sustain multiple pulses, but these have unequal heights.

Long delay regime

So far we have concentrated on the short delay regime. For increasing feedback delay times there are again similarities with the single feedback cavity case; the main and higher-order locking regions become wider and regions of multi-stability between single and multi-pulse dynamics develop. This can be seen in Fig. 3.75a-b, in which maps of the dynamics are shown for $\tau_1 \approx 100$, $\tau_2 \approx 100$ and $K_1 = K_2 = 0.05$. These maps are obtain for (a) up- and (b) down-sweeps in τ_2. The regions where different solutions are found for the two sweep directions are indicated by the hatching. The grey lines are resonance lines defined by Eq. (3.25). The lines

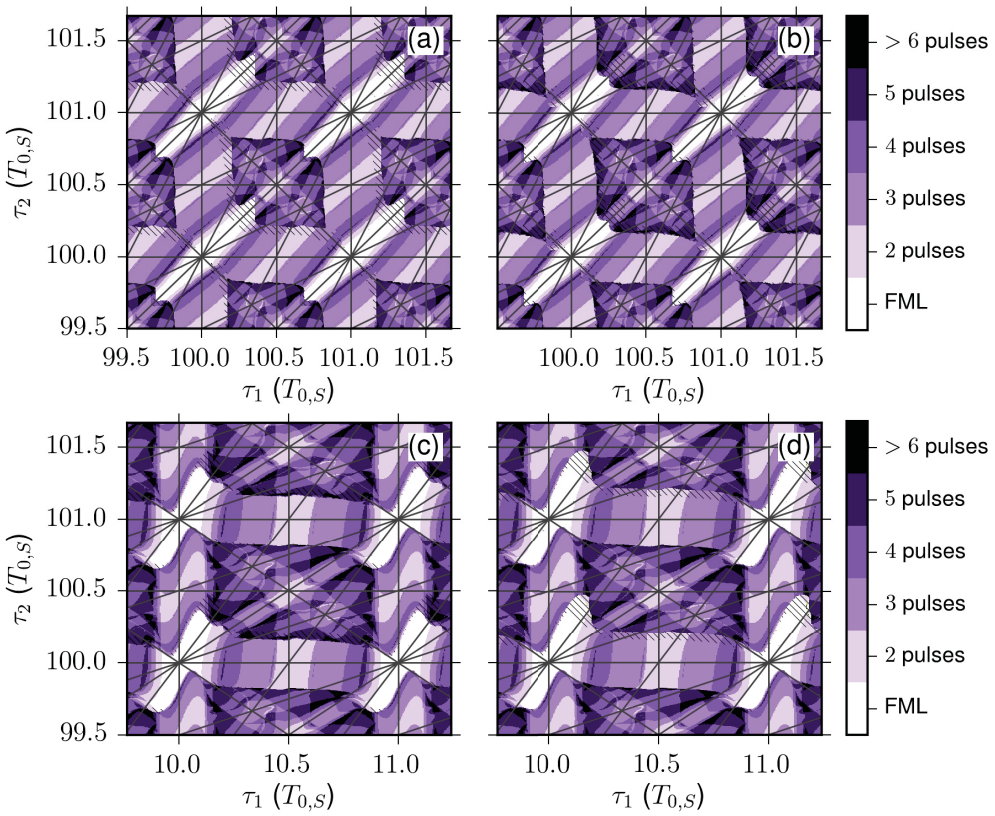

Figure 3.75.: **Long delay regime:** Map of the dynamics in dependence of τ_1 and τ_2 obtained for (a,c) up- and (b,d) down-sweeps in τ_2. For (c)-(d) τ_1 is in the intermediate delay regime. The feedback delay times are plotted in units of the period for $K = 0$, $T_{0,S} = 1.014$. The colour code indicates the number of pulses in the laser cavity and the type of dynamics that are exhibited. White indicates fundamental mode-locking (FML), purples indicate fundamental mode-locking with feedback induced pulses. Parameters: all other parameters as in Table 2.1.

for which resonance features are present are the same as those in Fig. 3.68, but for higher values of l. The main resonance locking regions (white regions) have a long ($(l, \pm 1, \mp 1)$ lines) and a short axis ($(l, 1, 1)$ lines). The width along the long axis is greater because in this direction pulses from both feedback cavities either arrive too early or too late and the system can adapt its period in the appropriate direction for locking to occur. However, along the short axis the pulses from one cavity arrive too early and from the other too late, meaning that synchronisation cannot occur when the delays deviate much in this direction [JAU16].

Over small feedback delay ranges the dynamics appear to have a $T_{0,K}$ periodicity in τ_1 and τ_2. However comparing the maps in Figs. 3.68 and 3.75 it is evident that the dynamics change over larger delay ranges. This is a consequence of the variation

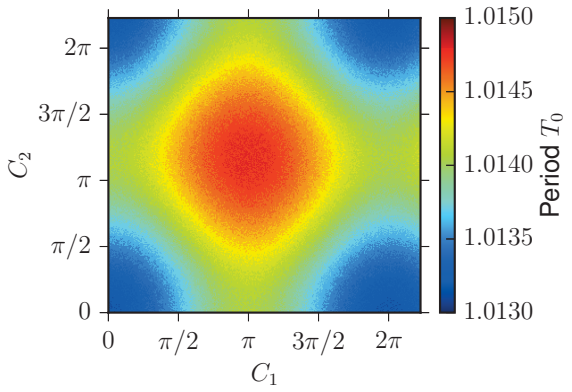

Figure 3.76.: Period of the mode-locked laser output in dependence of the feedback phases C_1 and C_2. Parameters: $\tau_1 = \tau_2 = 0$, $K_1 = K_2 = 0.05$, all other parameters as in Table 2.1.

in the period of the solutions between main resonances. As was described for the single feedback case in Section 3.3.4, periodic solutions repeat for feedback delay times which are increased by integer multiples of the period. Due to the difference in the period of different solutions, they can move further apart in τ_1-τ_2 space as the delays are increased. For example, if two solutions have periods differing by $\Delta\tilde{T}_0$ then their separation in τ_1-τ_2 space grows as $n\Delta\tilde{T}_0$ for integer n. This leads to a deformation of the locking regions when the two feedback delay times are very different, as is shown in Fig. 3.75c-d, where $\tau_1 \approx 10$ and $\tau_2 \approx 100$.

Aspects of the delay dependence of dynamics which have been predicted in this section have been observed experimentally. This is shown in Subsection 4.5.3, where a comparison between simulation results and experimental results for a passively mode-locked laser subject to dual-cavity feedback is presented.

Feedback phase dependence

The results on dual cavity feedback, which have been presented thus far, have been obtained for $C_1 = C_2 = 0$. For single cavity feedback we know that as C is varied the lasing modes shift with respect to the center of the spectral filter such that destructive interference between the pulses in the laser and feedback cavities is minimised (see Section 3.3.1). With dual cavity feedback a stronger dependence on the feedback phases can be expected, since the lasing modes must be resonant with both external cavities if destructive interference is to be minimised.

In Fig. 3.76 the phase dependence is shown for $\tau_1 = \tau_2 = 0$ and $K_1 = K_2 = 0.05$. Depicted is the variation of the period that arises due to the change in the non-resonant losses as the phases are varied. In this example the trends are the same as in the single feedback cavity case, i.e. the feedback phases only influence the

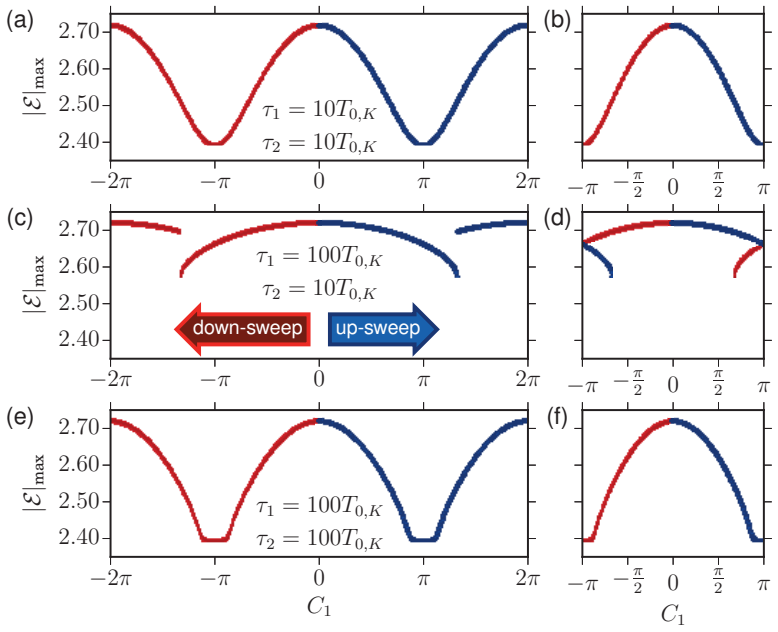

Figure 3.77.: Numerical bifurcation diagrams showing the C_1 dependence of the mode-locked laser output for $C_2 = 0$. Plotted in blue (red) are electric field maxima $|\mathcal{E}|_{\max}$ for an up-sweep (down-sweep) in the initial conditions. In (b), (d) and (f) the phases are shifted into the range $-\pi$ to π. Parameters: $K_1 = K_2 = 0.05$, (a)-(b) $\tau_1 = \tau_2 = 10T_{0,K}$, (c)-(d) $\tau_1 = 100T_{0,K}$ and $\tau_2 = 10T_{0,K}$, (e)-(f) $\tau_1 = \tau_2 = 100T_{0,K}$, all other parameters as in Table 2.1.

total non-resonant losses because the delay times are zero. Because the feedback strengths are low, there is no qualitative dependence on the feedback phases in this example and the fundamentally mode-locked solution remains stable for all C_1 and C_2 values.

For dual cavity feedback, in contrast to the single feedback cavity case, the influence of the feedback phases is not always reduced when the feedback delay times are long. The behaviour is dependent on whether the feedback phases and feedback delay times are equal. If $\tau_1 = \tau_2$ and $C_1 = C_2$, then the system reduces to the single feedback cavity case and the influence of the feedback phases is reduced for longer delay times. However, if $\tau_1 = \tau_2$ but $C_1 \neq C_2$, then the phase dependence does not decrease as the delay lengths are increased. This can be seen by comparing subplots (a) and (e) in Fig. 3.77, which shows results of sweeps in C_1 for $C_2 = 0$. For Fig. 3.77a $\tau_1 = \tau_2 = 10T_{0,K}$ and for Fig. 3.77e $\tau_1 = \tau_2 = 100T_{0,K}$. Despite the difference in the delay lengths, the pulse heights show the same degree of variation over a 2π window in C_1. The reason that the influence of the feedback phases is not reduced for longer feedback delay times when τ_1 and τ_2 are equal is that, although

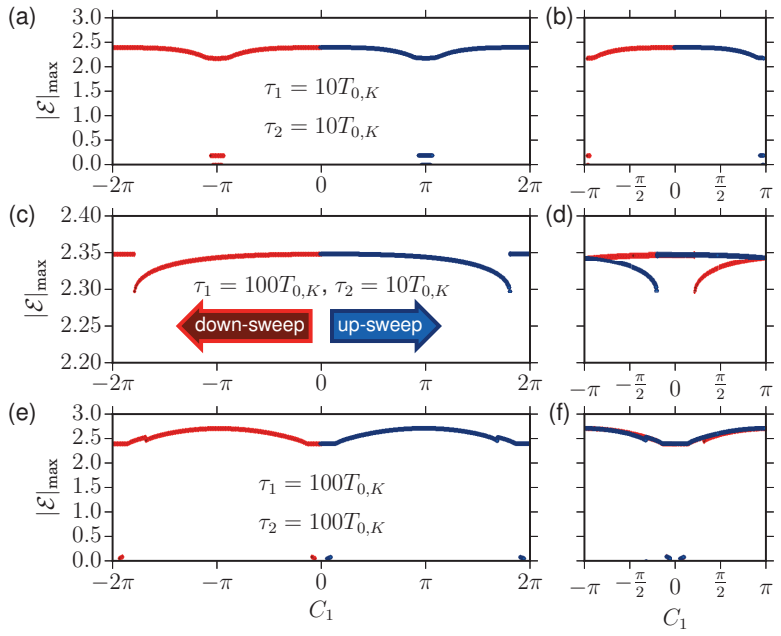

Figure 3.78.: Numerical bifurcation diagrams showing the C_1 dependence of the mode-locked laser output for $C_2 = \pi$. Plotted in blue (red) are electric field maxima $|\mathcal{E}|_{\max}$ for an up-sweep (down-sweep) in the initial conditions. In (b), (d) and (f) the phases are shifted into the range $-\pi$ to π. Parameters: $K_1 = K_2 = 0.05$, (a)-(b) $\tau_1 = \tau_2 = 10T_{0,K}$, (c)-(d) $\tau_1 = 100T_{0,K}$ and $\tau_2 = 10T_{0,K}$, (e)-(f) $\tau_1 = \tau_2 = 100T_{0,K}$, all other parameters as in Table 2.1.

shifts in the frequency of the lasing modes can partially compensate for the phase shift introduced by C_1 and C_2, the phase difference between the feedback cavities is fixed. This means that no matter what the shift of the lasing modes is, the phase difference between the laser cavity and one of the feedback cavities will always be at least $|C_1 - C_2|$, independent of the length of $\tau_1 = \tau_2$. The same trend can be seen in Fig. 3.78 which shows results of sweeps in C_1 for $C_2 = \pi$.

When $\tau_1 \neq \tau_2$, then the phase difference that arises due to shifts in the lasing modes is different for the two feedback cavities, i.e. $\Delta\phi_1 = \omega\tau_1$ and $\Delta\phi_2 = \omega\tau_2$. Therefore, depending on the delay and feedback phase configurations, the system can adapt to effectively reduce the destructive interference between the pulses in the laser and feedback cavities. Examples of this are depicted in Fig. 3.77c and Fig. 3.78c, for which $\tau_1 = 100T_{0,K}$ and $\tau_2 = 10T_{0,K}$. In both of these examples tuning C_1 has a smaller influence on the amplitude of the pulses than for the $\tau_1 = \tau_2 = 10T_{0,K}$ and $\tau_1 = \tau_2 = 100T_{0,K}$ cases.

For the experimental implementation of a dual cavity feedback setup, the sensitivity of the system to the feedback phases is problematic, since to is difficult

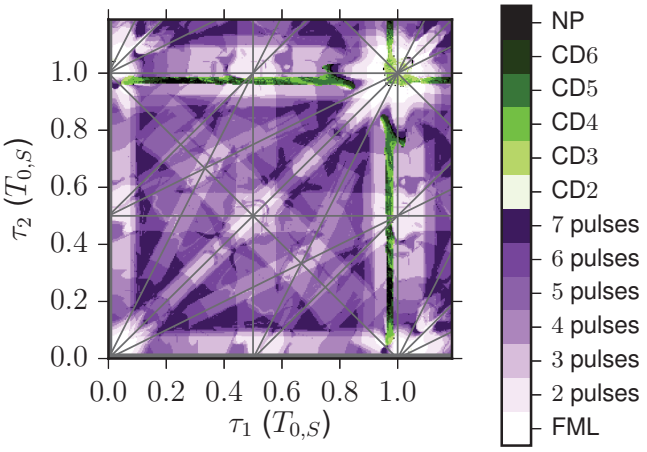

Figure 3.79.: **Influence of amplitude-phase coupling:** Maps of the dynamics in dependence of τ_1 and τ_2 with $\alpha_g = 2$ and $\alpha_q = 1.5$. The feedback delay time is plotted in units of the period for $K = 0$, $T_{0,S} = 1.0102$. The colour code indicates the number of pulses in the laser cavity and the type of dynamics that are exhibited. White indicates fundamental mode-locking (FML), purples indicate fundamental mode-locking with feedback induced pulses, greens indicate complex dynamics (quasi-periodic and chaotic) with 2-5 pulses in the laser cavity (CD2-CD5), blues indicate harmonic mode-locking (HML) and black indicates non-periodic (NP) dynamics that do not fall into the previous categories. The grey lines correspond to the resonance lines defined by Eq. (3.25). Parameters: all other parameters as in Table 2.1.

to set the feedback phases. There have however been experimental realisations of such setups [HAJ12, JAU16, NIK16]. The comparison with experimental results in Subsection 4.5.3, shows that despite the phase sensitivity, it is possible to experimentally obtain mode-locked dynamics over a range of feedback delay times.

Influence of amplitude-phase coupling

As for single cavity feedback, there are two factors that influence the feedback-induced dynamics when amplitude-phase coupling is non-zero. The first is the feedback delay and feedback strength dependent phase difference between the laser and feedback cavities, which was discussed in Subsection 3.3.1. The second is the increased phase sensitivity due to the chirp of the pulses. Figure 3.79 shows an example of the τ_1-τ_2 dependent dynamics for $\alpha_g = 2$ and $\alpha_q = 1.5$. Comparing this figure with Fig. 3.68, the resonance structure is qualitatively the same as in the zero α-factor case. The delay times for which quasi-periodic or chaotic dynamics are exhibited coincide with the single feedback cavity case (see Fig. 3.49).

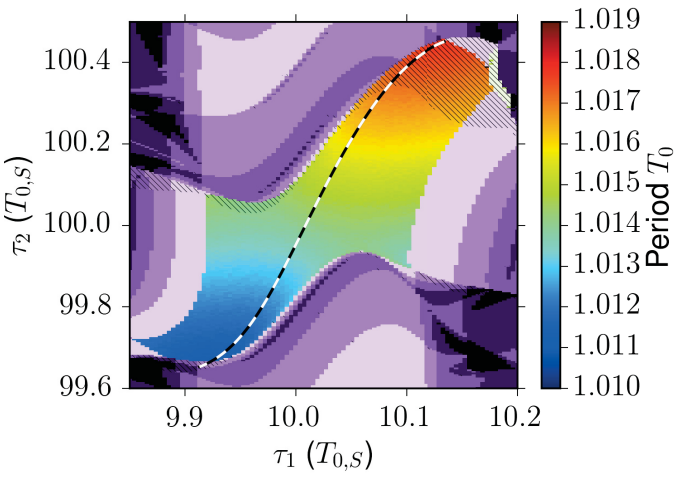

Figure 3.80.: Period of the fundamentally mode-locked single-pulse solutions in the τ_1-τ_2 plane for $K_1 = K_2 = 0.05$. The feedback delay time is plotted in units of the period for $K = 0$, $T_{0,S} = 1.014$. For the regions exhibiting multi-pulse dynamics, the colour code is as in Fig. 3.75. The dashed black and white curve indicates the solutions that are defined by Eq. (3.26). Parameters: all other parameters as in Table 2.1.

3.4.2. Frequency pulling

In this section we shall focus on the main-resonance regions and compare the frequency pulling in the dual feedback case with the single feedback cavity case. The results presented here are for the case $C_1 = C_2 = 0$.

Within the main-resonance locking regions there is a set of solutions that are identical to the solutions for single cavity feedback with the same total feedback strength. This set of solutions can be defined by the solutions in the zeroth-main-resonance locking range for single cavity feedback. As previously defined, we let τ_0 be a delay offset from zero, within the locking range of the zeroth main resonance, and T_0 the period of the corresponding solution (see Section 3.3.4). Then, in the dual feedback case the same solutions are found for

$$\tau_1 = \tau_0 + n_1 T_0 \quad \text{and} \quad \tau_2 = \tau_0 + n_2 T_0, \tag{3.26}$$

for integer n_1 and n_2, if $K = K_1 + K_2$. These solutions are the same in the single and dual feedback cases because regardless of the path taken, the same pulse is coupled into the laser cavity each period.

Low feedback strength regime

In Fig. 3.80 the main resonance region for $\tau_1 = 10T_{0,K}$ and $\tau_1 = 100T_{0,K}$ is shown. The single-pulse region is colour coded according to the period of the solutions.

Outside the single-pulse region the colour code indicates the number of feedback-induced satellite pulses, as in Fig. 3.75. The black and white dashed line is defined by Eq. (3.26), i.e. this is the set of solutions that are identical to those in the main-resonance locking regions of the system with feedback from a single external cavity. In the low feedback strength regime the solutions along this line remain stable as n_1 and n_2 are increased and the maximum frequency pulling range is given by the solutions at either end of this line, i.e. the solutions corresponding to $T_0^{\min}$ and $T_0^{\max}$ as defined for Eqs. (3.17)-(3.18). This is also shown in Fig. 3.81, where the second delay time has been increased to $n_2 = 300$. In Fig. 3.81 results are shown for up- and down-sweeps in τ_2 and for various feedback strength combinations. In each case the total feedback strength is kept the same but the contribution from the two cavities is varied. Despite the change in the relative feedback strengths from the two cavities the locked solutions defined by Eq. (3.26) are the same. This is because the contributions from the feedback cavities are perfectly synchronised, making them indistinguishable from the single-cavity feedback case with $K = K_1 + K_2$. Therefore, in the low feedback strength regime the maximum frequency pulling range is not influence by diverting some of the out-coupled light into a second feedback cavity. However, the addition of a second feedback cavity can lift the multistability between fundamentally mode-locked solutions which are locked to neighbouring main resonances. This can be seen in Fig. 3.81. Projected onto the τ_2 axis the locked solutions defined by the white and black dashed line overlapped, i.e. if $K_2 = K$ and $K_1 = 0$ there would be regions of multistability between these solutions. However, with part of the light also coupled into the second feedback cavity, the requirement that $\tau_1 = \tau_0 + n_1 T_0$ and $\tau_2 = \tau_0 + n_2 T_0$ are both fulfilled means that there is no longer multistability between these solutions when $n_1 \neq n_2$. This can be advantageous for experiments as it reduces the possibility of jumping between different solutions. There are however still regions of bistability with multi-pulse solutions, as indicated by the hatched regions in Fig. 3.81.

Intermediate feedback strength regime

In the intermediate feedback strength regime solutions also repeat according to Eq. (3.26). However, in this case the stability of the solutions changes in dependence of n_1 and n_2. This is because the locking regions are bounded by torus bifurcations, as was shown for single cavity feedback, and as n increases the torus bifurcations occur at smaller $|\tau_0|$ values (see Section 3.3.4). If the total feedback strength is kept the same then the addition of a second shorter feedback cavity can increase the range of stable locked solutions. This is demonstrated in Fig. 3.82, where the locking range is shown as a function of τ_0 for various ratios of the feedback strength with $\tau_1 = 300 T_{0,K}$ and $\tau_2 = T_{0,K}$. The feedback strength ratio is given by k, which is defined as $k = K_1/(K_1 + K_2)$, i.e. $K_1 = kK_{\mathrm{TOT}}$ and

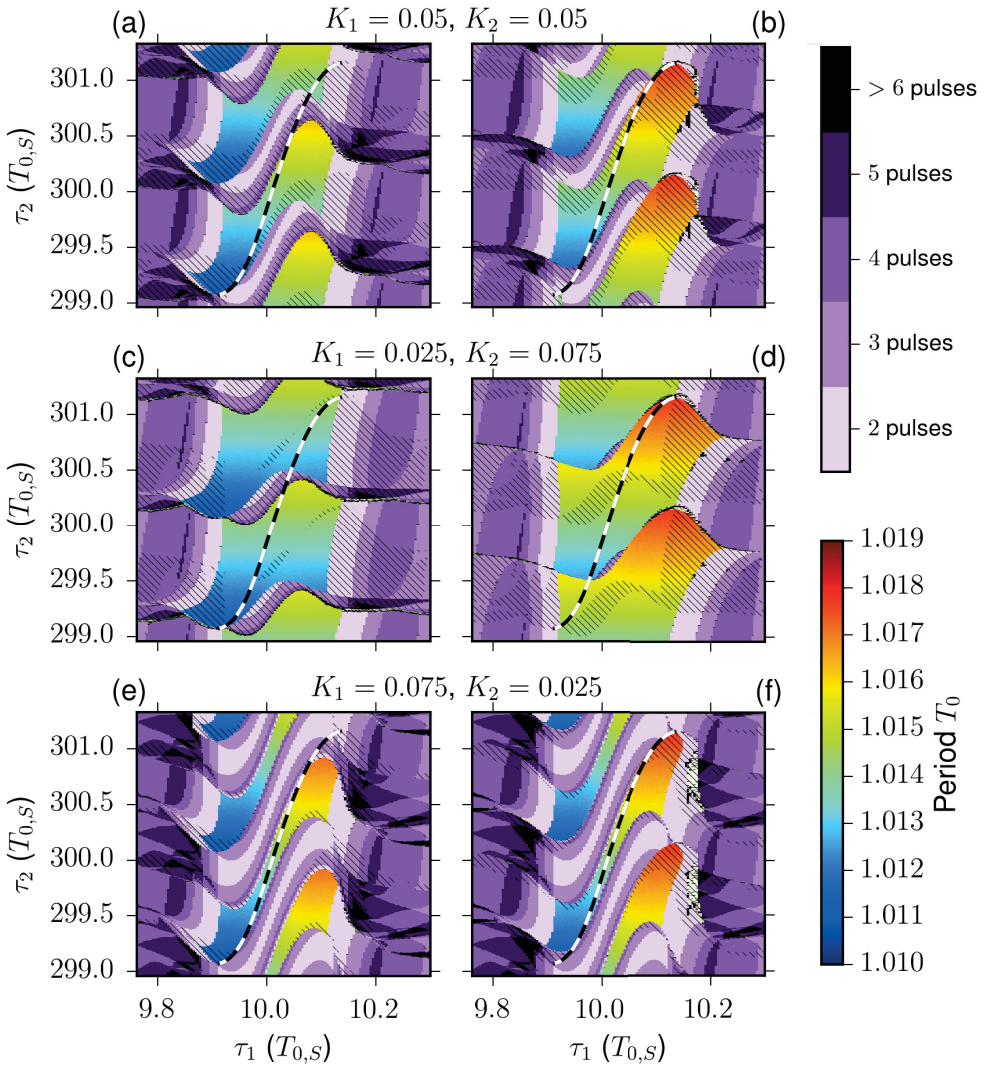

Figure 3.81.: Period of the fundamentally mode-locked single-pulse solutions in the τ_1-τ_2 plane for up- (a,c,e) and down-sweeps (b,d,f) in τ_2, with feedback strengths as indicated in the figure. The feedback delay time is plotted in units of the period for $K = 0$, $T_{0,S} = 1.014$. For the regions exhibiting multi-pulse dynamics, the colour code is as in Fig. 3.75 and the hatching indicates regions where different solutions were obtained in the up- and down-sweeps. The dashed black and white curve indicates the solutions that are defined by Eq. (3.26). Parameters: all other parameters as in Table 2.1.

$K_2 = (1 - k)\, K_{\mathrm{TOT}}$ with $K_{\mathrm{TOT}} = K_1 + K_2$. The results are obtained by numerically integrating the DDE system (Eq. (3.20) and Eqs. (2.43)-(2.44)), starting with initial conditions given by the solutions in the locking range for $\tau_1 = \tau_2 = T_{0,K}$ and

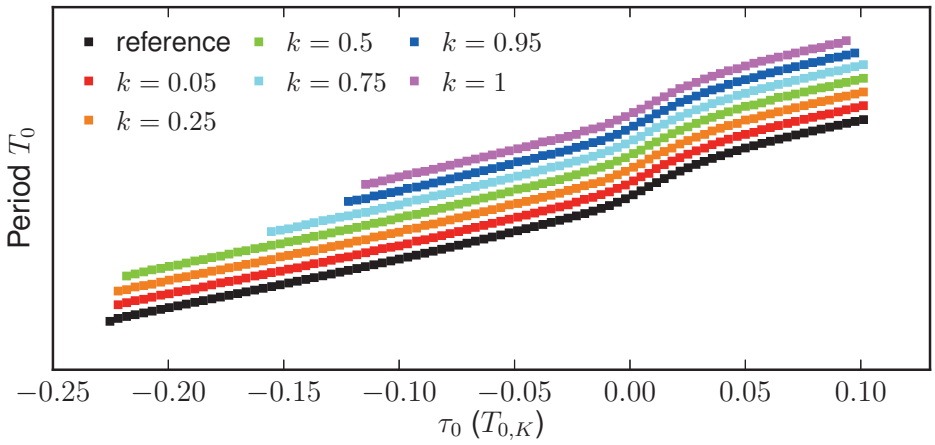

Figure 3.82.: **Intermediate feedback strength regime:** Locking ranges for various feedback strength ratios k, with $K_1 = 0.2k$, $K_2 = 0.2\,(1-k)$, $\tau_1 = 300T_{0,K}$ and $\tau_2 = T_{0,K}$. Plotted in black is the locking range for $\tau_1 = \tau_2 = T_{0,K}$. Parameters: all other parameters as in Table 2.1.

then slightly perturbing these solutions. Figure 3.82 shows that even for relatively weak feedback from a second short cavity (for example $k = 0.75$) the locking range can be significantly increased. Since the locking ranges (in terms of τ_0) appear to get increasingly smaller for longer delay times, the influence of adding a second feedback cavity which is relatively short, should have an increasingly greater influence on the stability of solutions as the length of the first feedback cavity is increased.

3.5. Summary

In this chapter we have investigated the dynamics of a passively mode-locked semiconductor laser. We have first performed an analysis of the bifurcations of the solitary laser, then we have studied the influence on the dynamics of optical feedback from one and two external cavities.

A passively mode-locked semiconductor laser can exhibit a range of dynamics depending on the operating conditions. At low pump currents there is a regime of Q-switched mode-locking in which the amplitude of pulses is modulated by a slow frequency. This regime is followed by fundamental mode-locking. In the fundamentally mode-locked regime a periodic pulse train is produced, the period of which is determined primarily by the laser cavity roundtrip time. The pulses are sustained due to a positive net gain window which arises due to the difference in saturation energies of the gain and absorber sections. At higher pump currents the increased unsaturated gain can cause harmonic mode-locking to become stable. The parameter ranges for which periodic dynamics are exhibited, are strongly influenced by the amplitude-phase coupling. This is due to the chirp which is introduced to the pulses by the presence of amplitude-phase coupling and leads to a decrease in the current range for stable mode-locking.

Following the analysis of the dynamics of the solitary laser, we have studied the influence of adding time-delayed optical feedback from one external cavity. Here we have concentrated on pump currents at which the solitary mode-locked laser exhibits fundamental mode-locking. Since the dynamics are periodic in this current regime the influence of the feedback depends strongly on the ratio of the feedback delay time to the period. When choosing feedback delay times which are resonant to the period of the fundamentally mode-locked solution, the feedback term mainly influences the non-resonant losses. Whether these are increased or decreased depends on the phase with which the light is coupled back into the laser cavity. If the feedback phase is zero then the losses are reduced which leads to an increase in the pulse energy in the laser cavity. On the other hand, if the light is coupled back destructively then the losses are increased, which, depending on the feedback strength, can lead to the periodic mode-locked dynamics being destroyed. When the feedback delay time is not an integer multiple of the mode-locking period then various dynamics can be induced. At low feedback strengths the feedback can induce satellite pulses, which in contrast to the main pulse, are sustained by the continual re-injection of pulses from the feedback cavity. For intermediate feedback strengths, pulses which are coupled in from the feedback cavity can cause competition for the gain in the laser cavity, leading to quasi-periodic dynamics in which multiple pulse exist in the laser cavity, the heights of which vary as the net gain window is transferred between them. When the feedback strength is sufficiently large, then the gain competition ceases and multiple pulses

can be sustained. Such feedback induced harmonic mode-locking has been observed experimentally and is of interest as a means of achieving higher repetition rates.

Due to the periodic nature of the mode-locked solutions, solutions reappear at feedback delay times which are increased by integer multiples of the period. This means that the same dynamics are exhibited for all main resonant feedback delay times. Surrounding each of the main resonances, there is a locking range in which the period of the system adapts to changes in the feedback delay times such that fundamentally mode-locked single-pulse dynamics are exhibited. This means that the repetition rate can be externally controlled. However, this is also accompanied by a broadening of the pulses. Since the solutions in the locking regions are also periodic, these also repeat at all delay times which are increased by integer multiples of their respective periods. Due to the difference in the periods within the locking regions, these regions become wider for higher main resonances. For sufficiently long delay times, this leads to regions of multistability between fundamentally mode-locked solutions which are locked to different main resonances. Via an analysis of the bifurcations of the mode-locked solutions we were able to identify two distinct locking regimes. For low feedback strengths the locking regions of the main resonances are bounded by solutions corresponding to minima and maxima in the periods and all solutions within the locking regions remain stable as they are repeated at higher main resonances. Whereas for intermediate feedback strengths the locking regions are bounded by torus bifurcations, which shift to solutions with smaller changes in the period as the delay time is increased. This means that the frequency pulling range decreases for longer delay times in the intermediate feedback strength regime.

The influence of the feedback phase is very important since this parameter cannot be easily set to a particular value in an experiment. As with single-mode lasers subject to feedback, for short delay lengths the dynamics can be strongly influenced by the feedback phase, but as the delay times are increased the impact of this parameter on the dynamics reduces. This is because smaller shifts in the frequency of the lasing modes are required to compensate for the feedback phase when the delay time is longer. For long delay times, this is another source of multistability.

After studying the dynamics induced by one feedback cavity we have investigated the influence of adding a second cavity. For the second feedback cavity the same resonance conditions apply as for the first. Therefore, for fundamentally mode-locked dynamics to be exhibited both delay times must be close to integer multiples of the period and outside the main resonance locking regions multi-pulse dynamics are exhibited. When both feedback delays are integer multiples of the period, plus the same offset from the zeroth main resonances, then the dynamics are the same as in the single feedback cavity case with the same total feedback strength. The difference compared with the single feedback case is that the multistability between solutions locked to different main resonances, which arises for longer delay times,

can be lifted due to the added control parameter, i.e. the second delay time. For the intermediate feedback strength regime, the second feedback cavity can also affect the stability of the solutions. Meaning that, by diverting a portion of the out-coupled light into a shorter feedback cavity, solutions that would otherwise be unstable with one long feedback cavity can be stabilised. One disadvantage of dual cavity feedback is that the dynamics are more sensitive to the feedback phases, since if these are different for the two external cavities, shifts in the lasing modes cannot generally compensate for both.

For both single and dual-cavity feedback, the dependence on the feedback parameters is qualitatively the same if amplitude-phase coupling is included, i.e. the same sort of resonance conditions apply. However, with amplitude-phase coupling the system is more sensitive to the feedback phases and there are large parameter regions of quasi-periodic and chaotic dynamics.

To conclude, time-delayed optical feedback can be used to tailor the dynamics exhibited by a passively mode-locked laser. This includes tuning the repetition rate of fundamentally mode-locked solutions, inducing satellite pulses and generating quasi-periodic or chaotic dynamics. For long delay times there is a large degree of multistability between different solutions. This multistability can partially be reduced by adding a second feedback cavity. Furthermore, the second feedback cavity can be used to influence the stability of solutions within the main resonance locking regions.

Chapter 4

Timing jitter of the mode-locked laser

4.1. Introduction

The timing jitter is a measure of temporal fluctuations of the laser output which arises due to noise sources which are intrinsic to the laser. For passively mode-locked lasers these fluctuations can lead to significant drifts in the pulse positions due to the absence to an external reference clock, as was discussed in the introductory chapter. Since most applications of mode-locked lasers require very steady pulse streams it is important to understand how the operating conditions of the laser influence the timing jitter and to find methods of reducing it. In this chapter we therefore investigate the timing jitter of the solitary passively mode-locked laser, as well as its behaviour under the influence of optical feedback.

Via comparison of experimentally measured power spectra with theoretically expected frequency dependencies for different noise sources, the authors of [HAU93a] have shown that contributions to the timing jitter are dominated by spontaneous emission noise. In this chapter we therefore include a Gaussian white noise term in the equation for the electric field (Eq. (2.42) with $R_{sp} \neq 0$) to model spontaneous emission noise. The influence of spontaneous emission on the carrier density is not included, as this is negligible in comparison to the total carrier density. In addition to fluctuations in the pulse positions, the inclusion of spontaneous emission noise also results in fluctuations in the pulse amplitudes, the phase of the electric field and the optical frequencies. We focus on the timing fluctuations, as for many applications it is the relative pulse positions which are of importance and not the absolute frequencies [ELI97].

There have been a number of experimental studies on the influence of optical feedback on the timing jitter of passively mode-locked semiconductor lasers [SOL93, BRE10, LIN10e, ARS13]. These have demonstrated that optical feedback can lead to a reduction in the timing jitter, and that longer feedback cavities generally lead

to a greater improvement. There have also been previous theoretical studies on this topic, which have shown that longer feedback cavities lead to a greater reduction in the timing jitter [OTT14, SIM14]. However this has so far only been demonstrated for isolated feedback delay regimes and the mechanism for the reduction in the timing jitter has not been clearly elucidated. We address these issues in this chapter by presenting systematic study for the feedback dependence over a large range of feedback delay times.

This chapter will be structured as follows. In the next section methods of calculating the timing jitter will be introduced. We will firstly introduce two time-domain methods in Subsections 4.2.1 and 4.2.2 which allow the timing jitter to be calculated directly. The first method is purely numerical and involves the integration of the stochastic DDE system (Eqs. (2.42)-(2.44) with $R_{sp} \neq 0$) in order to perform statistics on the pulse positions, while the second method is semi-analytic and allows the timing jitter to be determined from the dynamics of the unperturbed DDE system (Eqs. (2.42)-(2.44) with $R_{sp} = 0$). In Subsection 4.2.3 we shall then discuss various measures of the timing jitter which are commonly used experimentally and are based on extracting information on the timing jitter from the power spectral density. Under certain limits the two time domain methods can be directly related to the frequency domain timing jitter measures. In Section 4.3 the time domain methods will then be employed to study the influence of various key parameters on the timing jitter of the solitary laser. The influence of optical feedback, from one and two external cavities, will be presented in Sections 4.4 and 4.5.

Parts of this chapter have been published in [OTT14b, JAU15, NIK16].

4.2. Calculating the timing jitter

4.2.1. Long-term timing jitter

The timing jitter is a measure of how much the temporal positions of pulses deviate from an ideal jitter-free pulse train. Numerically this can be calculated directly from the pulse positions in the time domain. From the numerically obtained time traces the pulse positions can be defined in several ways. One approach is to use the time at which the pulse reaches its maximum value. However, this definition of the pulse position can be susceptible to fluctuations in the pulse amplitude. A more robust method is to use the "center of mass" positions of the pulses. In [PAS04, MUL06] this is done by weighting the time with the pulse intensity. We shall use the positive net gain window instead of the pulse intensity. The reason for this is, as discussed in previous chapter, in the presence of feedback the mode-locked laser can exhibit periodic dynamics with multiple feedback induced pulses of varying heights. If one were to use the pulse intensity to define the positions

then the pulse detection algorithm would need to be able to distinguish between the various pulses within one period. However, since the feedback induced satellite pulses do not coincide with a positive net gain window, such a complication does not arise if the positive net gain window is used to define the positions of the main pulses.[1]

The timing positions of the pulses are defined as follows [OTT14, OTT14b]. For the time interval within the m^{th} pulse, in which the net gain $\mathcal{G} = G - Q - |\ln\left(\kappa\left(1+K\right)^2\right)|$ exceeds a threshold value $\mathcal{G}_{\text{thres}}$, we define a probability density

$$\rho_m\left(t\right) \equiv \frac{\mathcal{G}^2\left(t\right)}{\mathcal{G}_m}, \quad \text{with} \quad \mathcal{G}_m \equiv \int_{t_{m,b}}^{t_{m,e}} \mathcal{G}^2\left(t\right) dt, \tag{4.1}$$

where $t_{m,b}$ ($t_{m,e}$) is the time point at which the leading (trailing) edge of the m^{th} pulse first exceeds (falls below) $\mathcal{G}_{\text{thres}}$, i.e. $\mathcal{G}\left(t_{m,b}\right) > \mathcal{G}_{\text{thres}}$ ($\mathcal{G}\left(t_{m,e}\right) < \mathcal{G}_{\text{thres}}$). The timing position of the m^{th} main pulse is then given by

$$t_m \equiv \int_{t_{m,b}}^{t_{m,e}} \rho_m\left(t\right) t dt. \tag{4.2}$$

For symmetric pulses, apart from noise fluctuations, t_m would coincide with the peak of the pulse.

An example of a time trace of the electric field amplitude $|\mathcal{E}|$ (blue) and the net gain $\mathcal{G}$ (black) is shown in Fig. 4.1. The level for $\mathcal{G}_{\text{thres}}$ is indicated by the dashed black line and the positive net-gain windows above this line, which are used to define the pulse positions, are shaded in grey. The time trace of $|\mathcal{E}|$ is much noisier than that of $\mathcal{G}$. This is because the noise term is only added to the equation for the electric field and therefore fluctuations only enter the gain and absorber equations via $|\mathcal{E}|$.

The timing deviation of the m^{th} pulse position from the ideal jitter-free case is defined as

$$\Delta t_m \equiv t_m - mT_C, \tag{4.3}$$

where T_C is the interspike-interval time for the ideal pulse train. In the case of active or hybrid mode-locking T_C is given by the external modulation period,

[1] Using this approach to define the pulse positions we neglect how the satellite pulses may deviate from their ideal positions. However, since the positions of the satellite pulses are coupled to the positions of the main pulses they cannot drift with respect to the main pulses. The distance to the main pulse could vary slightly between roundtrips, however this will mostly be due to the difference in the deviation of the main pulse, from the ideal case, at time t compared with time $t - \tau$, rather than due to spontaneous emission noise emitted near the satellite pulses. This is because the satellite pulses are sustained by continual re-injection of pulses from the feedback cavity rather than by gain within the laser. The satellite pulses should therefore not have a large influence on the overall timing jitter. This is confirmed by the excellent agreement we find with the semi-analytic method which uses the entire profile of the solution over one period.

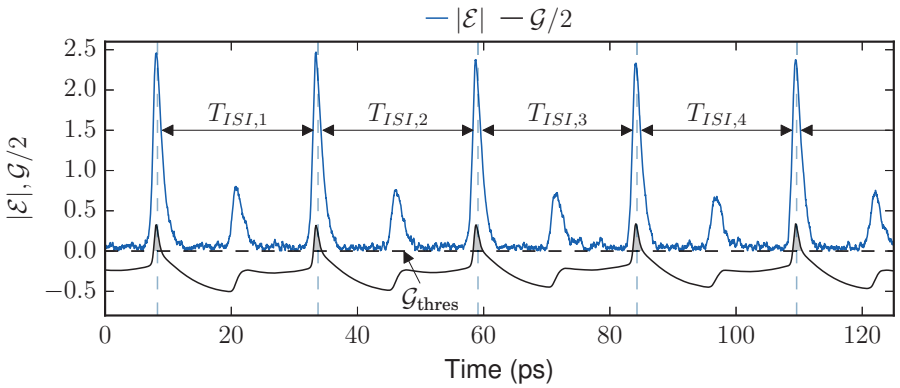

Figure 4.1.: Time traces of the electric field amplitude $|\mathcal{E}|$ (blue) and the net gain $\mathcal{G} = G - Q - |\ln\left(\kappa\,(1+K)^2\right)|$ (black) in the presence of noise. Positive net gain windows are shaded in grey. Parameters: $\tau = 0.5$, $K = 0.15$, $R_{sp} = 0.63$, all other parameters as in Table 2.1.

however since a passively mode-locked laser has no external reference clock we use the average interspike-interval time to define T_C. The interspike-interval times (between main pulses) are given by

$$T_{ISI,m} = t_m - t_{m-1}. \tag{4.4}$$

These are averaged over M laser cavity roundtrips and N noise realisations to give

$$T_C \equiv \left\langle \frac{1}{M}\,(t_M - t_0) \right\rangle_N, \tag{4.5}$$

where $\langle\,\cdot\,\rangle_N$ denotes the average over the noise realisations. For each noise realisation we now have a set of timing fluctuations $\{\Delta t_m\}_{m=1}^{M}$ for the first to the M^{th} main pulse. In Fig. 4.2 (a) examples of the timing fluctuations in dependence of the number of laser cavity roundtrips m is depicted for a number of noise realisations. The mean $\langle \Delta t_m \rangle_N$ for $N = 200$ noise realisations is indicated by the dashed black line. Figure. 4.2 (b) shows the variance,

$$\mathrm{Var}\,(\Delta t_m) = \langle \Delta t_m^2 \rangle_N - \langle \Delta t_m \rangle_N^2, \tag{4.6}$$

calculated for 200 noise realisations. Here it is evident that the timing fluctuations behave similar to a random walk, i.e. the mean is zero and the variance grows linearly with the roundtrip number [GAR02]. However, a true random walk is composed of statistically independent increments, which is not the case for the mode-locked laser. Due to the finite recovery times of the gain and absorber dynamics, and due to the internal delay time T, the interspike-interval times $T_{ISI,m}$ are correlated from one roundtrip to the next. Therefore the timing fluctuations can only be modelled by a random walk for roundtrip numbers that are much

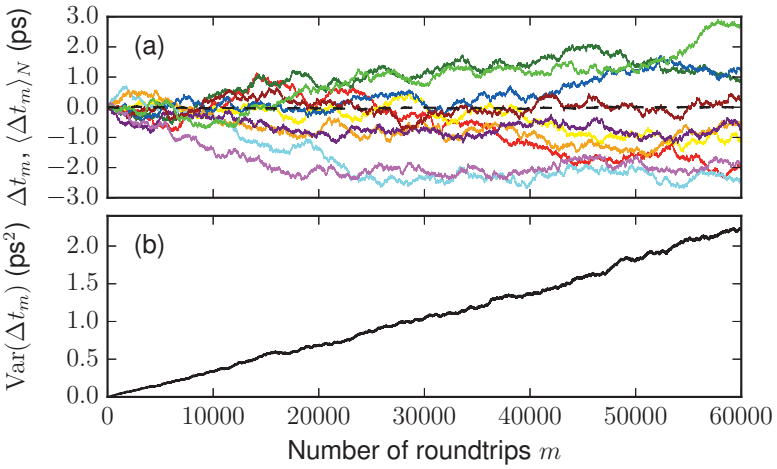

Figure 4.2.: (a) Timing fluctuations Δt_m as a function of the number of roundtrips m for various noise realisations (coloured lines). The dashed black line shows the mean $\langle \Delta t_m \rangle_N$ calculated for $N = 200$ noise realisations. (After [OTT14]) (b) Variance of the timing fluctuations calculated for 200 noise realisations. Parameters: $R_{sp} = 0.44$, all other parameters as in Table 2.1.

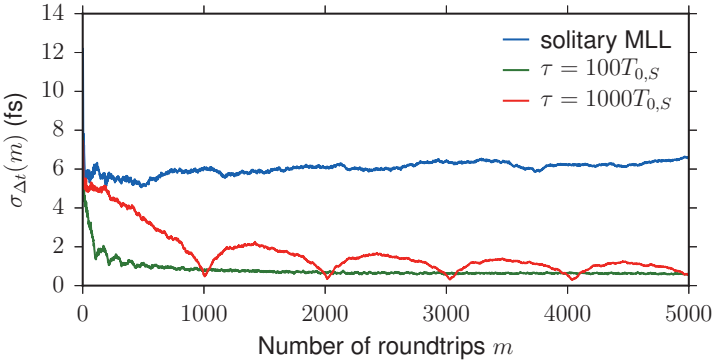

Figure 4.3.: $\sigma_{\Delta t}(m)$ (defined in Eq. (4.7)) plotted as a function of the number of laser cavity roundtrips for the solitary mode-locked laser (MLL) (blue) and the mode-locked laser with resonant feedback delay times of $\tau = 100T_{0,S}$ (green) and $\tau = 1000T_{0,S}$ (red) where $K = 0.1$. $N = 100$ noise realisations were used for these calculations. Parameters: $R_{sp} = 0.44$, all other parameters as in Table 2.1.

larger than any correlation times within the system. When the laser is subject to feedback, then the positions are correlated on time scales given by the feedback delay times, meaning that large roundtrip numbers are required for the statistics to resemble that of a random walk. This is illustrated in Fig. 4.3 which shows how the variance scales with the roundtrip number for the solitary laser (blue) and for

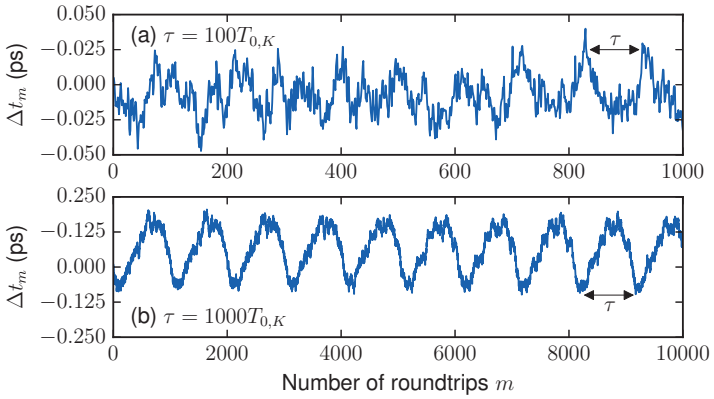

Figure 4.4.: Timing fluctuations Δt_m as a function of the number of roundtrips n for (a) $\tau = 100T_0$ and (b) $\tau = 1000T_0$. Parameters: $K = 0.1$, $R_{sp} = 0.44$, all other parameters as in Table 2.1

the laser subject to resonant feedback with delay times of $\tau = 100T_{0,S}$ (green) and $\tau = 1000T_{0,S}$ (red). The quantity

$$\sigma_{\Delta t}(m) = \sqrt{\frac{\mathrm{Var}(\Delta t_m)}{m}} \tag{4.7}$$

is plotted, which for a statistical process behaving like a random walk should be constant in m. For the solitary laser case (blue) this quantity converges to a constant value, apart from statistical fluctuations, after only a few roundtrips. For $\tau = 100T_{0,S}$ (green) a constant value is only reached after approximately 2000 roundtrips. In the $\tau = 1000T_{0,S}$ (red) case the long correlation times introduced by the feedback lead to periodic variations in the variance, and $\sigma_{\Delta t}(m)$ only converges to a constant value after a roundtrip number on the order of 10^6 (not depicted here). This behaviour for long feedback delay times is caused by noise-induced modulations of the timing fluctuations that arise due to the excitation of weakly damped eigenmodes of the system. Figure 4.4 shows examples of such modulations of Δt_m. For $\tau = 100T_0$ (Fig. 4.4a) the oscillations are not pronounced, however, for $\tau = 1000T_0$ (Fig. 4.4b) the oscillations in Δt_m are very defined. The noise-induced modulation of the dynamics will be discussed further in Chapter 5.

In this chapter we will mainly restrict our analysis to feedback delay times for which the noise-induced modulations are sufficiently small that the variance of the timing fluctuations grows linearly with the roundtrip number for m of the order of 10^4. For such cases we define the **long-term timing jitter** [LEE02c] as

$$\sigma_{lt} \equiv \sqrt{\frac{\mathrm{Var}(\Delta t_m)}{m}} \tag{4.8}$$

for large m, i.e. the value that $\sigma_{\Delta t}(m)$ converges to for large m. This quantity is a measure of the fluctuation of pulse arrival times on long time scales. Any fluctuations on short times scales cannot be described by this quantity, i.e. the statistics on long time scales are equivalent to those of a true random walk with a diffusion constant of $\sigma_{lt}^2/2$, but not on short time scales.

Using Eq. (4.7) another measure of the timing jitter can also be defined. For $m = 1$ Eq. (4.7) becomes

$$\sigma_{pj} \equiv \sqrt{\mathrm{Var}\left(\Delta t_1\right)}, \tag{4.9}$$

which gives the standard deviation of the interspike interval times and is referred to as the **period jitter** [LEE02c] or the **pulse-to-pulse jitter** [KEF08]. For a true random walk σ_{lt} and σ_{pj} are equivalent.

4.2.2. Semi-analytic timing jitter

Fully numerical calculations of the timing jitter, such as the long-term timing jitter calculation which was introduced in the previous subsection, require the simulation of many noise realisations and can therefore be computationally very expensive. Additionally, only limited insight into the physical mechanisms influencing the timing jitter can be gained. In this section we will introduce a semi-analytic method of calculating the timing jitter, which has the advantages that it is based on the dynamics of the unperturbed system and that it provides information of the influence of feedback on the timing jitter. The main idea of the semi-analytic method is to treat the spontaneous emission noise as a perturbation to the linearised system and to project the perturbation on to the neutral Floquet mode which corresponds to the time-shift invariance of the unperturbed system. One can then derive an expression for the timing jitter which is equivalent to Eq. (4.8) under certain conditions. This semi-analytic method was first proposed in [PIM14b]. We have generalised this method to the mode-locked laser system with optical feedback in [JAU15].

There have been earlier theoretical studies on the influence of noise on the propagation of mode-locked pulses which have also used a perturbation theory approach. Such an analysis was first carried out by Haus, who used a master equation with secant-shaped solutions to describe the mode-locked pulses [HAU93a]. By linearising about the mode-locked solution, small perturbations to the secant-shaped pulses are described by perturbation of the pulse amplitude, timing, phase and frequency. This master equation approach was used to extensively study the spectral properties attributed to timing jitter [HAU93a, ELI96, ELI97]. Although the master equation approach was extended to take carrier dynamics into account [JIA01], its applicability to semiconductor lasers is still restricted due to the multitude of simplifying assumptions. Furthermore, it cannot be used to describe coupled cavities. For these reasons, previous theoretical studies of the timing jitter in mode-locked

semiconductor lasers have been performed by calculating the long-term timing jitter (Eq. (4.8)) or the root-mean-square timing jitter (defined in Eq. (4.37) in the next section) from direct numerical simulations of travelling wave [ZHU97, MUL06] and DDE [OTT12a, OTT14b, SIM14] models.

Derivation of the semi-analytic timing jitter

The following derivation has been published in [JAU15] and closely follows the text therein.

To derive the timing jitter we require the mode-locked solutions to be periodic in all variables. We therefore modify Eq. (2.42) to include a frequency shift ω, which accounts for possible offsets between the reference frequency and the nearest lasing mode, i.e. we make the transformation $\mathcal{E} \to \mathcal{E}e^{i\omega t}$ to obtain

$$\begin{aligned}\frac{d\mathcal{E}}{dt} &= -\left(\gamma + i\omega\right)\mathcal{E}\left(t\right) + \gamma R\left(t-T\right)e^{-i(\Delta\Omega+\omega)T}\mathcal{E}\left(t-T\right) + D\xi\left(t\right) \\ &\quad +\gamma\sum_{n=1}^{N} K_n e^{iC_n} R\left(t-T-\tau_n\right)e^{-i(\Delta\Omega+\omega)(T+\tau_n)}\mathcal{E}\left(t-T-\tau_n\right), \qquad (4.10)\end{aligned}$$

$$\frac{\partial G}{\partial t} = J_g\left(t\right) - \gamma_g G\left(t\right) - e^{-Q(t)}\Big(e^{G(t)}-1\Big)\left|\mathcal{E}\left(t\right)\right|^2 \qquad (4.11)$$

and

$$\frac{\partial Q}{\partial t} = J_q\left(t\right) - \gamma_q Q\left(t\right) - r_s e^{-Q(t)}\Big(e^{Q(t)}-1\Big)\left|\mathcal{E}\left(t\right)\right|^2. \qquad (4.12)$$

The dynamical equations for the gain and losses are unchanged by the transformation. For convenience we have relabeled $D \equiv \sqrt{R_{sp}}$. $R\left(t\right)$ is as defined in Eq. (2.23).

Let $\psi_0\left(t\right) = \left(\mathrm{Re}\,\mathcal{E}_0\left(t\right), \mathrm{Im}\,\mathcal{E}_0\left(t\right), G_0\left(t\right), Q_=\left(t\right)\right)^{\mathrm{T}}$ be a stable T_0 periodic mode-locked solution to Eqs. (4.10)-(4.12) for $D = 0$, where $\mathrm{Re}\,\mathcal{E}$ is the real part of the electric field and $\mathrm{Im}\,\mathcal{E}$ the imaginary part. The trajectory of this solution is represented by the solid black line in the state-space sketch shown in Fig. 4.5. Due to the symmetries of this system this trajectory also represents all phase-shifted (here we are referring to the electric field phase) and time-shifted versions of this solution

$$\Gamma_\varphi \Pi_\theta \psi_0\left(t\right) = \Big(\mathrm{Re}(e^{i\varphi}\mathcal{E}_0)\left(t+\theta\right), \mathrm{Im}(e^{i\varphi}\mathcal{E}_0)\left(t+\theta\right), G_0\left(t+\theta\right), Q_0\left(t+\theta\right)\Big)^{\mathrm{T}},$$

where Γ_φ is the matrix of rotation of the $\mathcal{E}_0$ plane and Π_θ is a time-shift operator, i.e. $\Pi_\theta\psi_0\left(t\right) = \psi_0\left(t+\theta\right)$. Now let $\psi\left(t\right) = \left(\mathrm{Re}\,\mathcal{E}\left(t\right), \mathrm{Im}\,\mathcal{E}\left(t\right), G\left(t\right), Q\left(t\right)\right)^T$ be a solution to the perturbed system, i.e. Eqs. (4.10)-(4.12) for $D \neq 0$. If the perturbation is small, $D \ll 1$, then the trajectory of $\psi\left(t\right)$ will stay within a distance of the order D from the trajectory of the family of unperturbed solutions $\Gamma_\varphi\Pi_\theta\psi_0$.[2]

[2] Here we are assuming that large fluctuations have a sufficiently small probability that they can be neglected over typical observation time spans of the system.

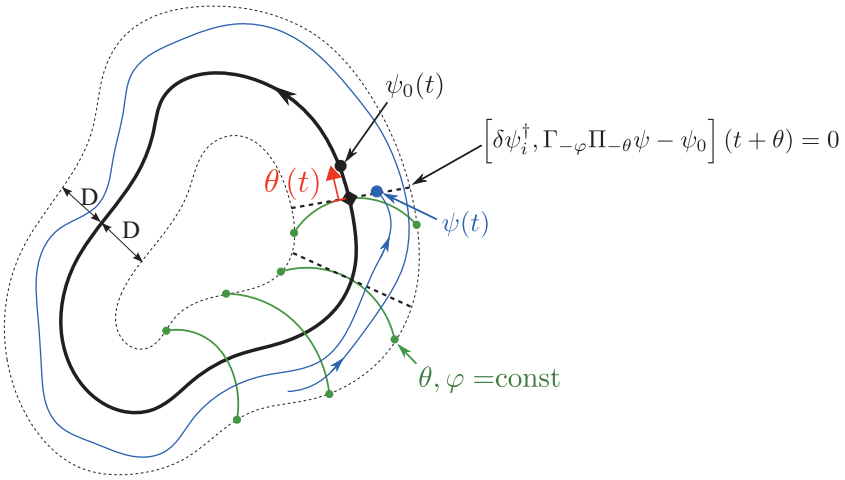

Figure 4.5.: Sketch of trajectories in the state-space of the mode-locked laser system. The bold black line represent the trajectory of the unperturbed mode-locked solution ψ_0 and all time and phase shifts of this solution $\Gamma_\varphi \Pi_\theta \psi_0$. The blue line represents the trajectory of the perturbed system for $D \ll 1$. The green lines represent codimension 2 surfaces of constant asymptotic time shift θ and angular phase shift φ which are transverse to the trajectory of ψ_0. The dashed black lines are the codimension 2 surfaces defined by Eq. (4.22), which are tangential to the surfaces of constant asymptotic time and angular phase shift, $\theta, \varphi = \text{const}$, at the points where ψ_0 is intersected. Figure modified from [JAU15]. Copyright (2015) by the American Physical Society.

The difference in the perturbed and unperturbed trajectories causes a time-shift $\theta(t)$ and phase-shift $\varphi(t)$ to accumulate between these solutions, and because the timing fluctuations are a non-stationary process that can be described by a random walk, as was shown in the previous section, the variance of $\theta(t)$ and $\varphi(t)$ should grow linearly with time. Here we point out that it is due to the timing fluctuations being non-stationary that the typical perturbation theory Ansatz that $\psi(t) = \psi_0(t) + \delta\psi(t)$ and $\delta\psi(t)$ is small does not hold, because $\delta\psi(t)$ can become large when a sufficient time-shift has accumulated between $\psi(t)$ and $\psi_0(t)$.

The blue curve in Fig. 4.5 represents the trajectory of the perturbed solution and the blue circle on the curve represents the position of the solution at time t. The reference unperturbed solution $\psi_0(t)$ is at the position indicated by the black circle at time t. There are several ways in which one could define the time-shift between these solutions, since, for example, the perturbed solution could be projected onto the trajectory of the unperturbed solution in various ways. Here we will make use of the fact that any solution $\psi'(t)$ to the unperturbed system (Eqs. (4.10)-(4.12) with $D = 0$), which starts in the vicinity of the trajectory of $\psi_0(t)$, will converge to $\Gamma_\varphi \Pi_\theta \psi_0(t)$ in the limit $t \to \infty$, where θ and φ are constant time- and phase-shifts with respect to the reference solution. These θ and φ values are referred to as

the asymptotic time- and phase-shifts and their values are dependent on the initial state of $\psi'(t)$.[3] In the state-space of the system there are surfaces along which the asymptotic time- and phase-shifts are constant. These are represented by the green curves in Fig. 4.5. Any solutions to the unperturbed system whose initial states lie on the same codimension 2 surfaces of constant asymptotic θ and φ will have the same asymptotic θ and φ values for all time. However, the asymptotic θ and φ values for the perturbed system will evolve in time and will be defined by the surfaces of constant asymptotic θ and φ that the solution happens to be on at each point in time, i.e. at each point in time $\theta(t)$ and $\varphi(t)$ of the perturbed solution are given by the asymptotic values the system would converge to if the perturbation were removed at that time.

The surfaces of constant asymptotic θ and φ are highly non-trivial to compute. However, since the perturbed solution is restricted to a small neighbourhood of $\psi_0(t)$, the asymptotic time- and phase-shift, and the evolution thereof, can be approximated using solutions to Eqs. (4.10)-(4.12) linearised about $\psi_0(t)$. The linearised system is given by

$$\frac{d}{dt}\delta\psi(t) = A(t)\,\delta\psi(t) + \sum_{n=0}^{N} B_n\left(t-\tau_n'\right)\delta\psi\left(t-\tau_n'\right) + Dw(t), \tag{4.13}$$

where $\delta\psi(t) = (\operatorname{Re}\delta\mathcal{E}(t), \operatorname{Im}\delta\mathcal{E}(t), \delta G(t), \delta Q(t))^{\mathrm{T}}$, $w(t) = (\xi_1(t), \xi_2(t), 0, 0)^{\mathrm{T}}$, A and B_n are T_0-periodic Jacobi matrices of the linearisation and the delay times are defined as $\tau_0' = T$ and $\tau_n' = T + \tau_n$ for $n \geq 1$. The Jacobi matrices are given in Appendix B.

The unperturbed linearised system (Eq. (4.13) with $D = 0$) has two neutral modes which correspond to the time-shift and phase-shift invariance of the original unperturbed system (Eqs. (4.10)-(4.12) with $D = 0$). These are given by

$$\delta\psi_1(t) = \left(\operatorname{Re}\dot{\mathcal{E}}_0(t), \operatorname{Im}\dot{\mathcal{E}}_0(t), \dot{G}_0(t), \dot{Q}_0(t)\right)^{\mathrm{T}} \tag{4.14}$$

and

$$\delta\psi_2(t) = \left(-\operatorname{Im}\mathcal{E}_0(t), \operatorname{Re}\mathcal{E}_0(t), 0, 0\right)^{\mathrm{T}}, \tag{4.15}$$

respectively. At the point of intersection with trajectory of $\psi_0(t)$, these neutral modes are transverse to the surfaces of constant asymptotic θ and φ. Therefore, assuming that all other Floquet modes are sufficiently damped the asymptotic θ and φ can be approximated by projections onto these neutral modes. The noise then results in a slow diffusion of $\theta(t)$ and $\varphi(t)$ along the neutral modes.

[3] The state of the system is defined on an interval $[-\tau_{\max}, 0]$, where $\tau_{\max}$ is the largest delay time, i.e. $\tau_{\max} = T + \tau$ for the single feedback cavity system.

In order to explicitly write out projections of the perturbed solutions onto the neutral modes, we must first define the bilinear form [HAL66, HAL77]:

$$\left[\delta\psi^\dagger, \delta\psi\right](t) = \delta\psi^\dagger(t)\delta\psi(t) + \sum_{n=1}^{M}\int_{-\tau_n'}^{0} \delta\psi^\dagger(t+r+\tau_n')B_n(t+r)\delta\psi(t+r)dr, \quad (4.16)$$

where $\delta\psi^\dagger$ are solutions to the unperturbed adjoint linear system.

The linear system adjoint to Eq. (4.13), for $D = 0$, is given by

$$\frac{d}{dt}\delta\psi^\dagger(t) + \delta\psi^\dagger(t)A(t) + \sum_{n=0}^{N}\delta\psi^\dagger(t+\tau_n')B_n(t) = 0, \quad (4.17)$$

where $\delta\psi^\dagger(t) = (\delta\psi_1^\dagger, \delta\psi_2^\dagger, \delta\psi_3^\dagger, \delta\psi_4^\dagger)$ is a row vector. The derivation of the adjoint system is shown in Appendix B. Using the bilinear form (Eq. (4.16)), the properly normalised neutral modes of the unperturbed linear system Eq. (4.13) and the adjoint linear system Eq. (4.17) fulfill the biorthogonality property

$$[\delta\psi_j^\dagger, \delta\psi_k](t) = \delta_{j,k}. \quad (4.18)$$

Furthermore, for every solution $\delta\psi(t)$ to the perturbed linear system Eq. (4.13),

$$\frac{d[\delta\psi^\dagger, \delta\psi](t)}{dt} = D\delta\psi^\dagger(t)w(t). \quad (4.19)$$

holds at all times, where $\delta^\dagger\psi(t)$ are solutions to the adjoint system Eq. (4.17) which is unperturbed. That this relation holds can be seen by substituting the bilinear form Eq. (4.16) into the left-hand side of Eq. (4.19):

$$\begin{aligned}
\frac{d}{dt}[\delta\psi^\dagger, \delta\psi](t) &= \frac{d}{dt}\left(\delta\psi^\dagger(t)\delta\psi(t) + \sum_n\int_{-\tau_n'}^{0}\delta\psi^\dagger(s+t+\tau_n')B_n(s+t)\delta\psi(s+t)ds\right)\\
&= \frac{d\delta\psi^\dagger(t)}{dt}\delta\psi(t) + \delta\psi^\dagger(t)\frac{d\delta\psi(t)}{dt} + \frac{d}{dt}\sum_n\int_{t-\tau_n'}^{t}\delta\psi^\dagger(s+\tau_n')B_n(s)\delta\psi(s)ds\\
&= -\left(\delta\psi^\dagger(t)A(t) + \sum_n\delta\psi^\dagger(t+\tau_n')B_n(t)\right)\delta\psi(t)\\
&\quad +\delta\psi^\dagger(t)\left(A(t)\delta\psi(t) + \sum_n B_n(t-\tau_n')\delta\psi(t-\tau_n') + w(t)\right)\\
&\quad +\sum_n(\delta\psi^\dagger(t+\tau_n')B_n(t)\delta\psi(t) - \delta\psi^\dagger(t)B_n(t-\tau_n')\delta\psi(t-\tau_n'))\\
&= D\,\delta\psi^\dagger(t)w(t).
\end{aligned}$$

This relation describes the evolution of the noise along different eigendirections of the unperturbed system. Using this relation one can see, as follows, that the

noise has the greatest effect along the neutral modes. We denote the eigenmodes of Eq. (4.17) as $\delta\psi_\lambda^\dagger(t)$, then the projection of $\delta\psi\,(t)$ onto $\delta\psi_\lambda^\dagger(t)$ can be written as

$$[\delta\psi_\lambda^\dagger, \delta\psi](t) = e^{-\lambda t} y_\lambda\,(t)\,, \tag{4.20}$$

where we have used the fact that the characteristic solutions of Eq. (4.13) and Eq. (4.17) have the form $\delta\psi_\lambda(t) = e^{\lambda t} p_\lambda(t)$ and $\delta\psi_\lambda^\dagger(t) = e^{-\lambda t} p_\lambda^\dagger(t)$, respectively, where $p_\lambda(t)$ and $p_\lambda^\dagger(t)$ are T_0-periodic functions and λ is a Floquet exponent of Eq. (4.13). The noise driven evolution along the eigenmode $\delta\psi_\lambda(t)$ is now described by the function $y_\lambda\,(t)$. Substituting Eq. (4.20) into Eq. (4.19), the equation of motion for $y_\lambda\,(t)$ is

$$\frac{dy_\lambda(t)}{dt} = \lambda y_\lambda(t) + D p_\lambda^\dagger(t) w(t). \tag{4.21}$$

For the neutral modes $\lambda = 0$ and Eq. (4.21) describes a process similar to Brownian motion, for which the variance grows as $D^2 t$, i.e. linearly with time. However, for all other eigenmodes $\mathrm{Re}\,\lambda < 0$, since we are only considering stable solutions to Eqs. (4.10)-(4.12), in which case Eq. (4.21) describes an Ornstein-Uhlenbeck-type process which has a bounded variance of the order D^2 [GAR02].

We now use the bilinear form (Eq. (4.16)) and the solutions to the adjoint system (Eq. (4.17)) to define $\theta\,(t)$ and $\varphi\,(t)$ implicitly for any given state $\psi(t+r)$ ($r \in [-\tau_N', 0]$) by the formulas

$$\left[\delta\psi_1^\dagger, \Gamma_{-\varphi}\Pi_{-\theta}\psi - \psi_0\right](t+\theta) = 0 \tag{4.22}$$

and

$$\left[\delta\psi_2^\dagger, \Gamma_{-\varphi}\Pi_{-\theta}\psi - \psi_0\right](t+\theta) = 0, \tag{4.23}$$

where $\delta\psi_i^\dagger$ are neutral modes of the unperturbed adjoint linear system. These equations define a surface, represented by the dashed black lines in Fig. 4.5, which is tangential to the surface of constant asymptotic θ and φ at the point of intersection with $\Gamma_\varphi\Pi_\theta\psi_0$ in the state space of the system.

Using the normalised neutral modes of the adjoint system, $\delta\psi_1^\dagger\,(t)$ and $\delta\psi_2^\dagger\,(t)$, and Eqs. (4.22)-(4.23), we can now obtain equations of motion for the time-shift $\theta\,(t)$ and the phase-shift $\varphi\,(t)$. To do this the partial derivatives of Eqs. (4.22)-(4.23), with respect to t, θ, φ, must be calculated. The partial derivative with respect to t is given by

$$\frac{\partial}{\partial t}\left[\delta\psi_i^\dagger, \Gamma_{-\varphi}\Pi_{-\theta}\psi - \psi_0\right](t+\theta) = D\,\delta\psi_i^\dagger(t+\theta)\Gamma_{-\varphi} w(t) \tag{4.24}$$

for $i = 1, 2$. This expression can be obtained from Eq. (4.19) by considering that $\psi(t) = \Gamma_\varphi \psi_0(t+\theta) + \delta\psi(t)$. The partial derivative with respect to θ is calculated as follows.

$$\frac{\partial}{\partial\theta}\left[\delta\psi_i^\dagger, \Gamma_{-\varphi}\Pi_{-\theta}\psi - \psi_0\right](t+\theta) = \frac{\partial}{\partial\theta}\left[\delta\psi_i^\dagger(t+\theta), \Gamma_{-\varphi}\psi(t) - \psi_0(t+\theta)\right]$$
$$= \left[\frac{\partial}{\partial\theta}\delta\psi_i^\dagger(t+\theta), \Gamma_{-\varphi}\psi(t) - \psi_0(t+\theta)\right] + \left[\delta\psi_i^\dagger(t+\theta), \Gamma_{-\varphi}\frac{\partial}{\partial\theta}\psi(t) - \frac{\partial}{\partial\theta}\psi_0(t+\theta)\right].$$

Now, $\frac{\partial}{\partial\theta}\psi(t) = 0$ and from Eq. (4.14) we see $\frac{\partial}{\partial\theta}\psi_0(t+\theta) = \delta\psi_1(t+\theta)$. Therefore, neglecting the terms that are proportional to $\psi - \Gamma_\varphi\Pi_\theta\psi_0$, since they are of the order of D in the vicinity of the trajectory of $\Gamma_\varphi\Pi_\theta\psi_0(t)$, the partial derivative of Eqs. (4.22)-(4.23) with respect to θ is given by

$$\frac{\partial}{\partial\theta}\left[\delta\psi_i^\dagger, \Gamma_{-\varphi}\Pi_{-\theta}\psi - \psi_0\right](t+\theta) = -\left[\delta\psi_i^\dagger, \delta\psi_1\right](t+\theta). \tag{4.25}$$

Similarly one obtains

$$\frac{\partial}{\partial\varphi}\left[\delta\psi_i^\dagger, \Gamma_{-\varphi}\Pi_{-\theta}\psi - \psi_0\right](t+\theta) = -\left[\delta\psi_i^\dagger, \delta\psi_2\right](t+\theta) \tag{4.26}$$

for the partial derivative with respect to φ. The total derivative of Eqs. (4.22)-(4.23) with respect to time,

$$\left(\frac{\partial}{\partial t} + \dot\theta\frac{\partial}{\partial\theta} + \dot\varphi\frac{\partial}{\partial\varphi}\right)\left[\delta\psi_i^\dagger, \Gamma_{-\varphi}\Pi_{-\theta}\psi - \psi_0\right](t+\theta) = 0, \tag{4.27}$$

can now be expressed in terms of the partial derivatives, Eqs. (4.24), (4.25) and (4.26). Using this, and the biorthogonality condition Eq. (4.18), the equations for the evolution of $\theta(t)$ and $\varphi(t)$ are obtained. For $i = 1$ we have

$$\left(\frac{\partial}{\partial t} + \dot\theta\frac{\partial}{\partial\theta} + \dot\varphi\frac{\partial}{\partial\varphi}\right)\left[\delta\psi_1^\dagger, \Gamma_{-\varphi}\Pi_{-\theta}\psi - \psi_0\right](t+\theta)$$
$$= D\,\delta\psi_1^\dagger(t+\theta)\Gamma_{-\varphi}w(t) - \dot\theta\left[\delta\psi_1^\dagger, \delta\psi_1\right](t+\theta) - \dot\varphi\left[\delta\psi_1^\dagger, \delta\psi_2\right](t+\theta)$$
$$= D\,\delta\psi_1^\dagger(t+\theta)\Gamma_{-\varphi}w(t) - \dot\theta = 0,$$

yielding

$$\dot\theta = D\,\delta\psi_1^\dagger(t+\theta)\Gamma_{-\varphi}w(t). \tag{4.28}$$

Similarly, for $i = 2$ we obtain

$$\dot\varphi = D\,\delta\psi_2^\dagger(t+\theta)\Gamma_{-\varphi}w(t). \tag{4.29}$$

The Fokker-Planck equation for the joint probability density $p(t, \theta, \varphi)$ of the stochastic process described by Eqs. (4.28)-(4.29) is given by [GAR02]

$$\frac{\partial p}{\partial t} = \left(\frac{1}{2}\frac{\partial^2}{\partial\theta^2}(d_{11}\,p) + \frac{\partial^2}{\partial\theta\partial\varphi}(d_{12}\,p) + \frac{1}{2}\frac{\partial^2}{\partial\varphi^2}(d_{22}\,p)\right), \tag{4.30}$$

with time dependent diffusion coefficients;

$$d_{11} = D^2\big(\big(\delta\psi^\dagger_{1,1}\big)^2 + \big(\delta\psi^\dagger_{1,2}\big)^2\big)(t+\theta), \tag{4.31}$$

$$d_{22} = D^2\big(\big(\delta\psi^\dagger_{2,1}\big)^2 + \big(\delta\psi^\dagger_{2,2}\big)^2\big)(t+\theta), \tag{4.32}$$

and

$$d_{12} = D^2\big(\delta\psi^\dagger_{1,1}\delta\psi^\dagger_{2,1} + \delta\psi^\dagger_{1,2}\delta\psi^\dagger_{2,2}\big)(t+\theta), \tag{4.33}$$

where $\delta\psi^\dagger_{i,k}$ are the components of the 4-dimensional vector-functions $\delta\psi^\dagger_i$. These diffusion coefficients are periodic with respect to time, however, since the probability density function $p(t,\theta,\varphi)$ changes slowly for $D \ll 1$, Eqs. (4.28)-(4.29) and the corresponding Fokker-Planck equation (Eq. (4.30)) can be averaged over the period T_0 of the functions $\delta\psi^\dagger_i(t+\theta)$ [KRO91]. The resulting constant diffusion coefficient of the time averaged Fokker-Planck equation,

$$\bar{d}_{11} = \frac{D^2}{T_0}\int_0^{T_0} \big(\delta\psi^\dagger_{1,1}(s)\big)^2 + \big(\delta\psi^\dagger_{1,2}(s)\big)^2 ds, \tag{4.34}$$

can be used to approximate the rate of diffusion of the time-shift $\theta(t)$. Using this diffusion coefficient the variance of the time-shift $\theta(m)$, where m is the number of roundtrips, can be estimated as

$$\mathrm{Var}(\theta) = \bar{d}_{11} m T_0, \tag{4.35}$$

where we have assumed that the average period, T_C, is approximately equal to T_0. Normalising this by the number of roundtrips, we obtain the semi-analytical estimate of the timing jitter[4]:

$$\sigma_{lt,s} = \sqrt{\bar{d}_{11} T_0} = D\sqrt{\int_0^{T_0} \big(\delta\psi^\dagger_{1,1}(s)\big)^2 + \big(\delta\psi^\dagger_{1,2}(s)\big)^2 ds}. \tag{4.36}$$

As long as other stable eigendirections do not play a significant role, this semi-analytic timing jitter is equivalent to the long-term timing jitter which was introduced in the previous section.

Comparison with the numerical long-term timing jitter

The semi-analytic timing jitter given by Eq. (4.36) is equivalent to the long-term jitter defined in Eq. (4.8), as long as all stable Floquet modes are sufficiently damped. Figure 4.6 shows a comparison between the two methods. In Fig. 4.6a the numerically calculated quantity $\sigma_{\Delta t}(m)$ (defined in Eq. (4.7)) is plotted as a

[4] The solutions to the adjoint system must be found numerically. This can be done by numerically integrating Eq. (4.17) backward in time.

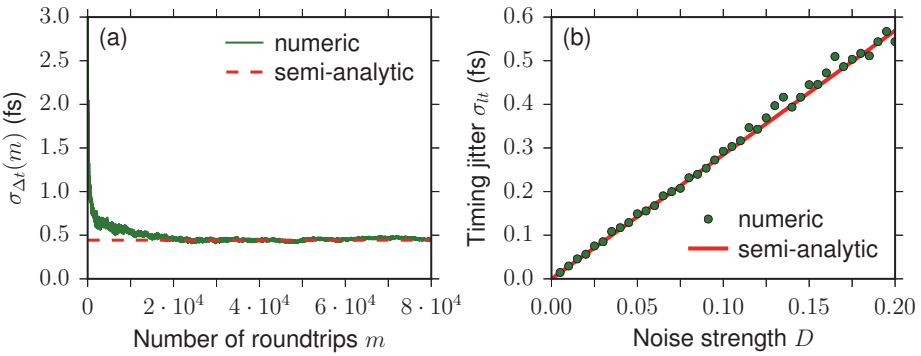

Figure 4.6.: **Semi-analytic and full numeric timing jitter:** (a) Numerically calculated $\sigma_{\Delta t}(m) = \sqrt{\mathrm{Var}(\Delta t_m)/m}$ plotted as a function of the number of laser cavity roundtrips for $\tau = 100T_{0,S}$ (green). $N = 100$ noise realisations were used for these calculations. The red dashed line indicates the values of the semi-analytically calculated long-term timing jitter. (b) Long-term jitter in dependence of the noise strength D, calculated semi-analytically from Eq. (4.36) (red) and numerically using Eq. (4.8) (green). For the full numerical calculation $N = 300$ noise realisations and $M = 4 \cdot 10^4$ roundtrips were used. Parameters: (a) $K = 0.1$ and $R_{sp} = 0.44$ ($D = 0.2$), (b) $\tau = 70T_{0,S}$ and $K = 0.1$, all other parameters as in Table 2.1.

function of the number of roundtrips (green). The long-term jitter is the value that this quantity converges to for large m. In this plot it can be seen that $\sigma_{\Delta t}(m)$ converges to the semi-analytically obtain long-term timing jitter, the value of which is indicated by the dashed red line. In Fig. 4.6b the numerically (green circles) and semi-analytically (red line) calculated values for the long-term jitter are depicted in dependence of the noise strength, showing excellent agreement between the two methods.

In the following sections we will make further comparisons between the semi-analytic and full numeric timing jitter calculations in order to demonstrate the limits in which these results are valid.

4.2.3. Experimental methods of measuring the timing jitter

For many applications of mode-locked lasers very high repetition rates are desirable. However at such high repetition rates (typically 5-80GHz [SOL93, BRE10, DRZ13, ARS14]) it is experimentally very difficult, or not practically possible due to technical limitations, to perform time domain measurements of the laser output. Therefore, information on the timing jitter is usually extracted from measurements of the power spectrum, which can be performed accurately using a fast photodiode with an electrical spectrum analyzer [KOL86, BRE10, ARS13]. The power spectrum contains contributions from both the timing fluctuations and the amplitude fluctuations, therefore it is necessary to know how these separate contributions

manifest themselves. To this end there have been a multitude of theoretical and experimental works pertaining to the spectral properties of timing and amplitude fluctuations [LIN86, HAU93a, ELI97, JIA01, PAS04, PAS04a, PAS06, KEF08]. Von der Linde showed that for uncorrelated timing and amplitude fluctuations the power spectrum at the h^{th} harmonic of the repetition frequency is composed of three contributions; a δ-function corresponding to the noise-free system, the power spectrum of the amplitude fluctuations and h^2 times the power spectrum of the timing fluctuations [LIN86]. Since the contribution from the amplitude fluctuations is independent of h, whereas the timing fluctuation contribution scales as h^2, the individual contributions can be resolved by measuring the power spectrum at the zeroth frequency component and at some higher harmonic of the repetition frequency. However, typically, it is assumed that the contribution of the amplitude fluctuations is small compared with the timing fluctuations and the timing jitter is estimated from the power spectrum at a single harmonic [KEF08, BRE10, ARS13]. Using this approach the so-called **root-mean-square (rms) timing jitter** is given by

$$\sigma_{rms}\left(f_{low}, f_{high}\right) \equiv \frac{1}{2\pi h f_{\text{rep}}} \sqrt{\int_{f_{low}}^{f_{high}} 2S_{\varphi}\left(f, h\right) df}, \tag{4.37}$$

where $S_{\varphi}\left(f, h\right)$ is the phase noise spectrum[5] and $f_{\text{rep}} = 1/T_C$ (with T_C as defined in Eq. (4.5)) is the fundamental pulse repetition frequency. The phase noise spectrum is calculated from the power spectrum of electric field amplitude $S_{|\mathcal{E}|}\left(f\right)$,

$$S_{\varphi}\left(f, h\right) \equiv \frac{S_{|\mathcal{E}|}\left(f, N\right)}{P\left(h, N\right)}, \tag{4.38}$$

where $P\left(h, N\right)$ is the power at the h^{th} harmonic [KOL86], i.e. it is the power spectrum normalised to the power at the h^{th} harmonic. Here N is the total number of integration steps. This is included to indciated that for non-stationary processes $S_{|\mathcal{E}|}\left(f, N\right)$ and $P\left(h, N\right)$ are dependent on the integration time $T_i = \Delta t N$, where Δt is the time step. The integral in Eq. (4.37) is over a single sideband of the h^{th} harmonic and runs from some low offset frequency f_{low} from hf_{rep}, to some high offset frequency f_{high}.

The Von der Linde method was developed for actively mode-locked lasers, for which the timing fluctuations are a stationary process. When applying the method to passively mode-locked lasers, for which the timing fluctuations are a non-stationary process, care must be taken because the h^2 scaling of the contribution to the power spectrum from the timing fluctuations is only true past some offset frequency f_0 from the peak of the h^{th} harmonic [KEF08, OTT14]. In [LIN11f] it was shown experimentally for a quantum-dot passively mode-locked laser that an offset of

[5] The phase noise spectrum refers to the timing phase and is not related to the phase of the optical field, as discussed in [PAS04].

1-2 MHz was required for the h^{th} scaling to hold. Below the offset f_0 there is a plateau in the peaks of phase noise spectra which arises due to the slow drift of the central frequency. Although the Von der Linde method is not valid at these low frequencies, excluding these can lead to an underestimate of the timing jitter [OTT14]. The choice of the integration limits f_{low} and f_{high} is therefore very important for passively mode-locked lasers. Since $\sigma_{rms}(f_{low}, f_{high})$ is dependent on the integration limits it is also important that these are stated with the value for the rms timing jitter.

In [OTT14, OTT14b] it was shown that, under certain conditions, the rms timing jitter is directly proportional to the long-term timing jitter which was introduced in Section 4.2.1 (Eq. (4.8)). Assuming that the timing fluctuations can be modelled by a random walk and that the integration time is long, i.e. the number of roundtrips m is large, then

$$\sigma_{rms}(f_{low}, f_{high}, T_i) \approx \frac{\sigma_{lt}}{\pi\sqrt{T_C}} \frac{1}{\sqrt{f_{low}}}. \tag{4.39}$$

The derivation of this relation can be found in [OTT14].

Another measure of the timing jitter that is commonly used experimentally is the **pulse-to-pulse timing jitter**, which is given by

$$\sigma_{\text{pp}} = T_C \sqrt{\frac{\Delta f m T_C}{2\pi}}, \tag{4.40}$$

where T_C is the mean period of the pulse train (Eq. (4.5)), m is the number of periods between the pulses being compared and Δf is the full width at half maximum of the first harmonic phase noise spectrum [KEF08]. This measure is based on the assumption that the phase noise spectrum has a Lorentzian line shape. Although the period-jitter which was introduction in Section 4.2.1 (Eq. (4.9)) is also referred to as the pulse-to-pulse jitter, these measures are different because σ_{pp} scales with $\sqrt{m}$ which is only correct for a true random walk, whereas the period-jitter depends on short-term correlations.

From Section 4.2.1 we know that for long resonant-feedback delay times the timing fluctuations can exhibit oscillations (Fig. 4.4). When these oscillations are pronounced, then the timing fluctuations cannot be modelled by a random walk, in which case σ_{lt} is ill defined and Eq. (4.39) does not hold. In the power spectra of the laser output this noise-induced modulation of the dynamics is manifested as sidepeaks offset from the main peaks (hf_{rep}) at multiples of approximately one over the feedback delay time, $1/\tau$. This is shown in Fig. 4.7 for (a) $\tau = 100T_0$ and (b) $\tau = 1000T_0$. In experimental studies of passively mode-locked lasers subject to feedback, in which such noise-induced sidepeaks are present, typically only the rms timing jitter is estimated [ARS13, DRZ13a]. However this gives only information of the long-term behaviour and not on the short-term fluctuations, which

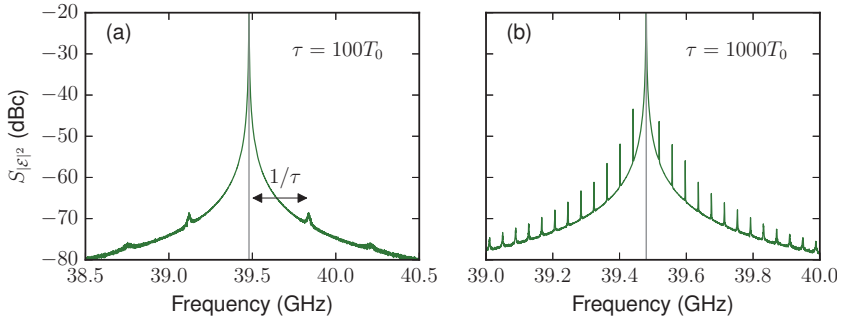

Figure 4.7.: Power spectra of the electric field amplitude $S_{|\mathcal{E}|^2}$ for (a) $\tau = 100T_0$ and (b) $\tau = 1000T_0$ averaged over $N = 100$ noise realisations. Parameters: $R_{sp} = 0.44$, $K = 0.1$, all other parameters as in Table 2.1.

can be significant for long feedback delay times. This will be discussed further in Section 5.3.

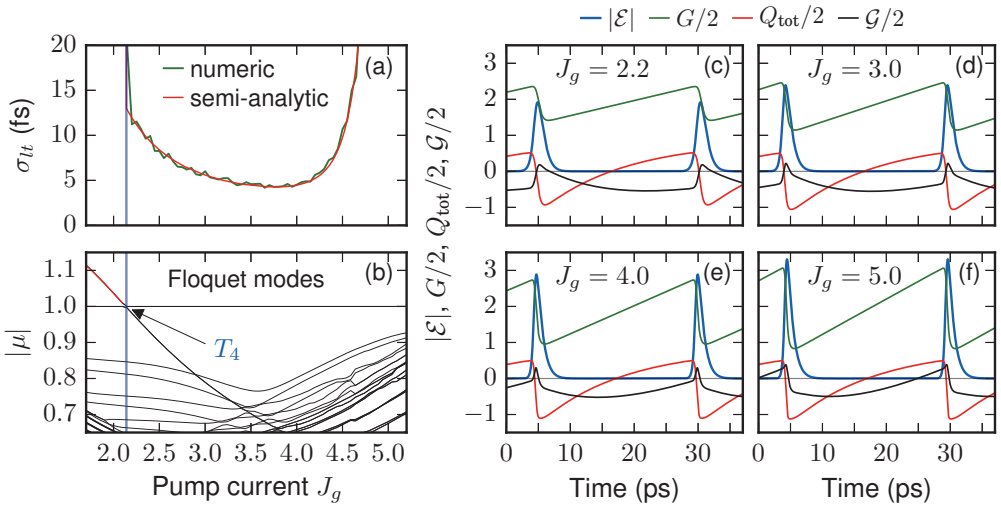

Figure 4.8.: (a) Long-term timing jitter in dependence of the pump current J_g calculated semi-analytically from Eq. (4.36) (red) and numerically using Eq. (4.8) (green). For the numerically calculated timing jitter $N = 200$ noise realisations were used. (b) Magnitude of the dominant Floquet multipliers $|\mu|$ of the solutions for $R_{sp} = 0$, in dependence of J_g. The vertical blue lines in (a) and (b) indicate the position of the T_4 torus bifurcation. (c)-(f) Time traces of the electric field amplitude $|\mathcal{E}|$ (blue), gain G (green), total losses $Q_{\rm tot} = Q - \ln(\kappa)$ (red) and the net gain $\mathcal{G} = G - Q_{\rm tot}$ (black) for J_g values indicated in the plots. Parameters: (a) $R_{sp} = 0.44$ ($D = 0.2$), all other parameters as in Table 2.1.

4.3. Timing jitter of the solitary mode-locked laser

In this section we shall investigate the influence of key laser parameters on the timing jitter. We will concentrate on the pump current J_g, the unsaturated absorption J_q, the spectral filter width γ and the amplitude-phase coupling α_g and α_q.

In Section 3.2 it was shown that various dynamics are exhibited by the solitary mode-locked laser in dependence of the pump current parameter J_g. Concentrating on the pump current range in which the laser exhibits fundamental mode-locking, the long-term timing jitter is shown in Fig. 4.8a, calculated both numerically (green) using Eq. (4.8) and semi-semi-analytically (red) using Eq. (4.36). First, we note that there is excellent agreement between the values obtained using these two methods, even near the torus bifurcation (vertical blue line) past which the fundamental mode-locked solution is stable. The onset of stable mode-locking occurs at approximately $J_g = 2.1$ for the parameters used in these calculations, this coincides with the position of the steep drop in the timing jitter.[6] As the

[6] In fact, below this point both the numerical and the semi-analytic methods of calculating the timing jitter are not applicable. For the numerical method this is because the timing fluctua-

pump current is increased from this point the timing jitter first decreases and then increases rapidly near $J_g = 4.5$.

In the derivation of the semi-analytic method it was assumed that only perturbations in the direction of the neutral mode, corresponding to the time-shift invariance of the deterministic system, contribute to the long-term timing jitter. To confirm that other eigendirections do not influence the timing jitter, the magnitude of the dominant Floquet multipliers $|\mu|$ of the solutions to the deterministic system ($R_{sp} = 0$) are shown in Fig. 4.8b. Below $J_g \approx 2.1$ the mode-locked solution is unstable, which is indicated by the $|\mu| > 1$ section plotted in red. Just past the torus bifurcation the excellent agreement between the semi-analytic and numerical methods indicates that the weakly damped modes do not influence the timing jitter. For all higher currents depicted in this figure the mode-locked solution remains stable, and where the timing jitter increases rapidly near $J_g = 4.5$, the stable modes are still highly damped and have no impact on the timing jitter.

In order to gain some insights into the mechanisms leading to variations in the timing jitter, time traces of the deterministic dynamics are shown for various pump currents in Fig. 4.8 (c)-(f). Comparing the dynamics depicted in these plots several trends can be identified. Firstly, in the current range from $J_g \approx 2.1$ to $J_g \approx 4.0$, in which the timing jitter decreases, the pulses becomes narrower. Secondly, in this current range the net gain (black) on the trailing side of the pulse decreases, while on the leading flank of the pulse it increases. Furthermore, the rapid increase in the timing jitter near $J_g = 4.5$ coincides with the pump current range where the net gain becomes positive before the leading edge of the pulse. All together these results indicate that narrower, more energetic pulses have a lower timing jitter, however, only as long as there is no leading edge instability, in the sense of New's stability criterion [NEW74]. Further evidence of the relation of the pulse width to the timing jitter is shown in Fig. 4.9, where the timing jitter is depicted in dependence of the pump current and the spectral filter width γ. From the results presented in Section 3.2 it is known that the pulses become narrower and have a higher peak intensity as γ is increased (see Fig. 3.15), and Fig. 4.9 shows that this coincides with a decrease in the timing jitter.

The pump current at which the timing jitter increases in Figs. 4.8 and 4.9 ($J_g \approx 4.5$) corresponds to the onset of bistability between the fundamental and 2^{nd} harmonic mode-locked solutions (see Fig. 3.17 in the previous chapter). The appearance of this second stable solution has no direct influence on the timing jitter of the fundamentally mode-locked solution, however, for large noise strengths there is the potential for noise-induced switching between bistable solutions. Indirectly the onset of stable 2^{nd} harmonic mode-locking is related to the increase in the tim-

tions, as they have been defined in Subsection 4.2.1, do not behave like a random walk, and for the semi-analytic method it is because the underlying deterministic dynamics are not periodic.

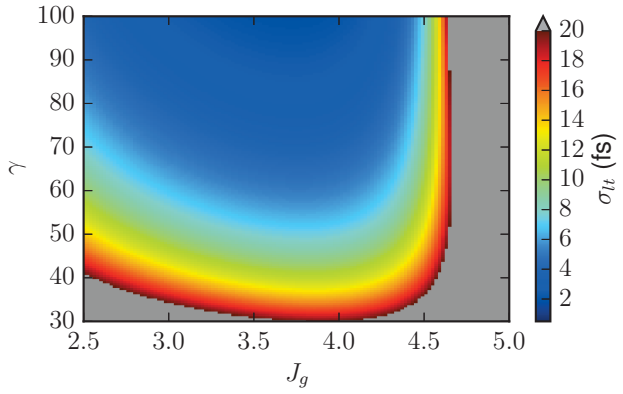

Figure 4.9.: Long-term timing jitter in dependence of the pump current J_g and the spectral filter width γ calculated semi-analytically using Eq. (4.36). The grey regions indicate timing jitter values above 20 fs. Parameters: $R_{sp} = 0.44$ ($D = 0.2$), all other parameters as in Table 2.1.

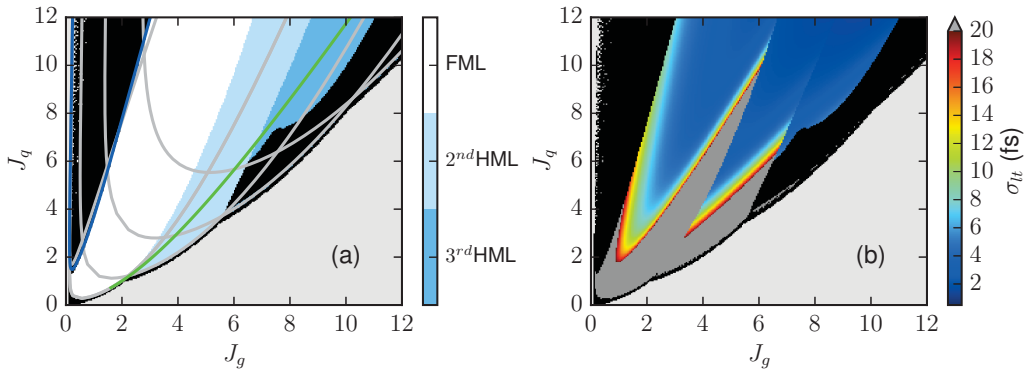

Figure 4.10.: (a) Map of the dynamics of solutions in the J_g-J_q parameter plane. Fundamental mode-locking is indicated by the white regions and the blues indicate harmonic mode-locking. In the light grey regions the laser is either in the off or cw states. Blacks indicates non-periodic dynamics. The grey, blue and green lines indicate the positions of the Hopf, torus and saddle-node bifurcations depicted in Fig. 3.10. (b) Semi-analytically calculated long-term timing jitter corresponding to the mode-locked solutions depicted in (a). The dark grey regions indicate timing jitter values above 20 fs. Parameters: $\kappa = 0.121$, $R_{sp} = 0.44$ ($D = 0.2$), all other parameters as in Table 2.1.

ing jitter of the fundamentally mode-locked solution since these are both caused by the net gain becoming too large for stable (in the sense of New's stability criterion [NEW74]) single pulse emission.

In Fig. 4.10 the timing jitter of fundamentally and harmonically mode-locked solutions is shown in the J_g-J_q parameter plane. Subplot (b) shows the timing jitter and the corresponding dynamics are indicated in subplot (a). No timing

jitter is indicated in the black and light grey regions because in these regions the dynamics are either non-periodic or the system is in a steady state. The parameters used here are the same as those used in the bifurcation diagram depicted in Fig. 3.10 and as a reference the positions of the Hopf bifurcations, saddle-node bifurcations and some of the torus bifurcations are indicated in Fig. 4.10a by the grey, green and blue lines, respectively. The general trends shown in Fig. 4.10b are that the timing jitter is lower for higher unsaturated absorption values and that the harmonically mode-locked solutions have a slightly lower timing jitter than the fundamentally mode-locked solution. The latter can be understood by considering that at higher pump currents there is more energy in the system and therefore the noise has a smaller influence. The result that lower timing jitter values are obtained for larger J_q values cannot be directly related to the bias dependence in real devices. This is because the reverse bias applied to the saturable absorber section also influences other parameters in the DDE model, as discussed in Subsection 2.2.2. However, the trend that higher pump currents are required when the reverse bias of the absorber section is increased still holds, meaning that if the timing jitter can be improved by increasing the reverse bias, this will be limited by device heating at high pump currents.

4.3.1. Influence of the amplitude-phase coupling on the timing jitter

For the dynamics of the mode-locked laser the amplitude-phase coupling was also found to be an important parameter. The results of Subsection 3.2.3 showed that with non-zero amplitude-phase coupling the dynamics generally become more complex and the regions of stable mode-locking become smaller. In light of these results, the influence of the amplitude-phase coupling on the timing jitter is at first slightly counter intuitive. Figure 4.11a depicts the timing jitter in dependence of the pump current for various α-factor values. These results show that the timing jitter is smaller for non-zero amplitude-phase coupling, despite the dynamics being more complex, i.e. the pulses also being chirped. The cause of this reduction in the timing jitter is not entirely clear. In Fig. 4.11b the pulse shapes are shown for $\alpha_g = \alpha_q = 0$ (red) and $\alpha_g = \alpha_q = 3$ (green) at a pump current of $J_g = 3.5$. This plot shows that for $\alpha_g = \alpha_q = 3$ the pulse is narrower than in the $\alpha_g = \alpha_q = 0$ case, which we earlier found to be a factor leading to lower timing jitter values. In order to ascertain whether the chirp also has an influence on the timing jitter, we have found parameters ($\gamma = 112$ and $J_g = 2.4$) for the zero α-factor case for which the pulse shape is identical to that for $\alpha_g = \alpha_q = 3$ with $J_g = 3.5$ (shown in Fig. 4.11c). Despite the identical pulse shapes, the timing jitter is still lower for the $\alpha_g = \alpha_q = 3$ case ($\sigma_{lt} = 2.87\,\text{fs}$ for $\alpha_g = \alpha_q = 3$ with $J_g = 3.5$ versus $\sigma_{lt} = 3.76\,\text{fs}$

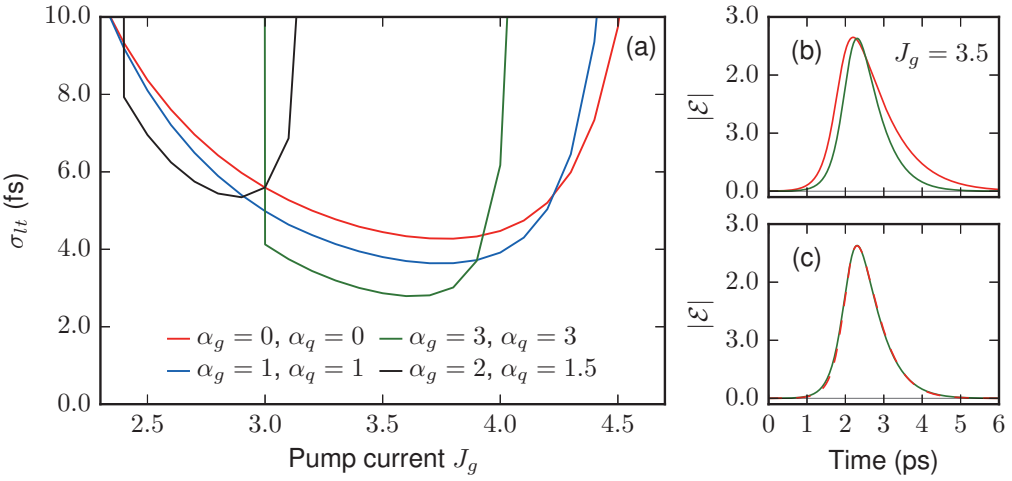

Figure 4.11.: (a) Semi-analytically calculated long-term timing jitter in dependence of the pump current J_g for various amplitude-phase coupling values. (b) The pulse shapes for $\alpha_g = \alpha_q = 0$ (red) and $\alpha_g = \alpha_q = 3$ (green), with $J_g = 3.5$. (c) The pulse shapes for $\alpha_g = \alpha_q = 3$ (green), with $J_g = 3.5$ and $\alpha_g = \alpha_q = 0$ (red dashed), with $\gamma = 112$ and $J_g = 2.4$. Parameters: $\kappa = 0.1$, $R_{sp} = 0.44$ ($D = 0.2$), all other parameters as in Table 2.1.

for $\alpha_g = \alpha_q = 0$ with $J_g = 2.4$ and $\gamma = 112$). The chirp therefore seems to lead to a reduction in the timing jitter.

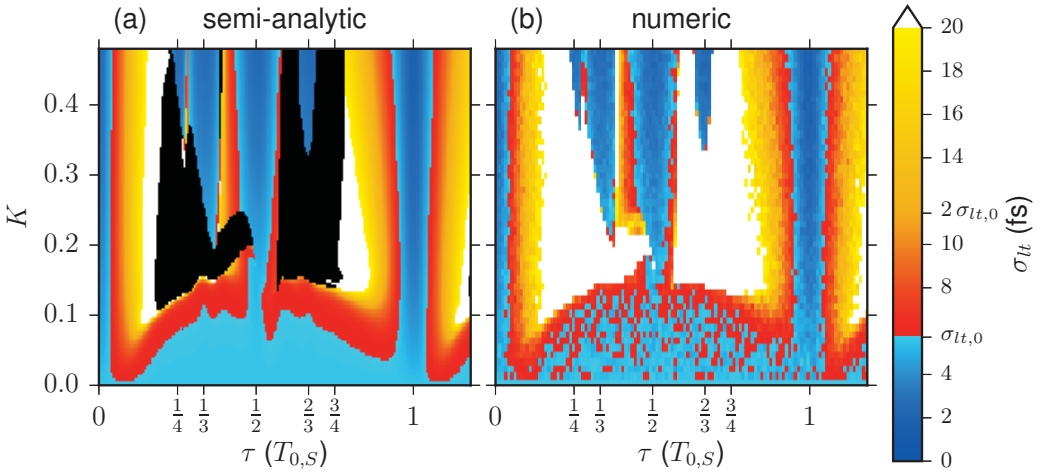

Figure 4.12.: (a) Semi-analytically calculated long-term timing jitter in the τ-K parameter plane. The black regions indicate parameter values where the dynamics are non-periodic and the semi-analytically method is not applicable. (b) Numerically calculated long-term timing jitter in the τ-K parameter plane. $N = 100$ noise realisations were used for these calculations. The value of the timing jitter is indicated by the colour code, where $\sigma_{lt,0}$ is the timing jitter of the solitary laser. Parameters: $R_{sp} = 0.44$ ($D = 0.2$), all other parameters as in Table 2.1.

4.4. Timing jitter under the influence of feedback from a single external cavity

In this section the impact of feedback, from one external cavity, on the timing jitter will be discussed. We will show that for resonant feedback delay times the timing jitter is reduced. Furthermore, we will derive an analytic expression for the dependence on resonant delay times which shows that the timing jitter reduction increases for longer feedback delay times.

4.4.1. Feedback delay time and feedback strength dependence of the timing jitter

In the short feedback delay regime ($\tau \approx 1$) the influence of single-cavity feedback on the timing jitter can largely be inferred from the dynamics discussed in Subsection 3.3.1 and the pulse shapes shown in Subsection 3.3.4. In parameter regions where the feedback causes the main pulses to become wide or not well separated from satellite pulses, the timing jitter will be increased. For resonant feedback, increasing the feedback strength lowers the losses which leads to peaks with a higher amplitude. These peaks are less influenced by the noise and hence, the timing jitter is decreased. These trends are confirmed by the timing jitter results depicted in Fig. 4.12. Here results are shown for both the semi-analytic (a) and the numeric

(b) timing jitter calculations (Eq. (4.36) and Eq. (4.8), respectively) to confirm that also in these parameter regions there is excellent agreement between the two methods. The magnitude of the timing jitter is given by the colour code, where blues indicate a reduction with respect to the solitary laser timing jitter $\sigma_{lt,0}$ and reds an increase. White regions indicate a timing jitter greater than 20 fs. The black regions in Fig. 4.12a are parameter ranges where the semi-analytic calculation is not applicable because the dynamics are non-periodic. Accordingly, the fully numerical calculations of the timing jitter yield very large values in these regions. The dynamics corresponding to these jitter calculations are depicted in Fig. 3.30 in the previous chapter. Figure 4.12 shows that the timing jitter is only reduced in a small range near the main resonances. For larger offsets the changes in the pulse shape cause the timing jitter to increase. This is shown more clearly in Fig. 4.13, which shows the timing jitter in the first main resonance region (a), as well as the pulse shape and net gain at selected delay times (b) (also see Fig. 3.66 for examples of the pulse shapes in the main resonance regions). At lower feedback strengths the timing jitter shows very little dependence on higher order resonant delay times (fractional resonances). This is because the timing jitter is mainly determined by the main pulse. When the satellite pulses are well separated from the main pulse, their exact position within the limit cycle has no significant influence on the timing jitter.

To study the feedback delay time dependence of the timing jitter over larger delay ranges, we concentrate on the low feedback strength regime. In Fig. 4.14a-b the timing jitter is shown as a function of τ for $\tau \approx 10$ and $\tau \approx 150$, respectively. The horizontal dashed line indicates the timing jitter of the solitary laser. Here it can be seen that near the main resonances the timing jitter is decreased and that a greater improvement in the timing jitter is achieved in the main resonances for longer delay times. To highlight the change in the timing jitter for long delay times, green has been introduced into the colour code, indicating a reduction in the timing jitter of a factor of 10 or greater. Figure 4.14a-b also shows that there is very little change in the timing jitter from one resonances to the next, but a drastic change over longer τ ranges. In order to see this change over longer τ ranges more clearly, in Fig. 4.14c the timing jitter is depicted in a pseudo space-time-like plot for the range $\tau = [0.5T_{0,K}, 200.5T_{0,K}]$, where the delay time is split into two components; $\tau = \tau_s + nT_{0,K}$. Changes on small scales are given by variations along the τ_s axis and large scale changes can be seen along the n axis. The exact main resonances are the solutions along $\tau_s = 0$ (dashed white line). The dashed black line indicates the extent of the main resonance locking regions as defined by Eqs. (3.17)-(3.18). For $n > 50$ these dashed lines intersect high timing jitter solutions which correspond to solutions with multi-pulse dynamics. This is because for large delay times there is bistability between the fundamentally mode-locked solution and solutions with feedback induced satellite pulses (for example

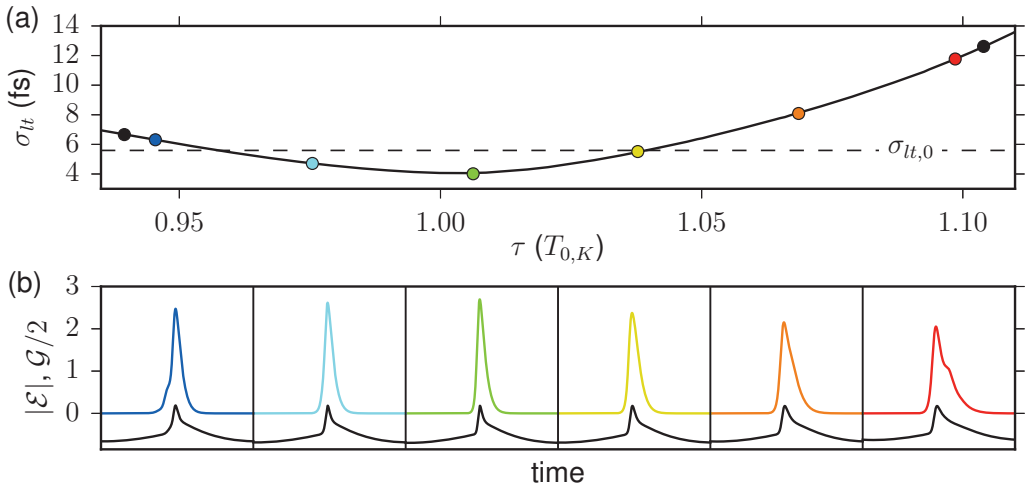

Figure 4.13.: **Influence of pulse shape on the timing jitter:** (a) Semi-analytically calculated long-term timing jitter in dependence of τ, near the first main resonance. The black circles indicate the extent of the locking region defined by Eqs. (3.17)-(3.18). (a) Electric field pulse profiles corresponding to the feedback delay times indicated by the coloured circles in (a). The net gain is depicted in black. Parameters: $K = 0.1$, $R_{sp} = 0.44$ ($D = 0.2$), all other parameters as in Table 2.1.

see Fig. 3.57). For the initial conditions used to obtain these results the system happens to converge to the multi-pulse solutions in these regions. The general trends shown in this plot are that the timing jitter decreases with increasing n and is smallest towards the center on the locking regions. However, the solution within each main resonance locking region with the minimum timing jitter is not the solution exactly at the main resonances, but rather is shifted to slightly larger delay times (dash-dotted white line). A possible reason for this is that the feedback delay time is slightly longer, while the pulse is not appreciably widened so close to the main resonance.

Analytic dependence of the timing jitter on the resonance number

To obtain the results present in Fig. 4.14 the semi-analytic method was applied at each feedback delay time value. However, provided that the phase difference between the light in the laser and feedback cavities is zero, and that the solutions are stable, if the timing jitter is known for the feedback delay times in the range $\tau = [0, T_{0,K}]$ then for all $\tau > T_{0,K}$ the feedback delay time dependence of the timing jitter can be described analytically. This can be done by making use of the fact that solutions repeat at delay times that are increased by integer multiples of the period (as discussed in Subsection 3.3.4). If $\tau = \tau_0$ is a delay time between zero and

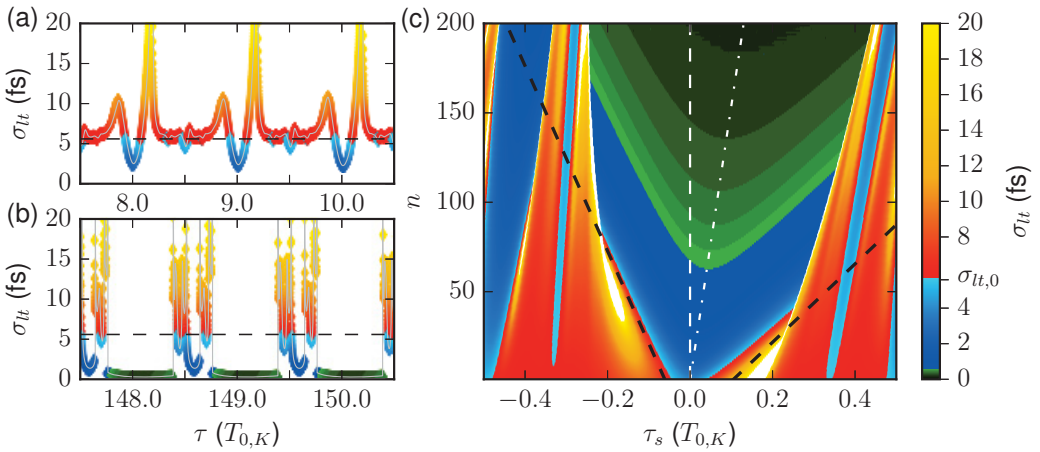

Figure 4.14.: (a)-(b) Semi-analytically calculated long-term timing jitter as a function of τ. (c) Semi-analytically calculated long-term timing jitter as a function of τ_s and q, where $\tau = \tau_s + qT_{ISI,K}$ and $T_{ISI,K}$ is the period of the solution for $\tau = 0$. The dashed black lines indicated the extent of the main resonance locking regions. The dashed and dash-dotted white lines indicate the position of the exact main resonances and the minimum jitter in each main resonance region, respectively. Parameters: $K = 0.1$, $R_{sp} = 0.44$ ($D = 0.2$), all other parameters as in Table 2.1. Figure modified from [JAU15]. Copyright (2015) by the American Physical Society.

$T_{0,K}$, and the corresponding solution is periodic, with period T_0, then the solution reappears at all

$$\tau = \tau_0 + nT_0 \tag{4.41}$$

for integer n. Following the analysis presented in [JAU15], the bilinear form (Eq. (4.16)) can be rewritten as

$$\begin{aligned}\left[\delta\psi^\dagger, \delta\psi\right](t) = \delta\psi^\dagger(t)\delta\psi(t) &+ \int_{-T}^{0} \delta\psi^\dagger\left(t+r+T\right) B_0\left(t+r\right) \delta\psi\left(t+r\right) dr \\ &+ \int_{-T-\tau_0}^{0} \delta\psi^\dagger\left(t+r+T\right) B_1\left(t+r\right) \delta\psi\left(t+r\right) dr \\ &+ \int_{-T-\tau_0-nT_0}^{-T-\tau_0} \delta\psi^\dagger\left(t+r+T\right) B_1\left(t+r\right) \delta\psi\left(t+r\right) dr\end{aligned} \tag{4.42}$$

for the single cavity feedback case. Due to the time shift invariance and periodicity of the integrand, the last term on the right-hand side can be further simplified, giving

$$\left[\delta\psi^\dagger, \delta\psi\right] = \left[\delta\psi^\dagger, \delta\psi\right]^{\tau=\tau_0} + n\int_{-T_0}^{0} \left(\delta\psi^\dagger\left(t+r+T\right)\right)^{\mathrm{T}} B_1\left(t+r\right) \delta\psi\left(t+r\right) dr, \tag{4.43}$$

where the first three terms on the rhs of Eq. (4.42) are now expressed as $\left[\delta\psi^{\dagger}, \delta\psi\right]^{\tau=\tau_0}$, which is the bilinear form for the K dependent solution with $\tau = \tau_0$. Equation (4.36) can now be expressed as

$$\sigma_{lt} = D\Bigg(\int_0^{T_0} \left(\frac{\delta\psi_{1,1}^{\dagger *}(t)}{\left[\delta\psi_1^{\dagger *}, \delta\psi_1^{*}\right]^{\tau=\tau_0} + Kn\mathcal{F}'(K,\tau_0)} \right)^2 + \left(\frac{\delta\psi_{1,2}^{\dagger *}(t)}{\left[\delta\psi_1^{\dagger *}, \delta\psi_1^{*}\right]^{\tau=\tau_0} + Kn\mathcal{F}'(K,\tau_0)} \right)^2 dt \Bigg)^{1/2}, \tag{4.44}$$

where $\frac{\delta\psi_1^{(\dagger)*}}{\left[\delta\psi_1^{\dagger *}, \delta\psi_1^{*}\right]} = \delta\psi_1^{(\dagger)}$ and

$$\mathcal{F}'(K,\tau_0) = \frac{1}{K}\int_{-T_0}^{0} \delta\psi_1^{\dagger *}(t+r+T)\, B_1(t+r)\, \delta\psi_1^{*}(t+r)\, dr,$$

which is a function of K and τ_0 but not of n. The explicit K dependence has been removed from $\mathcal{F}'(K,\tau_0)$ by dividing by K, but it still implicitly depends on K via the influence of the feedback strength on the dynamics of the unperturbed solution which enters in the Jacobian B_1 (see Appendix B). Equation (4.44) can be simplified to

$$\sigma_{lt} = \frac{1}{1 + Kn\mathcal{F}'(K,\tau_0)} \sqrt{D^2 \int_0^{T_0} \left(\delta\psi_{1,1}^{\dagger\tau=\tau_0}(t)\right)^2 + \left(\delta\psi_{1,2}^{\dagger\tau=\tau_0}(t)\right)^2 dt}, \tag{4.45}$$

where $\delta\psi_1^{\dagger\tau=\tau_0} = \left(\delta\psi_{1,1}^{\dagger\tau=\tau_0}, \delta\psi_{1,2}^{\dagger\tau=\tau_0}, \delta\psi_{1,3}^{\dagger\tau=\tau_0}, \delta\psi_{1,4}^{\dagger\tau=\tau_0}\right)^{\mathrm{T}}$ is the solution fulfilling the biorthogonality condition (Eq. (4.18)) for $\tau = \tau_0$, and $\mathcal{F}(K,\tau_0) = \frac{\mathcal{F}'(K,\tau_0)}{\left[\delta\psi_1^{\dagger *}, \delta\psi_1^{*}\right]^{\tau=\tau_0}}$. Finally, the timing jitter is given by

$$\sigma_{lt}(\tau_0, n, K) = \frac{\sigma_{lt}(K,\tau_0)}{1 + Kn\mathcal{F}(K,\tau_0)}, \tag{4.46}$$

where $\sigma_{lt}(K,\tau_0)$ is the K dependent timing jitter for $\tau = \tau_0$. This means that if $\sigma_{lt}(K,\tau_0)$ and $\mathcal{F}(K,\tau_0)$ are calculated for any periodic solutions in the delay range $\tau = [0, T_{ISI,K}]$ the timing jitter for all reappearances of that solution at longer delay times is given analytically by Eq. (4.46). This holds up to delay times where the semi-analytic method is valid.

For timing jitter reduction it is mainly the main resonant delay times ($\tau = nT_{0,K}$ with integer n) which are of interest, since the dynamics are not qualitatively changed under such feedback conditions. In Fig. 4.15 the timing jitter (a) and $\mathcal{F}(K,\tau_0)$ (b) are shown as a function of K for $\tau = 0$. The dashed black lines show fits of the semi-analytic results, where the fit functions are

$$\sigma_{lt}^{\tau=0}(K) = \frac{\sigma_{lt,0}}{1 + 2.6K + 0.2K^2} \tag{4.47}$$

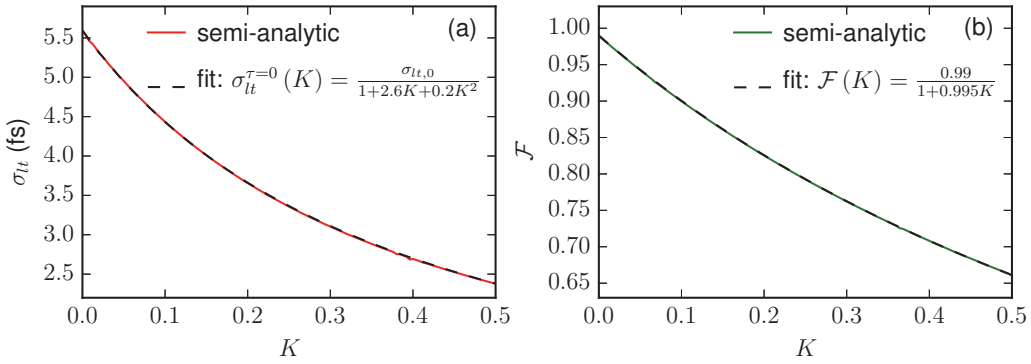

Figure 4.15.: (a) Semi-analytically calculated long-term timing jitter as a function of K for $\tau = 0$. (b) Semi-analytically calculated $\mathcal{F}(K, \tau_0)$ for $\tau = \tau_0 = 0$. The dashed black lines are the fit functions given in (a) and (b), where $\sigma_{lt,0} = 5.593\,\text{fs}$ is the timing jitter of the solitary laser. Parameters: $\tau = 0$, $R_{sp} = 0.44$ ($D = 0.2$), all other parameters as in Table 2.1.

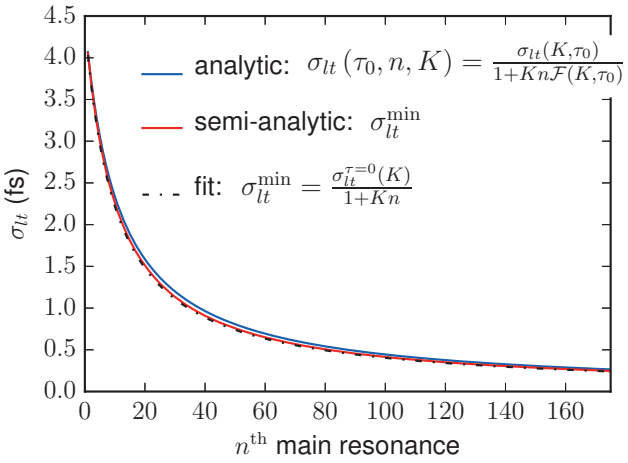

Figure 4.16.: Timing jitter at the main resonances (blue) given by Eqs. (4.46), (4.47) and (4.48) for $K = 0.1$ The red line shows the minimum timing jitter within each main resonance region and corresponds to the τ along the dsah-dotted white line in Fig. 4.14 (c). The dash-dotted black is the fit of Eq. (4.49) to the minimum timing jitter. Parameters: $K = 0.1$, $R_{sp} = 0.44$ ($D = 0.2$), all other parameters as in Table 2.1. Figure modified from [JAU15]. Copyright (2015) by the American Physical Society.

and

$$\mathcal{F}(K) = \frac{0.99}{1 + 0.995K}, \tag{4.48}$$

where $\sigma_{lt,0} = 5.593\,\text{fs}$ is timing jitter of the solitary laser. Using these fitted functions and Eq. (4.46) the timing jitter at the main resonances can be determined. For $K = 0.1$, i.e. corresponding to the results along the dashed white line in

Fig. 4.14c, the n dependence of the timing jitter is depicted in Fig. 4.16 (blue line). Also shown in this plot is the semi-analytically obtained minimum timing jitter (red line), which corresponds to the dash-dotted white line in Fig. 4.14c. For the solutions along this line the n dependence cannot be analytically derived because the dynamics of the solutions vary. However, fitting these solutions shows that the minimum jitter can be described by

$$\sigma_{lt}^{\min} = \frac{\sigma_{lt}^{\tau=0}(K)}{1+Kn}. \tag{4.49}$$

Although this is only shown in Fig. 4.16 for $K = 0.1$, this n dependence of the minimum timing jitter was also found to hold for other K values. A similar dependence on τ and K is found for the linewidth of a single-mode laser subject to feedback. The authors of [KIK82] and [AGR84] found that the variance of phase-fluctuations, which are related to the linewidth of the lasing mode, decrease by a factor $(1+\tau K X)^2$ where X is some function of the system parameters.

From the derivation of Eq. (4.46) the reduction of the timing jitter with increasing n can be directly attributed to the increased history of the solutions. A physically intuitive explanation is that the feedback term causes the current pulse to be correlated with the position of the pulse at time $t-\tau$, i.e. it gets pulled towards this position. This continual pulling back of the pulse positions means that the timing fluctuations cannot deviate as far from the mean, hence the variance is smaller so the timing jitter is reduced.

Very long feedback delay times - failure of the semi-analytic method

We have previously mentioned that the semi-analytic method is only valid if all eigenmodes apart from the neutral modes are sufficiently damped. For the solitary laser, despite this condition, excellent agreement was found between the fully numerical and semi-analytic calculations even when the system was very close to a bifurcation (see Fig. 4.8). However, with feedback, if the delay time is long, this is no longer the case. For longer delay times some eigenmodes of the system are only weakly damped and these can be excited by the noise term, which leads to a modulation of the dynamics with frequency components given by the imaginary part of the weakly damped Floquet exponents. This will be discussed in detail in the next chapter.

For the laser parameters used in this section (see Table 2.1) the semi-analytic method is valid up to feedback delay times of approximately $\tau = 200 T_{0,K}$. For larger delay times, the noise-induced modulations lead to the numerical estimates of the long-term timing jitter being larger than the semi-analytic value. This is shown in Fig. 4.17, where the red line shows the analytic n dependence given by Eq. (4.46) and the green circles show the fully numerical results estimated from

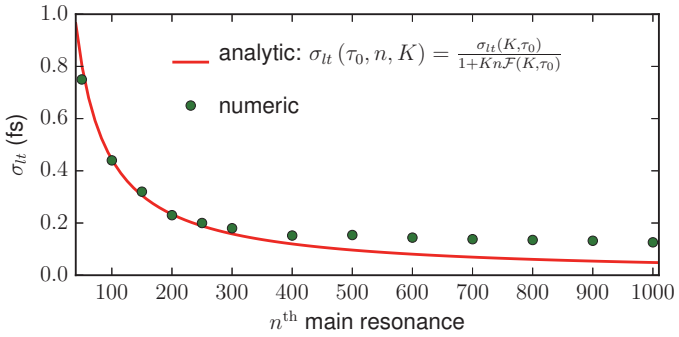

Figure 4.17.: Long-term timing jitter in dependence of resonant feedback delay times $\tau = nT_{0,K}$. The red line shows the analytically derived n dependence (Eq. (4.46)) and the green circles show results of numerical estimations of the long-term timing jitter. Parameters: $K = 0.1$, $R_{sp} = 0.44$ ($D = 0.2$), all other parameters as in Table 2.1.

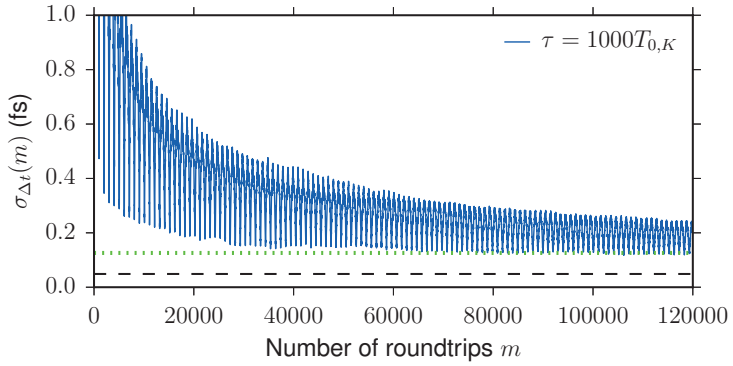

Figure 4.18.: $\sigma_{\Delta t}(m) = \sqrt{\text{Var}(\Delta t_m)/m}$ plotted as a function of the number of laser cavity roundtrips for $\tau = 1000T_{0,K}$. $N = 100$ noise realisations were used for these calculations. The dashed black line indicates the value of the semi-analytically calculated long-term timing jitter. The dotted green line indicates the value of the long-term timing jitter estimated from $\sigma_{\Delta t}(m)$. Parameters: $K = 0.1$, $R_{sp} = 0.44$ ($D = 0.2$), all other parameters as in Table 2.1.

the roundtrip number dependence of $\sigma_{\Delta t}(m)$ (defined in Eq. (4.7)). Due to the noise-induced modulation of the dynamics for large delay times (see Fig. 4.4 for examples of the noise-induced modulation of the timing fluctuations), the variance of the timing fluctuations oscillates with a periodicity given by τ, as shown in Fig. 4.18 for $\tau = 1000T_{0,K}$ (also see Fig. 4.3). Thus, there is no clear value that $\sigma_{\Delta t}(m)$ converges to, in such case. Therefore, for the large τ values in Fig. 4.17, we have estimated the long-term timing jitter as the value that the minima of $\sigma_{\Delta t}(m)$ converge to for large m. In Fig. 4.18 this estimate corresponds to the dotted green line. The horizontal dashed line indicates the semi-analytically obtained value.

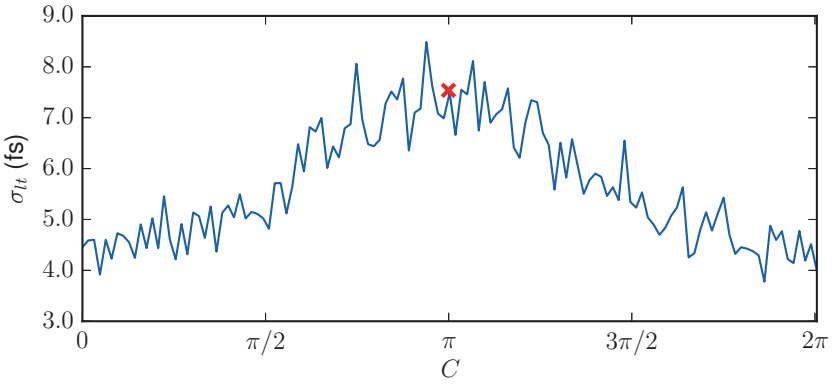

Figure 4.19.: Numerically calculated long-term timing jitter in dependence of the feedback phase C. $N = 100$ noise realisations were used for these calculations. The red cross markers timing jitter value obtained from Eq. (4.47) for $K = -0.1$, which is equivalent to Ke^{iC} with $C = \pi$. Parameters: $K = 0.1$, $\tau = 0$, $R_{sp} = 0.44$ ($D = 0.2$), all other parameters as in Table 2.1.

4.4.2. Feedback phase dependence of the timing jitter

So far we have not considered the influence of the feedback phase on the timing jitter. We have addressed the influence of the feedback strength and feedback delay time, and have shown that there are two main factors contributing to the timing jitter. Firstly, the timing jitter depends on the feedback induced dynamics of the unperturbed system and secondly, for all periodic solutions the timing jitter decreases for increasing resonance number n. The influence of the feedback phase is entirely encompassed in the first factor, i.e. the phase only influences the timing jitter insofar that it influences the dynamics. As discussed in depth in Subsections 3.3.1, 3.3.2 and 3.3.3 the feedback phase changes the effective non-resonant losses and can cause the frequency of the lasing modes to shift with respect to the center of the spectral filter in order to minimise destructive interference. For mode-locked solutions this just means that the timing jitter can increase slightly when $C \neq 2\pi n$ for $n = 0, 1, 2...$, since the pulse heights are reduced (see Fig. 3.41), meaning that the comparative influence of the noise is increased. In Fig. 4.19 an example of the feedback phase dependence of the timing jitter is shown for $\tau = 0$ and $K = 0.1$. These results are obtained using the numerical method, i.e. using Eq. (4.8). For $C = \pi$ the fed-back light interferes entirely destructively with the light in the laser cavity and the feedback conditions are equivalent to $K = -0.1$ with $C = 0$, since $e^{i\pi} = -1$. Using the fitted equation for the semi-analytically calculated K dependence at $\tau = 0$ (Eq. (4.47)) the timing jitter value marked by the red cross in Fig. 4.19 is obtained for $K = -0.1$, which is in excellent agreement with the numerical results.

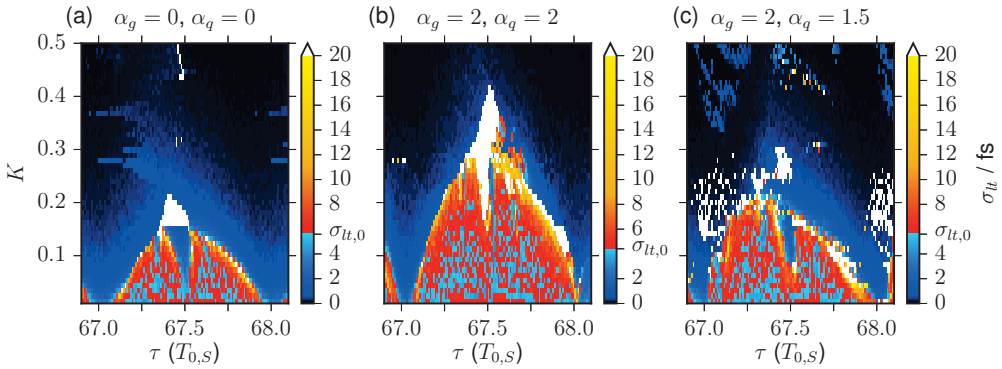

Figure 4.20.: **Influence of amplitude-phase coupling:** Numerically calculated long-term timing jitter in dependence of the feedback delay time τ and the feedback strength K for (a) $\alpha_g = \alpha_q = 0$, (b) $\alpha_g = \alpha_q = 2$ and (c) $\alpha_g = 2$ and $\alpha_q = 1.5$. $N = 50$ noise realisations were used for these calculations. Parameters: $R_{sp} = 0.44$ ($D = 0.2$), all other parameters as in Table 2.1.

4.4.3. Influence of amplitude-phase coupling on the timing jitter

Including non-zero amplitude phase coupling does not qualitatively change the trends found for the dependence of the timing jitter on the feedback parameters. As discussed in Subsection 3.3.1, as the feedback delay time is varied the phase difference between the field in the laser and feedback cavities also changes. Therefore if only τ is varied then the timing jitter can change non-monotonically between main resonances regions. However, if the feedback phase is varied simultaneously to achieved constructive interference, then the same trends are found as in the zero α-factor case. However, the system is still more phase sensitive with non-zero amplitude-phase coupling. But the influence of this is again manifested through the underlying deterministic dynamics.

In Fig. 4.20 examples of τ-K dependence of the timing jitter are shown for (a) $\alpha_g = \alpha_q = 0$, (b) $\alpha_g = \alpha_q = 2$ and (c) $\alpha_g = 2$ and $\alpha_q = 1.5$.[7] in all three cases a cone shaped region can be identified near the main resonances, in which the timing jitter is reduced. However, in the $\alpha_g = 2$ and $\alpha_q = 1.5$ case there are τ-K parameters for which the timing jitter is very high. These high timing jitter values are due to the underlying dynamics being non-periodic due to the phase difference

[7] Figure 4.20 was obtain by numerically calculating the long term jitter using Eq. (4.8). For the stochastic method care needs to be taken when the delay times are long because when the noise term is switched on the system can converge to different solutions, i.e. apart from statistical deviations the system can converge to solutions with distinctly different mean interspike-interval times. This was also found by the authors of [SIM14] who studied the influence of feedback on a quantum-dot passively mode-locked laser. This leads to erroneously large timing jitter values and is different from situations in which there is noise-induced switching between different solutions.

between the field in the laser and feedback cavities. The speckled appearance of these regions is related to the fact that the same initial conditions were used for each τ-K point in Fig. 4.20.

The results shown in Fig. 4.20 are qualitatively very similar to the experimental results presented in [ARS13]. In [ARS13] the results of timing jitter measurements for a quantum-dot passively mode-locked laser subject to optical feedback are presented. These measurements show a cone shaped region of low timing jitter. At low feedback strengths, between the cones of low timing jitter, there are regions where the timing jitter is approximately the same as in the solitary laser case, which corresponds to the multi-pulse regions in the numerical simulations where the timing jitter is also close to $\sigma_{lt,0}$.

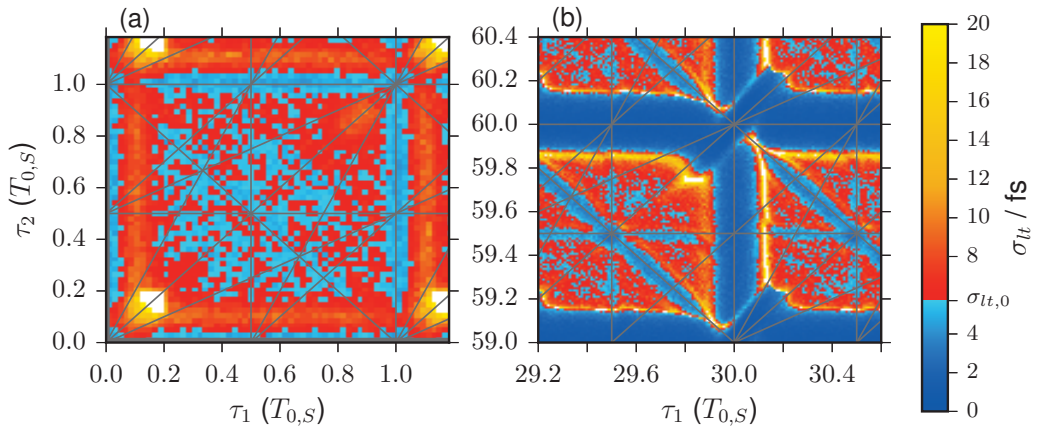

Figure 4.21.: Numerically calculated long-term timing jitter in dependence of the feedback delay times τ_1 and τ_2 for $K_1 = K_2 = 0.05$. $N = 100$ noise realisations were used for these calculations. The grey lines correspond to the resonance lines defined by Eq. (3.25). The value of the timing jitter is indicated by the colour code, where $\sigma_{lt,0}$ is the timing jitter of the solitary laser. Parameters: $R_{sp} = 0.44$ ($D = 0.2$), all other parameters as in Table 2.1.

4.5. Timing jitter under the influence of feedback from two external cavities

For feedback from a single external cavity we have shown that the timing jitter is largely determined by the underlying deterministic dynamics of the mode-locked laser system and by the resonance number of the feedback delay time. With a second feedback cavity added to the system the results are qualitatively the same, as will be shown in this section. In this section we will also present a comparison with experimental results for a passively mode-locked quantum-dot semiconductor laser subject to feedback from two external cavities.

4.5.1. Feedback delay time and feedback strength dependence of the timing jitter

The timing jitter is shown in dependence of the two delay times in Fig. 4.21. In Fig. 4.21a the delay times are in the short delay regime and the corresponding dynamics are indicted in Fig. 3.68. This figure shows that as in the single feedback cavity case, the timing jitter is increased for delay times at the edges of the main resonance regions, i.e. where the pulses are wide and deformed. Towards the center of Fig. 4.21a the timing jitter is nearly unchanged compared with the solitary laser case. Again, this is because the positions of the satellite pulses do not have a significant influence on the timing jitter when they are well separated from the main pulse. The resonance lines defined by Eq. (3.25) are also plotted in Fig. 4.21a.

Along the lines $(l, 1, 0)$ and $(l, 0, 1)$ the timing jitter is reduced. This is because along these lines one of the feedback cavities is always resonant. Features along other resonance lines become more evident for long feedback delay times. This can be seen in Fig. 4.21b, where $\tau_1 \approx 30$ and $\tau_2 \approx 60$. Due to the increase of the delay times the timing jitter is decreased along the prominent resonance lines compared with the $\tau_1 \approx 1$ and $\tau_2 \approx 1$ case (Fig. 4.21a).

Analytic dependence of the timing jitter on the feedback strength ratio and resonance numbers

The lowest timing jitter values are found in the main resonance locking regions for the delay times that are defined by Eqs. (3.26):

$$\tau_1 = \tau_0 + n_1 T_0 \quad \text{and} \quad \tau_2 = \tau_0 + n_2 T_0. \tag{4.50}$$

These are the solutions that are identical to those in the main resonance locking regions for single cavity feedback (see Subsection 3.4.2). For delay times satisfying Eqs. (3.26) the impact of varying n_1 and n_2, as well as the influence of varying the ratio of K_1 and K_2, when $K_{\mathrm{TOT}} = K_1 + K_2$ is kept constant, can be described analytically. The derivation of the analytic expression is as follows.

In the dual feedback case the bilinear form (Eq. (4.16)) is given by

$$\begin{aligned}\left[\delta\psi^\dagger, \delta\psi\right](t) = \delta\psi^\dagger(t)\delta\psi(t) &+ \int_{-T}^{0} \delta\psi^\dagger(t+r+T)\, B_0(t+r)\, \delta\psi(t+r)\, dr \\ &+ \int_{-T-\tau_1}^{0} \delta\psi^\dagger(t+r+T)\, B_1(t+r)\, \delta\psi(t+r)\, dr \\ &+ \int_{-T-\tau_2}^{0} \delta\psi^\dagger(t+r+T)\, B_2(t+r)\, \delta\psi(t+r)\, dr.\end{aligned} \tag{4.51}$$

This can be rewritten as

$$\begin{aligned}\left[\delta\psi^\dagger, \delta\psi\right](t) = \delta\psi^\dagger(t)\delta\psi(t) &+ \int_{-T}^{0} \delta\psi^\dagger(t+r+T)\, B_0(t+r)\, \delta\psi(t+r)\, dr \\ &+ K_1 \int_{-T-\tau_0}^{0} \delta\psi^\dagger(t+r+T)\, \tilde{B}_1(t+r)\, \delta\psi(t+r)\, dr \\ &+ K_1 \int_{-T-\tau_0-n_1T_0}^{-T-\tau_0} \delta\psi^\dagger(t+r+T)\, \tilde{B}_1(t+r)\, \delta\psi(t+r)\, dr \\ &+ K_2 \int_{-T-\tau_0}^{0} \delta\psi^\dagger(t+r+T)\, \tilde{B}_2(t+r)\, \delta\psi(t+r)\, dr \\ &+ K_2 \int_{-T-\tau_0-n_2T_0}^{-T-\tau_0} \delta\psi^\dagger(t+r+T)\, \tilde{B}_2(t+r)\, \delta\psi(t+r)\, dr,\end{aligned} \tag{4.52}$$

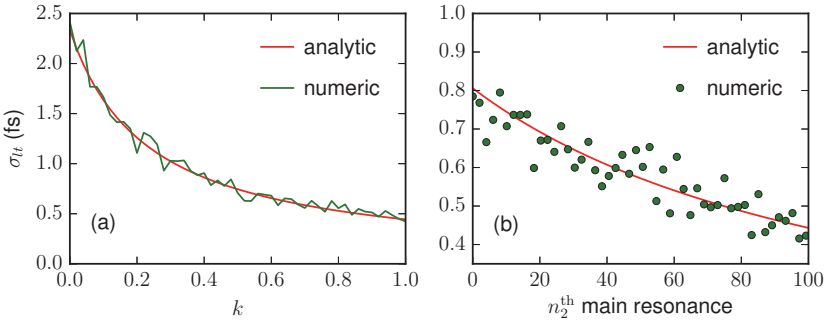

Figure 4.22.: **Dependence on feedback ratio and resonance number:** (a) Long-term timing jitter in dependence of the feedback ratio k for $\tau_1 = 100T_{0,K}$ and $\tau_2 = 10T_{0,K}$. (b) Long-term timing jitter in dependence of the resonance number of the second feedback cavity n_2 for $n_1 = 100$ ($\tau_1 = 100T_{0,K}$), with $k = 0.5$. The results were calculated analytically using Eq. (4.54) (red) and numerically using Eq. (4.8) (green). $N = 100$ noise realisations and $4 \cdot 10^4$ roundtrips were used for the numerical calculations. Parameters: $K_{\text{TOT}} = 0.1$, $R_{sp} = 0.44$ ($D = 0.2$), all other parameters as in Table 2.1.

where $K_n \tilde{B}_n = B_n$. With the K dependence removed from $\tilde{B}_n$, $\tilde{B} = \tilde{B}_1 = \tilde{B}_2$, giving

$$\begin{aligned}\left[\delta\psi^\dagger, \delta\psi\right](t) = \delta\psi^\dagger(t)\delta\psi(t) + \int_{-T}^{0} \delta\psi^\dagger(t+r+T)\, B_0(t+r)\, \delta\psi(t+r)\, dr \\ + K_{\text{TOT}} \int_{-T-\tau_0}^{0} \delta\psi^\dagger(t+r+T)\, \tilde{B}(t+r)\, \delta\psi(t+r)\, dr \\ + K_{\text{TOT}}\left(kn_1 + (1-k)\, n_2\right) \int_{-T_0}^{0} \delta\psi^\dagger(t+r+T)\, \tilde{B}(t+r)\, \delta\psi(t+r)\, dr, \end{aligned} \tag{4.53}$$

where we have introduced the feedback ratio k, i.e. $K_1 = kK_{\text{TOT}}$ and $K_2 = (1-k)\, K_{\text{TOT}}$. Following the analysis presented in the previous section this then gives

$$\sigma_{lt}(\tau_0, n_1, n_2, K_{\text{TOT}}, k) = \frac{\sigma_{lt}(K_{\text{TOT}}, \tau_0)}{1 + K_{\text{TOT}}\left(kn_1 + (1-k)\, n_2\right) \mathcal{F}(K_{\text{TOT}}, \tau_0)}, \tag{4.54}$$

where $\sigma_{lt}(K_{\text{TOT}}, \tau_0)$ and $\mathcal{F}(K_{\text{TOT}}, \tau_0)$ only depend on the total feedback strength K_{TOT} and the delay offset τ_0. This equation describes analytically how the timing jitter depends on the ratio of feedback strengths k and the resonance numbers, n_1 and n_2, of the feedback delay times.

Figure 4.22a shows the k dependence predicted by Eq. 4.54 (red line) for $\tau_1 = 100T_{0,K}$ and $\tau_2 = 10T_{0,K}$. Also shown are numerically obtained results (green), which show excellent agreement with the analytic results. As k is increased, the contribution from the longer feedback cavity becomes greater, which leads to a reduction in the timing jitter. The same trend is shown in Fig. 4.22b, where n_2 is

increased up to $n_1 = 100$. In this case increasing the length of the second feedback cavity leads to a reduction in the timing jitter. In both examples, Fig. 4.22a-b, the total feedback strength is the same. Therefore the timing jitter is the same for $k = 1$ in Fig. 4.22a, as it is for $n_2 = 100$ in Fig. 4.22b.

Equation (4.54) shows that, for comparable dynamics, the timing jitter reduction that can be achieved with two external feedback cavities is at most the same as for single cavity feedback (assuming $K = K_{\mathrm{TOT}}$), i.e. setting $n_1 = n_2$ Eq. (4.54) reduces to Eq. (4.46). However, a requirement for Eqs. (4.46) and (4.54) to hold, is of course that the solutions are stable. And, as discussed in Subsection 3.4.2, in the intermediate feedback strength regime the addition of a second short feedback cavity can increase the range of stable solutions. In addition to this requirement, it is also necessary that all stable eigenmodes of the system are sufficiently damped that they do not influence the long-term timing jitter. For single cavity feedback, for the parameters used, we found that for delay times greater than $\tau \approx 200$ noise-induced modulations are large enough that the semi-analytic method is not valid. In this very long delay limit the timing jitter can be reduced more effectively with dual cavity feedback than with feedback from a single cavity. This is because the second feedback cavity can be used to suppress the noise-induced modulations, which leads to a reduction in the long-term timing jitter. This will be addressed in detail in Chapter 5.

4.5.2. Feedback phase dependence of the timing jitter

As discussed in Subsection 4.4.2, the influence of the feedback phases on the timing jitter is related to how the feedback phases influence the dynamics. If changes in the feedback phases cause the pulses to become wider or deformed, or the pulse height to be reduced, then the timing jitter will increase. This also holds for dual cavity feedback. See Subsection 4.4.2 for more details.

4.5.3. Comparison with experimental results

In this section we present a comparison between numerical results and experimentally obtained results for a passively mode-locked quantum-dot semiconductor laser subject to feedback from two external cavities.[8]

In the experiment a linear-cavity monolithic quantum-dot mode-locked laser was used. The device consisted of two sections; a 0.3 mm long saturable absorber section and a 2.7 mm long gain section. The laser was coupled to two external cavities with lengths of approximately 3.18 m and 1.84 m, corresponding to feedback delay times of approximately $\tau_1 = 143T_0$ and $\tau_2 = 83T_0$ with $T_0 = 75$ ps. The lengths of the feedback cavities were finely tuned in order to measure the repetition rate,

[8] The results presented in this section have been published in [NIK16].

the pulse height ratio and the timing jitter, in dependence of the delay lengths. In the absence of feedback the pulse repetition rate was approximately 13.5 GHz. Further details on the structure of the laser and experimental setup can be found in [NIK16].

parameter	value	dimensionless	parameter	value	dimensionless
T	75 ps	1	γ	0.97 ps^{-1}	70
γ_g	1 ns^{-1}	0.075	γ_q	75 ns^{-1}	5.625
J_g	0.013 ps^{-1}	1.0	J_q	0.1 ps^{-1}	7.5
r_s	25.0	25.0	R_{sp}	0	0
κ	0.1	0.1	$\Delta\Omega$	0	0
α_g	0	0	α_q	0	0
K_1	0.05	0.05	K_2	0.05	0.05
C_1	0	0	C_2	0	0

Table 4.1.: Parameter values used for numerical simulation results presented in Fig. 4.23.

For the numerical simulations the parameters of the DDE model (Eq. (3.20) and Eqs. (2.43)-(2.44)) were adjusted such that the repetition rate of the fundamentally mode-locked solution was approximately the same as for the experiment. For this the cold cavity roundtrip time was chosen as $T = 75\,\text{ps}$. All other parameters are as given in Table 4.1. In choosing these parameters we did not attempt to fit the experimental results. The parameters were selected such that the DDE model produced fundamentally mode-locked solutions with repetition rates and pulse widths similar to those observed in the experiment. The model was not modified in order to take into account the sophisticated quantum-dot charge carrier scattering dynamics, nor were modifications made to take into account the linear-cavity geometry of the laser used in the experiment.

The results of the experiment and simulations are shown in Fig. 4.23. Figure 4.23a-b shows the repetition rate of the mode-locked solutions as a function of the two feedback delay times. The delay times are given as offsets from reference delay values. For the simulation results (Fig. 4.23a) $\tau_1 = 142.01T_{0,S} + \delta\tau_1$ and $\tau_2 = 81.72T_{0,S} + \delta\tau_2$, with $T_{0,S} = 1.0267$, which corresponds to a period of 77 ps. For the experimental results the reference delay times are not accurately determined, they are $\tau_1^{\text{ref}} = (143.5 \pm 3.5)\,T_0$ and $\tau_2^{\text{ref}} = (83 \pm 3)\,T_0$. In Fig. 4.23d the type of dynamics obtained in the simulations is indicated by the colour code. In the blue regions the laser exhibits fundamental mode-locking without feedback-induced satellite pulses. In the purple, green and yellow regions fundamental mode-locking with one, two and three satellite pulses is exhibited, respectively. The white regions indicate non-periodic dynamics. For parameter ranges where the system exhibits non-periodic dynamics, the value plotted in Fig. 4.23b is the dominant

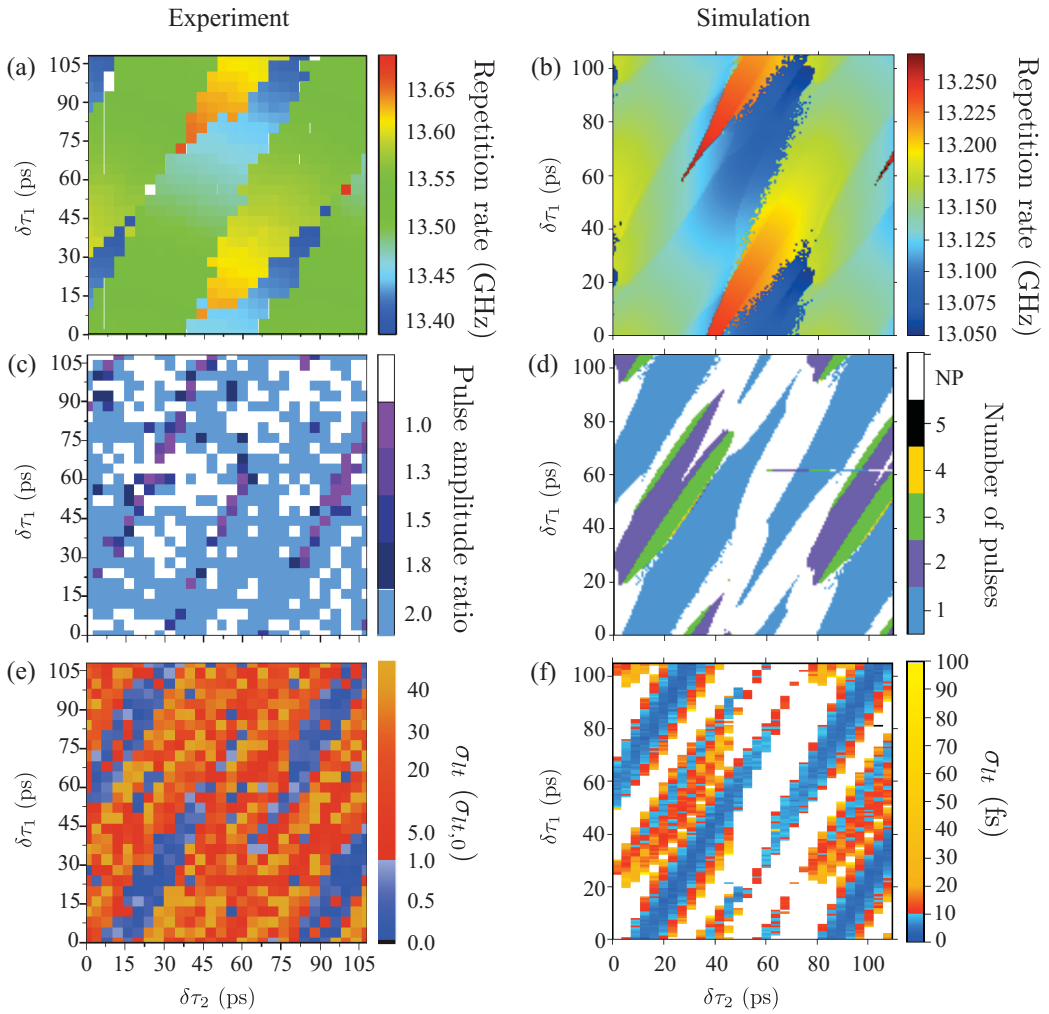

Figure 4.23.: **Comparison of experiment and simulations:** (a) Experimentally measured pulse repetition rate as function of the delay offsets from the reference delay times $\tau_1^{\text{ref}} = (143.5 \pm 3.5)\,T_0$ and $\tau_2^{\text{ref}} = (83 \pm 3)\,T_0$. (b) Numerically simulated repetition rates as a function of the delay offsets from $\tau_1 = 142.01 T_{0,S}$ and $\tau_2 = 81.72 T_{0,S}$. (c) Experimental results showing the ratio of the auto-correlation signal at zero delay and at a delay of $T_0/2 = 37.5\,\text{ps}$. (d) Map of the dynamics of the simulated solutions. The colour code indicates the number of pulses in the laser cavity and regions in white indicate non-periodic (NP) dynamics. (e) Experimentally measured timing jitter. (f) Numerically calculated timing jitter. Simulation parameters: (f) $R_{sp} = 0.45$, all other parameters as in Table 4.23. Reproduced from [NIK16].

frequency component. Experimental results equivalent to Fig. 4.23d were not obtained, however in Fig. 4.23c results of auto-correlation measures are shown, which indicate regions where one satellite pulse is present. Plotted is the ratio of the auto-correlation signal at zero delay and at a delay of $T_0/2 = 37.5\,\text{ps}$. An amplitude

ratio of one indicates 2nd harmonic mode-locking. For the regions plotted in white, no meaningful results were obtained. For the experimental results the repetition rates plotted in Fig. 4.23a were determined from the position of the peak in the power spectrum near the fundamental frequency of the laser cavity ($\approx 13.5\,\mathrm{GHz}$). For feedback parameters where Fig. 4.23c indicates harmonic mode-locking the repetition rate shown in Fig. 4.23a is not actually the dominant frequency. Finally, in Fig. 4.23e-f the timing jitter is shown for the experiment (e) and for the simulations (f). These results show that there is very good qualitative agreement between the experimental results and the simulation results, despite the DDE model being relative simple in terms of the modelling of the gain medium and the model assuming a ring cavity geometry. The results show regions of fundamental mode-locking within main resonance locking regions, in which the repetition rate can be tuned by varying the two feedback delay times and in which the timing jitter is reduced with respect to the solitary laser case. The experimental results also show that, as predicted by the DDE model, dynamics with feedback induced satellite pulses can be exhibited.

The experimental auto-correlation results (Fig. 4.23c) show that there are feedback conditions in which harmonic mode-locking is exhibited. This is not observed in the simulation results presented in Fig. 4.23. However, the results from Section 3.3 predict that optical feedback can induce harmonic mode-locking if the feedback strength is sufficiently high. Therefore, by adjusting the simulation parameters it could be possible to reproduce the feedback-induced harmonic mode-locking.

4.6. Summary

This chapter was dedicated to the timing jitter of the mode-locked laser in the presence of spontaneous emission noise. We first introduced various methods of calculating the timing jitter, then we investigated its parameter dependence for the solitary laser. Following this we studied the impact of optical feedback on the timing jitter.

There are various methods of calculating the timing jitter. Experimentally the rms timing jitter is determined from the power spectrum of the laser output. Numerically the timing jitter can be calculated directly from time-domain results. We have introduced two methods of doing this. The first is a fully numerical method that involves integrating the stochastic DDE system in order to determine the fluctuation of the pulse positions. The second method is semi-analytic and allows the timing jitter to be determined from deterministic solutions to the linearised unperturbed system.

For the solitary laser we use the semi-analytic and numerical methods to determine what factors influence the timing jitter of the mode-locked solutions. The two key factors are the pulse width and the net gain window. For narrower pulses the timing jitter is smaller, and if a positive net gain window opens before or after the pulse, the timing jitter can be increased, which is in agreement with previous studies. For the pump current dependence this means that the timing jitter first decreases as the pulses become narrower and higher with increasing current. Then as the unsaturated gain becomes larger, eventually a leading edge instability develops, i.e. a positive net gain window before the pulse, and the timing jitter increases again. This means that there should be an optimal current where the timing jitter is lowest. We have also found that amplitude-phase coupling decreases the timing jitter when comparing pulses with the same amplitude profile. This indicates that the chirp leads to a reduction in the timing jitter. However, the mechanism for this is not yet understood and requires further investigation.

We have found that with optical feedback added to the mode-locked laser system there are two aspects which determine the long-term timing jitter. The first is the dynamics induced by the feedback, i.e. how the feedback influences the pulse shape and the net gain window. Here the same trends apply as for the solitary laser, meaning that the lowest timing jitter values are achieved close to the main resonances where the pulses have not been significantly broadened. The second factor that determines the timing jitter is the feedback delay time. Using the semi-analytic method we were able to derive an analytic dependence of the long-term timing jitter on the delay time for resonant feedback. This analytic dependence shows that the timing jitter decreases for increasing resonant delay lengths. For long delay times it scales as approximately one over the delay time. However, this is only applicable as long as noise-induced modulations do not influence the long-term timing jitter. For very long feedback delay times, noise can excite weakly stable eigenmodes of the system which leads to a modulation of the dynamics. If these modulations are large then the semi-analytic method is no longer valid.

For dual-cavity feedback a similar formula can be derived for the dependence of the timing jitter on the resonance numbers. This formula also describes analytically the dependence on the ratio of the feedback strengths. From this expression one can see that in the limit that noise-induced modulations do not play a role, with dual cavity feedback the timing jitter is at best the same as for single cavity feedback. We will see in the next chapter that an improvement only comes in the regime of very long feedback delay times, where the second feedback cavity can be used to suppress noise-induced modulations.

Finally, we wish to remark that the semi-analytic method is not specific to the mode-locked laser model. The method can be applied to other autonomous systems exhibiting periodic dynamics, which have time-delayed variables and are subject to additive Gaussian white noise. Furthermore, the same form of the analytic

dependencies on the resonant feedback delay times, and the feedback strength ratios, will also apply to other systems that have a similar form.

Chapter 5

Noise-induced modulations

5.1. Introduction

In the previous chapter we found that the regularity of the mode-locked laser output can be improved by subjecting the system to resonant time-delayed optical feedback. Considering only the influence of the noise in the direction of the neutral mode corresponding to the time shift invariance of the mode-locked laser system, the timing jitter scales approximately as $1/\tau$ due to the pulse positions being correlated over longer times as the feedback delay time τ is increased to larger resonant values. However, as the feedback delay time becomes large, the influence of noise on other eigenmodes of the system plays an increasingly important role. Eigenmodes associated with the feedback terms become more weakly damped, which leads to pronounced noise-induced excitations of these modes. The excitation of these weakly damped modes causes a modulation of the timing fluctuations on a time scale of approximately τ, and for strong modulations this leads to an increase in the long-term timing jitter. In this chapter we will investigate how a second feedback loop can be used to suppress these noise-induced modulations and what the impact of this is on the long-term timing jitter.

Noise-induced excitation of eigenmodes is a topic which is of relevance to any physical system which has weakly damped eigenmodes and some form of noise source. Physical systems in which such an effect has been observed include fiber ring-cavity lasers [POT02a], passively mode-locked semiconductor lasers subject to optical feedback [ARS13, DRZ13], delay-coupled lasers [SOR13], neural networks [VIC08] and gene regulatory networks [CHE05d]. There have also been extensive theoretical works on this topic. However, these have mostly been in the context of systems in a deterministically stable steady state which are close to a bifurcation leading to oscillatory dynamics [SIG89, JAN03, GOL03, BAL04, SCH04b, POM05], or which have weakly damped eigenmodes [STE04b, FLU07]. For example, in

[BAL04] a Van-der-Pol oscillator close to a Hopf bifurcation is investigated. Below a Hopf bifurcation a system has one pair of complex conjugate eigenvalues, of which the real part is approaching zero. This means that noise-induced oscillations, with a frequency given by the imaginary part of the eigenmode, decay slowly as the eigenmodes are only weakly damped. Note that we refer to noise-induced oscillations when the deterministic system is in a stable steady state and noise-induced modulations when the deterministic system is already oscillatory.

Several works have been published on the control of noise-induced oscillations using time-delayed feedback, either with the aim of suppressing [FLU07] or stabilising [MAS02, JAN03, BAL04, POM05a] the oscillations. In [FLU07] a damped harmonic oscillator is studied and it is shown that the noise-induced oscillations can be optimally suppressed when feedback is added with a delay length equal to half the period of the induced oscillations. Intuitively this makes sense, as oscillations would interfere destructively in the feedback loop. In the damped harmonic oscillator case this works well because the original system has only one complex conjugate pair of eigenvalues. However, if one considers a system already subject to time-delayed feedback then there will be infinitely many Floquet exponents and a finite number of these can be weakly damped. The most prevalent frequency of the noise-induced modulations will correspond to the Floquet exponent with the smallest modulus of the real part, which, for sufficiently strong feedback or sufficiently long delay times, is given by approximately $1/\tau_1$. In this scenario, due to the multitude of Floquet exponents, the noise-induced modulations cannot be optimally suppressed by simply choosing the second feedback delay-time equal to half the modulation period, as this delay-time will be resonant with the second harmonic of the first feedback term and would therefore enhance modulations at a frequency of $\approx 2/\tau_1$. Some work has already been carried out on the suppression of noise-induced dynamics in systems involving time delay, especially in the fiber laser community [WU00, YUH98, POT02a, YAN07a, ZHU15]. However, many of these works are experimental and those containing theory either only take into account rudimentary considerations of cavities resonances or present only numerical results for a specific system that does not allow for a general understanding of this topic. For example, in [POT02a] the theoretical considerations for the choice of the feedback conditions were based on the Vernier principle[1], which is not sufficient for determining conditions for optimal modulation suppression. Although not optimised, experimental studies do show that an additional feedback cavity can be used to suppress modulations of the dynamics. For example, in [HAJ12] a passively mode-locked laser is subjected to feedback from two external cavities in order to suppress the modulations that arise with feedback from just one cavity. In this chapter we address the theoretical understanding needed to optimise such a setup.

[1]The free spectral range is limited to cavity modes which can exist in both cavities [POT02a].

This chapter is structured as follows. In Section 5.2 the suppression of noise-induced modulations will be investigated in dependence of the parameters of the second feedback term. This will first be done for a simple oscillatory system, the Stuart-Landau oscillator, and then the results will be compared with our system of interest, the mode-locked laser. For the Stuart-Landau oscillator we will derive a simple characteristic equation for the dominant Floquet exponents and for the mode-locked laser, by comparison with numerical results, we will show that the dominant Floquet exponents can be described by a characteristic equation of the same form. Then in Section 5.3 we will look at how the noise-induced modulations, and the suppression thereof, influence the long-term timing jitter.

Parts of this chapter have been published in [JAU16a].

5.2. Suppression of noise-induced modulations

Due to the complexity of the mode-locked laser system we shall first study the suppression of noise-induced modulations in a very simple oscillatory system, the Stuart-Landau oscillator. The idea behind this is that if we to restrict the analysis to feedback delay times that are integer multiples of the oscillation period, it could be expected that the suppression of noise-induced modulations in different dynamical systems will show the same trends with respect to the resonant delay time dependence, and to a certain extent the feedback strength dependence. This is because when the delay times are restricted to resonant values, then the dynamics of the particular system do not change as the delay times are varied, only the stability of the solutions is affected. Indeed, we will show that this is true for three examples of dynamical systems exhibiting oscillatory dynamics; the Stuart-Landau oscillator, the mode-locked laser system and the FitzHugh-Nagumo oscillator (see Appendix C for the FitzHugh-Nagumo example). Additionally, restricting the feedback delay times to integer multiples of the period is motivated by experimental and theoretical results for passively mode-locked semiconductor lasers which show that the timing jitter reduction is best close to the main resonances, as shown in the previous chapter [OTT14b, JAU15, NIK16].

The noise-induced modulations are excitations along eigendirections of the periodic system, i.e. they are related to the Floquet modes of the underlying deterministic system. The imaginary part of the Floquet exponents determines the modulation frequency and the real part gives the damping rate of the perturbations. More weakly damped modes correspond to more pronounced modulations [JAN03]. Therefore, to determine the influence of the second feedback term on the noise-induced modulations we will study how this term effects the dominant Floquet modes of the unperturbed system. Assuming that the noise perturbations are small, we will first perform an analytic linear stability analysis for the Stuart-

Landau oscillator. Due to the complexity of the mode-locked laser system, we use DDE-BIFTOOL [ENG01] to numerically calculate the Floquet multipliers for this system.

5.2.1. Stuart-Landau oscillator

The Stuart-Landau oscillator is a generic oscillatory system which is widely used to study the dynamics, feedback control and synchronisation of delay-coupled oscillators [NAK05, DHU10, CHO11, DAH11b, WU12a, SCH13b, LEH15b]. The appeal of this system is that the oscillatory solution can be found analytically.

The dynamics of a solitary Stuart-Landau oscillator is described by

$$\dot{z} = \left(\lambda_0 + i\omega_0 - (1+i\gamma)\,|z|^2\right) z, \tag{5.1}$$

where $z(t) = r(t)\, e^{i\phi(t)}$ is a complex variable which can be split into an amplitude $r(t)$ and a phase $\phi(t)$ component. Substituting $z(t) = r(t)\, e^{i\phi(t)}$ into Eq. (5.1) the evolution of the amplitude and the phase are given by

$$\dot{r}(t) = \left(\lambda_0 - r(t)^2\right) r(t), \quad \text{and} \quad \dot{\phi}(t) = \omega_0 - \gamma r(t)^2. \tag{5.2}$$

For $\lambda_0 < 0$ these equations have only one fixed point solution, which is a stable focus. At $\lambda_0 = 0$ the system undergoes a supercritical Hopf bifurcation and a stable limit cycle is born with $r(t) = \sqrt{\lambda_0}$ and $\phi(t) = \Omega t$, where $\Omega = \omega_0 - \gamma\lambda_0$. We are interested in the effect of feedback on the stability of the oscillatory solution, therefore, in the following we will exclusively consider $\lambda_0 > 0$.

Adding time-delayed feedback to the Stuart-Landau system we have

$$\dot{z} = \left(\lambda_0 + i\omega_0 - (1+i\gamma)\,|z|^2\right) z + \sum_{n=1,2} K_n e^{i\theta_n} z(t-\tau_n), \tag{5.3}$$

where K_1 and K_2 are the feedback strengths, θ_1 and θ_2 are the feedback phases, and τ_1 and τ_2 are the feedback delay times. Here we have added two feedback terms. One represents the feedback term present in the original system and the second is the term that is added to suppress the noise-induced modulations that arise due to the first feedback term. Entering the solution ansatz $z(t) = re^{i\Omega t}$ into Eq. (5.3) the amplitude and the frequency are determined by

$$r^2 = \lambda_0 + K_1 \cos(\theta_1 - \Omega\tau_1) + K_2 \cos(\theta_2 - \Omega\tau_2) \tag{5.4}$$

and

$$\Omega = \omega - \gamma\lambda_0 + \sum_{n=1,2} K_n \sqrt{1+\gamma^2} \sin(\theta_n - \Omega\tau_n - \arctan(\gamma)). \tag{5.5}$$

To analyse the stability of the solutions, we linearise the system about the periodic solution $z(t) = re^{i\Omega t}$. To do this we use the system written in the coordinates of $r(t)$ and $\phi(t)$. The linearised system is given by

$$\delta\dot{\mathbf{x}}(t) = A\delta\mathbf{x}(t) + \sum_{n=1,2} B_n \delta\mathbf{x}(t-\tau_n), \tag{5.6}$$

where $\delta\mathbf{x} = (\delta r, \delta\phi)^{\mathrm{T}}$ and the Jacobi matrices[2] are given by

$$A = \begin{pmatrix} \lambda_0 - 3r^2 & K_n r \sin(\theta_n - \Omega\tau_n) \\ -2\gamma r - \frac{K_n \sin(\theta_n - \Omega\tau_n)}{r} & -K_n \cos(\theta_n - \Omega\tau_n) \end{pmatrix} \tag{5.8}$$

and

$$B_n = \begin{pmatrix} K_n \cos(\theta_n - \Omega\tau_n) & -K_n r \sin(\theta_n - \Omega\tau_n) \\ \frac{K_n \sin(\theta_n - \Omega\tau_n)}{r} & K_n \cos(\theta_n - \Omega\tau_n) \end{pmatrix}. \tag{5.9}$$

What sets the Stuart-Landau system apart from other systems exhibiting oscillatory dynamics is that these Jacobi matrices have no time dependence, which makes the stability analysis similar to that of a steady state solution. Accordingly, we insert the ansatz $\delta\mathbf{x} = \mathbf{p}e^{\lambda t}$, where $\mathbf{p}$ is time-independent, into Eq. (5.6) to obtain

$$\lambda\mathbf{p} = A\mathbf{p} + \sum_{n=1,2} B_n \mathbf{p} e^{-\lambda\tau_n}. \tag{5.10}$$

For this linear system to have a solution for $\mathbf{p}$

$$\mathrm{Det}\left[A + \sum_{n=1,2} B_n e^{-\lambda\tau_n} - \lambda\mathbb{I}\right] = 0 \tag{5.11}$$

must hold, where $\mathbb{I}$ is the identity matrix. From this we obtain the characteristic equation for the Floquet exponents, λ:

$$\begin{aligned} &\left(r^2 + \lambda + \textstyle\sum_{n=1,2} K_n \cos(\theta_n - \Omega\tau_n)\left(1 - e^{-\lambda\tau_n}\right)\right)^2 \\ &= r^4 - 2\gamma r^2 \textstyle\sum_{n=1,2} K_n \sin(\theta_n - \Omega\tau_n)\left(1 - e^{-\lambda\tau_n}\right) \\ &\quad - \textstyle\sum_{n=1,2} K_n^2 \sin^2(\theta_n - \Omega\tau_n)\left(1 - e^{-\lambda\tau_n}\right)^2. \end{aligned} \tag{5.12}$$

In the case of only one feedback term, i.e. $K_2 = 0$, this characteristic equation can be solved analytically by expanding λ in orders of τ^{-1} [DHU10]. However, since the order of magnitude of the second delay time can vary compared with the first,

[2] The entries of the Jacobi matrices are defined as

$$A_{i,j} = \frac{\partial \dot{x}_i}{\partial x_j(t)} \quad \text{and} \quad B_{n,i,j} = \frac{\partial \dot{x}_i}{\partial x_j(t-\tau_n)}, \tag{5.7}$$

where $\mathbf{x} = (r, \phi)^{\mathrm{T}}$.

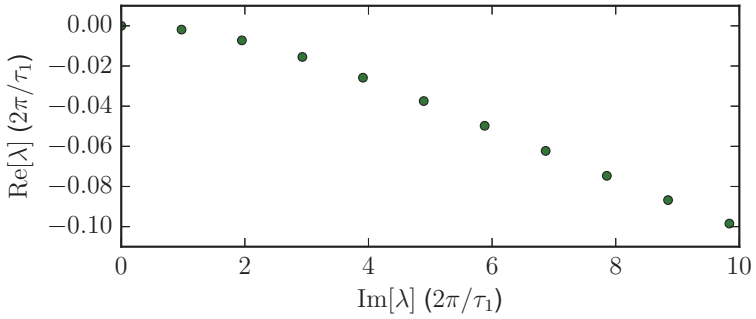

Figure 5.1.: Real versus imaginary parts of the dominant Floquet exponents of the Stuart-Landau system (Eq. (5.15)) with one feedback term. Parameters: $K_1 = 0.2$, $\tau_1 = 500T_0$, $K_2 = 0$, $\lambda_0 = 2$, $\omega_0 = 5$ and $\gamma = -5$.

the same approach cannot be applied to the dual feedback case. We can however simplify Eq. (5.12) by making use of the fact that we are interested only in resonant feedback conditions.

If we restrict ourselves to resonant feedback the delay-times are integer multiples n of the period $T_0 = 2\pi/\Omega$ of the oscillator, i.e., $\tau_{1,2} = nT_0$, and we restrict the feedback phases by considering that the feedback phase for perfectly resonant feedback is zero, then Eqs. (5.4) and (5.5) can be simplified to

$$r^2 = \lambda_0 + K_1 + K_2 \quad \text{and} \quad \Omega = \omega_0 - \gamma r^2, \tag{5.13}$$

where Ω no longer depends on the feedback delay times. The characteristic equation then reduces to

$$r^2 = \pm \left(r^2 + \lambda + \sum_{n=1,2} K_n \left(1 - e^{-\lambda \tau_n} \right) \right). \tag{5.14}$$

For $\lambda_0 > 0$ and sufficiently large delay times, the dominant Floquet exponents are given by the plus sign in Eq. (5.14)[3];

$$\lambda = -(K_1 + K_2) + K_1 e^{-\lambda \tau_1} + K_2 e^{-\lambda \tau_2}. \tag{5.15}$$

This expression only implicitly depends on the parameters of the Stuart-Landau system via the constraints that have been put on the delay times (i.e. $\tau_{1,2} = nT_0$). Here we also note that the same characteristic equation is obtained for a Pyragas type feedback scheme, i.e. $K[z(t-\tau)-z(t)]$, [PYR92]. Now, to find delay conditions for optimal modulation suppression we solve Eq. (5.15) numerically and find the Floquet exponents in dependence of the delay times and the feedback strengths.

With only one feedback term (i.e. $K_2 = 0$) the dominant Floquet exponents have imaginary parts which are given approximately by $2\pi n/\tau_1$, for integer n. An

[3]The Floquet exponents given by Eq. (5.14) with the minus sign are of the order of $-2r^2$.

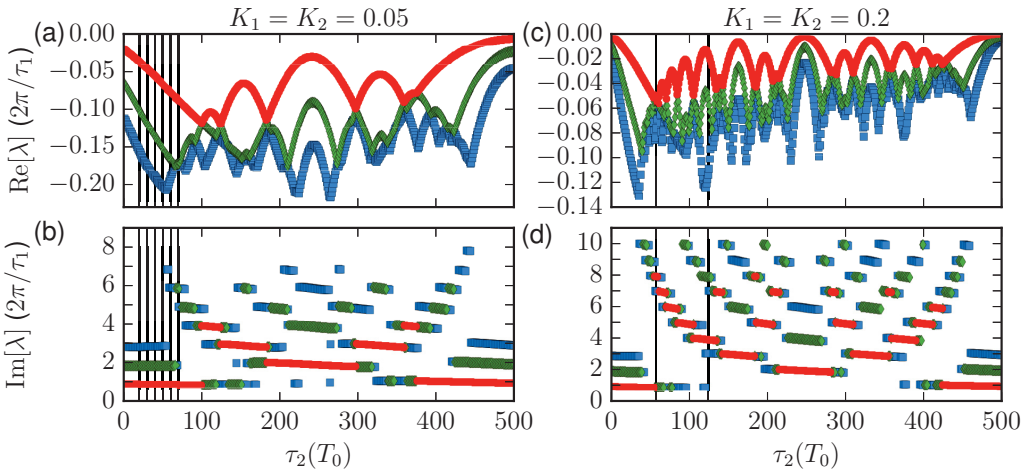

Figure 5.2.: Real (a,c) and imaginary (b,d) parts of the three dominant Floquet exponent of the Stuart-Landau system (Eq. (5.15)) with two feedback terms in dependence of τ_2 for $\tau_1 = 500T_0$ and with $K_1 = K_2 = 0.05$ in (a,b) and $K_1 = K_2 = 0.2$ in (c,d). The vertical black lines indicate the τ_2 values used in Figs. 5.6 and 5.7. Parameters: $\lambda_0 = 2$, $\omega_0 = 5$ and $\gamma = -5$.

example of this is shown for $\tau_1 = 500T_0$ in Fig. 5.1. Here it can be seen that the damping rates of the stable Floquet modes increase with n, i.e. $\mathrm{Re}[\lambda]$ becomes more negative. The mode with $\lambda = 0$ is the neutral mode, which is not relevant for the following analysis where we will only consider the stable modes.

Adding the second feedback term ($K_2 \neq 0$) modes will be enhanced or suppressed depending on whether τ_2 is resonant with the Floquet modes of the single feedback case or not. This is illustrated in Fig. 5.2 where the (a) real and (b) imaginary part of the three dominant Floquet exponents (neglecting the neutral modes) is plotted as a function of τ_2 for $K_1 = K_2 = 0.05$, with $\tau_1 = 500\,T_0$ and τ_2 ranging from zero to τ_1. When the second feedback delay time is $\tau_2 = 500T_0$ the feedback terms are equal and the situation is identical to the case with only one feedback term. The frequencies of the dominant Floquet exponents are again given by approximately $2\pi n/\tau_1$ and the damping rates increases with n. If $\tau_2 = 250T_0$ then the mode with the fundamental frequency of the first feedback term, i.e. $\mathrm{Im}[\lambda] \approx 2\pi/\tau_1$, is strongly suppressed. This can be seen in Fig. 5.2 by the fact that there is no $\mathrm{Im}[\lambda] \approx 2\pi/\tau_1$ mode plotted at $\tau_2 = 250T_0$ in subplot (b). In this case the dominant mode corresponds to $n = 2$, as τ_2 is resonant with the second harmonic of the first feedback term. Similarly, there are peaks in $\mathrm{Re}[\lambda]$, i.e. minima in the damping rate, at other τ_2 values where τ_1 and τ_2 have low common multiples.

The frequencies of the most dominant Floquet modes ($\mathrm{Im}[\lambda]$) all correspond to harmonics of the fundamental frequency of the first feedback cavity, i.e. $\mathrm{Im}[\lambda] \approx 2\pi n/\tau_1$, for integer n. In Fig. 5.2 the most dominant Floquet exponent is plotted in

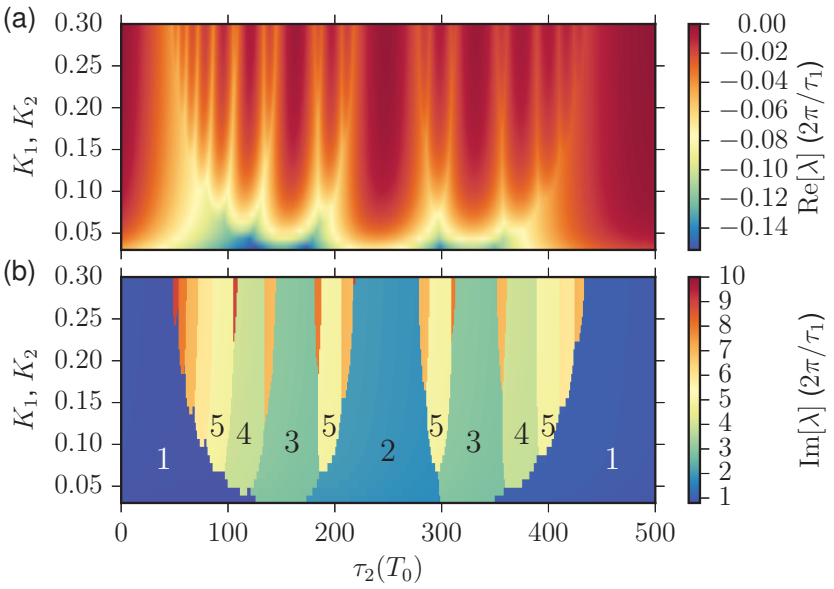

Figure 5.3.: Real (a) and imaginary (b) parts of the dominant Floquet exponent of the Stuart-Landau system (Eq. (5.15)) with two feedback terms in dependence of $K_1 = K_2$ and τ_2, with $\tau_1 = 500T_0$. In (b) the integer labels indicate multiples of $2\pi/\tau_1$. Parameters: $\lambda_0 = 2$, $\omega_0 = 5$ and $\gamma = -5$.

red. Concentrating only on the red symbols in Fig. 5.2b, the frequency components of the dominant Floquet exponent form a Farey-tree-like structure [COB03], as is common for systems with two competing characteristic times. The extent of the various frequency plateaus decreases as n increases and the number of plateaus is related to the feedback strength. This can be seen by comparison with Fig. 5.2d, where the feedback strengths are increased to $K_1 = K_2 = 0.2$. At the center of the frequency plateaus the modes are most weakly damped as τ_1 and τ_2 are resonant with one another. As τ_2 is varied the frequency of the dominant mode is no longer resonant with τ_2 and becomes more strongly damped. At the same time τ_2 becomes resonant with some other modes, which then become more weakly damped. This can be seen in Fig. 5.2a,c. As Re[λ] of the dominant mode (red) decreases, it increases for other modes (green and blue).

The dominant frequency of noise-induced modulations is determined by the dominant Floquet mode. From Fig. 5.2 it can therefore be deduced that this modulation frequency and amplitude can be varied by adjusting τ_2. The greatest suppression of these modulations will occur when the dominant modes are most damped. Comparing Fig. 5.2a with Fig. 5.2b it can be seen that the τ_2 value for which the modes are most damped is not given by a fixed ratio of the feedback delay times, but rather is dependent on the feedback strength. For the dominant mode (red symbols in

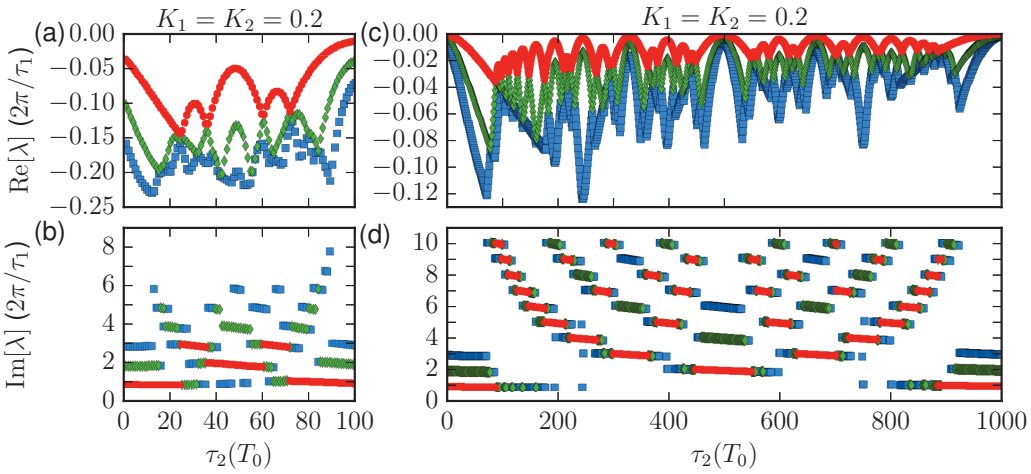

Figure 5.4.: Real (a,c) and imaginary (b,d) parts of the three dominant Floquet exponent of the Stuart-Landau system (Eq. (5.15)) with two feedback terms for $K_1 = K_2 = 0.2$, $\tau_1 = 100T_0$ in (a,b) and $\tau_1 = 1000T_0$ in (c,d). Parameters: $\lambda_0 = 2$, $\omega_0 = 5$ and $\gamma = -5$.

Fig. 5.2) the dependence on the feedback strength is shown more clearly in Fig. 5.3. Here the real (a) and imaginary (b) parts of the dominant Floquet exponent are depicted as a function of τ_2 and $K_1 = K_2$, the magnitudes given by the colour code. Again, the Farey-tree-like structure can be seen in the frequency component, with the number of frequency plateaus increasing with the feedback strength. As the feedback strengths are increased, overall the damping rates decrease and the τ_2 value for which the damping rate is greatest shifts to lower multiples of T_0. The same trends are found in dependence of τ_1. This is demonstrated in Fig. 5.4, where the three dominant Floquet modes are shown for $\tau_1 = 100T_0$ (a,b) and $\tau_1 = 1000T_0$ (c,d).

So far we have only addressed situations where $K_1 = K_2$. If $K_2 < K_1$ then varying τ_2 still has a similar effect on the dominant Floquet modes. This can be seen by comparing Fig. 5.2c-d with Fig. 5.5a-b. In these figures the total feedback $K_1 + K_2$ is keep constant, however in Fig. 5.5a,b the contribution from the second feedback term is decreased. The overall structure is the same but the increased contribution from the long feedback term (τ_1) means that the maximum damping rate of the dominant mode is reduced. For $K_2 > K_1$ the Farey-tree-like structure of the frequency plateaus becomes skewed, an example of this is shown in Fig. 5.5c-d.

The relative magnitude of the real part of the dominant Floquet exponents gives an indication of which frequency components will be more or less present in the noise-induced modulations. We shall now look at some explicit examples. To do this we add a Gaussian white noise term to Eq. (5.3) and numerically calculate

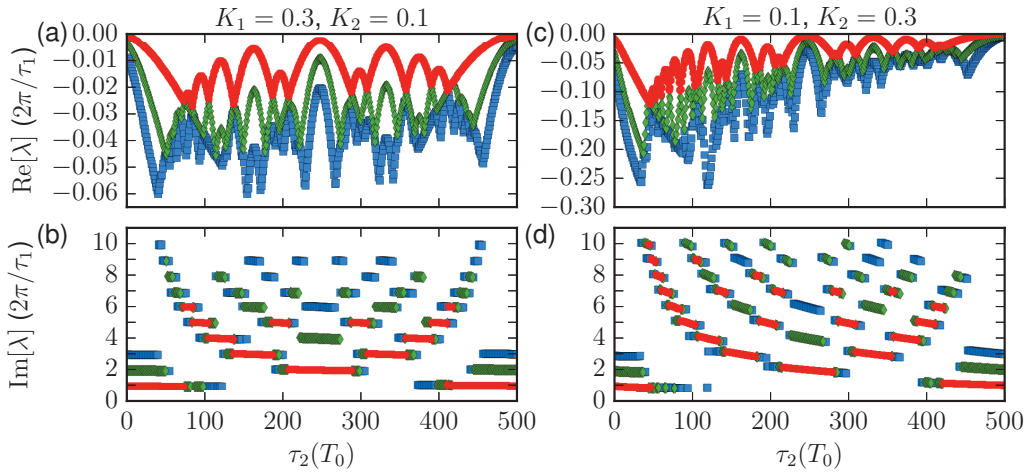

Figure 5.5.: Real (a,c) and imaginary (b,d) parts of the three dominant Floquet exponent of the Stuart-Landau system (Eq. (5.15)) with two feedback terms for $\tau_1 = 500T_0$, $K_1 = 0.3$ and $K_2 = 0.05$ in (a,b), and $K_1 = 0.1$ and $K_2 = 0.3$ in (c,d). Parameters: $\lambda_0 = 2$, $\omega_0 = 5$ and $\gamma = -5$.

power spectra of $|z(t)|$ for various feedback configurations. The system with noise is given by

$$\dot{z} = \left(\lambda_0 + i\omega_0 - (1 + i\gamma)|z|^2\right) z + \sum_{n=1,2} K_n e^{i\theta_n} z(t - \tau_n) + D\xi(t), \tag{5.16}$$

where D is the noise strength and $\xi(t') = \xi_R + i\xi_I$ has the properties

$$\langle \xi_i(t) \rangle = 0 \quad \text{and} \quad \langle \xi_i(t)\, \xi_j(t') \rangle = \delta_{i,j}\delta(t - t')$$

for $i, j \in \{R, I\}$. Figure 5.6 shows power spectra for parameters corresponding to Fig. 5.2c,d. Shown in grey is the power spectrum for $\tau_1 = \tau_2 = 500T_0$, i.e. equivalent to the single feedback case with $K_1 = 0.4$. The peaks in the power spectrum are caused by the noise-induced modulations and are found at multiples of $2\pi/\tau_1$, corresponding to the frequencies of the dominant Floquet modes. The spectra for $\tau_2 = 57T_0$ and $\tau_2 = 124T_0$ are shown in green in Fig.5.6a-b, respectively. For $\tau_2 = 57T_0$, in accordance with Fig. 5.2c-d, the noise-induced modulations are significantly suppressed. For $\tau_2 = 124T_0$, modulation at certain frequencies is significantly suppressed, however not at multiples of $4 \cdot 2\pi/\tau_1$, since $\tau_2 \approx \tau_1/4$.

Considering the damping rate of the dominant Floquet exponent gives a good indication of the τ_2 values for which the modulations are suppressed. However, to find feedback conditions for optimal suppression it is not sufficient to only consider the dominant Floquet exponent. This is because, as discussed earlier, as the damping rate of the dominant exponent increases, the damping rates of other

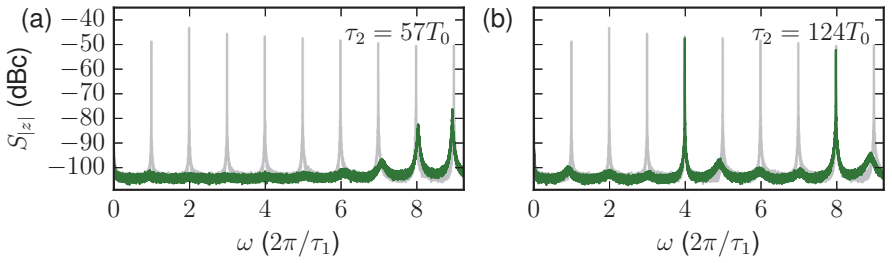

Figure 5.6.: Power spectra of $|z|$ for the Stuart-Landau system with two feedback terms for $K_1 = K_2 = 0.2$, $\tau_1 = 500T_0$ and τ_2 as indicated in (a) and (b). Depicted in grey is the power spectrum for $\tau_1 = \tau_2 = 500T_0$. The τ_2 values used here correspond to the positions of the vertical black lines in Fig. 5.2 (c,d). The results are averaged over 50 noise realisations. Parameters: $D = 0.1$, $\beta = 2$, $\omega = 5$ and $\gamma = -5$.

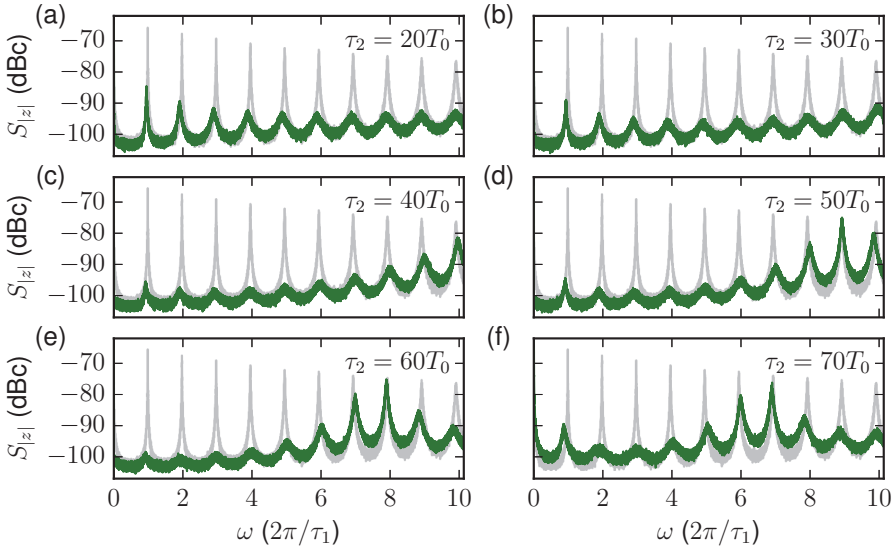

Figure 5.7.: Power spectra of $|z|$ for the Stuart-Landau system with two feedback terms for $K_1 = K_2 = 0.05$, $\tau_1 = 500T_0$ and τ_2 as indicated in (a)-(f). Depicted in grey is the power spectrum for $\tau_1 = \tau_2 = 500T_0$. The τ_2 values used here correspond to the positions of the vertical black lines in Fig. 5.2 (a,b). The results are averaged over 50 noise realisations. Parameters: $D = 0.1$, $\beta = 2$, $\omega = 5$ and $\gamma = -5$.

modes decrease. The impact of this on the noise-induced modulations is shown in Fig. 5.7, where power spectra are plotted for the parameter values corresponding to the vertical black lines in Fig. 5.2a,b. Starting at $\tau_2 = 20T_0$ in Fig.5.7a τ_2 is increased in steps of $10T_0$ in subplots (b)-(f). In all cases the modulations are reduced with respect to the single feedback case (grey spectra), however the frequency components change. As τ_2 is increased the $\omega \approx 2\pi/\tau_1$ component decreases

but the power at higher frequencies increases. In this example the suppression is best for $\tau_2 \approx 40T_0$, which is before the damping rates of higher frequency modes have significantly increased (see Fig. 5.2a-b).

For the Stuart-Landau oscillator we can conclude that the suppression of the noise-induced modulations depends on τ_2 in a non-trivial way. Delay conditions for optimal modulation suppression depend on both the feedback strengths and on τ_1, with the general trend that τ_2 should be an increasingly smaller fraction of τ_1 as either τ_1 or the feedback strengths are increased. In the next section we will compare these results with those for the mode-locked laser and show that the qualitative trends are the same.

5.2.2. Mode-locked laser

The mode-locked laser system with feedback from two external cavities (Eqs. (2.43)-(2.44) and (3.20)) is vastly more complicated than the Stuart-Landau oscillator. Due to the delay times and the time dependence of the Jacobi matrices (see Eqs. (B.2) and (B.3) in Appendix B), although the existence of some characteristic equation is mathematically proven for the linearised system [SZA06, SIE11a, HAL93], it cannot easily be derived. Therefore, it is necessary to use software packages such as DDE-BIFTOOL [ENG01] to numerically calculate the Floquet exponents. However, the noise-induced modulations become prominent when the feedback delay times are relatively long and for long delay times using software packages such as DDE-BIFTOOL very quickly becomes problematic due to memory requirements and long computation times. In this section we will show that under certain conditions this problem can be circumvented, because it turns out that despite the mode-locked laser system having vastly more complicated dynamics, the dominant Floquet exponents can be described with a simple characteristic equation of the same form as that obtained for the Stuart-Landau oscillator (Eq. (5.15)). We will then use this equation to find optimal feedback delay lengths for the second cavity when τ_1 is very long.

In the following analysis we will only consider the case of zero feedback phases, $C_1 = C_2 = 0$. This is because we are mainly interested in determining the influence of the second feedback delay time on the suppression of noise-induced modulations, while keeping the dynamics exhibited by the system the same. As was shown in Chapter 3, introducing non-zero feedback phases causes a shift of the cavity modes and this shift is also dependent on the feedback delay times. This means that if the feedback phases are non-zero the dynamics change even if the feedback delay times are varied by integer multiples of the pulse repetition period. The influence of the feedback phases on the dynamics, and hence on the timing jitter, has been addressed in Section 3.4 and Chapter 4.

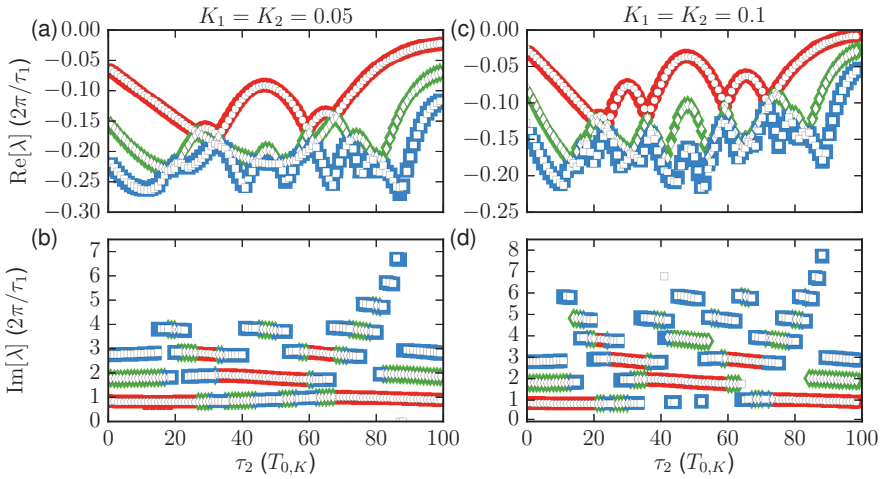

Figure 5.8.: Real (a,c) and imaginary (b,d) parts of the three dominant Floquet exponents of a passively mode-locked laser subject to feedback from two external cavities for (a,b) $K_1 = K_2 = 0.05$ and (c,d) $K_1 = K_2 = 0.1$. The white symbols indicate the numerically calculated values and the coloured symbols indicate the results of the fitted characteristic equation (Eq. (5.17)). Parameters: $\tau_1 = 100T_{0,K}$ and, $K_1^{\text{eff}} = K_2^{\text{eff}} = 0.0465$ for (a,b) and $K_1^{\text{eff}} = K_2^{\text{eff}} = 0.089$ for (c,d), all other parameters as in Table 2.1.

Feedback strength and feedback delay time dependence

We shall first concentrate on feedback delay times which are integer multiples of the period of the mode-locked solutions, i.e. $\tau_m = n_m T_{0,K}$ for integer n_m and $m = 1, 2$. In Fig. 5.8a-b the real and imaginary parts of the three dominant Floquet exponents, calculated using DDE-BIFTOOL, are depicted by the white symbols for $\tau_1 = 100T_{0,K}$ and $K_1 = K_2 = 0.05$.[4] The τ_2 dependence of these Floquet exponents is very similar to the Stuart-Landau case. In fact, despite the more complex dynamics, with time-varying amplitudes, fitting of the numerically obtained results shows that the dominant Floquet exponents can be described with a simple characteristic equation of the same form as Eq. (5.15),

$$\lambda = -(K_1^{\text{eff}} + K_2^{\text{eff}}) + K_1^{\text{eff}} e^{-\lambda\tau_1'} + K_2^{\text{eff}} e^{-\lambda\tau_2'}, \tag{5.17}$$

the difference being that the feedback strengths in Eq. (5.15) are now replaced with effective feedback strengths K_n^{eff} that depend on the dynamics of the mode-locked laser. Here τ_m' are the total delay times in the feedback terms, i.e. $\tau_m' = T + \tau_m$. The fit of Eq. (5.17) is depicted by the coloured symbols in Fig. 5.8a-b. The only fit

[4] For $\tau_1 = 100T_{0,K}$ the DDE-BIFTOOL calculations already require a significant amount of memory and computation time. And, because these scale non-linearly with the delay time, $\tau_1 = 100T_{0,K}$ is already close to limit for which stability calculations are in practice possible using DDE-BIFTOOL.

parameters are K_1^{eff} and K_2^{eff}, which in this case are $K_1^{\text{eff}} = K_2^{\text{eff}} = 0.0465$. Results for $K_1 = K_2 = 0.1$ are shown in Fig. 5.8c-d. In this case $K_1^{\text{eff}} = K_2^{\text{eff}} = 0.089$.

That the dominant Floquet exponents can be described by Eq. (5.17) is a non-trivial result since the monodromy matrix (see Appendix A) depends on the delay times of the system in the form $\mathbf{M}(t_0) = \mathbf{M}\left(t_0, e^{\lambda T}, e^{\lambda(T+\tau_1)}, e^{\lambda(T+\tau_2)}\right)$ and a characteristic equation would involve terms of the form $e^{\lambda(T+\tau_m)}e^{\lambda(T+\tau_{m'})}$ for $m, m' = \{1, 2\}$, as well as higher order terms. To understand what conditions are required such that fitting Eq. (5.17) to the dominant Floquet exponents works, it is helpful to remember that for the Stuart-Landau system the dominant Floquet exponents are only given by Eq. (5.15) as long as the $\lambda_0 > 0$ and for sufficiently large feedback delay times. Otherwise dominant Floquet exponents can also come from the component of Eq. (5.14) with the minus sign, which explicitly depends on a parameter of the Stuart-Landau oscillator, λ_0. This suggests that in the mode-locked laser case Eq. (5.17) may also only describe the dominant Floquet exponents if at least one of the feedback delay times is sufficiently large. Intuitively, this makes sense, since for large feedback delay times terms of the form $e^{\lambda(T+\tau_m)}$ will dominant over higher order terms and T will become negligible compare with τ_m. Indeed, by comparison with results obtained using DDE-BIFTOOL we find that for smaller τ_1 values there are additional dominant Floquet exponents which cannot be described by Eq. (5.17). This is shown for $\tau_1 = 50T_0$ in Fig. 5.9c-d, where $K_1 = K_{\text{TOT}}k = 0.05$ and $K_2 = K_{\text{TOT}}(1-k) = 0.05$. Here some of the Floquet exponents can be fitted well by Eq. (5.17), but there are also some which show a nearly linear dependence on τ_2 and have a zero frequency component.

The feedback strengths used in Fig. 5.9c-d are the same as those used in Fig. 5.8a-b, therefore the fitted values for the effective feedback strengths are also the same, i.e. $K_1^{\text{eff}} = K_2^{\text{eff}} = 0.0465$ also for Fig. 5.9c-d. In fact, for sufficiently large feedback delay times it is to be expected that K_1^{eff} and K_2^{eff} are independent of the feedback delay times since we have restricted τ_1 and τ_2 to integer multiples of the period which means that the Jacobians of the linearised system are independent of τ_1 and τ_2. Furthermore, the feedback strength dependence of the Jacobi matrices B_n (Eq. (B.3) in Appendix B) can be split into two contributions. We can write

$$B_n = K_n \tilde{B}_n, \tag{5.18}$$

where $\tilde{B}_n$ now only depends on $K_{\text{TOT}} = K_1 + K_2$ and not individually on K_n. This is because $\tilde{B}_n$ is a function of the periodic solution of the full system (Eqs. (2.43)-(2.44) and (3.20)), which depends only on K_{TOT} when τ_1 and τ_2 are integer multiples of the period, since under these delay conditions the contributions from the two cavities are indistinguishable from the single feedback cavity case with $K = K_{\text{TOT}}$. This means that if we write $K_1 = K_{\text{TOT}}k$ and $K_2 = K_{\text{TOT}}(1-k)$, it should also

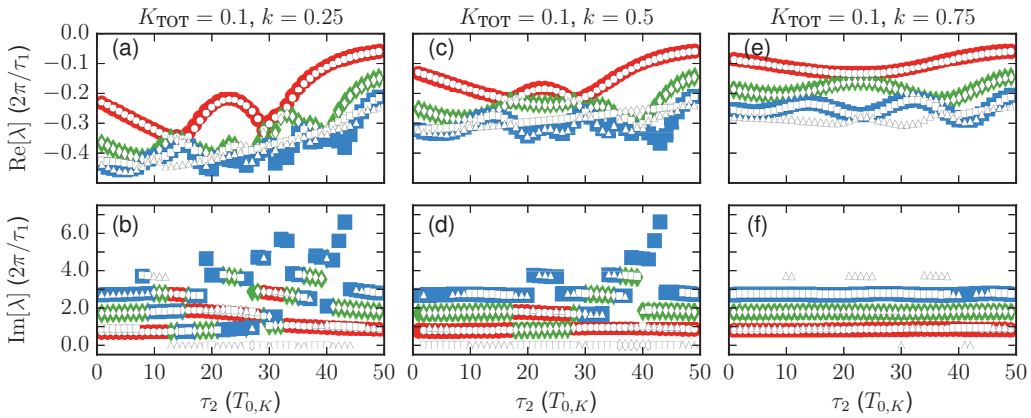

Figure 5.9.: Real (a,c,e) and imaginary (b,d,f) parts of the three dominant Floquet exponents of a passively mode-locked laser subject to feedback from two external cavities for (a,b) $k = 0.25$, (c,d) $k = 0.5$ and (e,f) $k = 0.75$. The white symbols indicate the numerically calculated values and the coloured symbols indicate the results of the fitted characteristic equation (Eq. (5.19)). Parameters: $\tau_1 = 50T_{0,K}$, $K_{TOT} = 0.1$ and $K_{TOT}^{eff} = 0.093$, all other parameters as in Table 2.1.

hold that $K_1^{eff} = K_{TOT}^{eff} k$ and $K_2^{eff} = K_{TOT}^{eff}(1-k)$, where $K_{TOT}^{eff} = K_1^{eff} + K_2^{eff}$. Equation (5.17) can then be written as

$$\lambda = -K_{TOT}^{eff}\left(1 - ke^{-\lambda\tau_1'} - (1-k)\,e^{-\lambda\tau_2'}\right), \tag{5.19}$$

where the only fit parameter is K_{TOT}^{eff}. Examples of the fit of Eq. (5.19) for $k = 0.25$, $k = 0.5$ and $k = 0.75$ are shown in Fig. 5.9, where in each case $K_{TOT}^{eff} = 0.094$.

Off resonant feedback delay times

In terms of timing jitter reduction, feedback delay times that are close to $\tau_n = n_m T_0$, but not necessarily exact integer multiples, are of interest (see Section 4.4). It is therefore also of interest to investigate the dependence of the Floquet exponents on delay times that are slightly detuned from $\tau_m = n_m T_0$, i.e. for $\tau_m = \tau_0 + n_m T_0$ where τ_0 is some small delay offset. Here the question arises if Eq. (5.19) can also be used to describe the dominant Floquet exponents when τ_0 is non-zero.

In Fig. 5.10 results for the four dominant Floquet exponents, calculated using DDE-BIFTOOL, are plotted in the white symbols for delay offsets of $\tau_0 = 0.006T$ (a,b), $\tau_0 = 0.02T$ (c,d) and $\tau_0 = 0.07T$ (e,f). The coloured symbols again show the fit of Eq. (5.19). For the delay offsets $\tau_0 = 0.006T$ and $\tau_0 = 0.02T$, Eq. (5.19) describes the dominant Floquet exponents very well with effective total feedback strengths of $K_{TOT}^{eff} = 0.101$ and $K_{TOT}^{eff} = 0.097$, respectively. However, for $\tau_0 = 0.07T$ Eq. (5.19) fails to fit the τ_2 dependence of any of the exponents. These results suggest that another requirement, for Eq. (5.19) to hold for the dominant

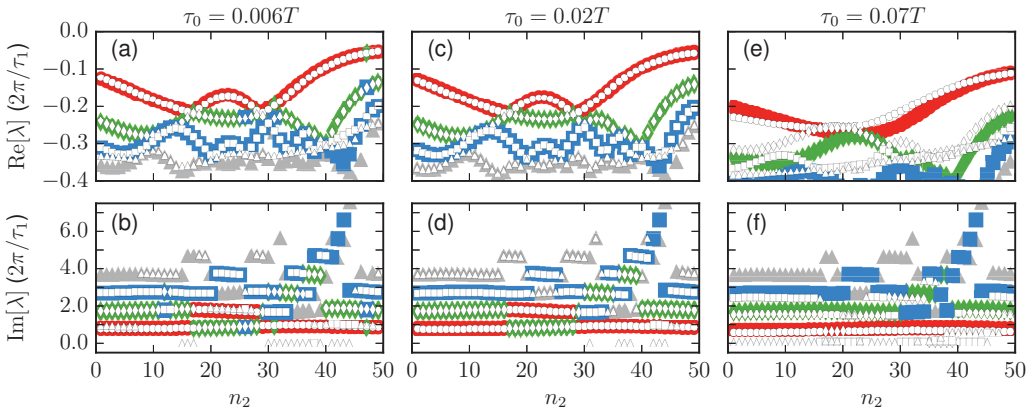

Figure 5.10.: Real (a,c,e) and imaginary (b,d,f) parts of the three dominant Floquet exponents of a passively mode-locked laser subject to feedback from two external cavities for (a,b) $\tau_0 = 0.006T$, (c,d) $\tau_0 = 0.02T$ and (e,f) $\tau_0 = 0.07T$. The white symbols indicate the numerically calculated values and the coloured symbols indicate the results of the fitted characteristic equation (Eq. (5.19)). Parameters: $n_1 = 50$, $K_{\mathrm{TOT}} = 0.1$, $k = 0.5$ and $K_{\mathrm{TOT}}^{\mathrm{eff}} = 0.101$ for (a,b), $K_{\mathrm{TOT}}^{\mathrm{eff}} = 0.097$ for (c,d) and $K_{\mathrm{TOT}}^{\mathrm{eff}} = 0.052$ for (e,f), all other parameters as in Table 2.1.

Floquet exponents, is that the total delay time τ_m' is close to an integer multiple of the period of the mode-locked solution. In the earlier examples, where we had $\tau_m = n_m T_0$, the total delay time τ_m' was nearly an integer multiple of T_0, apart from a small offset due to T being slightly smaller than the period T_0. For example, for $K_{\mathrm{TOT}} = 0.1$ the period is $T_0 = 1.01318$ compared with $T = 1$. As the delay offset τ_0 is increased from zero, the total delay time τ_m' initially becomes closer to an integer multiple of the period T_0. This is because the increase in T_0 is less than linear as τ_0 is increased, as can be seen in Fig. 3.60. For example, in the $\tau_0 = 0.02T$ case the period is $T_0 = 1.01507$, therefore the total delay time τ_m' is only offset from an integer multiple of T_0 by about 0.005 ($T + \tau_0 - T_0 \approx 0.005$), compared with 0.01 in the $\tau_0 = 0$ ($K_{\mathrm{TOT}} = 0.1$) case. However, as τ_0 is increased further, eventually τ_m' becomes more offset from an integer multiple of T_0, which coincides with the fit of Eq. (5.19) becoming poorer. For $\tau_0 = 0.07T$ the solution has a period of $T_0 = 1.01747$ and the offset of the total delay time τ_m' from an integer multiple of T_0 is about 0.05. Apart from providing information on the applicability of Eq. (5.19), Fig. 5.10 also shows that overall the damping rates are much higher for $\tau_0 = 0.07T$. However, for $\tau_0 = 0.07T$ the solutions are already shifted far enough from the main resonances that the pulse shape is deformed (see Fig. 3.63) and hence timing jitter is relatively large (see Fig. 4.14).

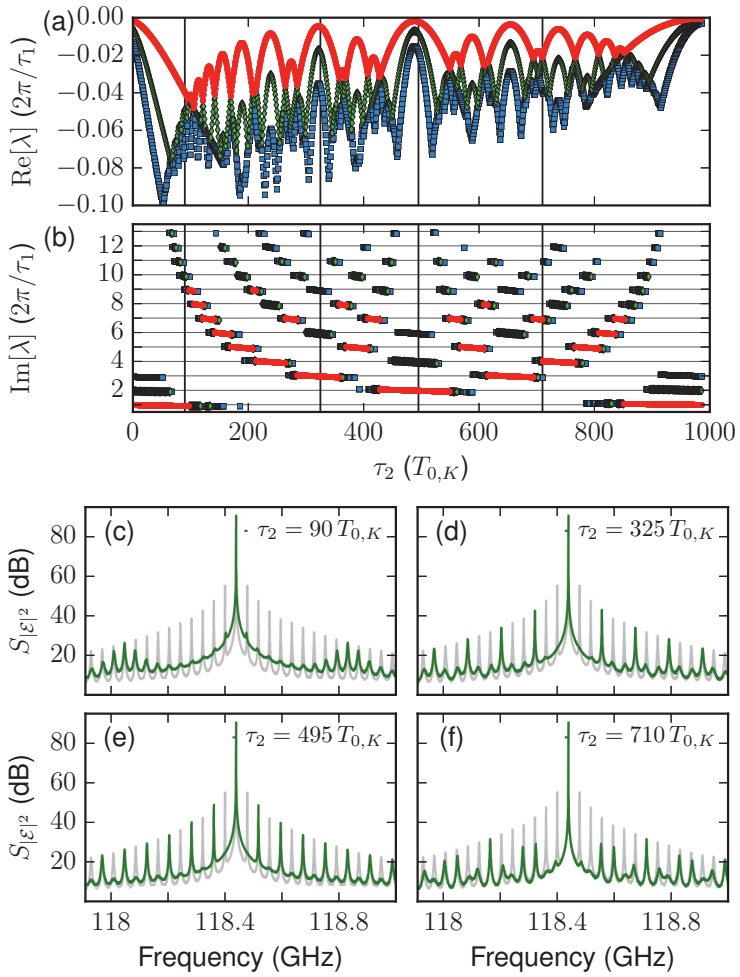

Figure 5.11.: (a) Real and (b) imaginary parts of the largest Floquet exponents of a passively mode-locked laser subject to feedback from two external cavities predicted from the fitted characteristic equation Eq. (5.19). Vertical black lines indicate parameters for power spectra shown in (c)-(f). (c)-(f) Power spectra $S_{|\mathcal{E}|^2}$ of the mode-locked laser output for the τ_2 indicated in each subplot (green). In grey is the spectrum for $\tau_2 = \tau_1 = 1000T_0$. Parameters:$K_{\mathrm{TOT}}^{\mathrm{eff}} = 0.093$ $K_1 = K_2 = 0.05$, $\tau_1 = 1000\,T_0$, $R_{sp} = 0.44$ ($D = 0.2$), all other parameters as in Table 2.1.

Modulation suppression for long feedback delay times

By using the $K_{\mathrm{TOT}}^{\mathrm{eff}}$ values which are fitted to the DDE-BIFTOOL results for shorter delay times, we can now use Eq. (5.19) to investigate the τ_2 dependence of the dominant Floquet exponents for very long τ_1 values. We demonstrate this in Fig. 5.11 for $K_{\mathrm{TOT}} = 0.1$ and $\tau_1 = 1000T_{0,K}$. For resonant delay lengths, i.e. $\tau_m = n_m T_{0,K}$, and a total feedback strength of $K_{\mathrm{TOT}} = 0.1$, we have $K_{\mathrm{TOT}}^{\mathrm{eff}} = 0.093$ from the fits for $\tau_1 = 50T_{0,K}$ and $\tau_1 = 100T_{0,K}$ (Fig. 5.8a-b and Fig. 5.9c-

d, respectively). Using Eq. (5.19), with $K_{\mathrm{TOT}}^{\mathrm{eff}} = 0.093$, the dominant Floquet exponents for $\tau_1 = 1000T_{0,K}$ are shown in Fig. 5.11a-b. To check this prediction of the dominant Floquet exponents, Fig. 5.11c-f shows power spectra of electric field amplitude $|\mathcal{E}|$ for the mode-locked laser system with noise ((Eqs. (4.10)-(4.12) with $D = 0.2$ and $N = 2$) for τ_2 values corresponding to the vertical black lines in Fig. 5.11a-b. The central peak in the power spectra corresponds to the third harmonic of the pulse repetition frequency and the side peaks arise due to the noise-induced modulations. As a reference, plotted in grey is the power spectrum for $\tau_2 = 1000T_{0,K}$, which is equivalent to single cavity feedback with $K = K_{\mathrm{TOT}}$. The side peaks are offset from the main peak by the frequency components of the noise-induced modulations. For the $\tau_2 = 1000T_{0,K}$ case (grey) these frequency components are multiples of $1/1000T_{0,K}$. For $\tau_2 = 90T_{0,K}$ Fig. 5.11a-b predicts that the fundamental frequency of feedback cavity one ($1/1000T_{0,K}$) should be significantly suppressed, but that the modes corresponding to the 9^{th}, 10^{th} and 11^{th} harmonic of this frequency are only weakly damped. In accordance with this the power spectrum for $\tau_2 = 90T_{0,K}$, depicted in green in Fig. 5.11c, shows that the side peaks close to the central peak are suppressed but that the suppression of 9^{th}, 10^{th} and 11^{th} side peaks is weak. In Fig. 5.11d the power spectrum is shown for $\tau_2 = 325T_0$, which corresponds to a maximum in $\mathrm{Re}[\lambda]$ for modes with frequencies which are multiples of the 3^{rd} harmonic of feedback cavity one, i.e. $\mathrm{Im}[\lambda] \approx 2\pi n/\tau_1$ for $n = 3, 6, 9....$ Accordingly, every third side peak is not suppressed. Similar comparisons with Fig. 5.11a-b also show agreement for $\tau_2 = 425T_{0,K}$ and $\tau_2 = 710T_{0,K}$, for which power spectra are shown in Fig. 5.11e-f. The conditions for optimal suppression of the noise-induced modulations (lowest power in the side peaks), for $K_1 = K_2 = 0.05$ and $\tau_1 = 1000T_{0,K}$, are found for τ_2 approximately 85-$90T_{0,K}$, as predicted from Fig. 5.11a which shows the largest damping rate of the dominant Floquet exponents in this range. Also in agreement with Fig. 5.11a, very good suppression of the side peaks in the power spectra is obtained for $\tau_2 \approx 210T_{0,K}$ and $\tau_2 \approx 435T_{0,K}$, as well as at other positions near maxima in the damping rate of the dominant Floquet exponent (minima in the red curve in Fig. 5.11a). The power spectrum for the $\tau_2 = 435T_{0,K}$ example is shown in Fig. 5.16a.

The results of this subsection show that, as for the Stuart-Landau oscillator, the optimal feedback delay lengths for the suppression of noise-induced modulations is not given by a fixed ratio of τ_1 and τ_2, but rather depends on the feedback strengths and τ_1. The general trends are that poor suppression is achieved if τ_1 and τ_2 have a low common multiple, and for increasing τ_1 optimal suppression is achieved for τ_2 values which are an increasingly smaller fraction of τ_1. Furthermore, we have shown that for delay times close to the main resonances, Eq. (5.19) can be used to calculate the dominant Floquet exponents for the mode-locked laser system.

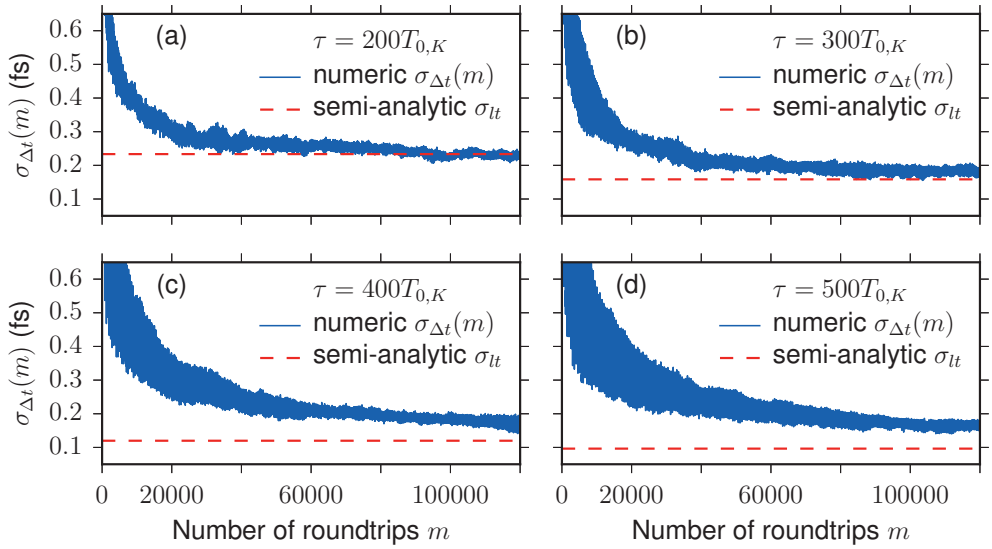

Figure 5.12.: **Single external-cavity feedback:** $\sigma_{\Delta t}(m) = \sqrt{\mathrm{Var}(\Delta t_m)/m}$ plotted as a function of the number of laser cavity roundtrips for various feedback delay times (as indicated in each plot). $N = 100$ noise realisations were used for these calculations. The dashed red line indicates the value of the semi-analytically calculated long-term timing jitter. Parameters: $K = 0.1$, $R_{sp} = 0.44$ ($D = 0.2$), all other parameters as in Table 2.1.

5.3. Impact of noise-induced modulations on the timing jitter

In this section we will address how the noise-induced modulations, and the suppression thereof, influences the timing jitter of the mode-locked laser output.

5.3.1. Timing jitter with noise-induced modulations

In Section 4.4 we investigated the dependence of the timing jitter on resonant feedback delay times from a single feedback cavity. There we found that past a certain feedback delay time, noise-induced modulations play a significant role and can no longer be neglected. When the noise-induced modulations are negligible,

$$\sigma_{\Delta t}(m) = \sqrt{\frac{\mathrm{Var}(\Delta t_m)}{m}}$$

converges to the semi-analytically calculated long-term timing jitter for large m. However, as the noise-induced modulations become large, this is no longer the case. This is illustrated in Fig. 5.12, where $\sigma_{\Delta t}(m)$ (blue line) is plotted as a function of the number of roundtrips for various feedback delay times. In each case the semi-analytically calculated timing jitter is indicated by the dashed red line. In Fig. 5.12a

the delay times is chosen to be $\tau = 200T_{0,K}$. For this delay time $\sigma_{\Delta t}(m)$ still converges to the semi-analytic value. However, in Fig. 5.12b-d increasingly larger feedback delay times are used and it can be seen that, for large m, $\sigma_{\Delta t}(m)$ becomes increasingly offset from the semi-analytic value (see Fig. 4.18 for the $\tau = 1000T_{0,K}$ example). This means that, as well as there being significant fluctuations in the pulse positions on time scales of τ (for examples of the modulation of the timing fluctuations see Fig. 4.4), the variance of the timing fluctuations on long time scales is also increased due to the short time-scale fluctuations. The semi-analytic results give the lower limit of the timing jitter in the absence of the noise-induced modulations.

To understand how the noise-induced modulations affect the variance of the timing fluctuations, it is helpful to consider a simple iterative map describing a random process with an added oscillatory term. We consider

$$T_{n+1} = T_n + T_0 + D\xi(n+1) + a\mathcal{H}, \tag{5.20}$$

where T_0 is a constant, $\xi(n)$ is a Gaussian white noise term with the properties

$$\langle \xi(n) \rangle = 0 \quad \text{and} \quad \langle \xi(n)\, \xi(n') \rangle = \delta(n - n'),$$

D is the noise strength and $\mathcal{H}$ is a sinusoidal function of either n, or T_n, i.e. $\mathcal{H}(n) = \sin\left(\frac{2\pi n}{\tau_s}\right)$ or $\mathcal{H}(T_n) = \sin\left(\frac{2\pi T_n}{\tau_s}\right)$, with amplitude a. For $\mathcal{H}(n)$ the oscillations are periodic, but for $\mathcal{H}(T_n)$ this term oscillates with an irregular period since T_n is a stochastic variable. If $a = 0$ then

$$T_n = nT_0 + D\sum_{i=1}^{n} \xi(i) \tag{5.21}$$

and the set of fluctuations $\{\Delta T_n\} = \{T_n - nT_0\}$ behaves like a random walk. In this case, apart from statistical fluctuations, the quantity

$$\sigma_{\Delta T_n}(n) = \sqrt{\frac{\mathrm{Var}\Delta T_n}{n}} \tag{5.22}$$

is constant in n. This is shown by the black line in Fig. 5.13. If a is non-zero and the periodic term $\mathcal{H}(n)$ is used, the sinusoidal term adds regular oscillations onto the variance. For n equal to integer multiples of the period of $\mathcal{H}(n)$, which is given by τ_s, the contribution from the oscillations is zero and $\sigma_{\Delta T_n}(n)$ is the same as in the $a = 0$ case. This can be seen by comparing the red line and the black line in Fig. 5.13. If $\mathcal{H}(T_n)$ is used instead of $\mathcal{H}(n)$, the contribution to T_n from the added irregular oscillations does not periodically cancel out, since the T_n values which enter $\mathcal{H}(T_n)$ vary stochastically. This means that the contributions from $\mathcal{H}(T_n)$ accumulate, which leads to an overall increase in the variance (Fig. 5.13 blue line). The mode-locked laser with feedback is comparable to the latter case as the noise-induced modulations are not perfectly periodic.

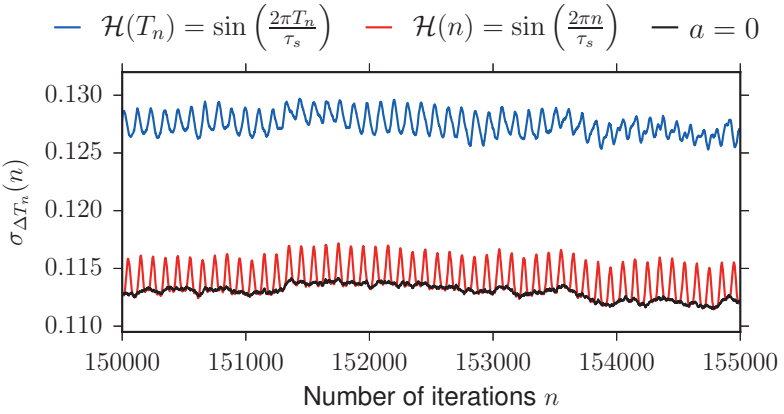

Figure 5.13.: $\sigma_{\Delta T_n}(n) = \sqrt{\mathrm{Var}\Delta T_n / n}$ of the timing fluctuations produced by the iterative map Eq. (5.20) for $a = 0$ (black), $\mathcal{H} = \mathcal{H}(n)$ (red) and $\mathcal{H} = \mathcal{H}(T_n)$ (blue). $N = 50$ noise realisations were used. Parameters: $T_0 = 1$, $a = 0.4$, $\tau_s = 100$, $D = 0.1$.

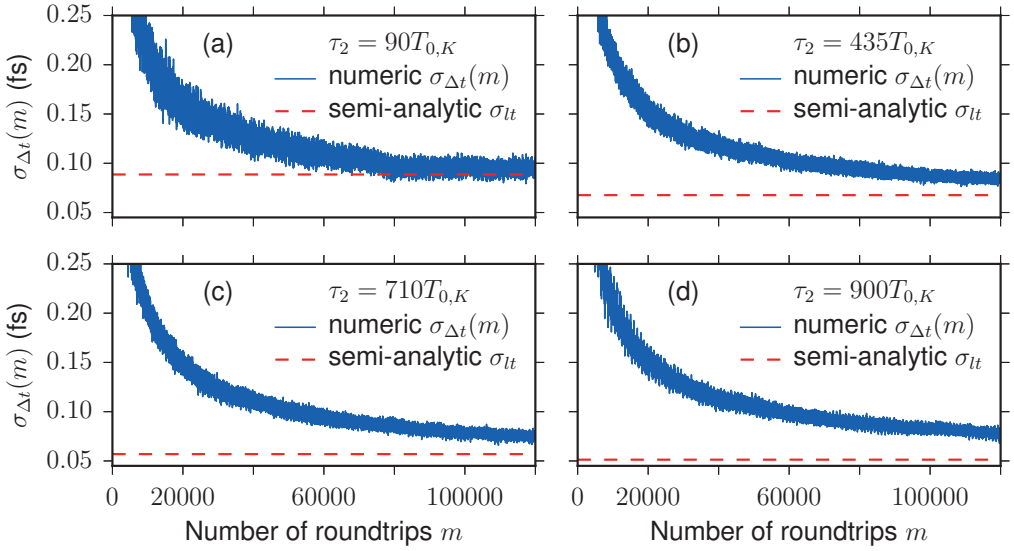

Figure 5.14.: **Dual external-cavity feedback:** $\sigma_{\Delta t}(m) = \sqrt{\mathrm{Var}(\Delta t_m)/m}$ plotted as a function of the number of laser cavity roundtrips for various τ_2 values (as indicated in each plot), with $\tau_1 = 1000T_{0,K}$. $N = 100$ noise realisations were used for these calculations. The dashed red line indicates the value of the semi-analytically calculated long-term timing jitter. Parameters: $K = 0.1$, $R_{sp} = 0.44$ ($D = 0.2$), all other parameters as in Table 2.1.

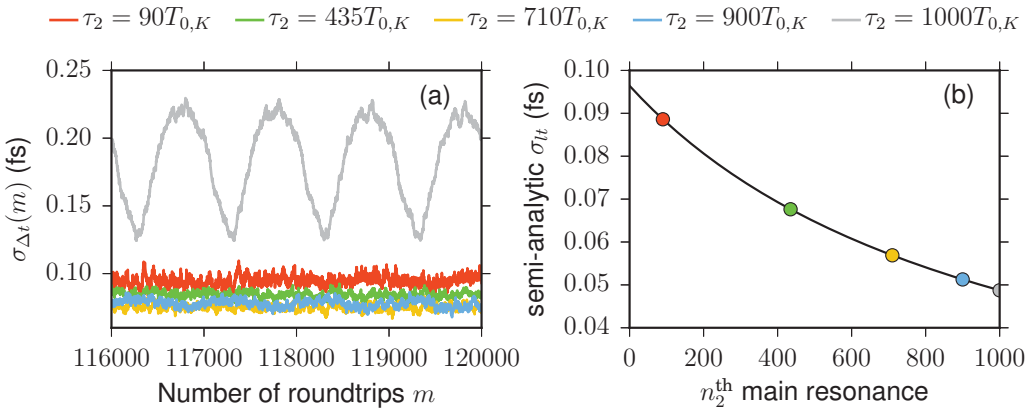

Figure 5.15.: **Dual external-cavity feedback:** (a) $\sigma_{\Delta t}(m) = \sqrt{\mathrm{Var}(\Delta t_m)/m}$ plotted as a function of the number of laser cavity roundtrips for various τ_2 values (as indicated in the legend), with $\tau_1 = 1000T_{0,K}$. $N = 100$ noise realisations were used for these calculations. (b) Semi-analytic prediction of the long-term timing jitter in dependence of the resonance number of the second feedback cavity. The colour circles correspond to the τ_2 values used in (b). Parameters: $K = 0.1$, $R_{sp} = 0.44$ ($D = 0.2$), all other parameters as in Table 2.1.

5.3.2. Reduction of the timing jitter via the suppression of noise-induced modulations

We will now look at the influence of suppressing the noise-induced modulations on the timing jitter. For this we will use the $\tau_1 = 1000T_{0,K}$ and $K_{\mathrm{TOT}} = 0.1$ example for which the prediction of the dominant Floquet exponents is shown in Fig. 5.11a-b. From Fig. 5.11a-b we concluded that the best suppression of the noise-induced modulations should occur for $\tau_2 \approx 90T_{0,K}$ as here the damping rate of the dominant Floquet exponent is greatest. However, from the analytic expression for the dependence of the timing jitter on the resonance numbers,

$$\sigma_{lt}(\tau_0, n_1, n_2, K_{\mathrm{TOT}}, k) = \frac{\sigma_{lt}(K_{\mathrm{TOT}}, \tau_0)}{1 + K_{\mathrm{TOT}}(kn_1 + (1-k)n_2)\mathcal{F}(K_{\mathrm{TOT}}, \tau_0)}$$

with $\sigma_{lt}(K_{\mathrm{TOT}}, \tau_0)$ and $\mathcal{F}(K_{\mathrm{TOT}}, \tau_0)$ as defined in Subsection 4.4.1, we know that the minimal long-term timing jitter, that can be achieved when the modulations are suppressed, is also dependent on the length of the second feedback cavity. Hence, there is a trade off between modulation suppression and reduced minimal long-term timing jitter. To investigate the influence of these two factors, the behaviour of the timing fluctuations is shown in Fig. 5.14 for various τ_2 values. Plotted in blue is $\sigma_{\Delta t}(m)$ as a function of the number of laser cavity roundtrips and indicated by the dashed red line is the semi-analytically predicted long-term timing jitter. For $\tau_2 = 90T_{0,K}$ (Fig. 5.14a) the suppression of the modulations is very effective and $\sigma_{\Delta t}(m)$

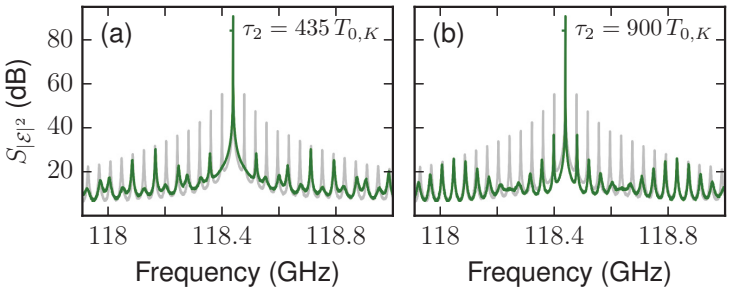

Figure 5.16.: Power spectra $S_{|\mathcal{E}|^2}$ of the mode-locked laser output for the $\tau_2 = 435T_{0,K}$ (a) and $\tau_2 = 900T_{0,K}$ (b) (green). In grey is the spectrum for $\tau_2 = \tau_1 = 1000T_{0,K}$. Parameters:$K^{\text{eff}}_{\text{TOT}} = 0.093$ $K_1 = K_2 = 0.05$, $\tau_1 = 1000T_{0,K}$, $R_{sp} = 0.44$ ($D = 0.2$), all other parameters as in Table 2.1.

converges to the semi-analytic value. Meaning that the variance of fluctuations in the pulse positions is not influenced by any residual noise-induced modulations when the roundtrip number is large (of the order of 10^5). In Fig. 5.14b the second delay time is $\tau_2 = 435T_{0,K}$. In this case the suppression of the modulations is not quite as pronounced (compare Fig. 5.11c with Fig. 5.16a) but due to the longer second feedback cavity $\sigma_{\Delta t}(m)$ is lower, for large m, than in the $\tau_2 = 90T_{0,K}$ case. Examples for $\tau_2 = 710T_{0,K}$ and $\tau_2 = 900T_{0,K}$ are shown in Fig. 5.14c-d. For a better comparison between these cases, $\sigma_{\Delta t}(m)$ is plotted for only large roundtrip numbers in Fig. 5.15a. A comparison of the semi-analytic prediction for these feedback delay times is shown in Fig. 5.15b. In all four cases the variance of the timing fluctuations, and hence the estimate of the long-term timing jitter, is lower than in the single feedback cavity case (grey curve in Fig. 5.15a). For the selected τ_2 values the best results are obtained for $\tau_2 = 710T_{0,K}$. For this delay time the long-term timing jitter is low (orange curve in Fig. 5.15a) and good suppression of the noise-induced modulations is achieved. The long-term timing jitter for $\tau_2 = 900T_{0,K}$ is approximately the same (blue curve in Fig. 5.15a) but due to the lower damping rates the modulations are more pronounced. This can be seen by comparing the power spectra in Fig. 5.16b and Fig. 5.11f.

For $\tau_2 = 710T_{0,K}$ the long-term timing jitter is reduced by about 40% compared with the estimate for single cavity feedback case (for the single cavity feedback case the long-term timing jitter is estimated from the minima in $\sigma_{\Delta t}(m)$, i.e. the level of the minima in the grey curve in Fig. 5.15a). Although the change in the long-term jitter is not very large, the reduction in the modulation amplitude of the timing fluctuations leads to a significant improvement in the regularity of the pulse train. For single cavity feedback, with $\tau = 1000T_{0,K}$ and $K = 0.1$, the noise-induced modulations cause fluctuations in the pulse arrival times of the order of 100 fs (see Fig. 4.4). With a long-term timing jitter of $\sigma_{lt} \approx 0.1$ fs, comparable

deviations due to the random-walk-like behaviour are only reached for roundtrip numbers of the order of 10^5. This means that depending on the intended application of the passively mode-locked laser, the short time scale fluctuations in the pulse positions can be just as important to take into account as the drift on long times and suppressing these effects can lead to vastly improved device performance.

Experimentally dual feedback configurations have been implemented and, although the delay lengths were not optimised, these studies showed a significant improvement in the rms timing jitter [JAU16, DRZ13a, HAJ12]. In these works the reduction in the rms timing jitter was larger than the reduction in the long-term jitter demonstrated numerical here. This is expected due to the delay lengths used in these experimental studies. In [JAU16] the delay length of the longer feedback cavity is about 3000 times the interspike-interval time. For longer delay times the damping rates are reduced, therefore the noise-induced modulations are expected to play a larger role. Hence, the suppression of noise-induced modulations becomes more important.

5.4. Summary

In this chapter we have studied how a second feedback term can be used to suppress noise-induced modulations that arise in periodic systems with feedback. We first looked at the Stuart-Landau oscillator and then the mode-locked laser system. For the mode-locked laser we also addressed how the noise-induced modulations influence the timing jitter.

As long as the noise source is sufficiently small the noise-induced modulations are related to the stability of the linearised system. For the Stuart-Landau oscillator subject to two feedback terms we have therefore performed a linear stability analysis to determine how the second feedback term affects the damping rates of the dominant Floquet exponents. To do this we restricted our analysis to resonant feedback conditions, i.e. feedback delay times that are integer multiples of the period and zero feedback phases. Under these conditions the dynamics remain the same for different delay times and one can ascertain how the delay lengths influence the dominant Floquet exponents, which are given by a simple characteristic equation that can be analytically derived. The results for the delay time and feedback strength dependence of the dominant Floquet exponents have shown that conditions for optimal suppression of the noise induced modulations, i.e. strongest damping of the Floquet modes, are not given by a fixed ratio of the feedback delay times. The general trends are that suppression is poor when the delay times have a low common multiple and for increasing delay times for the first feedback term, or for increasing feedback strengths, the second feedback delay time should be an increasingly smaller fraction of the long delay time for the suppression to be

optimised. Furthermore, the frequency of the dominant Floquet exponent follows a Farey-tree-like structure in dependence of the delay times. This means that the dominant frequency of the noise-induced modulations can be changed depending on the resonance between the two delay times.

The mode-locked laser system is vastly more complicated than the Stuart-Landau oscillator. We were therefore not able to derive a characteristic equation for this system. However, by fitting numerically calculated Floquet exponents we were able to show that for resonant feedback delay times the dominant Floquet exponents can be described by a simple characteristic equation which has the same form as the equation that was analytically derived for the Stuart-Landau oscillator, with the only fit parameter being an effective total feedback strength. By showing that this is also applicable for small offsets from the main resonances we can deduce that a condition for a good fit of the characteristic equation to hold is that the total delay times are close to integer multiples of the period. A further condition is that at least one of the delay times is sufficiently long, otherwise there are also other system-dependent dominant Floquet exponents that cannot be described by the simplified characteristic equation. Since the characteristic equation for the mode-locked laser has the same form as for the Stuart-Landau oscillator, the same trends hold for the conditions for optimal suppression of the modulations in the mode-locked laser.

The fitted characteristic equation depends analytically on the feedback delay times, meaning that it can be used to make predictions about optimal delay times for the second feedback cavity, when the first feedback cavity is very long. This is useful because for long delay times fully numerical methods of determining the Floquet exponents require very long computation times and large amounts of memory. By comparison with numerically calculated power spectra for the system with noise, we demonstrated that there was very good agreement between the frequency components predicted from the dominant Floquet exponents which are given by the characteristic equation and those present in the power spectra. And, for optimally chosen delay times, i.e. delay times for which the damping rates of the dominant Floquet exponents are large, very good suppression of the noise-induced modulations can be achieved.

The noise-induced modulations cause the pulse positions to fluctuate on short time scales, which we have shown to also lead to an increase in the variance of the timing fluctuations on long time scales. Therefore, suppressing the noise-induced modulations is very important as this improves the regularity of the pulse train on short time scales, as well as reducing the long-term timing jitter. The optimal delay time conditions for this are not quite the same as those for optimal suppression of the noise-induced modulations because there is a trade-off between improved modulation suppression for shorter delay times and a lower minimum long-term timing jitter for longer delay times. The minimum long-term timing jitter that

can be achieved for any feedback delay configuration is given by the semi-analytic method, as this method provides the long-term timing jitter in the absence of noise-induced modulations. If the second delay time is chosen appropriately, dual cavity feedback can be an effective means of generating low timing jitter pulse trains.

Chapter 6

Summary and outlook

In this thesis we have investigated the dynamics and stochastic properties of a passively mode-locked semiconductor laser subject to time-delayed optical feedback.

A passively mode-locked semiconductor laser can produce ultra-short optical pulses at very high repetitions. By subjecting such a laser to optical feedback the mode-locked dynamics can be influenced in several ways. Firstly, time-delayed feedback can be used to alter the repetition rate of the pulsed laser output. There are two manifestations of this effect. One is a fine tuning of the repetition rate that occurs if the system is forced to adapt to slightly off-resonant feedback delay times. The other is a multiplication of the repetition rate that occurs via feedback induced harmonic mode-locking. These are effects that can be of use for applications which require precise, or very high, repetition rates. However, feedback can also have detrimental effects on the mode-locked dynamics. For example, non-resonantly chosen delay conditions can lead to a widening of the pulses or destabilisation of the periodic mode-locked dynamics, resulting in quasi-periodic or chaotic pulse trains. When the feedback delay time is chosen resonantly the dynamics are unchanged compared with solitary laser with the same total non-resonant losses. These resonances occur at delay times which are integer multiples of the period. Surrounding each of the resonant feedback delay time, there is a locking range in which fundamental mode-locking is exhibited. These locking ranges become wider as the delay times are increased, eventually leading to multistability between solutions locked to different resonances. This multistability can be lifted by adding a second feedback cavity which has a different delay time.

The unavoidable presence of spontaneous emission noise leads to a large timing jitter in passively mode-locked semiconductor lasers in comparison to actively modulated devices. This is a result of the time-shift invariance of passively mode-locked lasers, or in other words, due to the lack of a restoring force. Resonantly chosen feedback can be an effective passive means of combating this detrimental

effect. Using a semi-analytic method of calculating the timing jitter we have derived an expression for the resonant delay time dependence of the timing jitter. This semi-analytic method takes into account the influence of noise along the neutral mode of the linearised system which is related to the time-shift invariance of the mode-locked laser system. In the absence of noise-induced effects along other eigendirections of the system, our derived expression predicts that the timing jitter decreases monotonically as the feedback time delay is increased. This reduction in the timing jitter is a result of correlations between current and past pulse positions that are introduced via the delayed feedback. However, as the feedback delay times become long, noise can excite other weakly stable eigenmodes of the system, which leads to a modulation of the pulse positions and an increased variance of the timing fluctuations compared with the semi-analytic prediction. In experimental studies such noise-induced modulations are manifested as side-peaks in the power spectra of the laser output. These noise-induced modulations can cause fluctuations in the pulse arrival times that are significant for long feedback cavities, and depending on the desired application, should not be ignored.

The noise-induced modulations that arise for long feedback delay times can be suppressed by adding a second feedback cavity of the appropriate length. To study the suppression of noise-induced modulations we have first investigated this effect in a simple oscillatory system, the Stuart-Landau oscillator. For this system one can derive a simple characteristic equation for the dominant Floquet exponents. The damping rates and frequencies of these exponents are related to the amplitude and frequency of the noise-induced modulations. We have shown that, for resonant feedback, by selecting the delay length of the second cavity such that the damping rates are high, the noise-induced modulations can be effectively suppressed. Furthermore, for the mode-locked laser system, despite the complexity of this system, we have shown that, under certain conditions, the dominant Floquet exponents can be described by a simple characteristic equation which has the same form as the equation which can be analytically derived for the Stuart-Landau oscillator. Using this characteristic equation one can make predictions for delay configurations resulting in the optimal suppression of noise-induced modulations. For both the Stuart-Landau and the mode-locked laser systems, the optimal suppression of the noise-induced modulations is not given by a fixed ratio of the feedback delay times, but rather depends on the delay time of the longer feedback cavity and on the feedback strengths.

By suppressing the noise-induced modulations in the mode-locked laser system, the timing regularity can be significantly improved. On the one hand the regularity on short time scales is improved because the fluctuations on time scales of the feedback delay time are reduced. On the other hand the long-term timing jitter is also reduced. This is because the contribution to the variance of the timing fluctuations, from the irregular short-term oscillations of the pulse positions, is

removed. A dual feedback cavity configurations therefore has the potential to vastly improve the performance of passively mode-locked lasers. However, the implementation of such a setup is more difficult, compared with a single feedback cavity, due to the increased sensitivity of the dynamics to the feedback phases.

The mode-locked laser system with feedback is one example of a dynamical system where the suppression of noise-induced modulations is important. However, such effects can also arise in other periodic physical system that involve long delay times. In future studies, it would therefore be interesting to extend our work on the simple characteristic equation that we found to accurately describe the dominant Floquet exponents for the mode-locked laser. We have shown that this equation also applies to a FitzHugh-Nagumo oscillator subject to feedback. This raises the question, what conditions must a system fulfil such that the characteristic equation can be reduced to such a simple form for the dominant Floquet exponents? And, is it possible to derive this characteristic equation for a general oscillatory system subject to feedback? If so, this could be very useful, as then one could gain a better understanding of how the effective feedback strengths in the characteristic equation depend on the dynamics of the particular system, and hence how feedback impacts the stability of different systems.

We have extensively studied the feedback induced dynamics of a passively mode-locked laser using the now commonly applied delay differential equation model. This modelling approach includes various simplifying assumptions and we have used a relatively simple model for the charge carriers in the active medium. Nevertheless, a lot of the qualitative trends that are observed in more complicated modelling approaches, and in experiments, can be reproduced. Via comparison with experimental results for a quantum-dot passively mode-locked laser we have shown that the feedback induced trends agree well with those predicted using the DDE model. However, there are still some aspects that warrant investigation with a refined model. For example, how are the feedback induced dynamics affected if one uses a quantum-dot based model with dynamical amplitude-phase coupling? Or, how do the dynamics of a quantum-dot based gain medium influence the timing jitter reduction that can be achieved with optical feedback? Our semi-analytically derived expression for the timing jitter reduction has shown that if the delay is long, but noise-induced modulations are neglected, the timing jitter scales as one over the resonant delay time, however, with a proportionality factor that depends on the dynamics, which would be different for a quantum-dot based model. In terms of the timing jitter and the noise-induced modulations, a further point to investigate is the impact of coloured noise.

Another direction for future work is related to the feedback schemes. We have investigated the influence coupling to one and two passive external cavities. However, it is also of interest to investigate coupling to active cavities. For example, coupling two or more passively mode-locked lasers. Such a setup has the promise

of producing synchronised pulse trains, which could be used generated more energetic pulses, or higher repetition rates. From a non-linear dynamics point of view such a system is also interesting as a test bed for the dynamics arising in coupled pulsating systems.

To conclude, time-delayed feedback can induce a rich range of dynamics in passively mode-locked lasers and is a promising means of improving the performance of such devices without the need to introduce active elements.

Appendix A

Floquet theory

The stability of solutions to linear periodic differential systems can be studied using Floquet theory. Consider a linear first-order system

$$\dot{\mathbf{x}}(t) = A(t)\,\mathbf{x}(t), \tag{A.1}$$

where $A(t)$ is a $n \times n$ periodic matrix,

$$A(t+T) = A(t), \tag{A.2}$$

with period T.

The principle matrix solution of Eq. (A.1), $\mathbf{\Phi}(t, t_0)$, is a matrix whose columns are linearly independent solutions of Eq. (A.1) and at some time t_0 $\mathbf{\Phi}(t_0, t_0) = \mathbb{I}$, where $\mathbb{I}$ is the identity matrix. This matrix satisfies

$$\dot{\mathbf{\Phi}}(t, t_0) = A(t)\,\mathbf{\Phi}(t, t_0) \tag{A.3}$$

and

$$\mathbf{\Phi}(t+T, t_0+T) = \mathbf{\Phi}(t, t_0) \tag{A.4}$$

and can be written as

$$\mathbf{\Phi}(t, t_0) = \mathbf{P}(t, t_0)\, e^{(t-t_0)\mathbf{Q}(t_0)}, \tag{A.5}$$

where $\mathbf{Q}(t_0)$ is an $n \times n$ matrix and $\mathbf{P}(t+T, t_0) = \mathbf{P}(t, t_0)$ is T-periodic. The principle matrix describes the evolution of solutions to Eq. (A.1), i.e. if $\mathbf{x}(t+t_0)$ is a solution to Eq. (A.1) then the evolution from time t_0 is given by

$$\mathbf{x}(t+t_0) = \mathbf{\Phi}(t, t_0)\,\mathbf{x}(t_0). \tag{A.6}$$

The stability of the solution $\mathbf{x}(t+t_0)$ is then given by the eigenvalues of the so called monodromy matrix which is defined as

$$\mathbf{M}(t_0) = \mathbf{\Phi}(t_0+T, t_0) \tag{A.7}$$

and describes the evolution over one period T. The monodromy matrix can be written in the form

$$\mathbf{M}(t_0) = e^{T\mathbf{Q}(t_0)}. \tag{A.8}$$

The eigenvalues μ_j of $\mathbf{M}(t_0)$ are referred to as the Floquet multipliers (or characteristic multipliers) of the solution to Eq. (A.1) and the eigenvalues λ_j of $\mathbf{Q}(t_0)$ are the Floquet exponents (or characteristic exponents). A solution is stable if $|\mu_j| \leq 1$ ($\mathrm{Re}[\lambda_j] \leq 0$) for all j. For a more detailed introduction to Floquet theory see, for example, [TES12].

For linear delay differential equations, a complete Floquet theory does not exist [HAL93], however the characteristic multipliers and exponents can be defined in similar way. Consider a linear delay differential equation

$$\dot{\mathbf{x}}(t) = A(t)\,\mathbf{x}(t) - B(t-\tau)\,\mathbf{x}(t-\tau), \tag{A.9}$$

with periodic matrices $A(t+T) = A(t)$ and $B(t+T) = B(t)$. Let $U(t, t_0)$ be an operator that describes the time evolution of a solution $\mathbf{x}(t+t_0)$ to Eq. (A.9), i.e

$$\mathbf{x}(t+t_0) = U(t, t_0)\,\mathbf{x}(t_0). \tag{A.10}$$

Then the monodromy operator in defined as

$$\mathbf{M}(t_0) = U(t_0 + T, t_0) \tag{A.11}$$

and the characteristic multipliers μ_j are the eigenvalues of $\mathbf{M}(t_0)$. Details on the stability analysis of periodic linear delay differential can be found in [HAL93].

Note that in both the linear ordinary and delay differential equations case the characteristic multipliers are independent of the choice of t_0 and both systems (Eqs. (A.1) and (A.9)) have solutions of the form

$$\mathbf{x}(t) = \mathbf{p}(t)\, e^{\lambda_j t}, \tag{A.12}$$

where $\mathbf{p}(t+T) = \mathbf{p}(t)$ is T-periodic.

Appendix B

Linearised mode-locked laser system

B.1. Linearised DDE model

The DDE system for the mode-locked laser (Eqs. (4.10)-(4.12)), linearised about a periodic solution $\psi_0(t)$, is given by

$$\frac{d}{dt}\delta\psi(t) = A(t)\,\delta\psi(t) + \sum_{n=0}^{N} B_n\left(t-\tau_n'\right)\delta\psi\left(t-\tau_n'\right) + Dw(t), \tag{B.1}$$

where $\delta\psi(t) = \left(\mathrm{Re}\,\delta\mathcal{E}(t), \mathrm{Im}\,\delta\mathcal{E}(t), \delta G(t), \delta Q(t)\right)^{\mathrm{T}}$, $w(t) = (\xi_1(t), \xi_2(t), 0, 0)^{\mathrm{T}}$, A and B_n are T_0-periodic Jacobi matrices of the linearisation and the delay times are defined as $\tau_0' = T$ and $\tau_n' = T + \tau_n$ for $n \geq 1$. The Jacobi matrices are given by

$$A(t) = \begin{pmatrix} -\gamma & -\omega & 0 & 0 \\ \omega & -\gamma & 0 & 0 \\ e^{-Q_0(t)}\mathcal{G}(t)\,2\mathcal{E}_0^R(t) & e^{-Q_0(t)}\mathcal{G}(t)\,2\mathcal{E}_0^I(t) & -\gamma_g - e^{-Q_0(t)}e^{G_0(t)}|\mathcal{E}_0(t)|^2 & -e^{-Q_0(t)}\mathcal{G}(t)\,|\mathcal{E}_0(t)|^2 \\ -r_s\mathcal{Q}(t)\,2\mathcal{E}_0^R(t) & -r_s\mathcal{Q}(t)\,2\mathcal{E}_0^I(t) & 0 & -\gamma_q - r_s e^{-Q_0(t)}|\mathcal{E}_0(t)|^2 \end{pmatrix} \tag{B.2}$$

with $\mathcal{G}(t) = 1 - e^{G_0(t)}$ and $\mathcal{Q}(t) = 1 - e^{Q_0(t)}$, and

$$B_n(s) = K_n\gamma \begin{pmatrix} R_0^R(s) & -R_0^I(s) & R_0^R(s)\,\mathcal{E}_{RI}^g(s) - R_0^I(s)\,\mathcal{E}_{IR}^g(s) & -R_0^R(s)\,\mathcal{E}_{RI}^q(s) + R_0^I(s)\,\mathcal{E}_{IR}^q(s) \\ R_0^I(s) & R_0^R(s) & R_0^I(s)\,\mathcal{E}_{RI}^g(s) + R_0^R(s)\,\mathcal{E}_{IR}^g(s) & -R_0^I(s)\,\mathcal{E}_{RI}^q(s) - R_0^R(s)\,\mathcal{E}_{IR}^q(s) \\ 0 & 0 & 0 & 0 \\ 0 & 0 & 0 & 0 \end{pmatrix} \tag{B.3}$$

for $s = t - \tau_m'$ and $K_0 = 1$, with $\mathcal{E}_0^R = \mathrm{Re}\,\mathcal{E}_0$, $\mathcal{E}_0^I = \mathrm{Im}\,\mathcal{E}_0$, $R_0(s) = \sqrt{\kappa}e^{\frac{1}{2}(1-i\alpha_g)G_0(s) - \frac{1}{2}(1-i\alpha_q)Q_0(s) - i\omega(s-t)}$, $R_0^R = \mathrm{Re}\,R_0$, $R_0^I = \mathrm{Im}\,R_0$ $\mathcal{E}_{RI}^g(s) = \frac{1}{2}\left(\mathcal{E}_0^R(s) + \alpha_g\mathcal{E}_0^I(s)\right)$, $\mathcal{E}_{IR}^g(s) = \frac{1}{2}\left(\mathcal{E}_0^I(s) - \alpha_g\mathcal{E}_0^R(s)\right)$, $\mathcal{E}_{RI}^q(s) = \frac{1}{2}\left(\mathcal{E}_0^R(s) + \alpha_q\mathcal{E}_0^I(s)\right)$ and $\mathcal{E}_{IR}^q(s) = \frac{1}{2}\left(\mathcal{E}_0^I(s) - \alpha_q\mathcal{E}_0^R(s)\right)$.

These matrices are obtained by calculating the partial derivatives of the right-hand side of Eqs. (4.10,2.43,2.44) with respect to the dynamical variables, whereby delayed variables are treated separately.

B.2. Adjoint system

The linearised system Eq. (4.13) (Eq. (B.1)) can be expressed as

$$\dot{\delta\psi}\left(t\right) = \mathcal{L}\delta\psi\left(t\right), \tag{B.4}$$

for the appropriate operation $\mathcal{L}$. The adjoint problem to the homogeneous ($D = 0$) version of Eq. (4.13) is defined as the function

$$\dot{\delta\psi^{\dagger}}\left(t\right) = \mathcal{L}^{\dagger}\delta\psi^{\dagger}\left(t\right), \tag{B.5}$$

that fulfils

$$\left[\mathcal{L}\delta\psi\left(t\right), \delta\psi^{\dagger}\left(t\right)\right] = \left[\delta\psi\left(t\right), \mathcal{L}^{\dagger}\delta\psi^{\dagger}\left(t\right)\right], \tag{B.6}$$

where the square brackets represent the bilinear form (Eq. (4.16)). Substituting Eq. (4.13) into the left-hand side this Eq. (B.6) and writing out the bilinear form for this side, and comparing this with the bilinear form written out for the right-hand side of Eq. (B.6), one can see that the linear system adjoint to Eq. 4.13, for $D = 0$, is given by

$$\frac{d}{dt}\delta\psi^{\dagger}(t) + \delta\psi^{\dagger}(t)A(t) + \sum_{n=0}^{N}\delta\psi^{\dagger}(t+\tau_n')B_n(t) = 0, \tag{B.7}$$

where $\delta\psi^{\dagger}(t) = (\delta\psi_1^{\dagger}, \delta\psi_2^{\dagger}, \delta\psi_3^{\dagger}, \delta\psi_4^{\dagger})$ is a row vector.

Appendix C

Suppression of noise-induced modulations

C.1. FitzHugh-Nagumo oscillator

In this section we show that the characteristic equation Eq. (5.19) accurately describes the dominant Floquet exponents of a FitzHugh-Nagumo oscillator subject to resonant feedback from two non-invasive feedback terms.[1]

The FitzHugh-Nagumo oscillator subject to two non-invasive feedback terms is given by

$$\dot{u} = \frac{1}{\varepsilon}\left(u - \frac{u^3}{3} - v + K_1\left(u\left(t-\tau_1\right) - u\right) + K_2\left(u\left(t-\tau_2\right) - u\right)\right) \tag{C.1}$$

and

$$\dot{v} = u + a, \tag{C.2}$$

where u is the fast activator variable, v is the slow inhibitor variable, ε is the time separation parameter and a is the excitability parameter. We choose $a = 0.8$ (oscillatory regime) and $\varepsilon = 0.01$.

In Fig. C.1 the white symbols indicate the three dominant Floquet exponents obtained from the DDE-BIFTOOL calculations, plotted behind these are the results of the fitted characteristic equation Eq. (5.19) with the red circles indicating the most dominant Floquet exponent. The only fit parameter is the effective total feedback strength, which is $K_{\mathrm{TOT}}^{\mathrm{eff}} = 0.101$. Figure C.1 shows excellent agreement between the Floquet exponents given by Eq. (5.19) and those calculated using DDE-BIFTOOL.

[1] For examples of the dynamics and parameter dependence of the FitzHugh-Nagumo oscillator see [HOE09b].

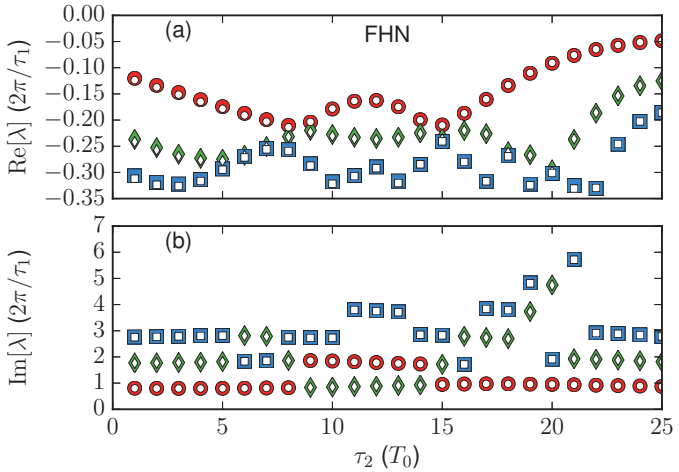

Figure C.1.: Real (a) and imaginary (b) parts of the four dominant Floquet exponents of a FitzHugh-Nagumo oscillator (FHN) with two feedback terms. The white markers indicate the numerically calculated values and the coloured markers indicate the results of the fitted characteristic equation. Parameters: $K_1 = K_2 = 0.005$, $K_{\mathrm{TOT}}^{\mathrm{eff}} = 0.101$, $\tau_1 = 25T_0$, $a = 0.8$ and $\varepsilon = 0.01$.

List of Figures

List of Tables

List of Publications

Parts of this work have been previously published in:

1. C. Otto, L. C. Jaurigue, E. Schöll, and K. Lüdge: *Optimization of timing jitter reduction by optical feedback for a passively mode-locked laser*, IEEE Photonics Journal **6**, 1501814 (2014).

2. L. C. Jaurigue, A. S. Pimenov, D. Rachinskii, E. Schöll, K. Lüdge, and A. Vladimirov: *Timing jitter of passively mode-locked semiconductor lasers subject to optical feedback; a semi-analytic approach*, Phys. Rev. A **92**, 053807 (2015).

3. L. C. Jaurigue, E. Schöll, and K. Lüdge: *Passively mode-locked laser coupled to two external feedback cavities*, in *Novel In-Plane Semiconductor Lasers XIV*, edited by (SPIE, 2015), vol. 9382 of *Proc. SPIE*.

4. L. C. Jaurigue, O. Nikiforov, E. Schöll, S. Breuer, and K. Lüdge: *Dynamics of a passively mode-locked semiconductor laser subject to dual-cavity optical feedback*, Phys. Rev. E **93**, 022205 (2016).

5. O. Nikiforov, L. C. Jaurigue, L. Drzewietzki, K. Lüdge, and S. Breuer: *Experimental demonstration of change of dynamical properties of a passively mode-locked semiconductor laser subject to dual optical feedback by dual full delay-range tuning*, Opt. Express **24**, 14301–14310 (2016).

6. L. C. Jaurigue, E. Schöll, and K. Lüdge: *Suppression of noise-induced modulations in multidelay systems*, Phys. Rev. Lett. **117**, 154101 (2016).

Bibliography

[AGR84] G. P. Agrawal: *Line narrowing in a single-mode injection-laser due to external optical feedback*, IEEE J. Quantum Electron. **20**, 468–471 (1984).

[AHM96] Z. Ahmed, H. F. Liu, D. Novak, Y. Ogawa, M. D. Pelusi, and D. Y. Kim: *Locking characteristics of a passively mode-locked monolithic dbr laser stabilized by optical injection*, IEEE Photonics Technol. Lett. **8**, 37–39 (1996).

[ALF68] Z. I. Alferov, V. M. Andreev, V. I. Korolkov, E. L. Portnoi, and D. N. Tretyakov: *Coherent radiation of epitaxial heterojunction structures in the AlAs-GaAs system*, Fiz. Tekh. Poluprovodn. **2**, 1545–1547 (1968).

[ALS96] P. M. Alsing, V. Kovanis, A. Gavrielides, and T. Erneux: *Lang and Kobayashi phase equation*, Phys. Rev. A **53**, 4429–4434 (1996).

[ARE84] F. T. Arecchi, G. L. Lippi, G. P. Puccioni, and J. R. Tredicce: *Deterministic chaos in laser with injected signal*, Opt. Commun. **51**, 308–315 (1984).

[ARK13] R. M. Arkhipov, A. S. Pimenov, M. Radziunas, D. Rachinskii, A. Vladimirov, D. Arsenijević, H. Schmeckebier, and D. Bimberg: *Hybrid mode locking in semiconductor lasers: Simulations, analysis, and experiments*, IEEE J. Quantum Electron. **19** (2013).

[ARK15a] R. M. Arkhipov, A. Amann, and A. Vladimirov: *Pulse repetition-frequency multiplication in a coupled cavity passively mode-locked semiconductor lasers*, Appl. Phys. B **118**, 539–548 (2015).

[ARS13] D. Arsenijević, M. Kleinert, and D. Bimberg: *Phase noise and jitter reduction by optical feedback on passively mode-locked quantum-dot lasers*, Appl. Phys. Lett. **103**, 231101 (2013).

[ARS14] D. Arsenijević, A. Schliwa, H. Schmeckebier, M. Stubenrauch, M. Spiegelberg, D. Bimberg, V. Mikhelashvili, and G. Eisenstein: *Comparison of dynamic properties of ground- and excited-state emission in p-doped InAs/GaAs quantum-dot lasers*, Appl. Phys. Lett. **104**, 181101 (2014).

[ASA84] M. Asada and A. Kameyama: *Gain and intervalence band absorption in quantum-well lasers*, IEEE J. Quantum Electron. **20**, 745–753 (1984).

[AVR00] E. A. Avrutin, J. H. Marsh, and E. L. Portnoi: *Monolithic and multi-gigahertz mode-locked semiconductor lasers: Constructions, experiments, models and applications*, IEE Proc. Optoelectron. **147**, 251 (2000).

[AVR09] E. A. Avrutin and B. M. Russell: *Dynamics and spectra of monolithic mode-locked laser diodes under external optical feedback*, IEEE J. Quantum Electron. **45**, 1456 (2009).

[BAL04] A. G. Balanov, N. B. Janson, and E. Schöll: *Control of noise-induced oscillations by delayed feedback*, Physica D **199**, 1–12 (2004).

[BAN06] U. Bandelow, M. Radziunas, A. Vladimirov, B. Hüttl, and R. Kaiser: *40GHz mode locked semiconductor lasers: Theory, simulation and experiments*, Opt. Quantum Electron. **38**, 495 (2006).

[BIM06] D. Bimberg, G. Fiol, M. Kuntz, C. Meuer, M. Lämmlin, N. N. Ledentsov, and A. R. Kovsh: *High speed nanophotonic devices based on quantum dots*, phys. stat. sol. (a) **203**, 3523–3532 (2006).

[BRA92] T. Brabec, C. Spielmann, P. F. Curley, and F. Krausz: *Kerr lens mode locking*, Opt. Lett. **17**, 1292–1294 (1992).

[BRA10a] T. Brandes: *Feedback control of quantum transport*, Phys. Rev. Lett. **105**, 060602 (2010).

[BRE10] S. Breuer, W. Elsäßer, J. G. McInerney, K. Yvind, J. Pozo, E. A. J. M. Bente, M. Yousefi, A. Villafranca, N. Vogiatzis, and J. Rorison: *Investigations of repetition rate stability of a mode-locked quantum dot semiconductor laser in an auxiliary optical fiber cavity*, IEEE J. Quantum Electron. **46**, 150 (2010).

[CHE05d] L. Chen, R. Wang, T. Zhou, and K. Aihara: *Noise-induced cooperative behavior in a multicell system*, Bioinformatics **21**, 2722–2729 (2005).

[CHO99] W. W. Chow and S. W. Koch: *Semiconductor-Laser Fundamentals* (Springer, Berlin, 1999).

[CHO11] C. U. Choe, T. Dahms, P. Hövel, and E. Schöll: *Control of synchrony by delay coupling in complex networks*, in *Proceedings of the Eighth AIMS International Conference on Dynamical Systems, Differential Equations and Applications*, edited by (American Institute of Mathematical Sciences, Springfield, MO, USA, 2011), pp. 292–301, DCDS Supplement Sept. 2011.

[COB03] C. Cobeli and A. Zaharescu: *The Haros-Farey sequence at two hundred years. a survey.*, Acta Universitatis Apulensis. Mathematics - Informatics **5**, 1–38 (2003).

[DAH11b] T. Dahms: *Synchronization in Delay-Coupled Laser Networks*, Ph.D. thesis, Technische Universität Berlin (2011).

[DEL91] P. J. Delfyett, D. H. Hartman, and S. Z. Ahmad: *Optical clock distribution using a mode-locked semiconductor laser diode system*, IEEE J. Lightwave Technol. **9**, 1646–1649 (1991).

[DER92] D. J. Derickson, R. J. Helkey, A. Mar, J. R. Karin, J. G. Wasserbauer, and J. E. Bowers: *Short pulse generation using multisegment mode-locked semconductor lasers*, IEEE J. Quantum Electron. **28**, 2186–2202 (1992).

[DHU10] O. D'Huys, R. Vicente, J. Danckaert, and I. Fischer: *Amplitude and phase effects on the synchronization of delay-coupled oscillators*, Chaos **20**, 043127 (2010).

[DRZ13] L. Drzewietzki, S. Breuer, and W. Elsäßer: *Timing phase noise reduction of modelocked quantum-dot lasers by time-delayed optoelectronic feedback*, Electron. Lett. **49**, 557–559 (2013).

[DRZ13a] L. Drzewietzki, S. Breuer, and W. Elsäßer: *Timing jitter reduction of passively mode-locked semiconductor lasers by self- and external-injection: Numerical description and experiments*, Opt. Express **21**, 16142–16161 (2013).

[DUB99a] J. L. A. Dubbeldam and B. Krauskopf: *Self-pulsations of lasers with saturable absorber: dynamics and bifurcations*, Opt. Commun. **159**, 325–338 (1999).

[EIN17] A. Einstein: *Zur Quantentheorie der Strahlung*, Phys. Z. **18**, 121–128 (1917).

[ELI96] D. Eliyahu, R. A. Salvatore, and A. Yariv: *Noise characterization of a pulse train generated by actively mode-locked lasers*, J. Opt. Soc. Am. B **13**, 1619 (1996).

[ELI97] D. Eliyahu, R. A. Salvatore, and A. Yariv: *Effect of noise on the power spectrum of passively mode-locked lasers*, J. Opt. Soc. Am. B **14**, 167 (1997).

[ENG01] K. Engelborghs, T. Luzyanina, and G. Samaey: *DDE-BIFTOOL v. 2.00: a matlab package for bifurcation analysis of delay differential equations*, Tech. Rep. TW-330, Department of Computer Science, K.U.Leuven, Belgium (2001).

[ERN10b] T. Erneux and P. Glorieux: *Laser Dynamics* (Cambridge University Press, UK, 2010).

[ERZ07] H. Erzgräber, B. Krauskopf, and D. Lenstra: *Bifurcation analysis of a semiconductor laser with filtered optical feedback*, SIAM J. Appl. Dyn. Syst. **6**, 1–28 (2007).

[FIO10] G. Fiol, D. Arsenijević, D. Bimberg, A. Vladimirov, M. Wolfrum, E. A. Viktorov, and P. Mandel: *Hybrid mode-locking in a 40 GHz monolithic quantum dot laser*, Appl. Phys. Lett. **96**, 011104 (2010).

[FIO11a] G. Fiol: *1.3μm Monolithic Mode-Locked Quantum-Dot Semiconductor Lasers*, Ph.D. thesis, Technische Universität Berlin (2011).

[FIO11] G. Fiol, M. Kleinert, D. Arsenijević, and D. Bimberg: *1.3μm range 40 GHz quantum-dot mode-locked laser under external continuous wave light injection or optical feedback*, Semicond. Sci. Technol. **26**, 014006 (2011).

[FLU07] V. Flunkert and E. Schöll: *Suppressing noise-induced intensity pulsations in semiconductor lasers by means of time-delayed feedback*, Phys. Rev. E **76**, 066202 (2007).

[FOR07] T. Fordell and A. M. Lindberg: *Experiments on the linewidth-enhancement factor of a vertical-cavity surface-emitting laser*, IEEE J. Quantum Electron. **43**, 6–15 (2007).

[GAR02] C. W. Gardiner: *Handbook of Stochastic Methods for Physics, Chemistry and the Natural Sciences* (Springer, Berlin, 2002).

[GOE83] E. O. Göbel, H. Jung, J. Kuhl, and K. Ploog: *Recombination enhancement due to carrier localization in quantum well structures*, Phys. Rev. Lett. **51**, 1588–1591 (1983).

[GOL03] D. Goldobin, M. G. Rosenblum, and A. Pikovsky: *Controlling oscillator coherence by delayed feedback*, Phys. Rev. E **67**, 061119 (2003).

[GRI09] F. Grillot, C. Y. Lin, N. A. Naderi, M. Pochet, and L. F. Lester: *Optical feedback instabilities in a monolithic InAs/GaAs quantum dot passively mode-locked laser*, Appl. Phys. Lett. **94**, 153503 (2009).

[GUC86] J. Guckenheimer and P. Holme: *Nonlinear Oscillations, Dynamical Systems, and Bifurcations of Vector Fields* (Springer, Berlin, 1986).

[HAB14] T. Habruseva, D. Arsenijević, M. Kleinert, D. Bimberg, G. Huyet, and S. P. Hegarty: *Optimum phase noise reduction and repetition rate tuning in quantum-dot mode-locked lasers*, Appl. Phys. Lett. **104**, 1–4 (2014).

[HAD04] J. Hader, J. V. Moloney, and S. W. Koch: *Structural dependence of carrier capture time in semiconductor quantum-well lasers*, Appl. Phys. Lett. **85**, 369–371 (2004).

[HAJ12] M. Haji, L. Hou, A. E. Kelly, J. Akbar, J. H. Marsh, J. M. Arnold, and C. N. Ironside: *High frequency optoelectronic oscillators based on the optical feedback of semiconductor mode-locked laser diodes*, Opt. Express **20**, 3268–3274 (2012).

[HAK83a] H. Haken: *Laser Theory* (Springer, 1983).

[HAK86] H. Haken: *Laser Light Dynamics*, vol. II (North Holland, 1st edition edition, 1986).

[HAK86a] H. Haken: *Laser Light Dynamics*, vol. I (North Holland, 1st edition edition, 1986).

[HAL62] R. N. Hall, G. E. Fenner, J. D. Kingsley, T. J. Soltys, and R. O. Carlson: *Coherent light emission from GaAs junctions*, Phys. Rev. Lett. **9**, 366–368 (1962).

[HAL66] A. Halanay: *Differential Equations: Stability, Oscillations, Time Lags* (Academic Press, 1966).

[HAL77] J. K. Hale: *Theory of functional differential equations* (Springer, New York, 1977).

[HAL93] J. K. Hale and S. M. Verduyn Lunel: *Introduction to Functional Differential Equations* (Springer, New York, 1993).

[HAR64] L. E. Hargrove, R. L. Fork, and M. A. Pollack: *Locking of he-ne laser modes induced by synchronous intracavity modulation*, Appl. Phys. Lett. **5**, 4–5 (1964).

[HAR83] C. Harder, K. Vahala, and A. Yariv: *Measurement of the linewidth enhancement factor alpha of semiconductor lasers*, Appl. Phys. Lett. **42**, 328–330 (1983).

[HAU75a] H. A. Haus: *Theory of mode locking with a slow saturable absorber*, IEEE J. Quantum Electron. **11**, 736 (1975).

[HAU93a] H. A. Haus and A. Mecozzi: *Noise of mode-locked lasers*, IEEE J. Quantum Electron. **29**, 983 (1993).

[HAU00] H. Haus: *Mode-locking of lasers*, IEEE J. Sel. Top. Quantum Electron. **6**, 1173–1185 (2000).

[HOH93] J. P. Hohimer and G. A. Vawter: *Passive mode locking of monolithic semiconductor ring lasers at 86 ghz*, Appl. Phys. Lett. **63**, 1598–1600 (1993).

[HOL00] R. Holzwarth, T. Udem, T. W. Hänsch, J. C. Knight, W. J. Wadsworth, and P. J. Russell: *Optical frequency synthesizer for precision spectroscopy*, Phys. Rev. Lett. **85**, 2264–2267 (2000).

[HOE05] P. Hövel and E. Schöll: *Control of unstable steady states by time-delayed feedback methods*, Phys. Rev. E **72**, 046203 (2005).

[HOE09b] P. Hövel: *Control of complex nonlinear systems with delay*, Ph.D. thesis, Technische Universität Berlin (2009).

[JAN03] N. B. Janson, A. G. Balanov, and E. Schöll: *Delayed feedback as a means of control of noise-induced motion*, Phys. Rev. Lett. **93**, 010601 (2004).

[JAU15] L. C. Jaurigue, A. S. Pimenov, D. Rachinskii, E. Schöll, K. Lüdge, and A. Vladimirov: *Timing jitter of passively mode-locked semiconductor lasers subject to optical feedback; a semi-analytic approach*, Phys. Rev. A **92**, 053807 (2015).

[JAU15a] L. C. Jaurigue, E. Schöll, and K. Lüdge: *Passively mode-locked laser coupled to two external feedback cavities*, in *Novel In-Plane Semiconductor Lasers XIV*, edited by (SPIE, 2015), vol. 9382 of *Proc. SPIE*.

[JAU16] L. C. Jaurigue, O. Nikiforov, E. Schöll, S. Breuer, and K. Lüdge: *Dynamics of a passively mode-locked semiconductor laser subject to dual-cavity optical feedback*, Phys. Rev. E **93**, 022205 (2016).

[JAU16a] L. C. Jaurigue, E. Schöll, and K. Lüdge: *Suppression of noise-induced modulations in multidelay systems*, Phys. Rev. Lett. **117**, 154101 (2016).

[JAV06] J. Javaloyes, J. Mulet, and S. Balle: *Passive mode locking of lasers by crossed-polarization gain modulation*, Phys. Rev. Lett. **97**, 163902 (2006).

[JAV10] J. Javaloyes and S. Balle: *Mode-locking in semiconductor fabry-pérot lasers*, IEEE J. Quantum Electron. **46** (2010).

[JAV11] J. Javaloyes and S. Balle: *Anticolliding design for monolithic passively mode-locked semiconductor lasers*, Opt. Lett. **36**, 4407–4409 (2011).

[JIA01] L. A. Jiang, M. E. Grein, H. A. Haus, and E. P. Ippen: *Noise of mode-locked semiconductor lasers*, IEEE J. Sel. Top. Quantum Electron. **7**, 159 (2001).

[JON95b] D. J. Jones, L. M. Zhang, J. E. Carroll, and D. Marcenac: *Dynamics of monolithic passively mode-locked semiconductor lasers*, IEEE J. Quantum Electron. **31**, 1051–1058 (1995).

[JUS00] W. Just, E. Reibold, K. Kacperski, P. Fronczak, J. A. Holyst, and H. Benner: *Influence of stable Floquet exponents on time-delayed feedback control*, Phys. Rev. E **61**, 5045 (2000).

[KAR94] J. R. Karin, R. J. Helkey, D. J. Derickson, R. Nagarajan, D. S. Allin, J. E. Bowers, and R. L. Thornton: *Ultrafast dynamics in field-enhanced saturable absorbers*, Appl. Phys. Lett. **64**, 676–678 (1994).

[KEF08] F. Kefelian, S. O'Donoghue, M. T. Todaro, J. G. McInerney, and G. Huyet: *RF linewidth in monolithic passively mode-locked semiconductor laser*, IEEE Photon. Technol. Lett. **20**, 1405 (2008).

[KEL03] U. Keller: *Recent developments in compact ultrafast lasers*, Nature **424**, 831–838 (2003).

[KIK82] K. Kikuchi and T. Okoshi: *Simple formula giving spectrum-narrowing ratio of semiconductor-laser output obtained by optical feedback*, Electron. Lett. **18**, 10–12 (1982).

[KIM14] B. Kim, N. Li, A. Locquet, and D. S. Citrin: *Experimental bifurcation-cascade diagram of an external-cavity semiconductor laser*, Opt. Express **22**, 2348 (2014).

[KOL86] B. Kolner and D. Bloom: *Electrooptic sampling in GaAs integrated circuits*, IEEE J. Quantum Electron. **22**, 79 (1986).

[KRA00a] B. Krauskopf, G. H. M. van Tartwijk, and G. R. Gray: *Symmetry properties of lasers subject to optical feedback*, Opt. Commun. **177**, 347–353 (2000).

[KRO91] M. S. Krol: *On the averaging method in nearly time-periodic advection-diffusion problems*, SIAM J. Appl. Math. **51**, 1622–1637 (1991).

[KUI70] D. Kuizenga and A. E. Siegman: *Fm and am mode locking of the homogeneous laser-part i: Theory*, IEEE J. Quantum Electron. **6**, 694–708 (1970).

[KUN07a] M. Kuntz, G. Fiol, M. Lämmlin, C. Meuer, and D. Bimberg: *High-speed mode-locked quantum-dot lasers and optical amplifiers*, Proc. IEEE **95**, 1767–1778 (2007).

[KUZ95] Y. A. Kuznetsov: *Elements of Applied Bifurcation Theory* (Springer, New York, 1995).

[LAN80b] R. Lang and K. Kobayashi: *External optical feedback effects on semiconductor injection laser properties*, IEEE J. Quantum Electron. **16**, 347–355 (1980).

[LAU87a] K. Y. Lau, P. L. Derry, and A. Yariv: *Ultimate limit in low threshold quantum well gaaias semiconductor lasers*, Appl. Phys. Lett. **52**, 88–90 (1987).

[LEE02c] D. C. Lee: *Analysis of jitter in phase-locked loops*, IEEE Trans. Circuits Syst. II **49**, 704 (2002).

[LEH15b] J. Lehnert: *Controlling synchronization patterns in complex networks*, Springer Theses (Springer, Heidelberg, 2016).

[LEN85] D. Lenstra, B. Verbeek, and A. Den Boef: *Coherence collapse in single-mode semiconductor lasers due to optical feedback*, IEEE J. Quantum Electron. **21**, 674–679 (1985).

[LEV95] A. M. Levine, G. H. M. van Tartwijk, D. Lenstra, and T. Erneux: *Diode lasers with optical feedback: Stability of the maximum gain mode*, Phys. Rev. A **52**, R3436 (1995), (4 pages).

[LIN10e] C. Y. Lin, F. Grillot, N. A. Naderi, Y. Li, and L. F. Lester: *rf linewidth reduction in a quantum dot passively mode-locked laser subject to external optical feedback*, Appl. Phys. Lett. **96**, 051118 (2010).

[LIN11f] C. Y. Lin, F. Grillot, and Y. Li: *Microwave characterization and stabilization of timing jitter in a quantum dot passively mode-locked laser via external optical feedback*, IEEE J. Sel. Top. Quantum Electron. **17**, 1311 (2011).

[LIN11d] C. Y. Lin, F. Grillot, N. A. Naderi, Y. Li, J. H. Kim, C. G. Christodoulou, and L. F. Lester: *RF linewidth of a monolithic quantum dot mode-locked laser under resonant feedback*, IET Optoelectron. **5**, 105 (2011).

[LIN13] B. Lingnau, W. W. Chow, E. Schöll, and K. Lüdge: *Feedback and injection locking instabilities in quantum-dot lasers: a microscopically based bifurcation analysis*, New J. Phys. **15**, 093031 (2013).

[LIN14] B. Lingnau, W. W. Chow, and K. Lüdge: *Amplitude-phase coupling and chirp in quantum-dot lasers: influence of charge carrier scattering dynamics*, Opt. Express **22**, 4867–4879 (2014).

[LIN15] B. Lingnau: *Nonlinear and Nonequilibrium Dynamics of Quantum-Dot Optoelectronic Devices*, Ph.D. thesis, TU Berlin (2015).

[LIN15a] B. Lingnau and K. Lüdge: *Analytic characterization of the dynamic regimes of quantum-dot lasers*, Photonics **2**, 402–413 (2015).

[LOE96] F. H. Loesel, M. H. Niemz, J. F. Bille, and T. Juhasz: *Laser-induced optical breakdown on hard and soft tissues and its dependence on the pulse duration: experiment and model*, IEEE J. Quantum Electron. **32**, 1717–1722 (1996).

[LUE11b] K. Lüdge: *Nonlinear Laser Dynamics - From Quantum Dots to Cryptography* (Wiley-VCH, Weinheim, 2012).

[MAI60] T. H. Maiman: *Stimulated optical radiation in ruby*, Nature **187**, 493 (1960).

[MAL06d] D. B. Malins, A. Gomez-Iglesias, S. J. White, W. Sibbett, A. Miller, and E. U. Rafailov: *Ultrafast electroabsorption dynamics in an InAs quantum dot saturable absorber at 1.3 μm*, Appl. Phys. Lett. **89**, 171111 (2006).

[MAR14c] M. Marconi, J. Javaloyes, S. Balle, and M. Giudici: *How lasing localized structures evolve out of passive mode locking*, Phys. Rev. Lett. **112** (2014).

[MAS02] C. Masoller: *Noise-induced resonance in delayed feedback systems*, Phys. Rev. Lett. **88**, 034102 (2002).

[MER09] K. Merghem, R. Rosales, S. Azouigui, A. Akrout, A. Martinez, F. Lelarge, G. H. Duan, G. Aubin, and A. Ramdane: *Low noise performance of passively mode locked quantum-dash-based lasers under external optical feedback*, Appl. Phys. Lett. **95**, 131111 (2009).

[MIC14a] W. Michiels and S. I. Niculescu: *Stability, Control, and Computation for Time-Delay Systems: An Eigenvalue-Based Approach, Second Edition*, Advances in Design and Control (SIAM, Philadelphia, 2014).

[MOR88] J. Mørk, B. Tromborg, and P. L. Christiansen: *Bistability and low-frequency fluctuations in semiconductor lasers with optical feedback: a theoretical analysis*, IEEE J. Quantum Electron. **24**, 123–133 (1988).

[MOR92] J. Mørk, B. Tromborg, and J. Mark: *Chaos in semiconductor lasers with optical feedback-Theory and experiment*, IEEE J. Quantum Electron. **28**, 93–108 (1992).

[MOS14] V. Moskalenko, J. Javaloyes, S. Balle, M. K. Smit, and E. A. J. M. Bente: *Theoretical study of colliding pulse passively mode-locked semiconductor ring lasers with an intracavity machâzehnder modulator*, IEEE J. Quantum Electron. **50** (2014).

[MOS15] V. Moskalenko, K. A. Williams, and E. A. J. M. Bente: *Integrated extended-cavity 1.5 -μm semiconductor laser switchable between self- and anti-colliding pulse passive mode-locking configuration*, IEEE J. Sel. Top. Quantum Electron. **21**, 1101306 (2015).

[MUL06] J. Mulet and J. Mørk: *Analysis of timing jitter in external-cavity mode-locked semiconductor lasers*, IEEE J. Quantum Electron. **42**, 249 (2006).

[NAK05] H. Nakao, K. Arai, K. Nagai, Y. Tsubo, and Y. Kuramoto: *Synchrony of limit-cycle oscillators induced by random external impulses*, Phys. Rev. E **72**, 026220 (2005).

[NAT62] M. I. Nathan, W. P. Dumke, G. Burns, J. F.H. Dill, and G. Lasher: *Stimulated emission of radiation from GaAs p-n junctions*, Appl. Phys. Lett. **1**, 62–64 (1962).

[NEW74] G. New: *Pulse evolution in mode-locked quasi-continuous lasers*, IEEE J. Quantum Electron. **10**, 115 (1974).

[HOL62] J. N. Holonyak and S. F. Bevacqua: *Coherent (visible) light emission from $Ga(As_{1-x}P_x)$ junctions*, Appl. Phys. Lett. **1**, 82–83 (1962).

[NIK16] O. Nikiforov, L. C. Jaurigue, L. Drzewietzki, K. Lüdge, and S. Breuer: *Experimental demonstration of change of dynamical properties of a passively mode-locked semiconductor laser subject to dual optical feedback by dual full delay-range tuning*, Opt. Express **24**, 14301–14310 (2016).

[NIZ06] M. Nizette, D. Rachinskii, A. Vladimirov, and M. Wolfrum: *Pulse interaction via gain and loss dynamics in passive mode locking*, Physica D **218**, 95–104 (2006).

[OSI87] M. Osinski and J. Buus: *Linewidth broadening factor in semiconductor lasers – an overview*, IEEE J. Quantum Electron. **23**, 9–29 (1987).

[OTT10] C. Otto, K. Lüdge, and E. Schöll: *Modeling quantum dot lasers with optical feedback: sensitivity of bifurcation scenarios*, phys. stat. sol. (b) **247**, 829–845 (2010).

[OTT12] C. Otto, B. Globisch, K. Lüdge, E. Schöll, and T. Erneux: *Complex dynamics of semiconductor quantum dot lasers subject to delayed optical feedback*, Int. J. Bifurcation Chaos **22**, 1250246 (2012).

[OTT12a] C. Otto, K. Lüdge, A. Vladimirov, M. Wolfrum, and E. Schöll: *Delay induced dynamics and jitter reduction of passively mode-locked semiconductor laser subject to optical feedback*, New J. Phys. **14**, 113033 (2012).

[OTT14] C. Otto: *Dynamics of Quantum Dot Lasers – Effects of Optical Feedback and External Optical Injection*, Springer Theses (Springer, Heidelberg, 2014).

[OTT14b] C. Otto, L. C. Jaurigue, E. Schöll, and K. Lüdge: *Optimization of timing jitter reduction by optical feedback for a passively mode-locked laser*, IEEE Photonics Journal **6**, 1501814 (2014).

[PAL91] J. Palaski and K. Y. Lau: *Parameter ranges for ultrahigh frequency mode locking of semiconductor lasers*, Appl. Phys. Lett. **59**, 7–9 (1991).

[PAN12] A. Panchuk, D. P. Rosin, P. Hövel, and E. Schöll: *Synchronization of coupled neural oscillators with heterogeneous delays*, Int. J. Bifurcation Chaos **23**, 1330039 (2013).

[PAS04] R. Paschotta: *Noise of mode-locked lasers (part i): numerical model*, Appl. Phys. B: Lasers and Optics **79**, 153–162 (2004).

[PAS04a] R. Paschotta: *Noise of mode-locked lasers (part ii): timing jitter and other fluctuations*, Appl. Phys B: Lasers and Optics **79**, 163–173 (2004).

[PAS06] R. Paschotta, A. Schlatter, S. C. Zeller, H. R. Telle, and U. Keller: *Optical phase noise and carrier-envelope offset noise of mode-locked lasers*, Appl. Phys. B: Lasers and Optics **82**, 265–273 (2006).

[PIM14b] A. S. Pimenov, T. Habruseva, D. Rachinskii, S. P. Hegarty, G. Huyet, and A. Vladimirov: *The effect of dynamical instability on timing jitter in passively mode-locked quantum-dot lasers*, Opt. Lett. **39**, 6815 (2014).

[PIM14] A. S. Pimenov, E. A. Viktorov, S. P. Hegarty, T. Habruseva, G. Huyet, D. Rachinskii, and A. Vladimirov: *Bistability and hysteresis in an optically injected two-section semiconductor laser*, Phys. Rev. A **89**, 052903 (2014).

[POM05] J. Pomplun: *Time-delayed feedback control of noise-induced oscillations*, Master's thesis, TU Berlin (2005).

[POM05a] J. Pomplun, A. Amann, and E. Schöll: *Mean field approximation of time-delayed feedback control of noise-induced oscillations in the Van der Pol system*, Europhys. Lett **71**, 366 (2005).

[POT02a] O. Pottiez, O. Deparis, R. Kiyan, M. Haelterman, P. Emplit, P. Mégret, and M. Blondel: *Supermode noise of harmonically mode-locked erbium fiber lasers with composite cavity*, IEEE J. Quantum Electron. **38**, 252–259 (2002).

[PYR92] K. Pyragas: *Continuous control of chaos by self-controlling feedback*, Phys. Lett. A **170**, 421 (1992).

[RAD11a] M. Radziunas, A. Vladimirov, E. A. Viktorov, G. Fiol, H. Schmeckebier, and D. Bimberg: *Pulse broadening in quantum-dot mode-locked semiconductor lasers: Simulation, analysis, and experiments*, IEEE J. Quantum Electron. **47**, 935–943 (2011).

[RAF07] E. U. Rafailov, M. A. Cataluna, and W. Sibbett: *Mode-locked quantum-dot lasers*, Nature Photon. **1**, 395–401 (2007).

[REB10] N. Rebrova, T. Habruseva, G. Huyet, and S. P. Hegarty: *Stabilization of a passively mode-locked laser by continuous wave optical injection*, Appl. Phys. Lett. **97**, 1–3 (2010).

[REB11] N. Rebrova, G. Huyet, D. Rachinskii, and A. Vladimirov: *Optically injected mode-locked laser*, Phys. Rev. E **83**, 066202 (2011).

[ROS04] M. G. Rosenblum and A. Pikovsky: *Delayed feedback control of collective synchrony: An approach to suppression of pathological brain rhythms*, Phys. Rev. E **70**, 041904 (2004).

[ROS11d] M. Rossetti, P. Bardella, and I. Montrosset: *Modeling passive mode-locking in quantum dot lasers: A comparison between a finite- difference traveling-wave model and a delayed differential equation approach*, IEEE J. Quantum Electron. **47**, 569 (2011).

[ROS11c] M. Rossetti, P. Bardella, and I. Montrosset: *Time-domain travelling-wave model for quantum dot passively mode-locked lasers*, IEEE J. Quantum Electron. **47**, 139 (2011).

[ROT07] V. Rottschäfer and B. Krauskopf: *The ECM-backbone of the Lang-Kobayashi equations: A geometric picture*, Int. J. Bifurcation Chaos **17**, 1575–1588 (2007).

[SAN90] S. Sanders, A. Yariv, J. Paslaski, J. E. Ungar, and H. A. Zarem: *Passive mode locking of a two-section multiple quantum well laser at harmonics of the cavity round-trip frequency*, Appl. Phys. Lett. **58**, 681–683 (1990).

[SCH88j] E. Schöll: *Dynamic theory of picosecond optical pulse shaping by gain-switched semiconductor laser amplifiers*, IEEE J. Quantum Electron. **24**, 435–442 (1988).

[SCH04b] E. Schöll, A. G. Balanov, N. B. Janson, and A. B. Neiman: *Controlling stochastic oscillations close to a Hopf bifurcation by time-delayed feedback*, Stoch. Dyn. **5**, 281 (2005).

[SCH07] E. Schöll and H. G. Schuster (Editors): *Handbook of Chaos Control* (Wiley-VCH, Weinheim, 2008), Second completely revised and enlarged edition.

[SCH10g] H. Schmeckebier, G. Fiol, C. Meuer, D. Arsenijević, and D. Bimberg: *Complete pulse characterization of quantum dot mode-locked lasers suitable for optical communication up to 160 Gbit/s*, Opt. Express **18**, 3415 (2010).

[SCH13b] I. Schneider: *Delayed feedback control of three diffusively coupled Stuart-Landau oscillators: a case study in equivariant Hopf bifurcation*, Phil. Trans. R. Soc. A **371**, 20120472 (2013).

[SIE11a] J. Sieber and R. Szalai: *Characteristic matrices for linear periodic delay differential equations*, SIAM J. Appl. Dyn. Syst. **10**, 129–147 (2011).

[SIG89] D. Sigeti and W. Horsthemke: *Pseudo-regular oscillations induced by external noise*, J. Stat. Phys. **54**, 1217 (1989).

[SIM12a] H. Simos, C. Simos, C. Mesaritakis, and D. Syvridis: *Two-section quantum-dot mode-locked lasers under optical feedback: Pulse broadening and harmonic operation*, IEEE J. Quantum Electron. **48**, 872 (2012).

[SIM13] H. Simos, C. Mesaritakis, T. Xu, P. Bardella, I. Montrosset, and D. Syvridis: *Numerical analysis of passively mode-locked quantum-dot lasers with absorber section at the low-reflectivity output facet*, IEEE J. Quantum Electron. **49**, 3–10 (2013).

[SIM14] C. Simos, H. Simos, C. Mesaritakis, A. Kapsalis, and D. Syvridis: *Pulse and noise properties of a two section passively mode-locked quantum dot laser under long delay feedback*, Opt. Commun. **313**, 248–255 (2014).

[SLE13] S. Slepneva, B. Kelleher, B. O'Shaughnessy, S. P. Hegarty, A. Vladimirov, and G. Huyet: *Dynamics of fourier domain mode-locked lasers*, Opt. Express **21**, 19240–19251 (2013).

[SLO15] P. Slowinski, B. Krauskopf, and S. Wieczorek: *Mode structure of a semiconductor laser with feedback from two external filters*, Discret. Contin. Dyn. S. B **20**, 519–586 (2015).

[SMI70] P. W. Smith: *Mode-locking of lasers*, Proc. IEEE **58**, 1342–1357 (1970).

[SOL93] O. Solgaard and K. Y. Lau: *Optical feedback stabilization of the intensity oscillations in ultrahigh-frequency passively modelocked monolithic quantum-well lasers*, IEEE Photonics Technol. Lett. **5**, 1264 (1993).

[SOR13] M. C. Soriano, J. García-Ojalvo, C. R. Mirasso, and I. Fischer: *Complex photonics: Dynamics and applications of delay-coupled semiconductors lasers*, Rev. Mod. Phys. **85**, 421–470 (2013).

[SPU03] G. J. Spühler, P. S. Golding, L. Krainer, I. J. Kilburn, P. A. Crosby, M. Brownell, K. J. Weingarten, R. Paschotta, M. Haiml, R. Grange, and U. Keller: *Multi-wavelength source with 25 ghz channel spacing tunable over c-band*, Electronics Letters **39** (2003).

[STE04b] R. Steuer: *Effects of stochasticity in models of the cell cycle: from quantized cycle times to noise-induced oscillations*, J. Theor. Biol. **228**, 293–301 (2004).

[SUG05] M. Sugawara, N. Hatori, M. Ishida, H. Ebe, Y. Arakawa, T. Akiyama, K. Otsubo, T. Yamamoto, and Y. Nakata: *Recent progress in self-assembled quantum-dot optical devices for optical telecommunication: temperature-insensitive 10 Gbs directly modulated lasers and 40 Gbs signal-regenerative amplifiers*, J. Phys. D **38**, 2126–2134 (2005).

[SZA06] R. Szalai, G. Stepan, and S. J. Hogan: *Continuation of bifurcations in periodic delay-differential equations using characteristic matrices*, SIAM J. Sci. Comput. **28**, 1301–1317 (2006).

[TES12] G. Teschl: *Ordinary Differential Equations and Dynamical Systems* (American Mathematical Society, 2012).

[TRO94] B. Tromborg, H. E. Lassen, and H. Olesen: *Traveling wave analysis of semiconductor lasers: modulation responses, mode stability and quantum mechanical treatment of noise spectra*, IEEE J. Quantum Electron. **30**, 939 (1994).

[TUC88] R. S. Tucker, G. Eisenstein, and S. K. Korotky: *Optical time-division multiplexing for very high bit-rate transmission*, IEEE J. Lightwave Technol. **6**, 1737–1749 (1988).

[UDE02] T. Udem, R. Holzwarth, and T. W. Hänsch: *Optical frequency metrology*, Nature **416**, 233–237 (2002).

[UKH04] A. A. Ukhanov, A. Stintz, P. G. Eliseev, and K. J. Malloy: *Comparison of the carrier induced refractive index, gain, and linewidth enhancement factor in quantum dot and quantum well lasers*, Appl. Phys. Lett. **84**, 1058–1060 (2004).

[LIN86] D. von der Linde: *Characterization of the noise in continuously operating mode-locked lasers*, Appl. Phys. B **39**, 201 (1986).

[VIC08] R. Vicente, L. L. Gollo, C. R. Mirasso, I. Fischer, and P. Gordon: *Dynamical relaying can yield zero time lag neuronal synchrony despite long conduction delays*, Proc. Natl. Acad. Sci. U.S.A. **105**, 17157 (2008).

[VLA04a] A. Vladimirov and D. V. Turaev: *New model for mode-locking in semiconductor lasers*, Radiophys.Quantum Electron. **47**, 769–776 (2004).

[VLA04] A. Vladimirov, D. V. Turaev, and G. Kozyreff: *Delay differential equations for mode-locked semiconductor lasers*, Opt. Lett. **29**, 1221 (2004).

[VLA05] A. Vladimirov and D. V. Turaev: *Model for passive mode locking in semiconductor lasers*, Phys. Rev. A **72**, 033808 (2005).

[VLA09] A. Vladimirov, A. S. Pimenov, and D. Rachinskii: *Numerical study of dynamical regimes in a monolithic passively mode-locked semiconductor laser*, IEEE J. Quantum Electron. **45**, 462–46 (2009).

[VLA10] A. Vladimirov, U. Bandelow, G. Fiol, D. Arsenijević, M. Kleinert, D. Bimberg, A. S. Pimenov, and D. Rachinskii: *Dynamical regimes in a monolithic passively mode-locked quantum dot laser*, J. Opt. Soc. Am. B **27**, 2102 (2010).

[VLA11] A. Vladimirov, D. Rachinskii, and M. Wolfrum: *Modeling of passively mode-locked semiconductor lasers*, in *Nonlinear Laser Dynamics - From Quantum Dots to Cryptography*, edited by K. Lüdge (Wiley-VCH, Weinheim, 2011), Reviews in Nonlinear Dynamics and Complexity, chapter 8, pp. 183–213.

[TAR95a] G. H. M. van Tartwijk and D. Lenstra: *Semiconductor laser with optical injection and feedback*, Quantum Semiclass. Opt. **7**, 87–143 (1995).

[TAR98a] G. H. M. van Tartwijk and G. P. Agrawal: *Laser instabilities: a modern perspective*, Prog. Quantum Electronics **22**, 43–122 (1998).

[WU00] C. Wu and N. K. Dutta: *High-repetition-rate optical pulse generation using a rational harmonic mode-locked fiber laser*, IEEE J. Quantum Electron. **36** (2000).

[WU12a] Y. Wu, W. Liu, J. Xiao, W. Zou, and J. Kurths: *Effects of spatial frequency distributions on amplitude death in an array of coupled landau-stuart oscillators*, Phys. Rev. E **85** (2012).

[YAM93] M. Yamada: *A theoretical analysis of self-sustained pulsation phenomena in narrow-stripe semiconductor lasers*, IEEE J. Quantum Electron. **29**, 1330–1336 (1993).

[YAN07a] J. Yang, Y. Jin-Long, W. Yao-Tian, Z. Li-Tai, and Y. En-Ze: *An optical domain combined dual-loop optoelectronic oscillator*, IEEE Photon. Technol. Lett. **19**, 807–809 (2007).

[YAN09] S. Yanchuk and P. Perlikowski: *Delay and periodicity*, Phys. Rev. E **79**, 046221 (2009).

[YAN14] S. Yanchuk and G. Giacomelli: *Pattern formation in systems with multiple delayed feedbacks*, Phys. Rev. Lett. **112**, 174103 (2014).

[YUH98] L. Yuhua, L. Caiyun, W. Jian, W. Boyu, and G. Yizhi: *Novel method to simultaneously compress pulses and suppress supermode noise in actively mode-locked fiber ring laser*, IEEE Photonics Tech. Lett. **10** (1998).

[ZHU97] B. Zhu, I. H. White, R. V. Penty, A. Wonfor, E. Lach, and H. D. Summers: *Theoretical analysis of timing jitter in monolithic multisection mode-locked dbr laser diodes*, IEEE J. Quantum Electron. **33**, 1216–1220 (1997).

[ZHU15] J. P. Zhuang and S. C. Chan: *Phase noise characteristics of microwave signals generated by semiconductor laser dynamics*, Opt. Express **23**, 2777–2797 (2015).

[ZHU15a] J. P. Zhuang, V. Pusino, Y. Ding, S. C. Chan, and M. Sorel: *Experimental investigation of anti-colliding pulse mode-locked semiconductor lasers*, Opt. Lett. **40**, 617–620 (2015).

[ZIG09] M. Zigzag, M. Butkovski, A. Englert, W. Kinzel, and I. Kanter: *Zero-lag synchronization of chaotic units with time-delayed couplings*, Europhys. Lett. **85**, 60005 (2009).

Acknowledgments

First of all, I would like to thank my supervisor Prof. Dr. Kathy Lüdge for providing a supportive and stimulating work environment, and for always being available for discussions. The many discussions we had have helped me gain a deeper understanding of all topics surrounding my thesis. Moreover, I am grateful for all of the proofreading she has done for me over the years.

I am grateful to my co-supervisor Prof. Dr. Eckehard Schöll, PhD for giving me the opportunity to work in his group. Being a member of the extended AG Schöll has allowed me to interact with many distinguished scientists. Furthermore, I would like to especially thank him for his help in the paper submission and revision processes.

I would like to thank the members of AG Lüdge, especially Benjamin Lingnau, André Röhm, Christoph Redlich and Roland Aust. In particular, I thank Benjamin for the countless scientific discussions, for the many times he helped me with computer problems and for proofreading this thesis. I am also grateful to André for all his support.

I would like to thank Prof. Dr. Bernd Krauskopf for the time I spent visiting his group and for helping me with the path continuation.

I would like to thank Dr. Andrei Vladimirov and Dr. Alexander Pimenov for our fruitful collaborative work.

I would like to thank Dr. Stefan Breuer for our theoretical-experimental collaborations and for interesting discussions about the experiments.

I would like to thank Dr. Julien Javaloyes for taking the time to be the external reviewer of my thesis, and for the discussions we have had at conferences.

Finally, I would like to thank Jonnel for all of his love and support.